INFORMATION TO USERS

This manuscript has been reproduced from the microfilm master. UMI films the text directly from the original or copy submitted. Thus, some thesis and dissertation copies are in typewriter face, while others may be from any type of computer printer.

The quality of this reproduction is dependent upon the quality of the copy submitted. Broken or indistinct print, colored or poor quality illustrations and photographs, print bleedthrough, substandard margins, and improper alignment can adversely affect reproduction.

In the unlikely event that the author did not send UMI a complete manuscript and there are missing pages, these will be noted. Also, if unauthorized copyright material had to be removed, a note will indicate the deletion.

Oversize materials (e.g., maps, drawings, charts) are reproduced by sectioning the original, beginning at the upper left-hand corner and continuing from left to right in equal sections with small overlaps.

Photographs included in the original manuscript have been reproduced xerographically in this copy. Higher quality 6" x 9" black and white photographic prints are available for any photographs or illustrations appearing in this copy for an additional charge. Contact UMI directly to order.

Bell & Howell Information and Learning
300 North Zeeb Road, Ann Arbor, MI 48106-1346 USA

UMI®
800-521-0600

ELECTROCHEMICAL MEASUREMENTS AND THERMODYNAMIC PROPERTIES OF ALKALI FULLERIDES

By

JOON HONG KIM, M.S.

A Thesis

Submitted to the School of Graduate Studies

in Partial Fulfillment of the Requirements

for the Degree

Doctor of Philosophy

McMaster University

EMF MEASUREMENTS AND THERMODYNAMICS OF ALKALI FULLERIDES

DOCTOR OF PHILOSOPHY (1997) McMaster University

(Materials Science and Engineering) Hamilton, Ontario

TITLE: Electrochemical Measurements and Thermodynamic Properties of Alkali Fullerides.

AUTHOR: Joon Hong Kim, M.S. (Stevens Institute of Technology)

SUPERVISOR: Professor A. Petric

NUMBER OF PAGES: xiv, 238

Abstract

The systems Na - C_{60}, K - C_{60} and Sr - Al were studied by the Electromotive force (EMF) technique using electrochemical cells which were composed of beta-alumina tubes glass-sealed to α-alumina lids. EMF measurements of Na_xC_{60} at 599 K indicated solid solution regions at $1.7 < x < 3$ and $3.3 < x < 12$. (A sudden drop in EMF in the range of $3.3 < x < 3.7$ allows the possibility of a nearly stoichiometric phase in this range). No compounds were observed in the composition range of $0 < x < 1.7$. From EMF measurements, the Gibbs energies of mixing of $\frac{1}{4}Na_3C_{60}$ and $\frac{1}{7}Na_6C_{60}$ were determined as 85 and 81 kJ/mol, respectively. From EMF measurements of K_xC_{60} at 572 K, the Gibbs energies of mixing of $\frac{1}{x+1}K_xC_{60}$ were found to be 83, 117, 120 and 121 kJ/mol for x = 1, 3, 4 and 6, respectively. The ideal interstitial solution model of the Na - C_{60} system indicates that tetrahedral sites are favored by Na. The difference between Na_xC_{60} and K_xC_{60} seems to be related to the ionic size effects. EMF measurements of the Sr - Al system using a Sr beta-alumina solid electrolyte were unsuccessful. Thermodynamic consideration suggests that Sr beta-alumina is not compatible with pure Al or Sr.

A model for the intermolecular interactions between C_{60} molecules, based on the effective Lennard-Jones interaction centers and local charge distribution, was proposed and tested for the $Pa\bar{3}$ structure of pure C_{60} by both regular solution and cluster variation methods. As the effective Lennard-Jones interaction centers move from carbon atoms to

the centers of adjacent double bonds of the same molecule, the $Pa\bar{3}$ structure in which the pentagons of a molecule face double bonds of nearest molecules becomes more stable relative to the $Pa\bar{3}$ structure in which the hexagons face double bonds. By assigning charges to carbon atoms and to the centers of bonds, we can model the increase in activation energy for the jump between 22 and 82 degree orientations.

External vibrational frequencies of simple cubic (*sc*) C_{60} and M_3C_{60} (M = K, Rb) were computed by the harmonic approximation, using the model for the intermolecular interactions between C_{60} molecules. The computed frequencies of phonons are quite consistent with experiments. However, for librons there are some differences between computed and observed frequencies, which suggests that the harmonic approximation is not adequate for librons. By using group theory, the external vibrational modes of *sc* C_{60} at Γ, Σ, Δ and Λ are labeled and the corresponding symmetry adapted vectors are obtained.

Thermodynamic properties of *sc* C_{60} were computed using the canonical partition function. The lattice energy and configurational entropy terms are estimated by the regular solution model. The dispersion curves were approximated by the Debye model for acoustic modes and the Einstein model for optical modes. The Debye characteristic temperature and optimum Grüneisen constant were determined as 54.14 K and 7.5, respectively. The contribution of the 82 degree orientation of the molecules to the constant volume heat capacity was found to be significant in the temperature range of 20 to 100 K.

ACKNOWLEDGMENTS

I should like to acknowledge the people who helped me in studying at McMaster University: Dr. Petric, my supervisor, for his kindness and helpful instructions; Tadek and Gord for their technical help. I already miss the friends at the school: Ron, Jason, Pash, Jinhyung, Heekwon, Dongkyun, Sungkyu and many others. I cannot thank my family too much for their patient support and encouragement. This thesis is dedicated to my parents, wife Junghye and precious daughter Patricia.

Table of Contents

List of Figures

List of Tables

I. Introduction

Solid electrolytes have many potential applications in devices such as sensors, pumps, batteries and ion-selective membranes [1,2,3]. Such devices would operate on simple and straightforward electrochemical principles which should allow simple setup, control and measurement of thermochemical properties. However, the technique is materials dependent (or limited). Development of new electrolytes as well as improvements in their processing have become prominent research topics.

Beta-alumina is a well-known solid electrolyte which has been studied for decades. The ideal structure of Na β-alumina consists of alternating spinel-like blocks $(Al_9O_{16})^{-5}$ and conduction planes $(NaAl_2O)^{+5}$ [4,5]. The high sodium ionic conductivity is due to both a low energy barrier for jumps between sites and the number of sites available which is greater than the number of Na ions. As Na beta-alumina can be ion-exchanged with monovalent and multivalent ions [6,7], it is used as a host for preparing a variety of ionic conductors. This thesis demonstrates the use of beta-alumina for thermodynamic measurements of the Na - C_{60} and K - C_{60} binary systems as one of the electrochemical applications.

The recent discovery of C_{60} fullerene, the third major form of pure carbon, opened a new era in chemistry [8,9,10]. It is a very attractive material due not only to its symmetry but also to its potential applications. The stable C_{60} molecule can form a variety

of compounds [11] including the alkali metal doped C_{60} among which K, Rb and Cs fullerides exhibit superconductivity with critical temperatures as high as 41 K [12,13,14,15]. Because this family of superconductors has a simple intercalated face-centered-cubic structure [16,17] with three dimensional superconductivity, they may offer a window into the still mysterious mechanism of superconductivity [9]. Indeed, a simple correlation between lattice parameters and T_c's of fullerides has been proposed [17]. Though the absence of superconductivity in the smaller alkali (Li, Na) fullerides could be explained by the disproportionation of A_3C_{60} into A_2C_{60} and A_6C_{60} [15], the phase diagrams of these systems are not clear. Difficulties in synthesizing some fullerides (Li, Na, Cs, and their mixtures) [14,15,17] and conflicting structures of Na_xC_{60} have been reported [14,15]. When we consider the large size of interstitial sites (1.12 Å for tetrahedral sites and 2.07 Å for octahedral sites) [18] in the pristine C_{60}, the slow rate of reaction in alkali - C_{60} is unusual. The high degree of internal freedom [19], especially rotational or orientational, should play an important role in these compounds. The structural difference [15] between light alkali (Li, Na) and heavy alkali (K, Rb) fullerides is also interesting. Thermodynamic data will provide fundamental information about the intercalation process in these systems. In this paper, a simple model based on ideal interstitial solid solution has been developed to explain the phase relations in Na_xC_{60} which are obtained by the EMF measurements.

The thermodynamic properties of C_{60} have many interesting features. Above 400 K, the molecules, cubic-close-packed, rotate continuously [20]. That is to say, they are

restricted to solid-like freedom in translation but exhibit liquid-like freedom in rotation. Below 260 K, the molecules are ordered in orientation [21]. However, they are ratcheting between two orientations of which one is more favorable in energy by about 10 meV [22]. An understanding of the origins and magnitudes of intermolecular forces, and their dependence on molecular properties and intermolecular separation and orientation, is essential for understanding many properties of molecular crystals [23]. In this paper, a model for intermolecular interactions between C_{60} molecules has been developed based on van der Waals and local-charge interactions and has been used to compute some thermodynamic properties of pure alkali C_{60}. This model can be used to predict structures, lattice energies and the relative stability of proposed new C_{60} compounds.

In terms of statistical mechanics [24,25], the thermodynamics of solids may be separated by the static part and dynamic part. The static part consists of the lattice energy and configurational entropy terms. The dynamic part contains the thermal energy terms which are determined by the dispersion curves, the relation between the frequency and wave vector of phonons. Thus, the partition functions for the static part and dynamic part can be treated separately and from the resulting Helmholtz free energy we can derive thermodynamic properties using the relations between them [26]. The new model for intermolecular interactions has been used to compute the lattice energy and the vibrational frequencies by harmonic approximation [27]. To complete dispersion curves, the frequencies should be labeled by group theory [28]. The purpose of computing properties

of C_{60} is not only to predict the properties of C_{60} but also to test the model by comparison with experimental results.

This work consists of three parts; 1) preparation of solid electrolyte cells, 2) EMF measurements of alkali fullerides, and 3) modeling of the systems. The background on solid electrolytes, beta-alumina and alkali fullerides is reviewed in section II.1 to II.3. Principles of electrochemistry related to thermodynamic measurements are discussed in section II.4 which includes the concept of electrochemical potential, definitions of diffusion coefficients and Onsager's equation. Thermodynamic properties and their relations are given in section II.5. Section II.5.a introduces the statistical mechanics of solids, the quasi-harmonic model and the Grüneisen constant. In section II.5.b, the Ising model, lattice gas model, regular and quasi-regular solutions, order-disorder transformation and cluster variation method are discussed. Section II.6 provides formulations to obtain dispersion curves related to the dynamic part of thermodynamics of solids. In section II.6.a, the dynamical matrix is expressed by Born-von Karman constants and the Ewald Kellerman method is introduced to treat Coulomb interactions. Application of group theory to lattice dynamics is discussed in section II.6.b. Experimental procedure is given in chapter III. The fabrication of beta-alumina tubes and the assembly of cells are described in section IV.1 to 3. The electrochemical measurements of Na-C_{60} and K-C_{60} are given in IV.5 and IV.10. The static part of thermodynamics of C_{60} is discussed in section IV.6 which contains models for intermolecular interactions between C_{60} molecules and lattice statistics of *sc* and *fcc* C_{60}. Lattice dynamics and group theory of C_{60} are presented

in section IV.7 and IV.8. Using the results of section IV.6 to IV.8, the thermodynamic properties of C_{60} have been computed in section IV.9. The compatibility of Sr beta-alumina and pure Al is discussed in section IV.11.

II. Literature review

II.1) Solid electrolytes

Solid electrolytes are materials with high ionic conductivity and low electronic or hole conductivity (< 1%) [29]. These materials are also named superionic solids or fast ionic conductors. The electrical conductivities of useful solid electrolytes are in the range of 0.01 - 1 $\Omega^{-1}cm^{-1}$. A list of electrical conductivities of various materials at room temperature is shown below for comparison.

Solid electrolyte; Na-β-alumina [9]	$\sigma = 2 \times 10^{-2}\ \Omega^{-1}cm^{-1}$
RbAg4I5 [30]	$\sigma = 2.7 \times 10^{-1}$
Aqueous solution; 0.1 M NaCl [31]	$\sigma = 1.1 \times 10^{-1}$
Metal; Copper [31]	$\sigma = 6 \times 10^{5}$
Semiconductor; Ge (pure) [32]	$\sigma = 2.5 \times 10^{-2}$
Insulator; SiO_2 glass [32]	$\sigma \leq 10^{-14}$

The total electrical conductivity of a material is the sum of the conductivities contributed by each species in the material. The transference number (t) of the species j is defined by the equation [32];

$$t_j = \sigma_j / \sigma_t \qquad \text{(II.1.1)}$$

where σ_j is the conductivity due to the migration of the species j and σ_t is the total conductivity. For good solid electrolytes, the transference numbers of conducting ions are almost unity and those of electrons and holes are less than 10^{-4}. An electronic band gap larger than T/300 eV is required for low electronic conductivity, less than 10^{-6} $ohm^{-1}cm^{-1}$ [29].

Solid electrolytes can be classified by the material type as crystalline materials [33], glasses [34],polymers [35], and composites [36,37]. The transport mechanisms are described classically by the vacancy, interstitial, and interstitialcy models [31]. However, the mechanisms are unique to each material, although still not clearly identified in many cases. The ionic conductivity can be related to the chemical diffusion coefficient D of the ideal solution by Nernst-Einstein equation [102];

$$\sigma = \frac{Z^2 e^2 cD}{kT} \qquad \text{(II.1.2)}$$

Generally accepted common structural features characteristic of solid electrolytes are [34];

1) a highly ordered structural array in the form of tunnels, layers, or three dimensional arrays

2) a highly disordered complementary sublattice in which the number of equivalent sites is greater than the number of available ions to fill them.

For amorphous materials, the first point should be replaced by a more general statement:

3) a open framework with an abundance of physically interconnected and accessible sites and relatively large windows connecting these sites.

The following are common mobile ions in solid electrolytes:

1) protonic (H^+, NH_4^+, $H(H_2O)_x^+$ etc.) [38]

2) anionic (O^{2-}, F^-, Cl^-) [39,40]

3) alkaline (Li^+, Na^+, K^+, Rb^+) [29,41]

4) IB elements (Ag^+, Cu^+) [30,42]

5) multivalent (Ca^{2+}, Ba^{2+}, Cd^{2+}) [43]

Solid electrolytes have many applications [1,2,3]. Because galvanic sensors with solid electrolytes can be used for direct and rapid measurements of concentrations in gases and liquids, they are suitable for automated process control. Solid electrolytes can also be used in energy storage and conversion systems. Solid state primary and secondary batteries, fuel cells, and load-leveling storage batteries are major applications that offer advantages such as high efficiency and low pollution. Solid electrolytes have many other applications such as ionic or atomic pumps, thermoelectric devices, high temperature mixed conductors, electrochromic devices, etc.

II.2) Beta-alumina

II.2.a) Crystal structure [44]

The Na beta-aluminas are composed of alternating spinel-like blocks and conduction planes. The spinel-like blocks consist of four close-packed oxygen layers with Al^{3+} ions in both octahedral and tetrahedral interstices (figure II.2.1). The conduction planes are loosely packed with conducting cations (Na^+ for Na beta-alumina) and oxygen ions. The oxygen ions in the conduction planes form Al-O-Al bonds which hold the adjacent blocks apart. Beta-alumina may refer to either β- or β″-aluminas. (Hereafter, beta-alumina refers to both β- and β″-alumina phases unless otherwise specified.)

β-alumina containing a two-fold screw axis has a hexagonal structure (space group $P6_3/mmc$) with the ideal formula $Na_2O{\cdot}11Al_2O_3$ ($NaAl_{11}O_{17}$) . The unit cell consists of two spinel-like blocks. The conduction plane perpendicular to *c* is a mirror plane and the conducting cations are in the middle of the conduction planes. There are three types of sites for conducting ions: one Beever-Ross, one anti Beever-Ross and three mid-oxygen sites per conduction plane in a unit cell (figure I.2.2). β″-alumina with a three-fold screw axis has a rhombohedral structure ($R\bar{3}m$). The unit cell contains three spinel-like blocks. The ideal formula of β″-alumina is $Na_2O{\cdot}5.33Al_2O_3$ ($Na_2Al_{11\text{-}1/3}O_{17}$). The conduction plane is not a mirror plane but staggered. Beever-Ross and anti Beever-Ross sites are not distinguishable in β″-alumina.

The difference in the structures of the two phases comes from the sequence of close-packed oxygen layers.

β-alumina: C′-ABCA-B′-ACBA-C′

β″-alumina: C′-ABCA-B′-CABC-A′-BCAB-C′

where primed characters represent conduction planes in which only one fourth of sites are occupied by oxygen ions. The sequence of close-packed oxygen layers is like cubic close packing. However, the sequence in the β-alumina is modified by the mirror image in the conduction planes.

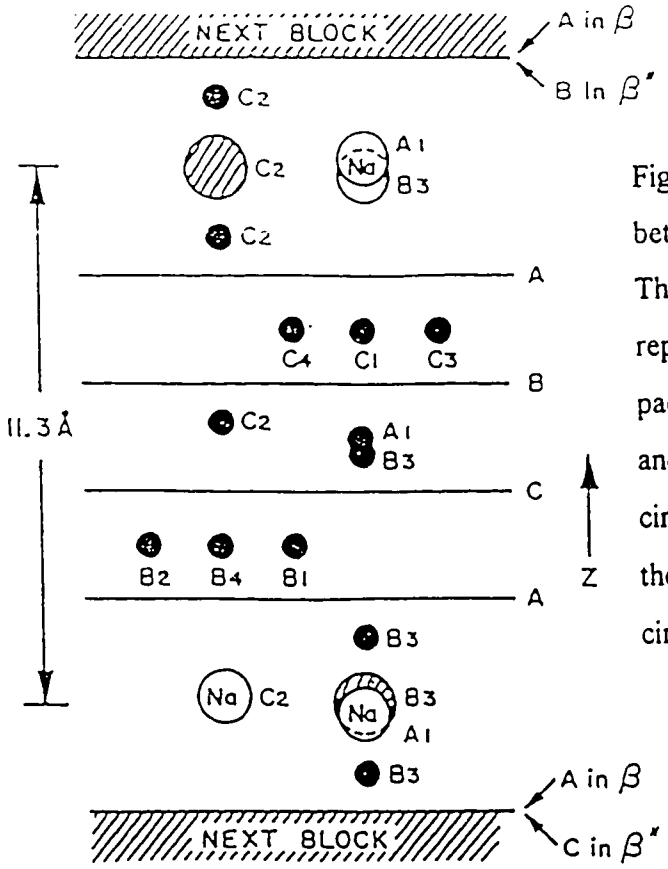

Figure II.2.1. Schematic projection of beta-alumina onto the b-c plane [4]. The horizontal lines A, B, C, and A represent the sequence of close packed oxygen layers. Aluminums and sodiums are solid and open circles, respectively. The oxygens in the conduction plane are hatched circles.

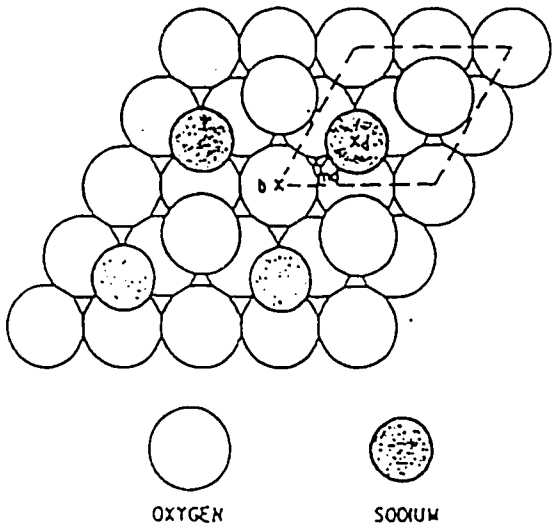

Figure II.2.2. Conduction plane of beta-alumina [5]. The base layer consists of close packed oxygens (all A sites in figure II.2.1) In the conduction plane oxygens are placed at one fourth of B sites (B_3 in figure II.2.1). Sodiums are at the Beever-Ross sites (C_2). The anti-Beever-Ross site is marked as b (A_1). The mid oxygen sites (md) are vacant B sites.

II.2.b) Phase relationships between Na β- and β″-aluminas

The phase diagram of this system is not clear. The beta-aluminas are non stoichiometric phases of the compositions between $Na_2O{\cdot}5.33Al_2O_3$ and $Na_2O{\cdot}9Al_2O_3$ where both β- and β″ phases coexist. In the undoped Na_2O-Al_2O_3 system, it is suggested that β″-alumina is metastable above 1585 °C and that β and β″ phases coexist at temperatures below this, where the β phase may be metastable [45]. Doping of beta-alumina with cations such as Li^+ or Mg^{2+} stabilises the β″ phase at high temperatures. TEM study showed that beta-aluminas form a syntactic intergrowth of β and β″ structures [44] in a single phase, which explains the sluggish kinetics of equilibrium in this system.

Newsam [46] calculated the upper limit of the sodium content in β-alumina considering two charge compensation mechanisms.

1) $Na_{1+x}Al_{11}O_{17+x/2}$ ($x<0.571$, $\sim Na_2O{\cdot}7Al_2O_3$). Excess Na^+ ions occupy mid oxygen sites, which requires the adjacent Beever-Ross site to be empty. Additional oxygen ions charge-compensating for excess Na^+ ions reside at interstitial sites in the conduction planes. The additional oxygen ions are bonded to the two adjacent spinel-like blocks by an Al^{3+}-O^{2-}-Al^{3+} bridge where the two Al^{3+} ions are from Al sites in the spinel-like block, leaving two vacant Al sites.

2) $Na_{1+y}Mg_yAl_{11-y}O_{17}$ ($y<0.667$, $\sim Na_2O{\cdot}0.4MgO{\cdot}6Al_2O_3$). The excess charge is compensated by dopants which have lower valency than Al. The dopants substitute Al in spinel-like blocks.

However, if another charge compensation mechanism is available, the sodium content will exceed the above limit in Na β-alumina. Ions with a radius < 0.97 (Li^+ and Mg^{2+}) can substitute for Al^{3+} ions in the spinel-like blocks [45].

The end composition $Na_{1.67}Mg_{0.67}Al_{10.33}O_{17}$ of β-alumina is also the ideal composition for β″-alumina [44]. At that composition, a maximum in mid-oxygen site occupancy and Beever-Ross site vacancy seems to maximize the electric conductivity (vacancy diffusion).

II.2.c) Powder preparation

Polycrystalline beta-alumina is fabricated by high temperature reaction (sintering) of powder compacts which range from fully crystallized beta-alumina to a mixture of raw materials. The powder preparation consists of mixing of raw materials and reaction (calcination or fusion) of the mixture followed by milling. The powder prepared should be suitable for the subsequent forming processes. The properties of the sintered body so strongly depend on the properties of the powder used that without close control of powder preparation one can not produce good ceramics.

Milling of fused beta-alumina is the most direct way to prepare the beta-alumina powder. The fused material is crushed and then milled in a stainless steel ball mill. Metallic impurities are removed by leaching with HCl which also removes any sodium aluminates [47].

Sol-gel processes yield very homogeneous mixtures on the ionic or microcrystalline (<100 Å) scale [48]. The components are mixed in liquid form as either colloidal sols or aqueous solution and are subsequently converted into a solid gel by either chemical or physical

means without segregation [45]. The intimate mixing and fine particle size results in very homogeneous fine microstructures.

Slurry solution spray drying [48] produces powder suitable for isostatic pressing. Non-soluble raw materials such as α-alumina or boehmite (AlOOH) are mixed with a solution of sodium and lithium hydroxides. The slurry is spray-dried resulting in a chemically homogeneous, flowable, soft powder. The beta-alumina phases are formed during sintering. Calcined beta-alumina powder is spray-dried in order to get agglomerates of powder suitable for isostatic pressing.

The conventional and most simple way is to mill raw materials in wet or dry medium. Milling provides both mixing and size reduction of raw materials which are in the form of oxides (aluminum oxide, lithium oxide), carbonates (sodium carbonate, lithium carbonate) or nitrates (sodium nitrate). In order to avoid reaction during milling, organic liquids such as acetone and alcohol are used as a medium.

Calcination is employed before sintering because it will reduce the evolution of a gas phase, shrinkage due to phase transformation and time for chemical reactions during the sintering. However, calcination is not necessary when above effects are not significant (e.g., slurry solution spray drying).

The zeta process is developed for making lithium stabilized Na β″-alumina [49]. The process uses zeta phase ($LiAl_5O_8$) as a source of lithium. The $LiAl_5O_8$ is milled with α-alumina and sodium carbonate and then calcined. In another route, the $LiAl_5O_8$ is milled with a precalcined mixture of alumina and sodium carbonate and, without calcining, fired. Due to the

good distribution of lithium compared with other conventional methods, almost complete conversion to β″-alumina and a small grain size (~50 μm) can be attained.

II.2.d) Foming beta-alumina tubes

In isostatic pressing, the green body is formed by compressing the powder which is contained between a concentric metal mandrel and a tubular polymer bag through which the pressure is transmitted to the powder. Compared to die pressing, isostatic pressing can form more complicated shapes with uniform density [48]. Isostatic pressing can compact almost all the powders with less restrictions and is suitable for mass production. Spray drying is a prerequisite for isostatic pressing. It provides uniform filling of the mould (flowability) and high compaction with small pores (softness).

In electrophoretic deposition, electrically charged beta-alumina powder suspended in an organic liquid (e.g., amyl alcohol) deposits in an electric field on either anode or cathode [50,51]. The powder can be charged negatively or positively depending on the mechanism of charging.

$$\text{beta-alumina} \rightarrow (\text{beta})^{-} + Na^{+} \text{ (dissociation mode)}$$

$$\text{beta-alumina} + HA \rightarrow (H/\text{beta})^{+} + A^{-} \text{ (absorption mode)}$$

The excellent sinterability of electrophoretically deposited greenware results from very fine pores in the green articles (~1 μm compare to 5~10 μm in isostatic pressing). However, a prerequisite for the powder is the ability to form a stable suspension. The properties of the suspension depend on the electrical double layer between the particle and the liquid vehicle. Well-crystallized particles have a greater tendency to be charged properly.

Adequate mobility (mobility of particles in an electric field), low drying shrinkage and ease of removing the greenware from the mandrel are the factors for successful forming.

In slip-casting, the beta-alumina powder in suspension deposits on the porous mould as the mould absorbs the liquid from the slip. For even dense deposits, high stability and low viscosity of the slip are crucial requirements which limit the powders available for this process. In order to reduce the shrinkage during drying, a higher ratio of powder to liquid is used than in electrophoretic deposition. The DLVO (Deryaguin, Landau, Verwey and Overbeek) theory explains the stability of suspensions in terms of the London-van der Waals attraction and the coulombic repulsion associated with charged particles [52]. The attraction between particles is mainly van der Waals which is proportional to r^{-6} (short ranged). The repulsion due to the double layer is roughly proportional to the surface potential and ranges over the thickness of the double layer. The thickness of the double layer is a good measure of the stability of the slip. The thickness (κ^{-1}) of the electrical double layer of an infinite flat interface is given as [52]

$$\kappa^{-1} = \sqrt{\frac{DkT}{8\pi \sum_i n_i Z_i^2 e^2}} \qquad \text{(II.1.3)}$$

where the parameters are defined as follows

D : the dielectric constant of the liquid

k , T : the Boltzmann constant and absolute temperature

n_i , Z_i : the concentration and the valency of the ionic species i in the liquid

e : the elementary charge.

II.2.e) Sintering

Sintering is the most difficult step to control in the fabrication of beta-alumina. The final products should have dense, uniform, fine microstructures for good electrical conductivity and high mechanical strength.

The high volatility of sodium oxide results in a high rate of loss during sintering. The loss of sodium will reduce the sinterability and electrical conductivity. Beta-alumina crucibles, platinum lining, MgO crucibles and α-alumina crucibles treated with sodium oxides are used to prevent the reaction between beta-aluminas and crucibles [53]. Packing sodium rich powders around the greenware reduces the sodium loss during firing. Zone sintering (passing beta-alumina through a small hot zone) also minimises the sodium loss.

Another problem is duplex microstructure: fine grain matrix (<10 μm) and isolated large grains (~100 μm). Duncan [54] observed in lithium doped Na beta-alumina that the overgrown grains were β″-alumina. It was suggested that the poor distribution of lithium should cause this problem. Zeta processed products [49] which must have more uniform distribution of lithium showed an increased proportion of β″-alumina and well-controlled grain size distribution.

Two peak sintering (presintering, annealing and cooling down followed by final sintering at higher temperature) is a another route to control the microstructure [54]. Moderately coarse (20 μm) but uniform microstructures have high mechanical strength.

For the sintering of stabilized β″-alumina, where a high ratio of β″ to β phase is desirable for high conductivity, the densification seems much faster than the conversion to the

β″-alumina. The postsintering annealing [55] was employed to promote the conversion while at the same time inhibiting exaggerated grain growth.

The seeding catalysis (addition of a small amount of β″-alumina crystals (<5 μm) into the green ceramic) [56] can enhance the phase conversion to β″-alumina and even eliminate the need for pre- or postsintering annealing.

Hot pressing produces the best beta-aluminas with almost full density and extremely fine (~1 μm) uniform microstructures. However, this method is limited to simple shapes such as disks and rods.

II.2.f) Ion exchange

Na beta-aluminas can be ion-exchanged with monovalent (K^+, Li^+, Rb^+, Ag^+) [6] and multivalent (Cd^{2+}, Ca^{2+}, Sr^{2+}, Pb^{2+}) [7] cations. Ion exchange is performed in the melts or vapour phases of salts. During ion exchange the difference in the lattice parameters between different beta-aluminas produces internal stresses which may lead to cracking of the product. The lattice parameters of beta-aluminas are given in the Table II.2.1.

Ion exchange of polycrystalline beta-aluminas in molten salts can cause corrosive attack which leads to a considerable increase in the porosity [57]. Two types of stresses can be formed in Na-K ion exchange [58]. The macrostresses are developing due to the macroscopic compositional gradient and the resulting uneven lattice expansions between grains. Microstresses are caused by the anisotropy of the lattice expansion due to both ion exchange and the subsequent cooling.

Table II.2.1. Lattice parameters [Å] of beta-aluminas [44,48,59]

	c axis	one block	a axis	ion size
Na β"(Li doped)	33.539	11.180	5.617	0.95
K β"(Li doped)	34.078	11.359	5.619	1.33
Rb β"(Li doped)	34.344	11.448	5.613	1.48
Na β	22.530	11.265	5.594	0.95
K β	22.729	11.365	5.596	1.33
Li β	22.642	11.321	5.593	0.60
Ag β	22.498	11.249	5.594	1.26

A phase transition from β" to β phase was observed in divalent ion exchange of Li-stabilized Na beta-aluminas [60]. The divalent ion exchange causes extreme stresses to the spinel-like blocks. Li-doped materials minimise these stresses with reorientation of the structure to the β phase.

Tan et al. [61] studied the strength controlling flaws in Na beta-aluminas which were isostatically pressed and zone sintered. The microstructures were a fine grained matrix (1.5~2.5 μm) containing a small proportion of larger secondary grains, up to 200 μm. For small samples, the fracture initiating flaws were surface irregularities and large crystal grains or a combination of these. The strengths of larger samples were governed by larger crystal grains, by regions of high porosity or by impurity areas associated with large grains.

In order to prevent the damage due to ion exchange, one can reduce the stresses or strengthen the materials in the following ways:

1) High temperature employed can enhance the diffusion in the beta-alumina and may induce stress relieving processes such as creep.

2) Using vapour phase of salts reduces the ion exchange rate at the interface relative to molten salts.

3) Salts of mixed cations (e.g., Na and K salts for K ion exchange) can reduce the compositional difference between the surface and the interior of beta aluminas.

4) Beta-aluminas which have the lattice parameters similar to those of final ion exchanged beta-alumina can be used as a precursor materials.

5) For high mechanical strength, homogeneous and fine grain microstructures are desirable.

6) Strengthening mechanisms such as zirconia second phase can be employed.

II.3) Alkali Fullerides

II.3.a) Pure C_{60}

In 1985, Kroto et al. [62] discovered the stable C_{60} species during experiments involving laser-vaporizing graphite in a pulsed jet of helium. The truncated icosahedral molecule (figure II.3.1) was named buckminsterfullerene or buckyball for short. The stability of C_{60} over planar graphite fragments is due to the absence of dangling bonds [63]. In 1990, Krätschmer et al. [64] found that the C_{60} molecules formed by graphite-arc discharge in low pressure helium. Due to the hexagonal carbon rings in the molecule, C_{60} can be extracted from the carbon soot by aromatic solvents such as benzene and toluene. The separation of C_{60} from coal has also been reported [65].

The shape of C_{60} is a truncated icosahedron (figure II.3.1b). The icosahedron has I_h (or $m\bar{3}$) symmetry with 12 vertices, 30 edges and 20 triangular sides (figure II.3.1a). There are 12 5-fold axes at each vertex, 15 2-fold axes each of which bisects 2 edges, and 10 $\bar{3}$-fold axes each of which connects the centers of 2 triangular sides. After truncation it has 60 vertices, 12 pentagons, 20 hexagons and 90 edges; 30 of them are between hexagons (double bonds) and 60 of them are between a hexagon and a pentagon (single bonds) (figure II.3.2). The lengths of double and single bonds are about 1.40 and 1.45 Å, respectively [66]. The mean ball diameter and ball outer diameter are 7.10 and 10.34 Å, respectively.

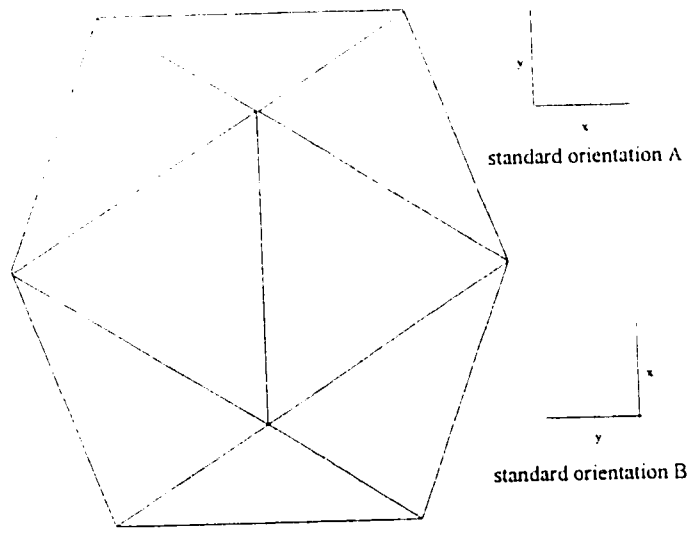

(a)

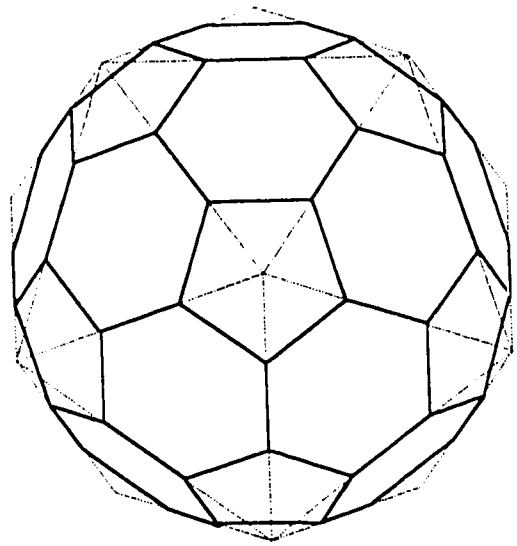

(b)

Figure II.3.1 (a) The icosahedron projected from 2-fold axis. The standard orientations are related by the 90 degree rotation about any coordinate axis (x, y, z) which is aligned with a 2-fold axis. (b) The truncated icosahedron. After truncation, the vertices and sides become pentagons and hexagons, respectively.

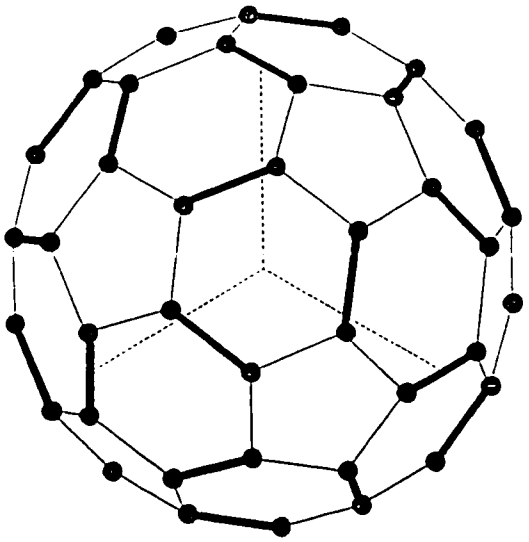

Figure II.3.2. The C_{60} molecule at standard orientation A projected from [1 1 1] direction. The double bonds (thick line) are between hexagons, the single bonds are between hexagon and pentagon. The dashed lines represent the direction of the lattice vectors.

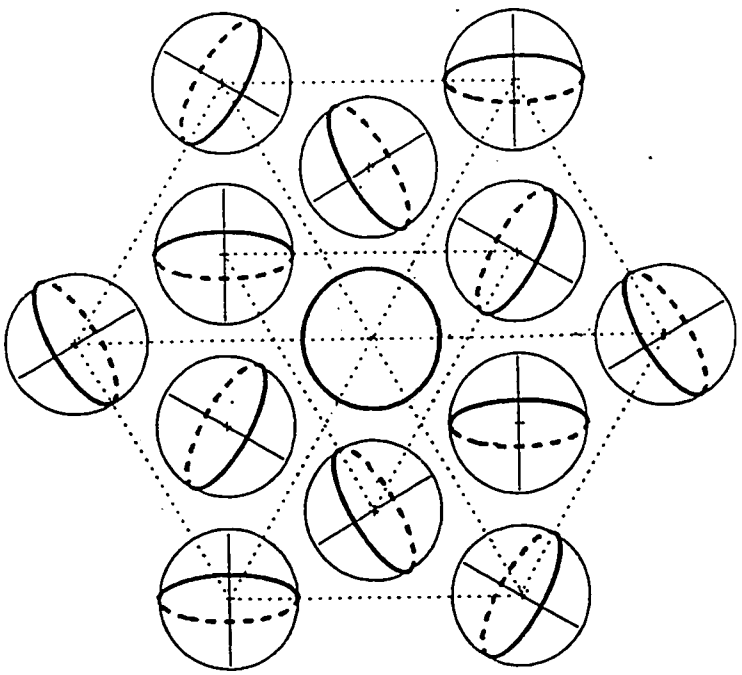

Figure II.3.3. The 12 nearest neighbors around the molecule at the origin in sc C_{60}. Each of them are rotated about four different <1 1 1> directions. The rotation axis of the molecule at the origin is perpendicular to the paper.

Pure C_{60}, fullerite, has a first-order phase transition at a temperature between 249 K [67,68] and 260 K [69]. In both phases the molecules are cubic-close-packed. Above the transition temperature the structure is face-centered-cubic with $Fm\bar{3}m$ symmetry [21]. In this phase the molecules are orientationally disordered. Above 400 K, the molecule exhibits continuous rotation [20]. Between 260 and 400 K there are some orientational correlation between adjacent molecules which seem to have rapid-ratcheting motions (jump reorientation between orientations) rather than constant angular momentum rotations [70]. The rotational reorientation time is about 9 to 12 ps at room temperature [22]. Below the transition temperature, the development of orientational order causes the transition to simple cubic structure with $Pa\bar{3}$ symmetry [21]. In the low temperature phase, the molecules are still ratcheting [71]. However, the rotational reorientation time is much slower (2 ns at 250 K) than in the high temperature phase. Below 90 K the reorientational motion is frozen although a small amount of static disorder still persists [69]. The values of enthalpy and entropy of transition are estimated as 6.7 kJ/mole and 28 J/mole K, respectively [72].

When three perpendicular 2-fold axes of the molecule are aligned in three Cartesian coordinates, the molecule is said to be at one of two standard orientations (figure II.3.1a); those are related to each other by 90 degree rotation about any Cartesian coordinate. Note that four out of twelve $\bar{3}$-fold axes of the molecule which is at one of the standard orientations are aligned in four different <1 1 1> directions. The structures of pure C_{60} [68] can be attained from the cubic-close-packed molecules which are orientationally

ordered with any one of the standard orientations (hereafter, if not specified, the standard orientation A will be used). When the orientation of the molecules is disordered, the structure is fcc ($Fm\bar{3}m$), the high-temperature form (above 260 K). The structure of the low-temperature phase (sc, $Pa\bar{3}$) consists of a basis of four molecules each of which is rotated about four different <1 1 1> axes through an equal angle from the standard orientation (figure II.3.3). The structure has energy minima at rotation angles of about 22 and 82 degrees clock-wise [69] from standard orientation A. At about 22 degrees (see figure II.3.2), the electron-rich double bonds face the centers of electron-poor pentagonal sides of the nearest neighbors (absolute minimum). At about 82 degrees, the electron-rich double bonds face the centers of hexagonal sides of the nearest neighbors (local minimum).

The coordinates of three C atoms in standard orientation A are given in table II.3.1 where the distance between C atom and the center of the molecule is about 3.55 Å and the lengths of single and double bonds are 1.45 and 1.40 Å, respectively. The whole set of coordinates can be obtained by cyclic permutations of (x, y, z) and the combinations of positive and negative signs ($\pm x$, $\pm y$, $\pm z$).

The standard enthalpy of formation of crystalline C_{60} was measured by combustion calorimetry: $\Delta_f H^\circ_m(298.15K) = 2422 \pm 14$ kJ/mole [73]. The vapour pressure of C_{60} was measured over the temperature range 730 to 990 K by the torsion effusion and Knudsen effusion methods [74]:

$$\log P = (8.28 \pm .020) - (9145 \pm 150) / T \qquad \text{(II.3.1)}$$

where the unit of P is kPa.

The C_{60} molecule has 174 vibrational modes and 46 distinct mode frequencies [75];

$$2A_g(1) + 3T_{1g}(3) + 4T_{2g}(3) + 6G_g(4) + 8H_g(5) + 1A_u(1) + 4T_{1u}(3) + 5T_{2u}(3) + 6G_u(4) + 7H_u(5) \quad \text{(II.3.2)}$$

where the subscript g and u denote even and odd parity, respectively and the number in the parenthesis is the degeneracy of the type of mode. Among them 10 Raman ($2A_g$ + $8H_g$) and 4 infrared ($4T_{1u}$) fundamental frequencies were observed by Bethune and Frum [76,77]. The non-active frequencies were observed by neutron scattering [78] or calculated [79,80].

Table II.3.1. The coordinates of C in C_{60} with the standard orientation A [66].

	x	y	z
C(1)	0	$D_2/2$	$C_1(2D_1 + D_2)$
C(2)	C_1D_1	$(D_1 + D_2)/2$	$C_1(2D_1 + D_2) - C_2D_1$
C(3)	$C_1(D_1 + D_2)$	$D_1/2$	$C_2D_1 + (2D_1 + D_2)/2$

where $C_1 = \frac{\sqrt{5}+1}{4}$, $C_2 = \frac{\sqrt{5}-1}{4}$, $D_1 = 1.45$ Å and $D_2 = 1.40$ Å.

II.3.b) Alkali fullerides

The routine way to synthesize A_xC_{60} (A = alkali) is the direct reaction of C_{60} with alkali-metal vapor in sealed Pyrex tubes at temperatures in the range of 200 - 500 K, for several hours to several days. A_6C_{60} (A = K, Rb, Cs) was reported to be an alkali saturated form of fulleride [15,81,82]. Difficulties in synthesizing Na and Cs containing fullerides were overcome by changing the starting materials [15,82]. Some superconducting phases could be metastable [14].

The electrical conductivities of alkali doped C_{60} films (Li, Na, K, Rb, Cs) were reported by [83]. A_xC_{60} is insulating for x = 0 or 6, and metallic for x = 3 [84,85]. However, Na and Li fullerides could be insulators across the entire range of composition [86]. The transitions to the superconducting state for K_3C_{60} [12] at 18 K, Rb_3C_{60} [13] at 28 K, Cs_3C_{60} [87] at 30 K, and other mixed alkali doped C_{60} have been reported. All of them have *fcc* structures with alkali metals in completely filled octahedral and tetrahedral sites [16,17,81,82]. Superconductivity at 8.4 K in Ca_5C_{60} was also found [18]. A simple cubic structure with multiple occupancy at octahedral sites was proposed for this compound. The effect of pressure [88,89] and isotope [90] on superconductivity were also studied. The critical temperature for the superconductivity of alkali fullerides increases monotonically as the unit-cell size increases [17,86].

A phase diagram of the Rb_xC_{60} system at room temperature was proposed [82]. The phase included an *fcc* structure (rock salt structure, $x < 1$), another *fcc* line phase (full occupancy of tetrahedral and octahedral sites, x = 3), a *bct* structure (x = 4) [91], and a

bcc structure ($5 < x \leq 6$) [81] as determined by X-ray diffraction. K_xC_{60} and Cs_xC_{60} systems are similar to Rb_xC_{60} except for the absence of Cs_3C_{60}. The proposed diagrams are shown in figure II.3.4 [92]. A polymeric cross-linking between the molecules was reported for both K_1C_{60} and Rb_1C_{60} [93], which have a pseudo-body-centered orthorhombic structure and transform reversibly on heating to the rock-salt phase [22].

The phases of Na_xC_{60} (x = 1, 2, 3, 6, 11) were reported [22]. In this system, the molecules are cubic-close-packed regardless of the composition. Stable Na_1C_{60} and Na_2C_{60} phases showed a phase transition to a simple cubic structure [94, 95] like pure C_{60} fullerite. Na_3C_{60} exhibited disproportionation into Na_2C_{60} and Na_6C_{60} [22, 94]. In Na_6C_{60}, each tetrahedral site is occupied by a Na atom and each octahedral site accommodates 4 Na atoms in a tetrahedral form [15]. For $Na_{11}C_{60}$, 9 Na atoms are expected to go into an octahedral site [96]. The Li_xC_{60} system was studied by the electrochemical technique [97]. Three domains were observed; 0 to 0.5, 2 to 3, and 4 to 12. Intercalation appeared reversible up to x = 3. The structures of the phases were not determined.

The Lennard-Jones type interaction between the molecules tends to order the orientation of the molecule as in pure C_{60} [94, 95] whereas the repulsion between the alkali metal and the molecule tends to align the molecules in one of the standard orientations. Na_2C_{60}, due to the small repulsion, has a phase transition to $Pa\bar{3}$ due to the orientational order as in pure C_{60}. For heavy alkalis such as K and Rb, the repulsion causes a merohedral disorder (random distribution between two equivalent orientations, A_3C_{60}) or order (A_6C_{60}) in the orientation of the molecule [66, 94].

(a)

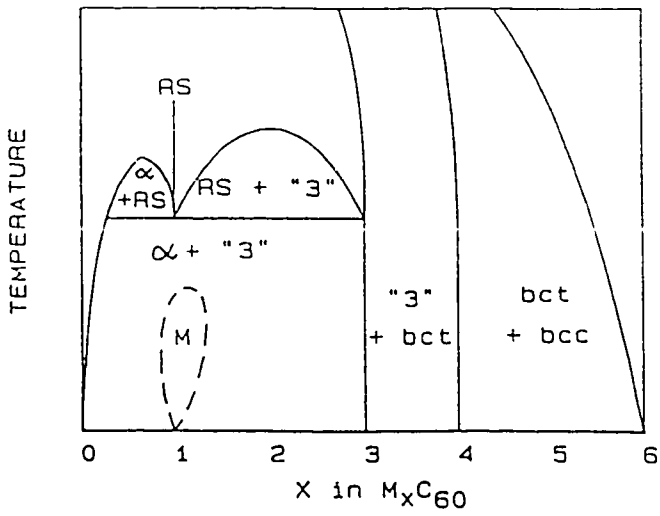

(b)

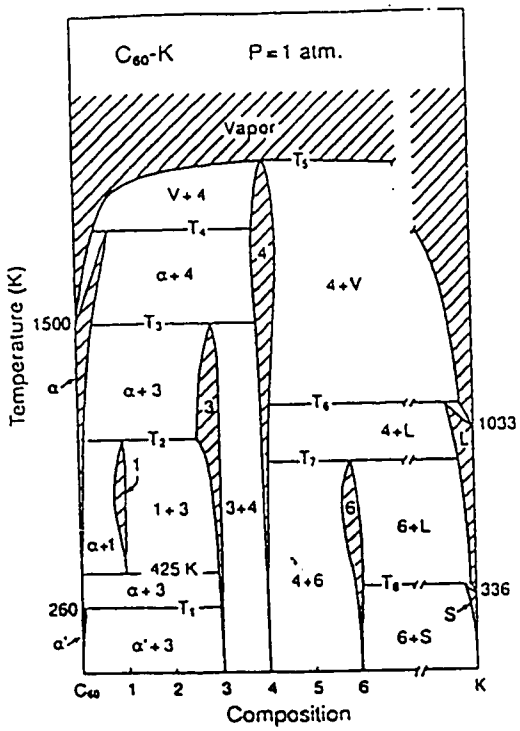

Figure II.3.4. (a) proposed phase diagram of M_xC_{60} (M = K, Rb) [94]. RS and M represent rocksalt and monoclinic structure, respectively. (b) Proposed phase diagram of K_xC_{60} [92].

II.4) Electrochemistry of solids

There are two approaches to electrochemistry: a traditional (thermodynamic) one and a modern (physical) one [98]. Traditional electrochemistry is derived from the concept of equality between chemical and electrical energies in the electrode reaction. This approach emphasizes chemical and energetic aspects of the problem, but the physical picture is certainly obscure. The modern approach is focused on a description of the molecular interaction at the interfacial region. Energetic aspects are less evident. However, it gives a general picture with insight beyond the traditional barriers. Although the interfacial phenomena such as the electrical double layer are not treated in this section, we need to know the concepts of electrochemical potential and transport in solids in order to understand the electrochemistry of not only ionic but also mixed ionic-electronic conductors.

II.4.a) Electrochemical potential

The definition of electrochemical potential of component i, $\tilde{\mu}_i$, is;

$$\tilde{\mu}_i = \mu_i + Z_i F\phi \qquad \text{(II.4.1)}$$

where μ_i, Z_i, F, and ϕ are chemical potential, charge of i, Faraday constant, and electrical potential, respectively. The electrochemical potential is the sum of the energy increase in the phase by adding an infinitesimally small amount of i (μ_i) and the work necessary to bring charge $Z_i F$ from a vacuum at infinity into the phase ($Z_i F\phi$). Thus electrochemical potential is not a material constant but depends on the size of the phase and the properties of the interface. In equation (II.4.1) ϕ is the electrical potential inside a

phase (the inner potential or Galvani potential) and is the sum of the outer potential ψ and the surface potential χ.

$$\phi = \psi + \chi \qquad \text{(II.4.2)}$$

The outer potential for a phase in vacuum is defined as the electrostatic work done to a +1 charge from infinity to a point just outside the phase. As the electrical potential is fairly constant over a wide region (10^{-5} to 10^{-3} cm), the exact position of the outer potential is not important [99]. Whereas the outer potential is proportional to the excess charge, the surface potential is related to the dipolar layer at the interface. The dipolar layer may be due to the spreading of electrons into vacuum (metal-vacuum interface) or the orientation of dipole moments of molecules (solution-vacuum interface) [98]. In either case, the electrical potential is related to the distribution of charges by Poisson's equation

$$\nabla^2\phi = -\frac{1}{\varepsilon}\rho \qquad \text{(II.4.3)}$$

where ε and ρ are the permittivity and the electric charge density.

When two phases (1 and 2) are at equilibrium, it is not the chemical potentials but the electrochemical potentials which are equal.

$$\tilde{\mu}_i\,(1) = \tilde{\mu}_i\,(2) \qquad \text{(II.4.4)}$$

It should be noted that for neutral species the electrochemical potential is equal to the chemical potential and that the electrochemical potential of the charged species is related to the chemical potential of the neutral species by

$$\tilde{\mu}_1 + Z_1\tilde{\mu}_2 = \mu_1, \qquad \text{(II.4.5)}$$

where 1, 2 and x denote ion, electron and neutral species, respectively.

In most good solid electrolytes, the chemical potential of the mobile ions is essentially constant throughout the bulk electrolyte because of the high ionic disorder. There is no major potential drop within the electrolyte in this case. Also, an electrical field may not build up within the electrodes because of high electronic conductivity. Thus the electrostatic potential drop occurs nearly exclusively at the interfaces between the electrodes and the electrolyte [100]. A half-cell or electrode is said to be reversible if the rates of its forward and reverse reactions are rapid compared to the rate at which conditions are changed. The electrode is polarizable when the reaction rate of oxidation or reduction is so slow that charges can accumulate at the interface.

II.4.b) Transport in solids

Some useful equations are summarized below [100,101,102].

$$j = -\tilde{D}\nabla c \qquad \text{(Fick's first law, chemical diffusion coefficient } \tilde{D}\text{)} \qquad \text{(II.4.6)}$$

$$\frac{\partial c}{\partial t} = \nabla \cdot (\tilde{D}\nabla c) \qquad \text{(Fick's second law)} \qquad \text{(II.4.7)}$$

$$B_m = \frac{|\vec{v}|}{|\vec{F}|} \qquad \text{(mechanical mobility or absolute mobility } B_m\text{)} \qquad \text{(II.4.8)}$$

$$j = c\vec{v} = -cB_m\vec{F} \qquad \text{(II.4.9)}$$

$$j = -cB_m \frac{\partial \mu}{\partial x} = -B_m kT\left(\frac{\partial \ln a}{\partial \ln c}\right)\frac{\partial c}{\partial x} = -D_k W \frac{\partial c}{\partial x} \qquad \text{(II.4.10)}$$

$$D_k = B_m kT \qquad \text{(component diffusion coefficient } D_k\text{)} \qquad \text{(II.4.11)}$$

$D_{tr} = fD_k$ (tracer diffusion coefficient D_{tr} and correlation factor f) (II.4.12)

$\tilde{D} = D_k W$ (Wagner factor or thermodynamic factor W) (II.4.13)

$\tilde{D} = B_m kT$ (Nernst-Einstein relation for ideal solutions) (II.4.14)

$$i = -\sigma \frac{\partial \phi}{\partial x} = -cu|Z|e \frac{\partial \phi}{\partial x}$$ (conductivity σ and electrical mobility u) (II.4.15)

$$j = -cB_m Ze \frac{\partial \phi}{\partial x} = -\frac{\sigma}{Ze} \frac{\partial \phi}{\partial x} = -cu \frac{|Z|}{Z} \frac{\partial \phi}{\partial x}$$ (II.4.16)

Thus, the particle flux in general case is expressed as

$$j = -cB_m \frac{\partial \tilde{\mu}}{\partial x} = -\frac{cD_k}{kT} \frac{\partial \tilde{\mu}}{\partial x} = -\frac{\sigma}{Z^2 e^2} \frac{\partial \tilde{\mu}}{\partial x}$$ (II.4.17)

The interrelations among diffusion coefficients and mobilities and conductivity are summarized in figure II.4.1 [101].

Diffusion is an irreversible process in which the total entropy increases [103, 102]. The scope of this review is limited to linear transport processes and near-equilibrium situations with microscopic reversibility (local equilibrium). The local equilibrium means that the thermodynamic state functions have the same values as they would have in an equilibrium situation.

The entropy production is the sum of the products of general forces X_j and fluxes J_j

$$\theta = \sum_j X_j J_j$$ (II.4.18)

where θ is the entropy increase per unit volume per time.

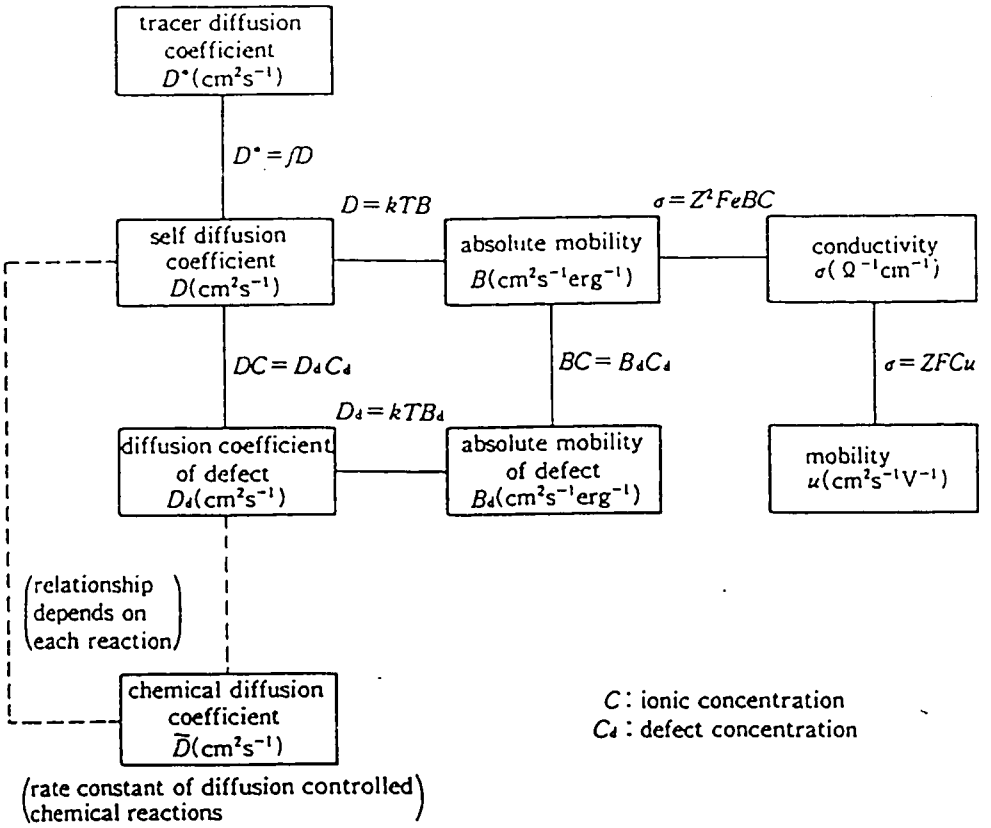

Figure II.4.1. Relationship among diffusion coefficients, mobility and conductivity of ions [101]. The self diffusion coefficient (or component diffusion coefficient in equation II.4.11) is used in a sense that the jump is random.

In a continuous adiabatic system, the entropy production due to the transfer of heat, mass and electric charge at constant pressure is given as

$$\theta = -\frac{1}{T}\frac{d\ln T}{dx}J_q - \sum_i \frac{1}{T}\frac{d\mu_{iT}}{dx}J_i - \frac{1}{T}\frac{d\phi}{dx}J_Q \qquad \text{(II.4.19)}$$

where $d\mu_{iT}$ is the change in the chemical potential only due to the composition gradient at temperature T and J_q, J_i and J_Q are the flux of heat q, species i and charge Q [103].

The entropy production leads to a dissipation of energy.

$$T\theta = -\frac{d\ln T}{dx}J_q - \sum_i \frac{d\mu_{iT}}{dx}J_i - \frac{d\phi}{dx}J_Q \qquad \text{(II.4.20)}$$

Onsager's equation in the isothermal case is

$$J_i = \sum_j L_{ij}X_j \qquad \text{(II.4.21)}$$

where L_{ij} is a phenomenological coefficient, independent of the forces.

Onsager's reciprocity relates the coefficients in the following way:

$$L_{ij} = L_{ji} \qquad \text{(II.4.22)}$$

Onsager's equation can explain many irreversible processes such as

Du four effect: flux of heat caused by a concentration gradient

Thermal diffusion: flux of matter caused by a temperature gradient

Soret effect: thermal diffusion in liquids

Peltier effect: flux of heat caused by a electrical gradient

Seebeck effect (or thermoelectric effect): flux of charge caused by temperature gradient.

For isothermal diffusion with three mobile species, Onsager's equations are

$$j_1 = L_{11}\frac{\partial \mu_1}{\partial x} + L_{12}\frac{\partial \mu_2}{\partial x} + L_{13}\frac{\partial \mu_3}{\partial x} + L_{14}\frac{\partial \phi}{\partial x} \tag{II.4.23}$$

$$j_2 = L_{21}\frac{\partial \mu_1}{\partial x} + L_{22}\frac{\partial \mu_2}{\partial x} + L_{23}\frac{\partial \mu_3}{\partial x} + L_{24}\frac{\partial \phi}{\partial x} \tag{II.4.24}$$

$$j_3 = L_{31}\frac{\partial \mu_1}{\partial x} + L_{32}\frac{\partial \mu_2}{\partial x} + L_{33}\frac{\partial \mu_3}{\partial x} + L_{34}\frac{\partial \phi}{\partial x} \tag{II.4.25}$$

$$j_4 = L_{41}\frac{\partial \mu_1}{\partial x} + L_{42}\frac{\partial \mu_2}{\partial x} + L_{43}\frac{\partial \mu_3}{\partial x} + L_{44}\frac{\partial \phi}{\partial x} \tag{II.4.26}$$

where J_1, J_2 are the fluxes of ions, J_3 is the flux of electron and J_4 is the electric current.

On the other hand, we have

$$j_1 = -\frac{\sigma_1}{Z_1^2 e^2}\frac{\partial \tilde{\mu}_1}{\partial x} = -\frac{\sigma_1}{Z_1^2 e^2}\frac{\partial \mu_1}{\partial x} - \frac{\sigma_1}{Z_1 e}\frac{\partial \phi}{\partial x} \tag{II.4.27}$$

$$j_2 = -\frac{\sigma_2}{Z_2^2 e^2}\frac{\partial \tilde{\mu}_2}{\partial x} = -\frac{\sigma_2}{Z_2^2 e^2}\frac{\partial \mu_2}{\partial x} - \frac{\sigma_2}{Z_2 e}\frac{\partial \phi}{\partial x} \tag{II.4.28}$$

$$j_3 = -\frac{\sigma_3}{e^2}\frac{\partial \tilde{\mu}_3}{\partial x} = -\frac{\sigma_3}{e^2}\frac{\partial \mu_3}{\partial x} + \frac{\sigma_3}{e}\frac{\partial \phi}{\partial x} \tag{II.4.29}$$

$$j_4 = i = -\frac{\sigma_1}{Z_1 e}\frac{\partial \tilde{\mu}_1}{\partial x} - \frac{\sigma_2}{Z_2 e}\frac{\partial \tilde{\mu}_2}{\partial x} + \frac{\sigma_3}{e}\frac{\partial \tilde{\mu}_3}{\partial x} \tag{II.4.30a}$$

$$= -\frac{\sigma_1}{Z_1 e}\frac{\partial \mu_1}{\partial x} - \frac{\sigma_2}{Z_2 e}\frac{\partial \mu_2}{\partial x} + \frac{\sigma_3}{e}\frac{\partial \mu_3}{\partial x} - (\sigma_1 + \sigma_2 + \sigma_3)\frac{\partial \phi}{\partial x} \tag{II.4.30b}$$

where by comparison we can determine the phenomenological coefficients and see the reciprocity of the coefficients. The fluxes are coupled since $L_{i4} = L_{4i} \neq 0$. From equation (II.4.30b), we have

$$\frac{\partial \phi}{\partial x} = -\frac{t_1}{Z_1 e}\frac{\partial \mu_1}{\partial x} - \frac{t_2}{Z_2 e}\frac{\partial \mu_2}{\partial x} + \frac{t_3}{e}\frac{\partial \mu_3}{\partial x} - \frac{j_4}{\sigma_1 + \sigma_2 + \sigma_3} \tag{II.4.31}$$

where t_j = transference number (equation II.1.1). Thus equation (II.4.27) is rewritten as

$$j_1 = -\frac{\sigma_1}{Z_1^2 e^2}\frac{kT}{c_1}\left[(1-t_1)\frac{\partial \ln a_1}{\partial \ln c_1} - \frac{Z_1 t_2}{Z_2}\frac{\partial \ln a_2}{\partial \ln c_1} + Z_1 t_3 \frac{\partial \ln a_3}{\partial \ln c_1}\right]\frac{\partial c_1}{\partial x} + \frac{t_1}{Z_1 e} j_4 \tag{II.4.32a}$$

$$= -D_1\left[(1-t_1)\frac{\partial \ln a_{1^x}}{\partial \ln c_{1^x}} - t_2 \frac{Z_1}{Z_2}\frac{\partial \ln a_{2^x}}{\partial \ln c_{1^x}}\right]\frac{\partial c_{1^x}}{\partial x} + \frac{t_1}{Z_1 e} j_4 \tag{II.4.32b}$$

where the superscript x denotes neutral species.

For chemical diffusion, $j_4 = 0$ because of the charge neutrality. We define the chemical diffusion coefficient as

$$j_1 = -\tilde{D}_1 \frac{\partial c_1}{\partial x} \tag{II.4.33}$$

Thus, from equation (II.4.32b)

$$\tilde{D}_1 = D_1 W_1 \tag{II.4.34}$$

where the general Wagner factor W_1 [100] is

$$W_1 = (1-t_1)\frac{\partial \ln a_{1^x}}{\partial \ln c_{1^x}} - t_2 \frac{Z_1}{Z_2}\frac{\partial \ln a_{2^x}}{\partial \ln c_{1^x}} \tag{II.4.35}$$

It is not only the component diffusion coefficient but also the Wagner factor that determine the chemical diffusion coefficient. For metals $t_3 \approx 1$ and in an ideal solution, the chemical diffusion

coefficient is equal to the component diffusion coefficient. For good solid electrolytes $t_1 \approx 1$ the chemical diffusion coefficient is almost nil. For good electrodes, t_3 should be close to one and the derivative of the activity with respect to the concentration should be large, which can be attained in nonstoichiometric compounds with a narrow range of stability.

II.4.c) thermodynamic measurements

The electrochemical techniques have general advantages over other methods [104];

1) Electrical quantities are readily measurable with high precision.

2) The fundamental thermodynamic and kinetic quantities are directly transduced into cell voltages and electrical current.

3) The composition may be precisely changed in-situ.

4) The experimental arrangement is generally very simple.

Solid electrolytes are the essential part of this technique. General requirements for solid electrolytes are [105];

1) high ionic conductivity

2) extremely low electronic conductivity

3) structural stability over a wide temperature interval

4) chemical stability and compatibility with electrode materials

5) ease of fabrication of thin and dense membranes

6) mechanical strength.

β-alumina is one of few materials which satisfy above requirements.

Thermodynamic approach

When $t_1 = 1$, the transfer of one mole of component i through the electrolyte accompanies the transfer of Z_iF moles of electrons through the external circuit. The electrical work done by the transfer of electrons is less than or equal to the change in the Gibbs free energy.

$$Z_1 F\mathcal{E} \le -\Delta\mu_{1,r} \tag{II.4.36}$$

The reversible potential is defined as

$$\mathcal{E}_{rev} = -\frac{\Delta\mu_{1,r}}{Z_1 F} \tag{II.4.37}$$

The limiting value of $\mathcal{E}$ measured as the current goes to zero is called the electro-motive force of the cell (the cell *EMF*) and is equal to the reversible cell potential $\mathcal{E}_{rev}$. *EMF* can be expressed in the form of the Nernst equation.

$$EMF = -\frac{2.303RT}{Z_1 F}\log\frac{a_{1,W}}{a_{1,R}} = EMF^{\circ} - \frac{2.303RT}{Z_1 F}\log a_{1,W} \tag{II.4.38}$$

where the subscripts R and W denote the reference and the working electrodes, respectively.

Kinetic approach

From equations (II.4.5) and (II.4.30)

$$j_4 = -\frac{\sigma_1}{Z_1 e}\frac{\partial\tilde{\mu}_1}{\partial x} - \frac{\sigma_2}{Z_2 e}\frac{\partial\tilde{\mu}_2}{\partial x} + \frac{\sigma_3}{e}\frac{\partial\tilde{\mu}_3}{\partial x} = -\frac{\sigma_1}{Z_1 e}\frac{\partial\mu_{1,r}}{\partial x} - \frac{\sigma_2}{Z_2 e}\frac{\partial\mu_{2,r}}{\partial x} + \frac{\sigma_1+\sigma_2+\sigma_3}{e}\frac{\partial\tilde{\mu}_3}{\partial x} \tag{II.4.39}$$

where subscript 1 and 2 represent ions and 3 denotes electrons.

Since for the open circuit, $i = j_4 = 0$.

$$\frac{\partial\tilde{\mu}_3}{\partial x} = +\frac{t_1}{Z_1}\frac{\partial\mu_{1^+}}{\partial x} + \frac{t_2}{Z_2}\frac{\partial\mu_{2^+}}{\partial x} \qquad \text{(II.4.40)}$$

At the interface, the electrochemical potentials of electrons on both phases are equal. As the compositions of the leads to the external circuit are identical, the difference in the electrochemical potentials of electrons is the same as in the electrical potentials.

$$EMF = \frac{\Delta\tilde{\mu}_3}{F} = \int \frac{t_1}{Z_1 F}\partial\mu_{1^+} + \int \frac{t_2}{Z_2 F}\partial\mu_{2^+} \qquad \text{(II.4.41)}$$

1) $t_2 = 0$

$$EMF = \frac{\bar{t}_1}{Z_1 F}\Delta\mu_{1^+} \qquad \text{(II.4.42)}$$

where the mean transference number is defined as

$$\bar{t}_1 = \frac{\int t_1 \partial\mu_{1^+}}{\int \partial\mu_{1^+}} = \frac{EMF}{\varepsilon_{rev}} \qquad \text{(II.4.43)}$$

Thus, the *EMF* is the same as in the thermodynamic approach only when the mean transference number is equal to unity.

2) stoichiometric compound $M_{|z_2|}X_{z_1}$

Using the Gibbs-Duhem relation, $|Z_2|d\mu_{1^+} + Z_1 d\mu_{2^+} = 0$, equation (II.4.41) is written as

$$EMF = \frac{\overline{t_1 + t_2}}{Z_1 F}\Delta\mu_{1^+} \qquad \text{(II.4.44)}$$

Thus the EMF is constant in the multi-phase region and it will change rapidly as the composition of the solution changes.

Equivalent circuit

The equivalent circuit of the solid electrolyte cell is shown in figure II.4.2 where $\mathcal{E}_i$ represents the reversible cell potential due to ion *i*. The sum of the potential difference along a closed loop is zero.

$$\mathcal{E}_1 + r_1 i_1 + r_3(i_1 + i_2) = 0 \tag{II.4.45}$$

$$\mathcal{E}_2 + r_2 i_2 + r_3(i_1 + i_2) = 0 \tag{II.4.46}$$

Thus,

$$EMF = \frac{r_2 r_3 \mathcal{E}_1 + r_3 r_1 \mathcal{E}_2}{r_1 r_2 + r_2 r_3 + r_3 r_1} = t_1 \mathcal{E}_1 + t_2 \mathcal{E}_2 \tag{II.4.47}$$

Equations (II.4.37), (II.4.41) and (II.4.47) indicate that the *EMF* is the sum of the products of the transference number times the chemical potential of the neutral species. If the transference number of the component *A* in the solid electrolyte is unity, then the *EMF* between phase 1 and 2 is given as

$$EMF = -\frac{RT}{ZF} \ln \frac{a_A(2)}{a_A(1)} \tag{II.4.48}$$

The following mixture properties can be derived from *EMF* measurements; from equation (II.4.48), when phase 1 is pure component *A*,

$$G_A^M = RT \ln a_A = -Z_A F \cdot EMF \tag{II.4.49}$$

$$\ln \gamma_A = -F / RT \cdot EMF - \ln X_A \tag{II.4.50}$$

$$S_A^M = F\left(\partial EMF / \partial T\right)_{X_A, P} \tag{II.4.51}$$

$$H_A^M = -F \cdot EMF + FT\left(\partial EMF / \partial T\right)_{X_A, P} \tag{II.4.52}$$

$$C_{P,A}^M = FT\left(\partial^2 EMF / \partial^2 T\right)_{X_A, P} \tag{II.4.53}$$

From Gibbs-Duhem integration [106], if phase 2 is a binary alloy,

$$\ln \gamma_B = -\frac{X_A}{X_B} \ln \gamma_A - \int_{X_B=1}^{X_B} \frac{\ln \gamma_A}{X_B^2} dX_B \tag{II.4.54}$$

we can derive partial mixture properties of B.

The integral property Y_m is given as

$$Y_m = X_A Y_A + X_B Y_B \tag{II.4.55}$$

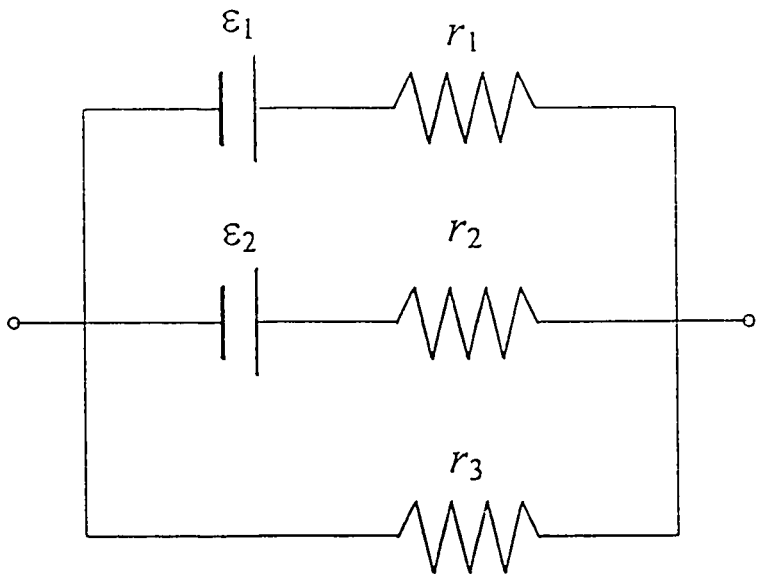

Figure II.4.2. The equivalent circuit of mixed ionic-electronic conductors. The subscripts 1 and 2 are for ions and 3 is for electrons. ε_i is given by equation (II.4.37).

II.5) Thermodynamics of solids

In thermodynamics the change in the internal energy is given as the sum of the products of the intensive variables and the conjugate extensive variables.

$$dU = TdS - PdV + \cdots + \sum_i \mu_i dN_i = \sum_j Y_j dX_j$$

where Y_j and X_j are the generalized force and the conjugate extensive variable [107]. Using the Legendre transformation, state functions are defined as a function of a combination of variables.

$$U = U(S,V,\cdots,N_i)$$

$$H = H(S,P,\cdots,N_i)$$

$$A = A(T,V,\cdots,N_i)$$

$$G = G(T,P,\cdots,N_i)$$

$$D = D(T,P,\cdots,\mu_i)$$

where the unspecified variables can be expressed as the partial derivative of corresponding conjugate variables. For example, $T = \frac{\partial U}{\partial S}$ and $S = -\frac{\partial G}{\partial T}$.

For a complete description of the thermodynamic properties of a substance, it is sufficient to have one of the thermodynamic potentials. The function $A(T, V)$ is most convenient because it is associated with the structural model of a body in the simplest way [26]. If $A = A(T, V)$ is known, we can easily derive other properties with the help of the relation

$$\left(\frac{\partial V}{\partial P}\right)_T \left(\frac{\partial P}{\partial T}\right)_V \left(\frac{\partial T}{\partial V}\right)_P = -1$$

Since $dA = -SdT - PdV$,

$$S = -\left(\frac{\partial A}{\partial T}\right)_V \tag{II.5.1}$$

$$P = -\left(\frac{\partial A}{\partial V}\right)_T \tag{II.5.2}$$

$$\left(\frac{\partial S}{\partial V}\right)_T = \left(\frac{\partial P}{\partial T}\right)_V \tag{II.5.3}$$

$$C_V = T\left(\frac{\partial S}{\partial T}\right)_V = -T\left(\frac{\partial^2 A}{\partial T^2}\right)_V \tag{II.5.4}$$

However, the easily measurable properties are C_P, α, β_T and β_S where

$$C_P = T\left(\frac{\partial S}{\partial T}\right)_P \tag{II.5.5}$$

$$\alpha = \frac{1}{V}\left(\frac{\partial V}{\partial T}\right)_P = -\frac{1}{V}\left(\frac{\partial V}{\partial P}\right)_T\left(\frac{\partial P}{\partial T}\right)_V = -\frac{1}{V}\frac{\partial^2 A}{\partial V \partial T}\Big/\frac{\partial^2 A}{\partial V^2} \tag{II.5.6}$$

$$\beta_T = \frac{1}{V}\left(\frac{\partial V}{\partial P}\right)_T = \left[V\left(\frac{\partial^2 A}{\partial V^2}\right)_T\right]^{-1} \tag{II.5.7}$$

$$\beta_S = \frac{1}{V}\left(\frac{\partial V}{\partial P}\right)_S \tag{II.5.8}$$

The auxiliary equations can be used to derive these properties from the function $A(T,V)$.

$$C_P - C_V = \frac{TV\alpha^2}{\beta_T} \tag{II.5.9}$$

$$\frac{\beta_S}{\beta_T} = \frac{C_V}{C_P} \tag{II.5.10}$$

$$\beta_S = \beta_T - \frac{TV\alpha^2}{C_P} \qquad \text{(II.5.11)}$$

Thus, if the proposed model gives the free energy $A(T,V)$, we can compute other properties. Conversely, if we measure C_P, α and β, other properties can be computed.

The change in the internal energy due to the change in state from (T_1, V_1, $P_1 = 0$) to (T_2, V_2, $P_2 = 0$) is given as

$$dU = dH = C_P dT \qquad \text{(II.5.12)}$$

Since $dU(T,V) = C_V dT + \left(\frac{\partial U}{\partial V}\right)_T dV$, the work of expansion is defined as

$$\left(\frac{\partial U}{\partial V}\right)_T dV = (C_P - C_V)dT \qquad \text{(II.5.13)}$$

If the internal energy can be represented by the sum of the lattice energy $u(V)$ and the vibrational energy $E^{vib}(T,V)$, the increment of the lattice energy can be computed with experimental results [26].

$$\text{The work of expansion} = \int_0^T \frac{TV\alpha^2}{\beta_T} dT = u - u_o + \Delta E^{vib} \qquad \text{(II.5.14)}$$

II.5.a) Statistical Thermodynamics

Suppose that the macrosystem is mechanically and chemically isolated, but in thermal equilibrium with its environment at T. The canonical ensemble partition function Q is defined as

$$Q(T,V,N_i) = \sum_j \exp\left(-\frac{E_j(V,N_i)}{kT}\right) \qquad \text{(II.5.15a)}$$

$$= \sum_{E} \Omega(E,V,N_i) \exp\left(-\frac{E(V,N_i)}{kT}\right) \qquad \text{(II.5.15b)}$$

where j, E_j and Ω are a microstste (or an eigenstate), the energy (the eigenvalue) and the degeneracy, respectively [24]. The probability that the microsystem is in the state j is given as

$$p_j = \frac{\exp\left(-\frac{E_j(V,N_i)}{kT}\right)}{Q} \qquad \text{(II.5.16)}$$

And the thermodynamic functions are written as

$$U = < E > = \sum_j E_j p_j = kT^2 \left(\frac{\partial \ln Q}{\partial T}\right)_{V,N_i} \qquad \text{(II.5.17)}$$

$$A = -kT \ln Q \qquad \text{(II.5.18)}$$

$$S = k \ln Q + kT \left(\frac{\partial \ln Q}{\partial T}\right)_{V,N_i} \qquad \text{(II.5.19)}$$

$$P = < P > = \sum_j P_j p_j = kT \left(\frac{\partial \ln Q}{\partial V}\right)_{T,N_i} \qquad \text{(II.5.20)}$$

$$\mu_i = < \mu_i > = \sum_j \mu_{i,j} p_j = -kT \left(\frac{\partial \ln Q}{\partial N_i}\right)_{T,V,N_j} \qquad \text{(II.5.21)}$$

where $U = \left(\frac{\partial A/T}{\partial 1/T}\right)_{V,N_i}$ and $Y_j = \frac{\partial A}{\partial X_j}$ are used to derive A and corresponding properties.

The extended version of the canonical partition function is given as the general partition function [107]. Assume that the system has (n+1) independent variables. In the canonical partition function, the system is specified by T and n intensive variables Q_i.

$$Q = Q(T, Q_1, \cdots, Q_r, Q_{r+1}, \cdots, Q_n) \tag{II.5.22}$$

where it should be noted that Q and Q_i are differentiated. The general partition function Z_r is defined by $(r+1)$ extensive variables ξ_i and $(n-r)$ intensive variables.

$$Z_r = Z_r(T, \xi_1, \cdots, \xi_r, Q_{r+1}, \cdots, Q_n) = \sum_{\Lambda} \exp(-\frac{H_r(\sigma)}{kT}) \tag{II.5.23}$$

where Λ is the space of the microstates σ compatible with $(Q_{r+1}, \cdots, Q_n)$.

$$H_r(\sigma) = E(\sigma) - \sum_{i=1}^{r} \xi_i Q_i(\sigma) \tag{II.5.24}$$

$$F_r = -kT \ln Z_r \tag{II.5.25}$$

Then

$$H_r = < H_r(\sigma) > = kT^2 \frac{\partial \ln Z_r}{\partial T} \tag{II.5.26}$$

$$Q_j = < Q_j(\sigma) > = kT \frac{\partial \ln Z_r}{\partial \xi_j} \qquad (j=1 \text{ to } r) \tag{II.5.27}$$

$$\xi_j = < \xi_j(\sigma) > = -kT \frac{\partial \ln Z_r}{\partial Q_j} \qquad (j=r+1 \text{ to } n) \tag{II.5.28}$$

$$S = k \ln Z_r + kT \frac{\partial \ln Z_r}{\partial T} \tag{II.5.29}$$

Note that

$$dH_r = TdS - Q_1 d\xi_1 - \cdots - Q_r d\xi_r + \xi_{r+1} dQ_{r+1} + \cdots + \xi_n dQ_n \tag{II.5.30}$$

$$F_r = H_r - TS \tag{II.5.31}$$

If H_r can be divided into kinetic and configurational terms,

$$H_r = H_{r,kin} + H_{r,conf} \tag{II.5.32}$$

then

$$Z_r = Z_{r,kin} \cdot Z_{r,conf} \tag{II.5.33}$$

The configurational degrees of freedom can be regarded as a separate system.

The relative fluctuation of the internal energy is given as

$$\frac{\sqrt{\mathrm{var}[E]}}{|U|} = \frac{T}{|U|}\left(\frac{\partial U}{\partial T}\right)^{\frac{1}{2}} \approx O\left(\frac{1}{\sqrt{n}}\right) \tag{II.5.34}$$

When the system consists of 1 mole of atoms, the relative fluctuation is extremely small (on the order of 10^{-12}). There is an overwhelming probability that the system will be in one of a set of Ω microstates [24, 107].

$$1 = \sum_{\Lambda} p(\sigma) \approx \frac{\Omega \exp\left(-\frac{U}{kT}\right)}{Q} = \Omega p(U) \tag{II.5.35}$$

$$\Omega = \frac{1}{p(U)} = \exp\left(\frac{U-A}{kT}\right) = \exp\left(\frac{S}{k}\right) \tag{II.5.36}$$

$$S = k \ln \Omega = k \ln \frac{1}{p(U)} \tag{II.5.37}$$

Thus, entropy is the measure of disorder. For large number of particles, the partition function can be expressed by the maximum-term (the maximum term method).

$$Q \approx \Omega \exp\left(-\frac{U}{kT}\right) \approx \Omega_m \exp\left(-\frac{E_m}{kT}\right) \tag{II.5.38}$$

In the harmonic approximation, the lattice component of the free energy of a crystal may be written as

$$a = u + kT\sum_i \left\{ \frac{\hbar\omega_i}{2kT} + \ln\left[1 - \exp\left(-\frac{\hbar\omega_i}{kT} \right) \right] \right\} \qquad \text{(II.5.39)}$$

where u is the lattice energy [108, 26]. Since the intermolecular vibrations can be separated from the intramolecular ones,

$$a = A + a_{mol} \qquad \text{(II.5.40)}$$

where A is the intermolecular part of the free energy and a_{mol} is the intramolecular part. Neglecting the zero-point energy,

$$A = u + kT\sum_s \sum_{\mathbf{k}} \ln\left[1 - \exp\left(-\frac{\hbar\omega_{\mathbf{k},s}}{kT} \right) \right] \qquad \text{(II.5.41)}$$

where $\mathbf{k}$ and s represent the wave vector and the branch of the dispersion surfaces. Thus if we know the lattice energy and the spectrum of the normal modes as functions of the volume, any thermodynamic property can be calculated.

$$S = -k\sum_s \sum_{\mathbf{k}} \ln\left[1 - \exp\left(-\frac{\hbar\omega_{\mathbf{k},s}}{kT} \right) \right] + \sum_s \sum_{\mathbf{k}} \frac{\hbar\omega_{\mathbf{k},s}}{T} \frac{1}{\exp\left(\frac{\hbar\omega_{\mathbf{k},s}}{kT} \right) - 1} \qquad \text{(II.5.42)}$$

$$U = u + \sum_s \sum_{\mathbf{k}} \hbar\omega_{\mathbf{k},s} \frac{1}{\exp\left(\frac{\hbar\omega_{\mathbf{k},s}}{kT} \right) - 1} \qquad \text{(II.5.43)}$$

$$C_V = \sum_s \sum_k k\left(\frac{\hbar\omega_{k,s}}{kT}\right)^2 \frac{\exp\left(\frac{\hbar\omega_{k,s}}{kT}\right)}{\left[\exp\left(\frac{\hbar\omega_{k,s}}{kT}\right)-1\right]^2} \qquad \text{(II.5.44)}$$

Introducing the density of the normal modes,

$$A = u + kT\int g(\omega)\ln\left[1-\exp\left(-\frac{\hbar\omega}{kT}\right)\right]d\omega \qquad \text{(II.5.45)}$$

where $g(\omega)d\omega$ is the number of normal modes between ω and $d\omega$ in the first Brillouin zone.

If a crystal has N unit cells and each unit cell consists of l atoms and m nonlinear molecules, there are $N(3l+6m)$ normal modes of external vibrations in the first Brillouin zone and N wave vectors for each of $(3l+6m)$ branches [26]. In the Einstein model, the dispersion of the frequencies is represented by one frequency. Hereafter in this section, we restrict our discussion to a crystal with $6N$ normal modes.

$$A = u + kT6N\ln\left[1-\exp\left(-\frac{\hbar\omega_E}{kT}\right)\right] \qquad \text{(II.5.46)}$$

In the Debye model, the dispersion is approximated by a parabolic equation.

$$A = u + \frac{18NkT}{\omega_{max}}\int_0^{\omega_{max}} \omega^2 \ln\left[1-\exp\left(-\frac{\hbar\omega}{kT}\right)\right]d\omega \qquad \text{(II.5.47)}$$

where $3\frac{V}{8\pi^3}\frac{4\pi}{3}\left(\frac{\omega_{max}}{v_s}\right)^3 = 6N$ and v_s = the average sound velocity.

Introducing the Debye function

$$D(x) = \frac{3}{x^3}\int_0^x \frac{z^3}{e^z-1}dz \qquad \text{(II.5.48)}$$

$$A = u + 2NkT\left\{3\ln\left[1-\exp\left(-\frac{\Theta}{T}\right)\right] - D\left(\frac{\Theta}{T}\right)\right\} \qquad \text{(II.5.49)}$$

where the characteristic temperature $\Theta = \frac{\hbar\omega_{max}}{k}$. The characteristic temperature is determined to fit the experimental results to the model.

From equation (II.5.1) and (II.5.4) and the relation $U = A + TS$, we obtain

$$U = u + 6NkTD\left(\frac{\Theta}{T}\right) \qquad \text{(II.5.50)}$$

$$S = -6Nk\ln\left[1-\exp\left(-\frac{\Theta}{T}\right)\right] + 8NkD\left(\frac{\Theta}{T}\right) \qquad \text{(II.5.51)}$$

$$C_V = 6Nk\left[D\left(\frac{\Theta}{T}\right) - \frac{\Theta}{T}D'\left(\frac{\Theta}{T}\right)\right] \qquad \text{(II.5.52)}$$

If the vibrational spectrum is constant, Θ is a constant. Such a model is called harmonic; $C_P = C_V$ and thermal expansion does not occur.

In the quasi-harmonic model [26], the characteristic temperature is a function of volume per unit cell.

$\Theta = \Theta(V)$

In this model the U, S and C_V are the same as in the harmonic model.

Using $D(x) = \frac{x}{e^x - 1} - \frac{x}{3}D'(x)$,

$$\left(\frac{\partial A}{\partial V}\right)_T = \frac{\partial u}{\partial V} - 6NkT\frac{\partial \ln\Theta}{\partial V}D\left(\frac{\Theta}{T}\right) \qquad \text{(II.5.53)}$$

Thus, the equation of state for a crystal is

$$-P = \frac{\partial u}{\partial V} - 6NkT\frac{\partial \ln\Theta}{\partial V}D\left(\frac{\Theta}{T}\right) \tag{II.5.54}$$

Other properties can be computed by the equalities (II.5.5 to II.5.7).

$$\frac{1}{\beta_T} = V\left[\frac{\partial^2 u}{\partial V^2} + 6NkT\frac{\partial^2 \ln\Theta}{\partial V^2}D\left(\frac{\Theta}{T}\right) + 6Nk\Theta\left(\frac{\partial \ln\Theta}{\partial V}\right)^2 D'\left(\frac{\Theta}{T}\right)\right] \tag{II.5.55}$$

$$\alpha = -\frac{6Nk}{V}\frac{\partial \ln\Theta}{\partial V}\left[\frac{\partial^2 u}{\partial V^2} + 6NkT\frac{\partial^2 \ln\Theta}{\partial V^2}D\left(\frac{\Theta}{T}\right) + 6Nk\Theta\left(\frac{\partial \ln\Theta}{\partial V}\right)^2 D'\left(\frac{\Theta}{T}\right)\right]^{-1} \times\left[D\left(\frac{\Theta}{T}\right) - \frac{\Theta}{T}D'\left(\frac{\Theta}{T}\right)\right] \tag{II.5.56}$$

$$C_P = -C_V\frac{\partial \ln\Theta}{\partial V}TV\alpha \tag{II.5.57}$$

The Grüneisen constant [108] is defined as

$$\gamma = \frac{\sum_{\mathbf{k},s}\gamma_{\mathbf{k}s}C_{vs}(\mathbf{k})}{\sum_{\mathbf{k},s}C_{vs}(\mathbf{k})} \tag{II.5.58}$$

where $\gamma_{\mathbf{k}s} = -\dfrac{V}{\omega_s(\mathbf{k})}\dfrac{\partial\omega_s(\mathbf{k})}{\partial V}$

$$C_{vs} = \frac{\hbar\omega_s(\mathbf{k})}{V}\frac{\partial}{\partial T}\left[\frac{1}{\exp\left(\dfrac{\hbar\omega_s(\mathbf{k})}{kT}\right) - 1}\right]$$

Then, the thermal expansion coefficient can be expressed as

$$\alpha = \frac{\gamma C_V \beta_T}{V} \tag{II.5.59}$$

In the Debye model the Grüneisen constant is written as

$$\gamma = -V\frac{\partial \ln \Theta}{\partial V} \qquad \text{(II.5.60)}$$

The experimental characteristic temperature depends on which thermodynamic function is used to determine it; usually C_V or S is used (equation (II.5.52) or (II.5.51)). Unfortunately the experimental characteristic temperature is not only a function of the volume but also of the temperature [26].

$\Theta = \Theta(V, T)$

This is the result of the anharmonicity of the vibrations.

II.5.b) Lattice statistics

Consider a lattice in which each site has two states [109]. If the states are 'spin up' and 'spin down' as in a magnetic system, we have an Ising model. In the lattice gas model, we interprete the states as 'full' or 'empty' which is suitable for intercalation compounds. A binary alloy can be modeled by lattice sites with 'atom A' and 'atom B'.

Ising model

Permanent magnetism is due to the exchange energy between unpaired spins. In the Ising model [25, 107] the internal energy due to the alignments of spins is given as

$$E = \mp J \sum_{i,j}^{(n.n.)} \sigma_i \sigma_j \qquad \text{(II.5.61)}$$

where the sign is negative for ferromagnetism and positive for anti-ferromagnetism, J is positive, (n.n.) means the summation is for nearest neighbor only and σ is one and negative one for spin up and spin down, respectively. The magnetic enthalpy is given as

$$H_1(\mathbf{H}, N) = E - \mathbf{HM} = \mp J\sum \sigma_i\sigma_j - \mathbf{H}\sum \sigma_i \qquad \text{(II.5.62)}$$

where **H** and **M** are the magnetic field and the magnetization, respectively. The general grand partion function for the ferromagnetism is written as

$$Z_1(T, \mathbf{H}, N) = \sum \exp\left(\frac{J\sum \sigma_i\sigma_j}{kT}\right)\exp\left(\frac{\mathbf{H}\sum \sigma_i}{kT}\right) \qquad \text{(II.5.63)}$$

If we apply the mean-field approximation to the Ising model,

$$\mathbf{M} = N < \sigma_i >= N\mathbf{m} \qquad \text{(II.5.64)}$$

$$E = -\frac{1}{2}ZJ < \sigma_i\sigma_j >= -J\mathbf{m}^2 \qquad \text{(II.5.65)}$$

where N and Z represent numbers of sites and coordinates, respectively.

Lattice gas model

In the lattice gas model (or cell model) [107, 109], the continuous domain V is replaced by a regular lattice of N sites or N equal cells. Assume that there is not more than one molecule in each cell and that the interaction energy between two molecules depends on the relative positions of the cells, not on their locations inside the cells. The enthalpy for the grand canonical distribution (T, μ, N) is given as

$$H_1(\mu, N) = E - \mu N_g = -\frac{1}{4}\varepsilon\sum (\sigma_i + 1)(\sigma_j + 1) - \frac{1}{2}\mu\sum (\sigma_i + 1) \qquad \text{(II.5.66)}$$

where $\mathbf{N_g}$ is the number of the molecules. If site i is occupied σ_i is one. Otherwise, it is negative one.

$$H_1 = -\frac{1}{2}N(\mu + \frac{1}{4}\varepsilon) - \frac{1}{4}\varepsilon\sum\sigma_i\sigma_j - \frac{1}{2}(\mu + \frac{1}{2}Z\varepsilon)\sum\sigma_i = -\frac{1}{2}N(\mu + \frac{1}{4}\varepsilon) + H_1^{(IM)} \tag{II.5.67}$$

Thus, the lattice gas model is equivalent to the Ising model for ferromagnetism.

Substitutional solid solutions

The model has two restrictions: (1) the volume per site is constant $\left(v_s = \frac{V}{N}\right)$ and (2) every lattice site is occupied. As in the Ising model only nearest neighbor interactions will be considered [107]. The numbers of A atoms, B atoms, AA bonds, BB bonds and AB bonds are expressed by σ_i which is one if site *i* is occupied by atom A and negative one if by atom B.

$$N_A = \frac{1}{2}\sum(1+\sigma_i) \tag{II.5.68}$$

$$N_B = \frac{1}{2}\sum(1-\sigma_i) \tag{II.5.69}$$

$$N_{AA} = \frac{1}{4}\sum(1+\sigma_i)(1+\sigma_j) \tag{II.5.70}$$

$$N_{BB} = \frac{1}{4}\sum(1-\sigma_i)(1-\sigma_j) \tag{II.5.71}$$

$$N_{AB} = \frac{1}{4}\sum[(1+\sigma_i)(1-\sigma_j) + (1-\sigma_i)(1+\sigma_j)] = \frac{1}{4}ZN - \frac{1}{2}\sum\sigma_i\sigma_j \tag{II.5.72}$$

Thus, internal energy is given as

$$E(N_A, N_B) = N_{AA}\varepsilon_{AA} + N_{BB}\varepsilon_{BB} + N_{AB}\varepsilon_{AB} \tag{II.5.73a}$$

$$= \frac{1}{2}Z(N_A\varepsilon_{AA} + N_B\varepsilon_{BB}) + \frac{1}{2}\varepsilon N_{AB} \tag{II.5.73b}$$

where $\varepsilon = 2\varepsilon_{AB} - \varepsilon_{AA} - \varepsilon_{BB}$ (II.5.74)

The enthalpy for the distribution $(T, \mu_A - \mu_B, N)$ is written as

$$H_1(\mu_A - \mu_B, N) = E - (\mu_A - \mu_B)N_A$$

$$= \frac{1}{8}ZN(2\varepsilon_{AB} + \varepsilon_{AA} + \varepsilon_{BB}) - \frac{1}{2}N(\mu_A - \mu_B) - \frac{1}{4}\varepsilon\sum\sigma_i\sigma_j$$
$$+ \frac{1}{2}[\frac{1}{2}Z(\varepsilon_{AA} - \varepsilon_{BB}) - (\mu_A - \mu_B)]\sum\sigma_i \quad \text{(II.5.75)}$$

It is equivalent to the ferromagnetic or antiferromagnetic Ising model depending on the sign of ε.

Using mean-field approximation, the correlation between adjacent sites is ignored.

$$N_{AB} = \frac{1}{4}ZN(1- <\sigma_i\sigma_j>) = \frac{1}{4}ZN(1- <\sigma_i>^2) = ZNX_AX_B \quad \text{(II.5.76)}$$

With the zeroth-order approximation (randomized approximation) and maximum-term method, we have the regular solution model [106].

$$\Omega(N_A, N_B) = \frac{N!}{N_A!N_B!} \quad \text{(II.5.77)}$$

$$Q = \Omega\exp\left(-\frac{E}{kT}\right) \quad \text{(II.5.78)}$$

$$A(T,V,N_A,N_B) = \frac{1}{2}ZN(\varepsilon_{AA}X_A + \varepsilon_{BB}X_B) + \frac{1}{2}\varepsilon ZNX_AX_B + NkT(X_A\ln X_A + X_B\ln X_B)$$

(II.5.79)

For the systems in which the deviation from randomness is considerable, the short-range order parameter α_s is introduced [110].

$$\alpha_s = 1 - \frac{N_{AB}}{N_{AB}^*} \tag{II.5.80}$$

where * means the value in a random distribution. For complete randomness $\varepsilon = 0$ and $\alpha_s = 0$. For association of unlike atoms $\varepsilon < 0$ and $\alpha_s < 0$. For clustering of like atoms $\varepsilon > 0$ and $\alpha_s > 0$. In the first-order approximation (quasi-chemical approximation) [106], the distribution of bonds between atoms is considered rather than the distribution of atoms.

$$\Omega(N_A, N_B, N_{AB}) = h \frac{\frac{1}{2}ZN!}{N_{AA}!N_{BB}![(N_{AB}/2)!]^2} \tag{II.5.81}$$

$$h = \frac{N!}{N_A!N_B!} \frac{N_{AA}^*!N_{BB}^*![(N_{AB}^*/2)]^2}{\frac{1}{2}ZN!} \tag{II.5.82}$$

Thus, the Helmholtz energy is a function of (T, V, N_A, N_B, N_{AB}). The equilibrium state is determined by

$$\left(\frac{\partial A}{\partial N_{AB}}\right)_{T,V,N_A,N_B} = 0$$

Thus

$$N_{AB} \cong ZNX_A X_B \left\{1 - X_A X_B \left[\exp\left(\frac{\varepsilon}{kT}\right) - 1\right]\right\} \tag{II.5.83}$$

$$\Delta G_m^{XS} \cong \frac{1}{2} ZN_\bullet X_A X_B \varepsilon \left(1 - \frac{X_A X_B \varepsilon}{2kT}\right) \tag{II.5.84}$$

where $N_\bullet$ is Avogadro's number [111].

For order-disorder transformation, assume that A atoms tend to order themselves on type α sites and B atoms tend to order themselves on the other type β sites [107]. Some parameters are given as

$$S = \frac{N_\beta}{N_\alpha} \tag{II.5.85}$$

$$X_{ij} = \frac{N_{ij}}{N_j} \tag{II.5.86}$$

where N, i and j represent number, atom i and site j, respectively.

The long-range order parameter θ is defined as

$$\theta = \frac{X_A - X_{A\beta}}{X_A} \tag{II.5.87}$$

For the disordered state, $\theta = 0$ and $X_{A\alpha} = X_{A\beta} = X_A$. For the ordered state, $\theta > 0$ and $X_{A\alpha} > X_A > X_{A\beta}$. Using the zeroth-order approximation, the difference from a regular solution in the Helmholtz energy is induced as

$$\Delta A(\theta) = \frac{NkT}{1+S}[X_A(1+S\theta)\ln(1+S\theta) + X_B(1-yS\theta)\ln(1-yS\theta) + SX_A(1-\theta)\ln(1-\theta) + SX_B(1+y\theta)\ln(1+y\theta)] + \frac{1}{2}N\varepsilon SX_A^2(Z - Z_{\alpha\alpha} - Z_{\beta\beta})\theta^2 \tag{II.5.88}$$

where $y = X_A / X_B$ and Zij is the number of site j around site i. In Landau expansion $\Delta A(\theta)$ is expressed in powers of θ [107].

$$\Delta A(\theta) = \frac{NSX_A}{2X_B}[kT - |\varepsilon|(Z - Z_{\alpha\alpha} - Z_{\beta\beta})X_A X_B]\theta^2 + \frac{NkTSX_A}{1+S}\sum_{n=3}^{\infty}\frac{[1+y(-y)^{n-2}][1+S(-S)^{n-2}]}{n(n-1)}\theta^n$$

(II.5.89)

For equal sublattices ($S = 1$)

$$\Delta A(\theta) = b_2\theta^2 + b_4\theta^4 + b_6\theta^6 + \cdots \qquad \text{(II.5.90)}$$

where θ is determined to minimize the energy. Because $b_{2n} > 0$, for $b_2 > 0$, $\theta = 0$ is the only solution, that is, the system is disordered. For $b_2 < 0$, there are two solutions $(\pm\theta \neq 0)$. Thus the system is ordered. The transformation is second-order.

For $S \neq 1$

$$\Delta A(\theta) = b_2\theta^2 + b_3\theta^3 + b_4\theta^4 + \cdots \qquad \text{(II.5.91)}$$

For fixed X_A, we need to solve the following equations.

$$\Delta A(\theta) = 0 \text{ and } \left(\frac{\partial \Delta A}{\partial \theta}\right)_{X_A} = 0$$

The solution will be $\theta = 0$ or θ_* and $T = T_*$. For $T < T_*$, minimum ΔA yields ordered phase $(\theta \neq 0)$. For $T > T_*$, the phase is disordered $(\theta = 0)$. The resulting transformation is first-order (see the figure II.5.1).

(a)

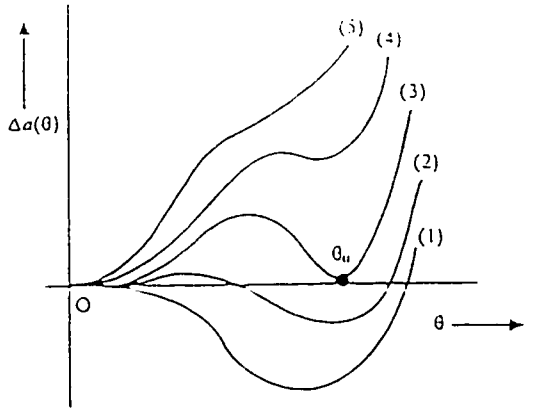

(b)

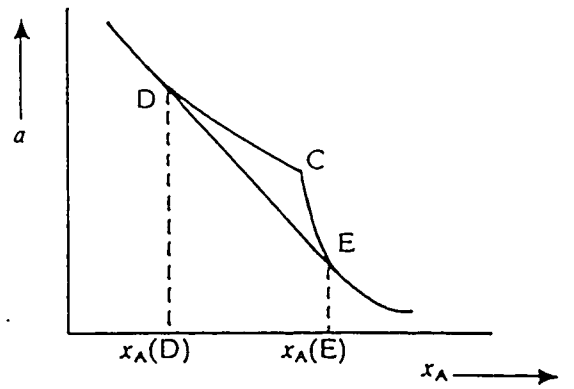

(c)

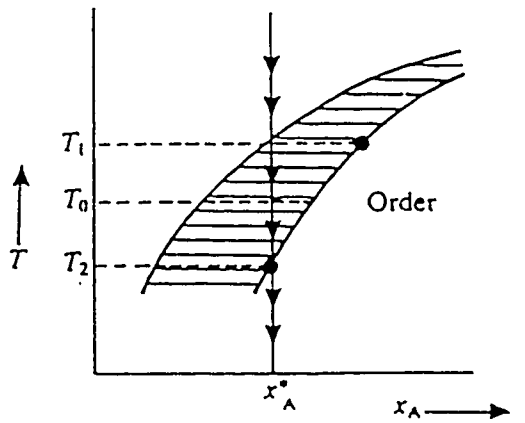

Figure II.5.1. (a) Free energy-order parameter isotherms for the unsymmetrical case ($S \neq 1$). Curve (3) corresponds to the transition temperature. Temperature increases with the number of the curves. (b) Free energy-mole-fraction isotherm showing convex envelope. Point C corresponds to curve (3). (c) Conjugate phases in the mole-fraction-temperature plane [107].

An extended version of the quasi-chemical method is the cluster variation method [107]. In the first-order approximation, energies and weights for the microsystems on a cluster or group of sites are treated exactly, but the correlations due to sites shared between groups are handled by plausible assumptions. The lattice is divided into N_g basic groups of sites in such a way that each nearest neighbor pair belongs to only one group and the sites in a group are equivalent. Some terms are defined as

N_g = the number of groups

ν = the number of nearest neighbor pairs in a group

p = the number of sites in a group

s = the number of species in the system

ω_k = the number of configurations of type k

p_{ik} = the number of sites occupied by species i

ψ_k = the probability that a group has a specific configuration of type k

where k refers to an energy level ε_k with multiple configurations.

The relations between them are

$$N_g = \frac{\frac{1}{2}ZN}{\nu} \tag{II.5.92}$$

$$\frac{pN_g}{N} = \frac{Zp}{2\nu} \tag{II.5.93}$$

$$\sum_{i=1}^{s} p_{ik} = p \tag{II.5.94}$$

$$\sum_k \omega_k \psi_k = 1 \tag{II.5.95}$$

$$X_i = \frac{1}{p}\sum_k p_{ik}\omega_k \psi_k \tag{II.5.96}$$

Note that each site belongs to $\frac{Zp}{2\nu}$ groups.

The first-order approximation is

$$\Omega(\psi_k) = \frac{N_g!}{\prod_k [(N_g\psi_k)!]^{\omega_k}} \Bigg/ \left[\frac{N!}{\prod_i^s (NX_i)!}\right]^{\frac{Zp}{2\nu}-1} \tag{II.5.97}$$

where the denominator is the correction factor which makes the degeneracy exact for random distribution. The configurational enthalpy for the distribution (V,μ_i,N) is

$$H_1(V,\mu_i,\psi_k,N) = N_g\sum_k \varepsilon_k\omega_k\psi_k - N\sum_i^s \mu_i X_i \tag{II.5.98}$$

$$f(T,V,\mu_i,\psi_k) = \frac{F}{N}$$

$$= \frac{Z}{2\nu}\sum_k \varepsilon_k\omega_k\psi_k + kT\frac{Z}{2\nu}\sum_k \omega_k\psi_k \ln\psi_k - kT\left(\frac{Zp}{2\nu}-1\right)\sum_i^s X_i \ln X_i - \sum_i^s \mu_i X_i \tag{II.5.99}$$

Using equations (II.5.95) and (II.5.96), at equilibrium

$$kT\ln\psi_k + \varepsilon_k - \sum_i^s p_{ik}\left[\left(1-\frac{2\nu}{Zp}\right)kT\ln X_i + \frac{2\nu}{Zp}\mu_i\right] - \alpha = 0 \tag{II.5.100}$$

where α is independent of ψ_k. Though the solution is not exact, we can simplify it by the relation

$$\frac{\psi_k}{\psi_l} = \exp\left(\frac{\varepsilon_l - \varepsilon_k}{kT}\right)\prod_i^{s-1}\left[\left(\frac{X_i}{X_s}\right)^{1-\frac{2\nu}{Zp}} \exp\frac{2\nu(\mu_i - \mu_s)}{ZpkT}\right]^{p_{ik}-p_{il}} \tag{II.5.101}$$

Thus, at equilibrium

$$f(T,V,\mu_i) = \frac{Z}{2\nu}\left\{kT\ln\psi_i + \varepsilon_i - \sum_i^s p_{ii}\left[\left(1-\frac{2\nu}{Zp}\right)kT\ln X_i + \frac{2\nu}{Zp}\mu_i\right]\right\} \tag{II.5.102}$$

where ψ_i and X_i are numerically determined.

An approximation of the nonconfigurational entropy terms is attempted here. Assume that the interaction is pairwise and additive and that the potential energy is spherical. The potential energy of atom A may be written as a function of displacement r and composition.

$$U_A(r) = Z[U_{AA}(r)p_{AA} + U_{AB}(r)p_{AB}] \tag{II.5.103}$$

where $P_{AA} = \dfrac{2N_{AA}}{ZN_A}$

$$P_{AB} = \frac{N_{AB}}{ZN_A}$$

P_{ij} is the probability that a site next to atom i is occupied by atom j.

At high temperatures the vibrational partition function is

$$q_A = \left(\frac{2\pi m_A^{\frac{1}{3}}kT}{h}\right)^3\left(\frac{\partial^2 U_A}{\partial r^2}\right)^{-\frac{3}{2}} = q_A^*(1+\alpha_A P_{AB})^{-\frac{3}{2}} \tag{II.5.104}$$

where $q_A^\circ = \left(\frac{2\pi m_A^{\frac{1}{2}} kT}{h}\right)^3 \left(\frac{\partial^2 ZU_{AA}}{\partial r^2}\right)^{-\frac{3}{2}}$ (the vibrational partition function of pure A)

$$\alpha_A = \frac{\partial^2 (U_{AB} - U_{AA})}{\partial r^2} \Big/ \frac{\partial^2 U_{AA}}{\partial r^2}$$

By analogy, for atom B

$$q_B = q_B^\circ (1 + \alpha_B P_{BA})^{-\frac{3}{2}} \qquad \text{(II.5.105)}$$

Thus, the nonconfigurational excess free energy is

$$G_{nonconf}^{XS} = \frac{3}{2} NkT\left(X_A \ln(1 + \alpha_A P_{AB}) + X_B \ln(1 + \alpha_B P_{BA})\right) \qquad \text{(II.5.106)}$$

Since $\alpha_i << 1$, we use the approximation

$$G_{nonconfig}^{XS} \cong NkT \frac{3}{2}(\alpha_A + \alpha_B)\frac{N_{AB}}{ZN} \qquad \text{(II.5.107a)}$$

$$\cong -\frac{\varepsilon T}{2\tau} N_{AB} \qquad \text{(II.5.107b)}$$

where $\tau = -\frac{Z\varepsilon}{3k(\alpha_A + \alpha_B)}$

Combining the nonconfigurational term to regular solution model results in the quasi-regular solution [106].

$$G_m^{XS} = \frac{1}{2} ZN_\circ X_A X_B \varepsilon\left(1 - \frac{T}{\tau}\right) \qquad \text{(II.5.108)}$$

The modified quasi-chemical solution model will be

$$G_m^{xs} \equiv \frac{1}{2} Z N_o X_A X_B \varepsilon \left(1 - \frac{T}{\tau}\right) \left[1 - \frac{X_A X_B \varepsilon \left(1 - \frac{T}{\tau}\right)}{2kT}\right] \qquad \text{(II.5.109)}$$

Interstitial solid solutions

There seems to be some confusion or difficulty in the choice of the reference state in interstitial solutions [112]. The difference between the substitutional and the interstitial solid solutions is that in the former, the end compositions of the solution are the pure components and customarily the standard state is chosen as the reference state. However, in the latter, the end composition (completely filled interstices) is not always experimentally accessible and the Henrian standard state is sometimes more convenient. Since the change in the nonconfigurational entropy terms of the interstitial solutions is more important than in the substitutional solutions, that should be considered in the model.

In the regular interstitial solution model, the assumptions are the same as in the regular substitutional solution model. The following terms are defined.

N_M = the number of solvent atoms M

N_S = the number of solute atoms S

N_I = the total number of interstial sites

N_V = the number of vacant interstitial sites

$$\beta = \frac{N_I}{N_M} \qquad \text{(II.5.110)}$$

$$X_M = \frac{N_M}{N_s + N_M} \tag{II.5.111}$$

$$X_S = \frac{N_S}{N_s + N_M} \tag{II.5.112}$$

$$Y_S = \frac{N_S}{N_I} = \frac{X_S}{\beta X_M} \tag{II.5.113}$$

$$Y_V = \frac{N_V}{N_I} = 1 - \frac{X_S}{\beta X_M} \tag{II.5.114}$$

Using the pairwise nearest neighbor interactions

$$E = N_{MM}\varepsilon_{MM} + N_{SM}\varepsilon_{SM} + N_{SS}\varepsilon_{SS} + N_{SV}\varepsilon_{SV} + N_{VV}\varepsilon_{VV} \tag{II.5.115}$$

Using mean-field theory

$$E = \frac{1}{2}Z_{MM}N_M\varepsilon_{MM} + Z_{SM}N_S\varepsilon_{SM} + \frac{1}{2}Z_{II}N_I\varepsilon_{SS}Y_S^2 + \frac{1}{2}Z_{II}N_I\varepsilon_{VV}Y_V^2 + Z_{II}N_{II}\varepsilon_{SV}Y_SY_V \tag{II.5.116}$$

where Z_{ij} is the number of the nearest j sites around atom i.

After rearranging the terms,

$$E = N_I\varepsilon_V Y_V + N_I\varepsilon_I Y_S + \frac{1}{2}Z_{II}N_I\varepsilon Y_SY_V \tag{II.5.117}$$

$$\text{where } \varepsilon_V = \frac{\frac{1}{2}Z_{MM}\varepsilon_{MM}}{\beta} + \frac{1}{2}Z_{II}\varepsilon_{VV} \tag{II.5.118}$$

$$\varepsilon_I = \frac{\frac{1}{2}Z_{MM}\varepsilon_{MM}}{\beta} + Z_{SM}\varepsilon_{SM} + \frac{1}{2}Z_{II}\varepsilon_{SS} \tag{II.5.119}$$

$$\varepsilon = 2\varepsilon_{SV} - \varepsilon_{SS} - \varepsilon_{VV} \tag{II.5.120}$$

The subscripts V and I represent the phase with completely vacant interstices and the phase with fully occupied interstices, respectively.

The zeroth-order approximation gives

$$\Omega = \frac{N_I!}{N_I Y_V! N_I Y_S!} \tag{II.5.121}$$

Thus, the interstitial solid solution corresponds to the substitutional solid solution in the pseudo-binary system which consists of two building blocks;

one is made of $\left(\frac{1}{\beta}M \text{ atoms and 1 vacant interstice}\right)$ and

the other is of $\left(\frac{1}{\beta}M \text{ atoms and 1 S atom at interstice}\right)$.

$$G = N_I\left[\varepsilon_V Y_V + \varepsilon_I Y_S + \frac{1}{2}Z_{II}\varepsilon Y_V Y_S + kT\left(Y_V \ln Y_V + Y_S \ln Y_S\right)\right] \tag{II.5.122}$$

$$\mu_V = \varepsilon_V + \frac{1}{2}Z_{II}\varepsilon Y_S^2 + kT\ln Y_V \tag{II.5.123}$$

$$\mu_I = \varepsilon_I + \frac{1}{2}Z_{II}\varepsilon Y_V^2 + kT\ln Y_S \tag{II.5.124}$$

Since $M = \beta\left(\frac{M}{\beta}\right)$ and $M + \beta S = \beta\left(\frac{M}{\beta} + S\right)$,

$$\mu_M = \beta\mu_V = \beta\left(\varepsilon_V + \frac{1}{2}Z_{II}\varepsilon Y_S^2 + kT\ln Y_V\right) \tag{II.5.125}$$

$$\mu_S = \mu_I - \frac{1}{\beta}\mu_M = \left(\varepsilon_I - \varepsilon_V + \frac{1}{2}Z_{II}\varepsilon\right) - Z_{II}\varepsilon Y_S + kT\ln\frac{Y_S}{1-Y_S} \tag{II.5.126}$$

where the last equation is the same as in the lattice-gas model [109].

We introduce the arbitrary reference state,

$$\mu_S = \mu_S^* + \left[-\mu_S^* + \varepsilon_I - \varepsilon_V + Z_{II}\varepsilon\left(\frac{1}{2} - \frac{X_S}{\beta X_M}\right) - kT\ln(\beta X_M - X_S) \right] + kT\ln X_S \quad \text{(II.5.127)}$$

For the Raoultian standard state,

$$\mu_S^* = \mu_S^\circ$$

$$kT\ln\gamma_S = -\mu_S^\circ + \varepsilon_I - \varepsilon_V + Z_{II}\varepsilon\left(\frac{1}{2} - \frac{X_S}{\beta X_M}\right) - kT\ln(\beta X_M - X_S) \quad \text{for } 0 \le X_S \le \frac{\beta}{\beta+1}$$

(II.5.128)

For the Henrian standard state, as X_S approaches zero, the activity coefficient goes to one.

$$\mu_S^* = \mu_S^{\circ(H)} = \varepsilon_I - \varepsilon_V + \frac{1}{2}Z_{II}\varepsilon - kT\ln\beta \quad \text{(II.5.129)}$$

$$kT\ln\gamma_S = -Z_{II}\varepsilon\frac{X_S}{\beta X_M} - kT\ln\left(\frac{\beta X_M - X_S}{\beta}\right) \qquad \text{for } 0 \le X_S \le \frac{\beta}{\beta+1} \quad \text{(II.5.130)}$$

Now consider the nonconfigurational terms. The treatments are similar to those in the quasi-regular solution model. The potential energy is a function of displacement and composition.

$$U_M(r) = U_{MM}(r) + U_{MS}(r)Y_S \quad \text{(II.5.131)}$$

$$U_S(r) = U_{SM}(r) + U_{SS}(r)Y_S \quad \text{(II.5.132)}$$

The partition functions are given as

$$q_M = q_M^*(1+\alpha_M Y_S)^{-\frac{3}{2}} \quad \text{(II.5.133)}$$

$$q_S = q_I^*(1+\alpha_S Y_S)^{-\frac{3}{2}} \quad \text{(II.5.134)}$$

where $\alpha_M = \dfrac{\partial^2 U_{MS}}{\partial r^2} \Big/ \dfrac{\partial^2 U_{MM}}{\partial r^2}$

$$\alpha_S = \frac{\partial^2 U_{SS}}{\partial r^2} \Big/ \frac{\partial^2 U_{SM}}{\partial r^2}$$

q_I° = the vibrational partition function of the solute in dilute solutions.

Note that α_i in interstitial solutions is not necessarily small compared to unity.

$$G_{nonconfig} = -NkT\left\{X_M \ln q_M^\circ + X_S \ln q_I^\circ - \frac{3}{2}\left[X_M \ln(1+\alpha_M Y_S) + X_S \ln(1+\alpha_S Y_S)\right]\right\} \tag{II.5.135}$$

$$\mu_{S,nonconfig} = -kT\left\{\ln q_I^\circ - \frac{3}{2}\left[\frac{\alpha_M}{1+\alpha_M Y_S}\frac{1}{\beta} + \ln(1+\alpha_S Y_S) + \frac{\alpha_S}{1+\alpha_S Y_S} Y_S\right]\right\} \tag{II.5.136}$$

Thus, the sum of the configurational terms and nonconfigurational terms results in

$$\mu_S = \left(\varepsilon_I - \varepsilon_V + \frac{1}{2} Z_{II}\varepsilon\right) - Z_{II}\varepsilon Y_S + kT \ln \frac{Y_S}{1-Y_S} + \mu_{S,nonconfig} \tag{II.5.137}$$

For dilute solutions, the chemical potential of solute is in the form of

$$\mu_S \cong H_1 + H_2 Y_S + kT \ln \frac{Y_S}{1-Y_S} - kT(S_1 + S_2 Y_S)$$

$$\cong H_1 - kTS_1 + (H_2 - kTS_2)Y_S + kT \ln \frac{Y_S}{1-Y_S} \tag{II.5.138}$$

II.6) Lattice dynamics

II.6.a) External vibrational modes

In molecular or complex ionic crystals it is advantageous to separate the rigid-body motions of the well-bound groups of atoms (external modes) from the relative motions of atoms in the group about its center of mass (internal modes). Such a situation is characterized by [27]:

1) close similarity in the vibrational frequencies of the isolated group and those of the group in the crystal
2) large differences between the scale of external vibrational frequencies and that of internal vibrational frequencies.

The behavior of the normal modes of a one-dimensional lattice with a basis is discussed by Ashcroft [108], which shows that when the force constants between atoms in a group are much larger than those between atoms in different groups, the modes can be separated as internal and external ones. Suppose that the primitive unit cell contains μ single atoms or ions and ν nonlinear well-bound groups. There are $3\mu + 6\nu$ external branches; three of them are acoustic branches and the rest of them behave like optic branches. If there are n atoms in the primitive cell, the number of internal branches equals $3n - (3\mu + 6\nu)$ which have the character of optic branches. In this section the dynamics of external vibrations will be discussed mainly following Venkataraman [27,113].

When the displacements, both linear and angular, of vibrating units are referred to a set of Cartesian axes fixed to the crystal, the frame of reference is referred to as the

fixed frame. Alternatively, when the displacements are referred to a set of local axes which coincide with the principal axes of the moment of inertia of the unit in question, this is known as the principal-axis frame. Hereafter the dynamics will be treated in the fixed frame.

Both linear and angular displacements can be represented by vectors (the angular displacements are supposed to be infinitesimal). Vectors for linear displacements change sign under inversion. However, vectors for angular displacements do not. Thus, under an orthogonal transformation **S**, those vectors transform in matrix representation as

$$\mathbf{u}'^{t} = \mathbf{S}\mathbf{u}^{t} \tag{II.6.1}$$

$$\mathbf{u}'^{r} = |\mathbf{S}|\mathbf{S}\mathbf{u}^{r} \tag{II.6.2}$$

where the superscript t and r denote linear and angular displacements, respectively [114]. The determinant of **S** is ± 1 depending on whether **S** is a proper or improper rotation.

The equilibrium position of the kth atom in the κth unit in the lth cell is given as

$$\mathbf{X}(l\kappa k) = \mathbf{X}(l) + \mathbf{X}(\kappa) + \mathbf{X}(k) \tag{II.6.3}$$

The kinetic energy is written as

$$T = \frac{1}{2}\sum_{l}\sum_{\kappa=1}^{\mu+\nu}\sum_{\alpha=x,y,z} m_{\kappa}\left[\dot{u}_{\alpha}^{t}(l\kappa)\right]^{2} + \frac{1}{2}\sum_{l}\sum_{\kappa=\mu+1}^{\mu+\nu}\sum_{\alpha,\beta=x,y,z} I_{\alpha\beta}(\kappa)\dot{u}_{\alpha}^{r}(l\kappa)\dot{u}_{\beta}^{r}(l\kappa) \tag{II.6.4a}$$

$$= \frac{1}{2}\sum_{l}\sum_{\kappa=1}^{\mu+\nu} m_{\kappa}\dot{\mathbf{u}}^{t}(l\kappa)\cdot\dot{\mathbf{u}}^{t}(l\kappa) + \frac{1}{2}\sum_{l}\sum_{\kappa=\mu+1}^{\mu+\nu}\dot{\mathbf{u}}^{r}(l\kappa)\cdot\mathbf{I}(\kappa)\cdot\dot{\mathbf{u}}^{r}(l\kappa) \tag{II.6.4b}$$

where m_{κ} = the mass of the unit κ (for all κ)

$\mathbf{I}(\kappa)$ = the moment of inertia of the unit κ ($\kappa = \mu+1$ to $\mu+\nu$).

In the harmonic approximation the potential energy can be expanded in a Taylor series of the displacements as

$$\Phi \equiv \Phi_0 + \Phi_1 + \Phi_2 \tag{II.6.5}$$

The first-order term is obviously zero and the second-order term is

$$\Phi_2 = \frac{1}{2}\sum_{l,l'}\sum_{\kappa=1}^{\mu+\nu}\sum_{\kappa'=1}^{\mu+\nu}\sum_{\alpha,\beta}\phi^{\alpha}_{\alpha\beta}(l\kappa;l'\kappa')u^{l}_{\alpha}(l\kappa)u^{l}_{\beta}(l'\kappa') + \frac{1}{2}\sum_{l,l'}\sum_{\kappa=1}^{\mu+\nu}\sum_{\kappa'=\mu+1}^{\mu+\nu}\sum_{\alpha,\beta}\phi^{\alpha r}_{\alpha\beta}(l\kappa;l'\kappa')u^{l}_{\alpha}(l\kappa)u^{r}_{\beta}(l'\kappa')$$
$$+\frac{1}{2}\sum_{l,l'}\sum_{\kappa=\mu+1}^{\mu+\nu}\sum_{\kappa'=1}^{\mu+\nu}\sum_{\alpha,\beta}\phi^{r\alpha}_{\alpha\beta}(l\kappa;l'\kappa')u^{r}_{\alpha}(l\kappa)u^{l}_{\beta}(l'\kappa') + \frac{1}{2}\sum_{l,l'}\sum_{\kappa=\mu+1}^{\mu+\nu}\sum_{\kappa'=\nu+1}^{\mu+\nu}\sum_{\alpha,\beta}\phi^{rr}_{\alpha\beta}(l\kappa;l'\kappa')u^{r}_{\alpha}(l\kappa)u^{r}_{\beta}(l'\kappa') \tag{II.6.6}$$

where the coupling coefficient between units is

$$\phi^{ll'}_{\alpha\beta}(l\kappa;l'\kappa') = \frac{\partial^2\Phi}{\partial u^{l}_{\alpha}(l\kappa)\partial u^{l'}_{\beta}(l\kappa')} \tag{II.6.7}$$

Thus, the Hamiltonian is, in the harmonic approximation, given as

$$H = T + \Phi_0 + \Phi_2 \tag{II.6.8}$$

The equation of motion for $\kappa = 1$ to $(\mu + \nu)$ is

$$m_{\kappa}\ddot{u}^{l}_{\alpha}(l\kappa) = -\sum_{l'}\sum_{\kappa'=1}^{\mu+\nu}\sum_{\beta}\phi^{\alpha}_{\alpha\beta}(l\kappa;l'\kappa')u^{l}_{\beta}(l'\kappa') - \sum_{l'}\sum_{\kappa'=\mu+1}^{\mu+\nu}\sum_{\beta}\phi^{\alpha r}_{\alpha\beta}(l\kappa;l'\kappa')u^{r}_{\beta}(l'\kappa') \tag{II.6.9a}$$

for $\kappa = (\mu + 1)$ to $(\mu + \nu)$

$$I_{\alpha\alpha}(\kappa)\ddot{u}^{r}_{\alpha}(l\kappa) = -\sum_{l'}\sum_{\kappa'=1}^{\mu+\nu}\sum_{\beta}\phi^{r\alpha}_{\alpha\beta}(l\kappa;l'\kappa')u^{l}_{\beta}(l'\kappa') - \sum_{l'}\sum_{\kappa'=\mu+1}^{\mu+\nu}\sum_{\beta}\phi^{rr}_{\alpha\beta}(l\kappa;l'\kappa')u^{r}_{\beta}(l'\kappa')$$

$$-\sum_{\beta\neq\alpha}I_{\alpha\beta}(\kappa)\ddot{u}^{r}_{\beta}(l\kappa) \tag{II.6.9b}$$

The solution may have the wavelike form [28] of

$$u_\alpha^l(l\kappa) = U_\alpha^l(\kappa|\mathbf{q})\exp\{i[\mathbf{q}\cdot\mathbf{X}(l) - \omega(\mathbf{q})t]\} \qquad \text{(II.6.10)}$$

where **q** is the wave vector.

Substituting it in the equation of motion, we obtain in matrix notation [27]

$$\omega^2(\mathbf{q})\mathbf{m}\mathbf{U}(\mathbf{q}) = \mathbf{B}(\mathbf{q})\mathbf{U}(\mathbf{q}) \qquad \text{(II.6.11)}$$

where the diagonal submatrices of **m** are

$$\mathbf{m}^n(\kappa\kappa) = m_k\,\mathbf{1}_3 \qquad (\mathbf{1}_3 = \text{unitary matrix in three dimensions}) \qquad \text{(II.6.12a)}$$

$$\mathbf{m}^r(\kappa\kappa) = \mathbf{I}(\kappa) \qquad \text{(II.6.12b)}$$

and the off-diagonal submatrices of **m** are null.

U(q) which has $(3\mu + 6\nu)$ elements may be written as

$$\mathbf{U}(\mathbf{q}) = \begin{bmatrix} U_x^l(\kappa=1|\mathbf{q}) \\ U_y^l(\kappa=1|\mathbf{q}) \\ U_z^l(\kappa=1|\mathbf{q}) \\ \vdots \\ U_x^l(\kappa=\mu|\mathbf{q}) \\ U_y^l(\kappa=\mu|\mathbf{q}) \\ U_z^l(\kappa=\mu|\mathbf{q}) \\ U_x^l(\kappa=\mu+1|\mathbf{q}) \\ U_y^l(\kappa=\mu+1|\mathbf{q}) \\ U_z^l(\kappa=\mu+1|\mathbf{q}) \\ U_x^r(\kappa=\mu+1|\mathbf{q}) \\ U_y^r(\kappa=\mu+1|\mathbf{q}) \\ U_z^r(\kappa=\mu+1|\mathbf{q}) \\ \vdots \\ U_x^l(\kappa=\mu+\nu|\mathbf{q}) \\ U_y^l(\kappa=\mu+\nu|\mathbf{q}) \\ U_z^l(\kappa=\mu+\nu|\mathbf{q}) \\ U_x^r(\kappa=\mu+\nu|\mathbf{q}) \\ U_y^r(\kappa=\mu+\nu|\mathbf{q}) \\ U_z^r(\kappa=\mu+\nu|\mathbf{q}) \end{bmatrix} \qquad \text{(II.6.13)}$$

The corresponding scheme of the dynamical matrix $\mathbf{B}(\mathbf{q})$ is

$$\mathbf{B}(\mathbf{q}) = \begin{bmatrix} \mathbf{B}^{ll}(\mathbf{q},11) & \cdots & \mathbf{B}^{ll}(\mathbf{q},1(\mu+1)) & \mathbf{B}^{lr}(\mathbf{q},1(\mu+1)) & \cdots \\ \vdots & \ddots & \vdots & & \ddots \\ \mathbf{B}^{ll}(\mathbf{q},(\mu+1)1) & \cdots & \mathbf{B}^{ll}(\mathbf{q},(\mu+1)(\mu+1)) & \mathbf{B}^{lr}(\mathbf{q},(\mu+1)(\mu+1)) & \cdots \\ \mathbf{B}^{rl}(\mathbf{q},(\mu+1)1) & & \mathbf{B}^{rl}(\mathbf{q},(\mu+1)(\mu+1)) & \mathbf{B}^{rr}(\mathbf{q},(\mu+1)(\mu+1)) & \\ \vdots & \ddots & \vdots & & \ddots \end{bmatrix}$$

(II.6.14)

where the element of the submatrix is

$$B_{\alpha\beta}^{ii'}(\mathbf{q},\kappa\kappa') = \sum_{l'} \phi_{\alpha\beta}^{ii'}(0\kappa;l\kappa') \exp[i\mathbf{q}\cdot\mathbf{X}(l')] \qquad \text{(II.6.15)}$$

The eigenvalues $\omega_j^2(\mathbf{q})$ are obtained by solving the secular equation

$$\left|\mathbf{B}(\mathbf{q}) - \omega^2(\mathbf{q})\mathbf{m}\right| = 0 \qquad \text{(II.6.16)}$$

We rewrite the amplitudes of the vibration in (II.6.13) as

$$U_\alpha^l(\kappa|\mathbf{q}j) = a(qj)e_\alpha^l(\kappa|\mathbf{q}j) \qquad \text{(II.6.17a)}$$

or

$$\mathbf{U}(\mathbf{q}j) = a(qj)\mathbf{e}(\mathbf{q}j) \qquad \text{(II.6.17b)}$$

Thus, $\mathbf{e}(\mathbf{q}j)$ is the eigenvector of the eigenvalue $\omega_j^2(\mathbf{q})$.

The normalization constraint is

$$\mathbf{e}^+(\mathbf{q}j)\mathbf{m}\mathbf{e}(\mathbf{q}j) = M \qquad \text{(II.6.18)}$$

where subscript + represents the Hermitian conjugate and M is the total mass of a primitive unit cell. We can construct $\mathbf{e}(\mathbf{q}j)$'s such that

$$\mathbf{e}^+(\mathbf{q}j)\mathbf{m}\mathbf{e}(\mathbf{q}j') = 0 \qquad (j \neq j' \text{ orthogonality}) \qquad \text{(II.6.19)}$$

Define a matrix $\mathbf{e}(\mathbf{q})$ by

$$\mathbf{e}(\mathbf{q}) = [\mathbf{e}(\mathbf{q}1), \mathbf{e}(\mathbf{q}2), \cdots \mathbf{e}(\mathbf{q}(3\mu + 6\nu))] \qquad \text{(II.6.20)}$$

Then, from (II.6.18) and (II.6.19)

$$\mathbf{e}^+(\mathbf{q})\mathbf{m}\mathbf{e}(\mathbf{q}) = M\mathbf{1}_{3\mu+6\nu} \qquad \text{(II.6.21)}$$

Combining (II.6.11) and (II.6.21)

$$\mathbf{e}^+(\mathbf{q})\mathbf{B}(\mathbf{q})\mathbf{e}(\mathbf{q}) = M\boldsymbol{\Omega}(\mathbf{q}) \qquad \text{(II.6.22)}$$

where $\Omega_{ij}(\mathbf{q}) = \omega_j^2(\mathbf{q})\delta_{ij}$

Thus, the matrix $\mathbf{e}(\mathbf{q})$ brings both m and $\mathbf{B}(\mathbf{q})$ into diagonal form.

The general solution of the equation of motion is the sum of the displacements (II.6.10) due to harmonic vibrations of all available $\mathbf{q}$ and $\omega_j^2(\mathbf{q})$.

$$u_\alpha^l(l\kappa) = \frac{1}{\sqrt{N}} \sum_{\mathbf{q}} \sum_j e_\alpha^l(\kappa|\mathbf{q}j) \exp[i\mathbf{q}\cdot\mathbf{X}(l)] a(\mathbf{q}j) \exp[-i\omega(\mathbf{q})t] \qquad \text{(II.6.23a)}$$

$$= \frac{1}{\sqrt{N}} \sum_{\mathbf{q}} \sum_j e_\alpha^l(\kappa|\mathbf{q}j) \exp[i\mathbf{q}\cdot\mathbf{X}(l)] A(\mathbf{q}j) \qquad \text{(II.6.23b)}$$

where the $A(\mathbf{q}j)$'s are referred to as the normal coordinates.

We can invert (II.6.23b) to express $A(\mathbf{q}j)$.

$$A(\mathbf{q}j) = \frac{1}{M\sqrt{N}} \sum_l \exp[-i\mathbf{q}\cdot\mathbf{X}(l)] \left[\sum_{\kappa\alpha} e_\alpha^{l*}(\kappa|\mathbf{q}j) m_\kappa u_\alpha^l(l\kappa) + \sum_{\kappa=\mu+1}^{\mu+\nu} \sum_{\alpha\beta} e_\alpha^{r*}(\kappa|\mathbf{q}j) I_{\alpha\beta}(\kappa) u_\beta^r(l\kappa) \right] \qquad \text{(II.6.24)}$$

where superscript * means the complex conjugate.

With (II.6.24) the vibrational Hamiltonian (II.6.8) can be written as

$$H = \frac{1}{2} M \sum_{\mathbf{q}j} \dot{A}^*(\mathbf{q}j)\dot{A}(\mathbf{q}j) + \frac{1}{2} M \sum_{\mathbf{q}j} \omega_j^2 A^*(\mathbf{q}j) A(\mathbf{q}j) \qquad \text{(II.6.25)}$$

where the Φ_0 term has been suppressed. The Hamiltonian (II.6.25) is just the sum of those of the independent simple harmonic oscillators of which the allowed energies are given in quantum mechanics as

$$E_n(\omega) = \hbar\omega\left(n + \frac{1}{2}\right) \qquad (n = \text{integer}) \qquad \text{(II.6.26)}$$

In the Born-von Karman treatment, the potential energy is expanded in a Taylor series (II.6.5) of the displacements of atoms rather than those of units. The second-order term is written as

$$\Phi_2 = \frac{1}{2}\sum_{ll'}\sum_{\kappa\kappa'}\sum_{kk'}\sum_{\alpha,\beta}\phi_{\alpha\beta}(l\kappa k; l'\kappa' k')u_\alpha(l\kappa k)u_\beta(l'\kappa' k') \qquad \text{(II.6.27)}$$

$$\text{where } \phi_{\alpha\beta}(l\kappa k; l'\kappa' k') = \frac{\partial^2\Phi}{\partial u_\alpha(l\kappa k)\partial u_\beta(l\kappa' k')} \qquad \text{(II.6.28)}$$

The displacements of the kth atom in the κth unit in the lth cell is due to the linear and angular displacements of the κth unit in the cell.

$$u_\alpha(l\kappa k) = u^t_\alpha(l\kappa) + [\mathbf{u}^r(l\kappa) \times \mathbf{X}(k)]_\alpha \qquad \text{(II.6.29)}$$

The cross product can be expressed by the Levi-Civita symbol $\varepsilon_{\alpha\beta\gamma}$.

$$[\mathbf{u}^r(l\kappa) \times \mathbf{X}(k)]_\alpha = \sum_{\mu\nu}\varepsilon_{\alpha\mu\nu}u^r_\mu(l\kappa)X_\nu(k) \qquad \text{(II.6.30)}$$

where the symbol $\varepsilon_{\alpha\beta\gamma}$ is defined as

$\varepsilon_{\alpha\beta\gamma}$ = 0 if any two of (α, β, γ) are equal

= 1 if (α, β, γ) corresponds to a cyclic order of (x,y,z)

= -1 if (α, β, γ) corresponds to a noncyclic order of (x,y,z).

Comparing (II.6.27) to (II.6.6) with the help of (II.6.29) and (II.6.30), we obtain the expression for the coupling coefficient (II.6.7) in terms of the Born-von Karman constants (II.6.28) [27,113].

$$\phi^{\alpha\beta}_{\alpha\beta}(l\kappa; l\kappa') = \sum_{kk'}\phi_{\alpha\beta}(l\kappa k; l'\kappa' k') \qquad \text{(II.6.31a)}$$

$$\phi^{rr}_{\alpha\beta}(l\kappa;l\kappa') = \sum_{kk'}\sum_{\gamma\delta}\phi_{\alpha\gamma}(l\kappa k;l'\kappa' k')\varepsilon_{\gamma\beta\delta}X_{\delta}(k') \qquad \text{(II.6.31b)}$$

$$\phi^{rr}_{\alpha\beta}(l\kappa;l\kappa') = \sum_{kk'}\sum_{\mu\nu}\phi_{\mu\beta}(l\kappa k;l'\kappa' k')\varepsilon_{\mu\alpha\nu}X_{\nu}(k) \qquad \text{(II.6.31c)}$$

$$\phi^{rr}_{\alpha\beta}(l\kappa;l\kappa') = \sum_{kk'}\sum_{\mu\nu}\sum_{\gamma\delta}\phi_{\mu\gamma}(l\kappa k;l'\kappa' k')\varepsilon_{\mu\alpha\nu}\varepsilon_{\gamma\beta\delta}X_{\nu}(k)X_{\delta}(k') \qquad \text{(II.6.31d)}$$

If we know the interaction potential of an atom pair, we can compute the coupling coefficient (the atom-atom potential method) [26,115]. The interatomic forces depend on the type of the bonds. For van der Waals interactions, the Lennard-Jones (II.6.32a) or Buckingham potential (II.6.32b) is used.

$$\Phi(r) = -\frac{A}{r^6} + \frac{B}{r^n} \qquad \text{(II.6.32a)}$$

$$\Phi(r) = -\frac{A}{r^6} + C\exp\left(-\frac{r}{\rho}\right) \qquad \text{(II.6.32b)}$$

In the covalent binding not only the stretching of the bonds but also the bending of the bond angle should be considered. In order to be rigorous about metallic binding, allowance must be made for electrostatic repulsion of the ion cores (screened by the electron gas), van der Waals attraction of ion cores and their overlap repulsion, binding due to incomplete inner shells (important in transition elements), and electron correlations within the electron gas [116]. For ionic crystals the evaluation of the electrostatic contribution to the dynamical matrix is difficult due to the long-range character of the Coulomb potential. The Coulombic contribution to the Born-von Karman constant in (II.6.28) is given by

$$\phi^{c}_{\alpha\beta}(l\kappa k; l'\kappa' k') = e^2 Z(\kappa k) Z(\kappa' k') \left(\frac{\delta_{\alpha\beta}}{|\mathbf{X}|^3} - \frac{3 X_\alpha X_\beta}{|\mathbf{X}|^5} \right) \tag{II.6.33}$$

where $\mathbf{X} = \mathbf{X}(l'\kappa' k') - \mathbf{X}(l\kappa k)$ and $l\kappa k \neq l'\kappa' k'$.

Using equations (II.6.31) and (II.6.33) we can compute the Coulombic contribution to the dynamical matrix (II.6.15)

$$B^{ii'}_{\alpha\beta}(\mathbf{q}, \kappa\kappa') = \sum_{l'} \phi^{ii'}_{\alpha\beta}(0\kappa; l\kappa') \exp[i\mathbf{q} \cdot \mathbf{X}(l')] \tag{II.6.15}$$

However, unlike van der Waals interactions where nearest or second nearest neighbor interactions are enough, in electrostatic interactions the summation in (II.6.15) rarely converges. Thanks to Ewald and Kellerman [27,113] the dynamical matrix is given by

for $\kappa \neq \kappa'$

$$B^{c,rr}_{\alpha\beta}(\mathbf{q}, \kappa\kappa') = e^2 \sum_{kk'} Z(\kappa k) Z(\kappa' k') \times \left[4\mathscr{B}_{\alpha\beta}(\mathbf{q}, \mathbf{X}(\kappa k) - \mathbf{X}(\kappa' k')) - \mathscr{C}_{\alpha\beta}(\mathbf{q}, \mathbf{X}(\kappa k) - \mathbf{X}(\kappa' k')) \right] \tag{II.6.34a}$$

$$B^{c,ir}_{\alpha\beta}(\mathbf{q}, \kappa\kappa') = e^2 \sum_{kk'} \sum_{\sigma\rho} Z(\kappa k) Z(\kappa' k') \varepsilon_{\sigma\beta\rho} X_\rho(k') \times \left[4\mathscr{B}_{\alpha\sigma}(\mathbf{q}, \mathbf{X}(\kappa k) - \mathbf{X}(\kappa' k')) - \mathscr{C}_{\alpha\sigma}(\mathbf{q}, \mathbf{X}(\kappa k) - \mathbf{X}(\kappa' k')) \right] \tag{II.6.34b}$$

$$B^{c,ri}_{\alpha\beta}(\mathbf{q}, \kappa\kappa') = e^2 \sum_{kk'} \sum_{\mu\nu} Z(\kappa k) Z(\kappa' k') \varepsilon_{\mu\alpha\nu} X_\nu(k) \times \left[4\mathscr{B}_{\mu\beta}(\mathbf{q}, \mathbf{X}(\kappa k) - \mathbf{X}(\kappa' k')) - \mathscr{C}_{\mu\beta}(\mathbf{q}, \mathbf{X}(\kappa k) - \mathbf{X}(\kappa' k')) \right] \tag{II.6.34c}$$

$$B^{c,ii}_{\alpha\beta}(\mathbf{q}, \kappa\kappa') = e^2 \sum_{kk'} \sum_{\sigma\rho} \sum_{\mu\nu} Z(\kappa k) Z(\kappa' k') \varepsilon_{\sigma\beta\rho} \varepsilon_{\mu\alpha\nu} X_\nu(k) X_\rho(k') \times \left[4\mathscr{B}_{\mu\sigma}(\mathbf{q}, \mathbf{X}(\kappa k) - \mathbf{X}(\kappa' k')) - \mathscr{C}_{\mu\sigma}(\mathbf{q}, \mathbf{X}(\kappa k) - \mathbf{X}(\kappa' k')) \right] \tag{II.6.34d}$$

for $\kappa = \kappa'$

$$B_{\alpha\beta}^{c,rr}(\mathbf{q},\kappa\kappa) = e^2 \sum_{kk'} Z(\kappa k)Z(\kappa k')\Big\{4\Big[\mathscr{B}_{\alpha\beta}(\mathbf{q},\mathbf{X}(k)-\mathbf{X}(k')) - \mathscr{B}_{\alpha\beta}(\mathbf{q}\equiv 0,\mathbf{X}(k)-\mathbf{X}(k'))\Big] - \Big[\mathscr{C}_{\alpha\beta}(\mathbf{q},\mathbf{X}(k)-\mathbf{X}(k')) - \mathscr{C}_{\alpha\beta}(\mathbf{q}\equiv 0,\mathbf{X}(k)-\mathbf{X}(k'))\Big]\Big\} - \sum_{\kappa'\neq\kappa} B_{\alpha\beta}^{c,rr}(q\equiv 0,\kappa\kappa') \tag{II.6.34e}$$

$$B_{\alpha\beta}^{c,r\sigma}(\mathbf{q},\kappa\kappa) = e^2 \sum_{kk'}\sum_{\sigma\rho} Z(\kappa k)Z(\kappa k')\varepsilon_{\sigma\beta\rho}X_\rho(k')\Big\{4\Big[\mathscr{B}_{\alpha\sigma}(\mathbf{q},\mathbf{X}(k)-\mathbf{X}(k')) - \mathscr{B}_{\alpha\sigma}(\mathbf{q}\equiv 0,\mathbf{X}(k)-\mathbf{X}(k'))\Big] - \Big[\mathscr{C}_{\alpha\sigma}(\mathbf{q},\mathbf{X}(k)-\mathbf{X}(k')) - \mathscr{C}_{\alpha\sigma}(\mathbf{q}\equiv 0,\mathbf{X}(k)-\mathbf{X}(k'))\Big]\Big\} - \sum_{\kappa'\neq\kappa} B_{\alpha\beta}^{c,r\sigma}(q\equiv 0,\kappa\kappa') \tag{II.6.34f}$$

$$B_{\alpha\beta}^{c,\sigma r}(\mathbf{q},\kappa\kappa') = e^2 \sum_{kk'}\sum_{\mu\nu} Z(\kappa k)Z(\kappa k')\varepsilon_{\mu\alpha\nu}X_\nu(k)\Big\{4\Big[\mathscr{B}_{\mu\beta}(\mathbf{q},\mathbf{X}(k)-\mathbf{X}(k')) - \mathscr{B}_{\mu\beta}(\mathbf{q}\equiv 0,\mathbf{X}(k)-\mathbf{X}(k'))\Big] - \Big[\mathscr{C}_{\mu\beta}(\mathbf{q},\mathbf{X}(k)-\mathbf{X}(k')) - \mathscr{C}_{\mu\beta}(\mathbf{q}\equiv 0,\mathbf{X}(k)-\mathbf{X}(k'))\Big]\Big\} - \sum_{\kappa'\neq\kappa} B_{\alpha\beta}^{c,\sigma r}(q\equiv 0,\kappa\kappa') \tag{II.6.34g}$$

$$\begin{aligned} B_{\alpha\beta}^{c,\sigma\sigma}(\mathbf{q},\kappa\kappa') = {} & e^2 \sum_{kk'}\sum_{\sigma\rho}\sum_{\mu\nu} Z(\kappa k)Z(\kappa' k')\varepsilon_{\sigma\beta\rho}\varepsilon_{\mu\alpha\nu}X_\nu(k)X_\rho(k') \\ & \times\Big\{4\Big[\mathscr{B}_{\mu\sigma}(\mathbf{q},\mathbf{X}(k)-\mathbf{X}(k')) - \mathscr{B}_{\mu\sigma}(\mathbf{q}\equiv 0,\mathbf{X}(k)-\mathbf{X}(k'))\Big] \\ & -\Big[\mathscr{C}_{\mu\sigma}(\mathbf{q},\mathbf{X}(k)-\mathbf{X}(k')) - \mathscr{C}_{\mu\sigma}(\mathbf{q}\equiv 0,\mathbf{X}(k)-\mathbf{X}(k'))\Big]\Big\} - \sum_{\kappa'\neq\kappa} B_{\alpha\beta}^{c,\sigma\sigma}(q\equiv 0,\kappa\kappa') \\ & -i\sum_{\kappa'}\sum_{\mu\nu}\left[\frac{\partial}{\partial q_\nu}B_{\alpha\mu}^{c,\sigma\sigma}(q,\kappa\kappa')\right]_{q=0}\varepsilon_{\beta\mu\nu} + \sum_{\kappa'\neq\kappa}\sum_{\mu\nu} B_{\alpha\mu}^{c,\sigma\sigma}(q\equiv 0,\kappa\kappa')\varepsilon_{\beta\mu\nu}\big[X_\nu(\kappa')-X_\nu(\kappa)\big] \end{aligned} \tag{II.6.34h}$$

where the superscript *c* represents Coulombic contribution to the dynamical matrix

The reciprocal space series and real space series are defined as

$$\mathscr{B}_{\alpha\beta}(\mathbf{q},\mathbf{X}) = \frac{\pi}{v}\sum_{\mathbf{G}}\frac{(\mathbf{G}+\mathbf{q})_\alpha(\mathbf{G}+\mathbf{q})_\beta}{(\mathbf{G}+\mathbf{q})^2}\exp\left[-\frac{(\mathbf{G}+\mathbf{q})^2}{4\eta^2}\right]\exp\big[i(\mathbf{G}+\mathbf{q})\cdot\mathbf{X}\big] \tag{II.6.35a}$$

$$\mathscr{C}_{\alpha\beta}(\mathbf{q},\mathbf{X}) = \sum_{l'} \exp[i\mathbf{q}\cdot\mathbf{X}(l')]$$
$$\times\left\{\frac{(\mathbf{X}(l')-\mathbf{X})_\alpha(\mathbf{X}(l')-\mathbf{X})_\beta}{|\mathbf{X}(l')-\mathbf{X}|^5}\left[3\operatorname{erfc}(y)+\frac{e^{-y^2}}{\sqrt{\pi}}(4y^3+6y)\right]-\frac{\delta_{\alpha\beta}}{|\mathbf{X}(l')-\mathbf{X}|^3}\left[\operatorname{erfc}(y)+\frac{2ye^{-y^2}}{\sqrt{\pi}}\right]\right\}$$

(II.6.35b)

where v = volume of the primitive cell and $y=\eta|\mathbf{X}(l')-\mathbf{X}|$. The parameter η can be chosen such that both the reciprocal space series and the real space series converge rapidly.

II.6.b) Group theory in lattice dynamics

The general terms and definitions in group theory are summarized from [117,118]. A set G is said to be a group if it has the following four properties.

1) There exits multiplication operation which associates with every pair of elements T and T' of G another T'' of G: if $T,T'\in G$, then $TT'=T''$ and $T''\in G$.

2) The elements obey a law of association: if $T,T'$and $T''\in G$, then $T(T'T'')=(TT')T''$.

3) There is an identity element E: $E\in G$ such that $TE=ET=T$ for any $T\in G$.

4) Every element has an inverse element: $T^{-1}\in G$ such that $TT^{-1}=T^{-1}T=E$ for any $T\in G$.

The number of elements in a group is said to be the order of the group. If every pair of elements is commutative, the group is called Abelian: $TT'=T'T$. If the number of elements is finite, the group is called a finite group. Otherwise, it is called as a Lie group. A subset $\mathscr{S}$ of a group G that is itself a group with the same multiplication operation as G is called a subgroup of G. An element T' of G is conjugate to another element T of G if,

for an X of G, $T' = XTX^{-1}$. A class of G is a set of mutually conjugate elements of G. A subgroup $\mathcal{S}$ of a group G is invariant if $XSX^{-1} \in \mathcal{S}$ for every $S \in \mathcal{S}$ and every $X \in G$. The coset of a subgroup $\mathcal{S}$ with respect to any fixed element T of G is defined as

Right coset = $\{ST;\ S$ = every element of $\mathcal{S}\}$

Left coset = $\{TS;\ S$ = every element of $\mathcal{S}\}$

Factor group $G/\mathcal{S}$ is defined as the set of the right cosets of an invariant subgroup $\mathcal{S}$ of a group G.

$$G/\mathcal{S} = \{\mathcal{S}, \mathcal{S}\mathrm{p}, \mathcal{S}\mathrm{q}, \mathcal{S}\mathrm{t}, \ldots\} \tag{II.6.36a}$$

$$G = \mathcal{S} + \mathcal{S}\mathrm{p} + \mathcal{S}\mathrm{q} + \mathcal{S}\mathrm{t} + \ldots \tag{II.6.36b}$$

where p, q and t are the elements of G.

If ϕ is a mapping of a group G onto another group G' such that $\phi(T_1)\phi(T_2) = \phi(T_1T_2)$ for all T_1 and T_2 of G, then the mapping ϕ is homomorphic. If ϕ is a one-to-one mapping of a group G onto another group G' such that $\phi(T_1)\phi(T_2) = \phi(T_1T_2)$ for all T_1 and T_2 of G, then the mapping ϕ is isomorphic. If there exits a homomorphic mapping of a group G onto a group of non-singular $d \times d$ matrices $\Gamma(T)$ for element T of G, with matrix multiplication as the group multiplication operation, then the group of matrices $\Gamma(T)$ forms a d-dimensional representation Γ of group G. If S is any $d \times d$ non-singular matrix, the similarity transformation is defined as

$$\Gamma'(T) = \mathbf{S}^{-1}\Gamma(T)\mathbf{S} \tag{II.6.37}$$

and Γ and Γ' are said to be equivalent representations of group G. A unitary representation of a group G ia a representation Γ in which the matrices $\Gamma(T)$ are unitary for every T of G, that is $\Gamma(T)^{+} = \Gamma(T)^{-1}$ where the superscript + represents the Hermitian conjugate (the complex conjugate of the transpose). Representation $\Gamma(T)$ of a group G is reducible if it is equivalent to a representation $\Gamma'(T)$ of the group G that has the form

$$\Gamma'(T) = \begin{bmatrix} \Gamma_{11}(T) & 0 \\ 0 & \Gamma_{22}(T) \end{bmatrix} \tag{II.6.38}$$

A representation $\Gamma(T)$ is irreducible if it can not be transformed by a similarity transformation to the reduced form. For all T of G, if the representation $\Gamma(T)$ is equivalent to the completely reduced form $\Gamma''(T)$ where all the diagonal submatrices are irreducible and all the off-diagonal submatrices are null, the representation $\Gamma(T)$ is completely reducible.

$$\Gamma''(T) = \begin{bmatrix} \Gamma_{11}(T) & & & 0 \\ & \Gamma_{22}(T) & & \\ & & \ddots & \\ 0 & & & \Gamma_{dd}(T) \end{bmatrix} \tag{II.6.39}$$

where $\Gamma_{jj}(T)$ = irreducible. The completely reducible representation is equivalent to the direct sum of $\Gamma_{jj}(T)$

$$\Gamma = \Gamma_{11} \oplus \Gamma_{22} \oplus \cdots \oplus \Gamma_{dd} \tag{II.6.40}$$

The orthogonality theorem for matrix representation says that if Γ^{p} and Γ^{q} are two unitary irreducible representations of a finite group G, then

$$\frac{1}{g}=\sum_{T\in G}\Gamma^{p}(T)^{*}_{jk}\Gamma^{q}(T)_{st}=\frac{1}{d_p}\delta_{pq}\delta_{js}\delta_{kt} \qquad \text{(II.6.41)}$$

where g and d_p are the order of G and the dimension of Γ^p, respectively.

The characters of a representation are defined as

$$\chi(T)=\text{trace of }\Gamma(T) \qquad \text{(II.6.42)}$$

The character system of a representation is the set of characters corresponding to the representation. A necessary and sufficient condition for two representations of a finite group to be equivalent is that they must have an identical character system. If $\chi^p(T)$ and $\chi^q(T)$ are characters of two irreducible representations of a finite group of order g, then

$$\frac{1}{g}\sum_{T\in G}\chi^{p}(T)^{*}\chi^{q}(T)=\delta_{pq} \qquad \text{(II.6.43)}$$

The number of times c_s that an irreducible representation Γ^s (or a representation equivalent to it) appears in a reducible representation Γ of a finite group is

$$c_s=\frac{1}{g}\sum_{T\in G}\chi(T)\chi^{s}(T)^{*} \qquad \text{(II.6.44)}$$

The symmetry of space about a point can be described by a collection of symmetry elements called a point group. It is convenient to use five symmetry elements for point groups; inversion through a point, rotation about an axis, reflection at a plane, rotation-reflection and identity. In a point group, the allowed combination of symmetry elements leaves at least one point unchanged. Only 32 crystallographic point groups are compatible with the translational symmetry of crystals. The mathematically allowed combinations of the symmetry elements of crystals are called the space group of crystals.

The symmetry operation S_m of a space group can be represented in the Seitz notation [28] by

$$S_m = \{\mathrm{S}|\mathbf{V}(S) + \mathbf{X}(m)\} \tag{II.6.45}$$

where S is a 3×3 real orthogonal matrix representation of one of the proper or improper rotations of the point group of the space group, $\mathbf{V}(S)$ is a vector which is smaller than any primitive translation vector of the crystal, and $\mathbf{X}(m)$ is a translation vector of the crystal. When the operation is applied to the position vector $\mathbf{X}(l\kappa)$ of the κth unit in the lth unit cell, the operation transforms it according to the rule

$$\{\mathrm{S}|\mathbf{V}(S) + \mathbf{X}(m)\}\mathbf{X}(l\kappa) = \mathbf{S}\mathbf{X}(l\kappa) + \mathbf{V}(S) + \mathbf{X}(m) = \mathbf{X}(LK) \tag{II.6.46}$$

To express the fact that κ is carried into K by $S_m = \{\mathrm{S}|\mathbf{V}(S) + \mathbf{X}(m)\}$, we write

$$K = F_0(\kappa; S) \tag{II.6.47}$$

Note that $\mathbf{X}(m)$ can not affect the relation between κ and K and only the rotational element S of S_m is required to specify the relationship because when S is determined the vector $\mathbf{V}(S)$ is specified. Space groups for which $\mathbf{V}(S)$ is zero for every rotation S are called symmorphic. All other space groups are called nonsymmorphic in which non-zero $\mathbf{V}(S)$'s are associated with glide planes or screw axes.

The application of group theory to the eigenvalue problem [27]

$$\omega^2(\mathbf{q})\mathbf{m}\mathbf{U}(\mathbf{q}) = \mathbf{B}(\mathbf{q})\mathbf{U}(\mathbf{q}) \tag{II.6.11}$$

not only enables us to classify the eigenvalues and the eigenvectors using group theoretical labels, but also simplifies the eigenvalue problem. The basic principle is to construct a set

of matrices each of which describes the effects of the symmetry element and commutes with both **B(q)** and **m**.

Defined as $G(\mathbf{q}) = \{R_m\}$, the space group of the wave vector **q** , is the subgroup of the space group $G = \{S_m\}$, which is composed of space group elements $R_m = \{\mathbf{R}|\ \mathbf{V}(R) + \mathbf{X}(m)\}$ whose rotational part **R** has the property [28]

$$\mathbf{Rq} = \mathbf{q} + \mathbf{G} \tag{II.6.48}$$

where **G** is a translation vector of the reciprocal lattice. Note that **G** vanishes if **q** lies inside the first Brillouin zone and it can be nonzero only if **q** lies on the boundary of the zone. We construct unitary matrices $\Gamma(\mathbf{q};R_m)$ whose elements are given by

$$\Gamma_{\alpha\beta}(\kappa\kappa'|\mathbf{q};R_m) = R_{\alpha\beta}\delta(\kappa, F_0(\kappa';R))\exp\left\{i\mathbf{q}\cdot\left[\mathbf{X}(\kappa) - R_m\mathbf{X}(\kappa')\right]\right\} \tag{II.6.49}$$

We see that those matrices commute with both **B(q)** and **m** and provide a unitary representation of the space group of the wave vector **q** [27].

$$\Gamma(\mathbf{q};R_m)\mathbf{B}(\mathbf{q}) = \mathbf{B}(\mathbf{q})\Gamma(\mathbf{q};R_m) \tag{II.6.50a}$$

$$\Gamma(\mathbf{q};R_m)\mathbf{m} = \mathbf{m}\Gamma(\mathbf{q};R_m) \tag{II.6.50b}$$

$$\Gamma(\mathbf{q};R_m)\Gamma(\mathbf{q};R_m') = \Gamma(\mathbf{q};R_mR_m') \tag{II.6.50c}$$

The purely rotational elements **R** in $G(\mathbf{q})$, the space group of wave vector **q**, comprise a point group $G_0(\mathbf{q})$ called the point group of the wave vector **q** [28]. We associate a unitary matrix **T(q;R)** with each element **R** of the point group $G_0(\mathbf{q})$.

$$\mathbf{T}(\mathbf{q};\mathbf{R}) = \exp\left[i\mathbf{q}\cdot(\mathbf{V}(R) + \mathbf{X}(m)\right]\Gamma(\mathbf{q};R_m) \tag{II.6.51a}$$

or

$$T_{\alpha\beta}(\kappa\kappa'|\mathbf{q};\mathbf{R}) = R_{\alpha\beta}\delta(\kappa, F_0(\kappa';R))\exp\left[i\mathbf{q}\cdot(\mathbf{X}(\kappa) - \mathbf{R}\mathbf{X}(\kappa')\right] \qquad \text{(II.6.51b)}$$

We can see that $\mathbf{T}(\mathbf{q};\mathbf{R})$ commutes with both $\mathbf{B}(\mathbf{q})$ and $\mathbf{m}$ and the set of them furnishes a unitary multiplier representation of $G_0(\mathbf{q})$ [27].

$$\mathbf{T}(\mathbf{q};\mathbf{R})\mathbf{B}(\mathbf{q}) = \mathbf{B}(\mathbf{q})\mathbf{T}(\mathbf{q};\mathbf{R}) \qquad \text{(II.6.52a)}$$

$$\mathbf{T}(\mathbf{q};\mathbf{R})\mathbf{m} = \mathbf{m}\mathbf{T}(\mathbf{q};\mathbf{R}) \qquad \text{(II.6.52b)}$$

$$\mathbf{T}(\mathbf{q};\mathbf{R})\mathbf{T}(\mathbf{q};\mathbf{R}') = \phi(\mathbf{q};\mathbf{R},\mathbf{R}')\mathbf{T}(\mathbf{q};\mathbf{R}\mathbf{R}') \qquad \text{(II.6.52c)}$$

where the multiplier is given by

$$\phi(\mathbf{q};\mathbf{R},\mathbf{R}') = \exp\left\{i\left[\mathbf{q} - \mathbf{R}^{-1}\mathbf{q}\right]\cdot\mathbf{V}(R')\right\} \qquad \text{(II.6.53a)}$$

Using equation (II.6.48),

$$\phi(\mathbf{q};\mathbf{R},\mathbf{R}') = \exp\left\{i\mathbf{G}\cdot\mathbf{V}(R')\right\} \qquad \text{(II.6.53b)}$$

If $\mathbf{q}$ lies entirely within the Brillouin zone, the reciprocal lattice $\mathbf{G}$ is zero and the multiplier equals unity. Alternatively, if the crystal belongs to a symmorphic space group, $\mathbf{V}(R')$ is zero and the multiplier is also equal to unity. In each of two cases the set $\{\mathbf{T}(\mathbf{q};\mathbf{R})\}$ provides an ordinary representation of the point group $G_0(\mathbf{q})$.

The same operation can be carried out with an alternative treatment known as the factor group method.

$$G/\mathcal{S} = \{\mathcal{S}, \mathcal{S}\mathfrak{p}, \mathcal{S}\mathfrak{q}, \mathcal{S}\mathfrak{t}, \ldots\} \qquad (\mathfrak{p},\mathfrak{q},\mathfrak{t},\ldots \in G) \qquad \text{(II.6.36a)}$$

If we take as the invariant subgroup $\mathcal{S}$ the set of the infinite number of translational elements, then for symmorphic crystals the factor group is identical with the point group

$G_0(\mathbf{q})$, and for nonsymmorphic crystals the factor group is isomorphic with the point group $G_0(\mathbf{q})$ [118].

$$\mathscr{S} = \left\{\left\{\mathbf{E}|\mathbf{X}(m)\right\}\right\} \tag{II.6.54a}$$

$$G/\mathscr{S} = \left\{\mathscr{S}, \mathscr{S}\left\{\mathbf{R}_1|\mathbf{V}(R_1)\right\}, \mathscr{S}\left\{\mathbf{R}_2|\mathbf{V}(R_2)\right\}, \mathscr{S}\left\{\mathbf{R}_3|\mathbf{V}(R_3)\right\}, \ldots\right\} \tag{II.6.54b}$$

where $\left\{\mathbf{R}_i\right\} \in G_0(\mathbf{q})$.

Using equation (II.6.44) and (II.6.51), we obtain c_s, the number of times the sth irreducible multiplier representation $\tau^{(s)}(\mathbf{q})$ of $G_0(\mathbf{q})$ whose dimension is f_s occurs in the reducible multiplier representation $T(\mathbf{q})$.

$$c_s = \frac{1}{h}\sum_{\mathbf{R}\in G_0(\mathbf{q})} \chi(\mathbf{q};\mathbf{R})\chi^{(s)}(\mathbf{q};\mathbf{R})^* \tag{II.6.55}$$

where h is the order of the group $G_0(\mathbf{q})$

$$\chi(\mathbf{q};\mathbf{R}) = \text{Trace of } \mathbf{T}(\mathbf{q};\mathbf{R}) \tag{II.6.56a}$$

$$\chi^{(s)}(\mathbf{q};\mathbf{R}) = \text{Trace of } \tau^{(s)}(\mathbf{q};\mathbf{R}) \tag{II.6.56b}$$

Thus, there are c_s eigenvalues each of which is f_s-fold degenerate. That is, c_s sets of eigenvectors are associated with c_s eigenvalues and each set has f_s eigenvectors. In other words, if there are $(3\mu + 6\nu)$ coordinates, $c_s \times f_s$ coordinates belong to the $\tau^{(s)}(\mathbf{q})$ multiplier representation and $c_s \times f_s$ coordinates divided by c_s sets, associated with c_s eigenvalues, contain f_s coordinates.

To simplify the eigenvalue problems the projection operator $P_{\lambda\lambda}^{(s)}(\mathbf{q})$ is constructed

$$P_{\lambda\lambda}^{(s)}(\mathbf{q}) = \frac{f_s}{h} \sum_{\mathbf{R}\in G_0(\mathbf{q})} \tau_{\lambda\lambda}^{(s)}(\mathbf{q};\mathbf{R})^* \mathbf{T}(\mathbf{q};\mathbf{R}) \qquad \text{(II.6.57)}$$

where λ could be any one of $(1, 2, \ldots, f_s)$ [28,118]. Applying this operator systematically on any set of $(3\mu + 6\nu)$ orthogonal vectors which have the dimension of $(3\mu + 6\nu)$, we project out c_s orthogonal vectors; there will be only c_s independent vectors. These after normalization may be labeled $\xi(\mathbf{q}s1\lambda)$, $\xi(\mathbf{q}s2\lambda)$, ... , $\xi(\mathbf{q}sc_s\lambda)$. The partners of these vectors may be generated by applying to them the operator

$$P_{\mu\lambda}^{(s)}(\mathbf{q}) = \frac{f_s}{h} \sum_{\mathbf{R}\in G_0(\mathbf{q})} \tau_{\mu\lambda}^{(s)}(\mathbf{q};\mathbf{R})^* \mathbf{T}(\mathbf{q};\mathbf{R}) \qquad (\mu = 1 \text{ to } f_s,\ \mu \neq \lambda) \qquad \text{(II.6.58)}$$

Thus, we have c_s orthonomal sets of symmetry-adapted vectors.

$$\begin{matrix} \{\xi(\mathbf{q}s11), \xi(\mathbf{q}s12), \cdots, \xi(\mathbf{q}s1f_s),\} \\ \{\xi(\mathbf{q}s21), \xi(\mathbf{q}s22), \cdots, \xi(\mathbf{q}s2f_s),\} \\ \vdots \\ \{\xi(\mathbf{q}sc_s1), \xi(\mathbf{q}sc_s2), \cdots, \xi(\mathbf{q}sc_sf_s),\} \end{matrix} \qquad \text{(II.6.59)}$$

Applying the same procedure to all irreducible multiplier representations, we finally have $(3\mu + 6\nu)$ symmetry-adapted vectors $\{\xi(\mathbf{q}sa\lambda)\}$ which have the property of

$$\begin{matrix} \xi^+(\mathbf{q}s'a'\lambda')\mathbf{B}(\mathbf{q})\xi(\mathbf{q}sa\lambda) = 0 \\ \xi^+(\mathbf{q}s'a'\lambda')\mathbf{m}\xi(\mathbf{q}sa\lambda) = 0 \end{matrix} \qquad \text{unless } s = s' \text{ and } \lambda = \lambda' \qquad \text{(II.6.60)}$$

Thus, by grouping the symmetry-adapted vectors with the same s and λ together, we can block-diagonalize $\mathbf{B}(\mathbf{q})$ and $\mathbf{m}$ [27].

$$\mathbf{B}_\mathbf{D}(\mathbf{q}) = \xi^+(\mathbf{q})\mathbf{B}(\mathbf{q})\xi(\mathbf{q}) \qquad \text{(II.6.61a)}$$

where subscript $\mathbf{D}$ represents the block-diagonalized form.

$$\xi(\mathbf{q}) = \text{transpose of} \begin{bmatrix} \vdots \\ \xi(\mathbf{q}s11) \\ \vdots \\ \xi(\mathbf{q}sc_s1) \\ \xi(\mathbf{q}s12) \\ \vdots \\ \xi(\mathbf{q}sc_s2) \\ \vdots \\ \xi(\mathbf{q}s1f_s) \\ \vdots \\ \xi(\mathbf{q}sc_sf_s) \\ \vdots \end{bmatrix} \qquad \text{(II.6.61b)}$$

For each s, the block-diagonal form has f_s diagonal blocks with the dimension of c_s.

Under special circumstances, time-reversal symmetry can produce extra degeneracies in the lattice vibrational frequencies in addition to those due to spatial symmetry. If the point group of the crystal contains a rotational element $\mathbf{S\_}$ such that

$$\mathbf{S\_}\,\mathbf{q} = -\mathbf{q} + \mathbf{G} \qquad \text{(II.6.62)}$$

the space group, which is the sum of the space group $G(\mathbf{q})$ plus the coset $\{\mathbf{S\_}|\mathbf{V}(S\_)\}G(\mathbf{q})$ is designated by the symbol $G(\mathbf{q};-\mathbf{q})$ [28]. Note that $G(\mathbf{q})$ is the invariant subgroup of $G(\mathbf{q};-\mathbf{q})$.

$$G(\mathbf{q};-\mathbf{q}) = \left\{\{\mathbf{R}|\mathbf{V}(R)+\mathbf{X}(m)\} \text{ and } \{\mathbf{S\_R}|\mathbf{V}(S\_R)+\mathbf{X}(m)\}\right\} \qquad \text{(II.6.63)}$$

The crystal symmetry operations can be represented by the matrix operators

$$\mathbf{\Gamma}(\mathbf{q};\{\mathbf{R}|\mathbf{V}(R)+\mathbf{X}(m)\}) \text{ and } \mathbf{K}_0\mathbf{\Gamma}(\mathbf{q};\ \{\mathbf{S\_R}|\mathbf{V}(S\_R)+\mathbf{X}(m)\}) \qquad \text{(II.6.64)}$$

where $\mathbf{K}_0$ is the complex conjugate operator.

The purely rotational elements {**R**} and {**S_R**} in $G(\mathbf{q};-\mathbf{q})$ form a point group $G_0(\mathbf{q};-\mathbf{q})$ in which $G_0(\mathbf{q})$ is an invariant subgroup. With each element **S_R** an anti-unitary matrix operator **T(q;S_R)** is associated.

$$\mathbf{T(q;S\_R)} = \mathbf{K}_0 \exp\left\{-i\mathbf{q}\cdot\left[\mathbf{V}(S\_R) + \mathbf{X}(m)\right]\right\}\Gamma(\mathbf{q};\ \left\{\mathbf{S\_R}|\mathbf{V}(S\_R) + \mathbf{X}(m)\right\}) \quad \text{(II.6.65)}$$

Introducing $\overline{\mathbf{R}}$ to denote the element {**R**} and {**S_R**} in the point group $G_0(\mathbf{q};-\mathbf{q})$, we can see that $\mathbf{T}(\mathbf{q};\overline{\mathbf{R}})$ commutes with both **B(q)** and **m** and the set of them furnishes a multiplier representation of $G_0(\mathbf{q})$ [27].

$$\mathbf{T}(\mathbf{q};\overline{\mathbf{R}})\mathbf{B}(\mathbf{q}) = \mathbf{B}(\mathbf{q})\mathbf{T}(\mathbf{q};\overline{\mathbf{R}}) \quad \text{(II.6.66a)}$$

$$\mathbf{T}(\mathbf{q};\overline{\mathbf{R}})\mathbf{m} = \mathbf{m}\mathbf{T}(\mathbf{q};\overline{\mathbf{R}}) \quad \text{(II.6.66b)}$$

$$\mathbf{T}(\mathbf{q};\overline{\mathbf{R}})\mathbf{T}(\mathbf{q};\overline{\mathbf{R}'}) = \phi(\mathbf{q};\overline{\mathbf{R}},\overline{\mathbf{R}'})\mathbf{T}(\mathbf{q};\overline{\mathbf{R}\mathbf{R}'}) \quad \text{(II.6.66c)}$$

where the multiplier is given by

for $\overline{\mathbf{R}} = \mathbf{R}$

$$\phi(\mathbf{q};\mathbf{R},\overline{\mathbf{R}'}) = \exp\left\{i\left[\mathbf{q} - \mathbf{R}^{-1}\mathbf{q}\right]\cdot\mathbf{V}(\overline{R'})\right\} \quad \text{(II.6.67a)}$$

for $\overline{\mathbf{R}} = \mathbf{S\_R}$

$$\phi(\mathbf{q};\mathbf{S\_R},\overline{\mathbf{R}'}) = \exp\left\{-i\left[\mathbf{q} + (\mathbf{S\_R})^{-1}\mathbf{q}\right]\cdot\mathbf{V}(\overline{R'})\right\} \quad \text{(II.6.67b)}$$

If either **q** lies entirely within the Brillouin zone or the space group $G(\mathbf{q};-\mathbf{q})$ of the crystal is symmorphic, the multiplier is unity.

Consideration of the transformation of the eigenvectors (II.6.61) by the additional operator (II.6.65) results in the criterion for the existence of the additional degeneracy due to the time-reversal symmetry given [28] by

$$\sum_{\mathbf{R}} \phi(\mathbf{q}; \mathbf{A}_0\mathbf{R}, \mathbf{A}_0\mathbf{R})\chi^{(s)}(\mathbf{q}; \mathbf{A}_0\mathbf{R}\mathbf{A}_0\mathbf{R}) = h \qquad \text{(no additional degeneracy)} \qquad \text{(II.6.68a)}$$

$$= -h \text{ or } 0 \qquad (2f_s \text{ degeneracy}) \qquad \text{(II.6.68b)}$$

where $\mathbf{A}_0$ is an arbitrary element of the coset $\mathbf{S}\_G_0(\mathbf{q})$.

III. Experiments

III.1) Fabrication of Na beta-alumina cells

II.1.a) slip-casting

Three kinds of powders were used to form green tubes: calcined Na β-alumina powder (Alcoa XB2-SG), calcined Li-doped β″-alumina powder (Ceramatec), and fused and then ground Na β-alumina powder (hereafter called well-crystallized powder). The fused β-alumina received as crushed nuggets (1~3 *cm* in size) was further crushed and ground in a vibromill for several days. The powder was separated and small particles (<50 μm) were collected by sieving.

Those powders were dried at temperatures higher than 400°C overnight. A mixture of 45% powder to 55% ethanol by weight was ball-milled for 3 to 5 days. The slip was degassed under vacuum to remove air bubbles and then slipcast. Coarse α-alumina powder moulds were used. The residence time of the slip in the moulds was 10 to 15 minutes. After three to five days drying, the green tubes were surface-finished with abrasive papers to remove α-alumina powder on the surface. The typical size of the green tubes was 6 *cm* in length, 1.3 *cm* in outer diameter and 1.5 *mm* in thickness.

III.1.b) sintering

β-alumina tubes were sintered at temperatures between 1550 and 1620°C for 2 to 12 hours. An α-alumina crucible and lid were used for sintering. The tubes were packed in excess β-alumina powder to reduce the loss of Na. β″-alumina tubes were sintered at 1550 to 1600 °C for 5 minutes and then annealed at 1475 °C for 45 minutes to promote the conversion to β″-alumina while suppressing the grain growth (two peak sintering). To minimize the loss of Na, the green tubes were pushed into the hot zone at the sintering temperature in 25 minutes (rapid heating).

III.1.c) glass-sealing

Dense beta-alumina tubes (He gas-tight) were glass-sealed to the α-alumina lids. α-alumina lids were formed by die-pressing reactive alumina powder (Alcoa A16), pre-firing at 800°C, perforating a 3 mm diameter hole and then sintering at 1600°C for two hours. Aluminosilicate glass was used as a sealant. The glass was ground and mixed with glycerol in a mortar and applied to the joint. The tube-glass-lid sealant was heated to 1315 °C to melt, held for 5 minutes, then annealed at 760 °C for 45 min during the cooling stage.

III.1.d) cell assembly

A helium leak test was employed to select tubes with a good seal, i.e., those having a leak rate less than 10^{-8} cm^3/s. After filling each cell with the working electrode or reference electrode component in an argon atmosphere, a tantalum cone was fixed to the α -alumina lid by a compression seal (figure III.1.1a). This provided a hermetic closure for

the cell as well as an electrical feed-through. Thereafter, the experiment was operated in an argon atmosphere glove box.

III.2) Fabrication of K beta-alumina cells

III.2.a) K ion exchange

Na beta-alumina tubes were ion exchanged in KCl vapour at temperatures between 950°C and 1100°C for two days and then immersed repeatedly into KCl melts at 750 to 800°C or KNO_3 melts at 400 to 450°C for a day until the ion exchange was completed. At each step fresh salts were used. The tubes were washed in water. The sealing procedure was the same as for Na beta-aluminas.

III.2.b) Direct synthesis of K beta-alumina

α-alumina (Alcoa A16) or boehmite (AlOOH), lithium carbonate and potassium carbonate were used to produce $K_{1.67}Li_{0.33}Al_{10.67}O_{17}$. All chemicals were dried before weighing at 300 to 400°C. Boehmite was added as either calcined (700 to 1100 °C) or raw. The materials were mixed in a ball mill with water, ethanol or acetone and calcined at 1200 to 1450 °C for 2 hours. The calcined powder was ball-milled in a liquid medium (ethanol or acetone) for 3 days and then slip-cast in a powder mould followed by sintering at 1550 to 1650 °C up to 4 hours.

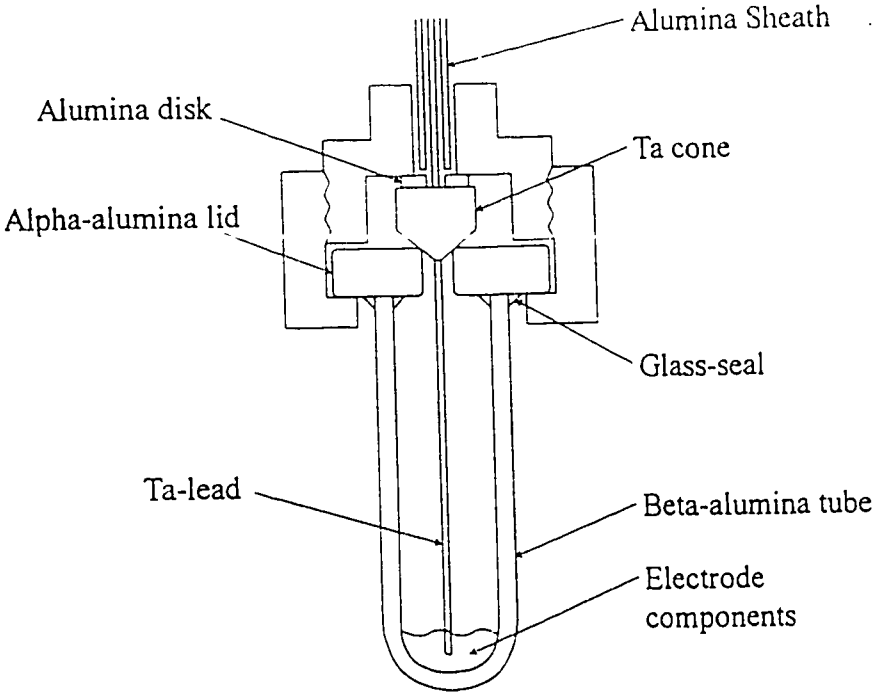

(a)

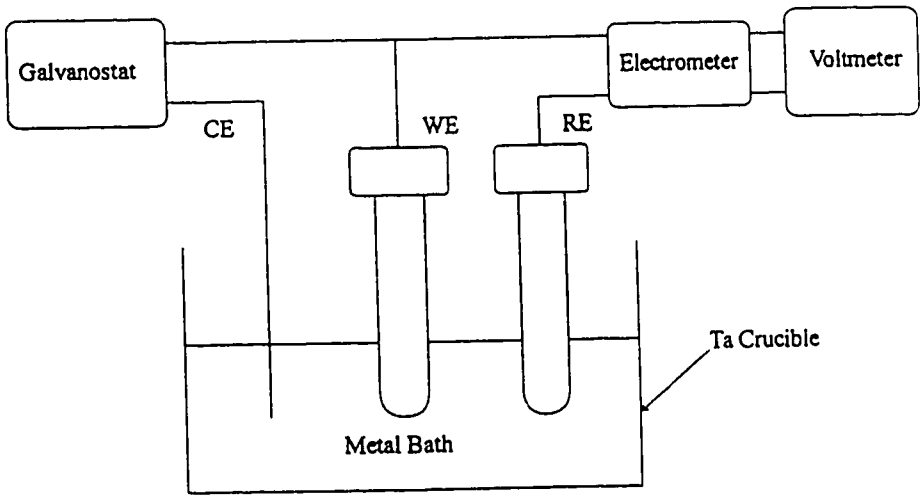

(b)

Figure III.1.1 (a) The cell assembly. (b) The experimental apparatus for EMF measurements.

III.3) EMF measurements

III.3.a) Na - C_{60} system

The experimental apparatus used for the electromotive force (EMF) measurements is shown in figure (III.1.1b). The cell consisted of a reference electrode (RE), a counter electrode (CE), and a working electrode (WE) which can be represented as

(RE) (CE) (WE)

Ta | Bi-17 at.% Na | Na β-alumina | Na-Pb-Bi | Na β-alumina | Na_xC_{60} | Ta

where the RE (Bi-17 at% Na) was calibrated against a pure sodium electrode using a similar cell configuration. All EMF readings are reported with respect to the pure sodium reference. The CE had a eutectic composition of Pb-Bi with a small amount of sodium (< 1 wt %). The role of the CE was to provide both a source of sodium for coulometric titration and a electric contact between the RE and CE. The WE was initially charged with about 50 mg of fullerene and 200 mg of nickel powder. Nickel powder, which is essentially unreactive to both sodium and carbon, provided the electrical contact between the ß-alumina and the tantalum lead. The composition of the WE was changed in precise increments by coulometric titration at low current (< 0.1 mA).

$$n = \frac{1}{ZF}\int_0^t i\,dt \qquad \text{(III.3.1)}$$

where n, i and t are the number of moles transferred, current and time, respectively. After each interval of coulometric titration, the galvanostat was switched off and the EMF was

monitored by a chart recorder. At 675 K it took a few days to several weeks to stabilize the EMF. Equilibrium was verified by cycling the temperature between 475 and 725 K and checking that the EMF returned to the initial value.

III.3.b) K - C_{60} system

The experimental procedure is similar to that of the Na system. The cell configuration is as follows:

(RE) (CE) (WE)

Ta | Pb-Bi-K | K β-alumina | K-Pb-Bi | K β-alumina | K_xC_{60} | Ta

The reference electrode contained 1 gram of the eutectic composition of Pb-Bi and 3.3 wt % of K. The counter electrode also contained the eutectic composition of Pb-Bi and small amount of K (< 1 wt %).

III.3.c) Sr - Al system

Sr β-alumina was used as a solid electrolyte. The counter electrode was an open crucible containing 700 g of Sn with 1 wt % Sr. The reference electrode contained 0.7 g of Sr with 0.37 wt % of Al. In the test range of 660 - 740 °C, this is a liquid-solid two phase mixture with unit activity for solid Sr. The working electrode was filled with about 1 g of 99.999 % pure Al at the start of the experiment.

(RE) (CE) (WE)

Ta | Sr-0.37 wt % Al | Sr β-alumina | Sn-1 wt % Sr | Sr β-alumina | Al-Sr | Ta

IV. Results and discussion

IV.1) slip-casting

The most important factor in this process is to control the amount of the moisture in the slip. A small amount of water in the slip increases the viscosity and tends to cause flocculation, resulting in a poor green density after drying. This point was discussed by Rivier et al. for β-alumina-methanol [119] and Whiteway et al. for magnesia-ethanol [120] systems. A trace of water in the alcohol seems to adsorb on the surface of the particles and form gels. Rivier et al. claimed casting should be done only in a dry room with relative humidity less than 30 %. Whiteway et al. claimed 0.5 % of water was the maximum that could be tolerated. Otherwise, the cast articles were soft and slow to dry. In order to dry ethanol, type 4A molecular sieves (bead) were used. The drying power of molecular sieves was reported as follows [121]: with 5% W/V desiccant loading for 24 hours, the water content of ethanol (initial water content 1500ppm) was reduced to 401 ppm. Molecular sieves were activated at 250 to 320 °C. Extremely dry ethanol was obtained simply by batchwise drying over molecular sieves [122]; allowing 500 *cc* of ethanol to stand over about 20 *g* of sieves for minimum 24 hours and changing molecular sieves 5 times. In spite of such an effort to keep the slip dry, sometimes the slip properties were poor especially on humid days. Water could be absorbed during the ball-milling or from the powder mould during slip-casting. Na β-aluminas (XB2-SG and well-

crystallized powders) showed better slip properties than Na β″-alumina (Ceramatec). The β″-alumina was more sensitive to moisture. The difference between β and β″ powders should be related to the surface structures. The slips were decreasingly stable in the order: well-crystallized, XB2-SG and Ceramatec powder. The more stable slip was less viscous and less sensitive to water. During slip-casting, a high deposition rate (>2 mm/min) due to high water content resulted in soft and low density green tubes, sometimes cracking on drying.

Drying should be slow enough not to cause cracks due to shrinkage. There were two types of cracks: parallel or perpendicular to the length of the green tubes. The parallel cracks seemed related to the high shrinkage resulting from poor slip properties. However, the perpendicular cracks seemed due to the high drying rate or to both factors. The drying shrinkage was not measurable (< 0.1 %) in most cases.

IV.2) Sintering

The loss of Na drastically changed the densification rate during firing. The α-alumina crucibles were not closed adequately to prevent the loss of Na. The final density was dependent on the total amount of beta-alumina used as packing powder.

Green XB2-SG tubes were packed in fresh (never used before) XB2-SG powder which was coarsened at 1200°C for one hour (fresh-powder-pack). After sintering, not only the tubes but also the powder pack shrunk by about 18 %. The effect of Na loss was so serious that when four tubes were sintered at once the density was lower than when one tube was sintered alone. Because the shrinkage of the powder pack left open space along the wall of the crucible,

as the number of tubes increased, the diffusion length to the open space decreased. The tubes with highest density was obtained at 1576 °C for 4 hours (Table IV.2.1 Set A). The density was measured by the Archimedes method in kerosene. Optical microscopy showed duplex microstructures; the extremely large (> 100 μ) and isolated grains (overgrown grains) were distributed in a fine grain matrix. This structure is typical for beta-aluminas. The number and size of overgrown grains increased with the sintering time and temperature. Though the density was high (~98 %), the duplex structure caused difficulties in the subsequent glass-sealing or ion-exchange because of a higher tendency to fracture.

The same green tubes were buried in a powder which had been used as packing powder several times (used-powder-pack). This powder was very coarse and the powder pack showed very little shrinkage (~1 %) after firing. The sintering behaviour of XB2-SG tubes in a used-powder pack was quite different from that in a fresh-powder pack. The densification rate was lower and constant with respect to time (Table IV.2.1 Set B). In a used-powder pack, higher sintering temperatures and longer times were required for a dense material than in a fresh-powder pack. The type of powder pack (fresh or used) may affect the sintering mechanism. The fresh powder maintains high Na pressure, especially at the initial stage of sintering, which may result in liquid phase sintering. Meanwhile, the used powder provides just enough Na vapour pressure to prevent the conversion to α-alumina. The slow and steady densification suggests only solid state sintering occurs with used-powder packs. The microstructures of the latter were finer and more homogeneous than the former (the overgrown

grains were rare). However, the control of sintering was not easy because too low Na vapour resulted in low density or second phase α-alumina.

Table IV.2.1. Density of XB2-SG

Set A. fresh powder pack (apparent density / bulk density)

	2 hours	4 hours	6 hours
1596 °C	-	3.22 / 3.18	-
1586 °C	3.22 / 3.18	3.23 / 3.19	-
1576 °C	3.21 / 3.17	3.23 / 3.20	3.21 / 3.17
1566 °C	-	3.22 / 3.17	-

Set B. used powder pack (bulk density)

	2 hours	4 hours	6 hours	8 hours
1585 °C	2.80	3.12	3.14	3.16
1596 °C	-	3.09	3.16	3.17

Another β-alumina powder (well-crystallized, < 50 μm) was ball-milled for 5 days, slip-cast and then sintered in a used powder pack at temperatures between 1550 to 1600 °C. The densities of tubes, given in Table IV.2.2, were measured by the Archimedes method in water. The full density (= 3.26) was determined by measuring a piece of crystal (as-received, ~1 *cm* in size). The high apparent density of β-alumina tubes (> 3.26) was due to the presence of α-alumina (d=3.98). A small grain size (~10 μm) for β-alumina and second phase α-alumina of the same size were observed by SEM. The α-alumina may have been introduced by extensive

pulverizing processes and the loss of Na during firing. No overgrown grains were observed. The α-alumina particles seemed to cause severe problems, such as cracking, in ion exchange.

Table IV.2.2. density of well-crystallized-powder tubes sintered at 1585 °C

	apparent density	bulk density	shrinkage (%)
4 hour	3.28	3.27	18.4
5 hour	3.29	3.27	18.5
6 hour	3.30	3.29	18.5

The critical factor in sintering beta-alumina is the Na vapour pressure [48]. A good seal on the crucible and a consistent powder pack should be used; otherwise, the results will not be reproducible. A second factor is the heating rate. Rapid heating is essential to avoid loss of sodium before reaching the sintering range. The Na_2O vapour pressure of β-alumina has been determined by EMF measurements [123].

$$\log p(atm) = 6.520 - \frac{19866}{T} \quad (1300 \text{ to } 1900\ \text{K}) \qquad \text{(IV.2.1)}$$

The maximum rate of vaporization of a substance is given by the Hertz-Langmuir expression [111].

$$J_{Na_2O} = \frac{(p_{Na_2O})_{eq}}{(2\pi MRT)^{1/3}} \qquad \text{(IV.2.2)}$$

where J_{Na_2O} : the evaporation rate of sodium oxide

p_{Na_2O} : the vapour pressure of sodium oxide

M : molecular weight of sodium oxide

R,T : the gas constant and absolute temperature

Thus at 1600 °C, the vapour pressure of sodium oxide is about 10^{-4} atm and the evaporation rate is 0.13 mol / m^2sec (= 8 g / m^2 sec). If there is a 0.1 mm gap between the crucible and lid with 5 cm diameter, the rate of evaporation is about 0.5 g / hr, about 7 % of the sodium oxide per hour with 100 g batch of β-alumina. Thus the loss of Na is significant. Two points should be noted. The above vaporization rate is the maximum possible rate under vacuum. Thus the real vaporization rate of β-alumina in air could be much lower. On the other hand, the green materials are not in equilibrium. They are neither completely crystallized nor chemically homogeneous. Thus the vapour pressure of Na could be higher than above estimate especially at the first stage of sintering.

IV.3) K ion exchange

K-ion exchange of β-alumina tubes of well-crystallized powder sintered at 1585 °C for 4 hours is shown in Table IV.3.1. In set A, the tubes were ion exchanged in KCl vapour (VP) with 0.73 : 1 = KCl : β-alumina by weight at 1050 °C for 18 hours, then in molten KCl (LP) with 2 : 1 = KCl : β-alumina five times at 1000 °C, one day each time. The variation of weight gain is very narrow. After LP4, the variation is increased, which suggests some tubes had chipped or cracked. After LP5, all 5 tubes were cracked. The prolonged (>5 days) ion exchange at high temperatures (> 800 °C) caused damage which might be related to chemical attack by KCl salt at high temperatures and to stress, that is, the sub-critical crack growth

occurring under stress assisted by the salt. The cracks occurred at the final stage (%EX > 99) and at high temperatures where the crack growth should be high. In set B, KNO_3 was used as a molten salt. The final weight gains are very consistent (WG =1.0298) which suggests the composition of β-alumina is $Na_2O{\cdot}10Al_2O_3$. The presence of α-alumina (~10%) causes a lower weight gain. KCl vapour exchange at 1050 °C and subsequent one or two batches of KNO_3 liquid exchange is the best route for the K-ion exchange of this β-alumina (well-crystallized) ceramic. However, the K-ion exchanged tubes all cracked during the glass sealing.

The XB2-SG tubes were K ion-exchanged and the results are given in table IV.3.2. For those tubes sintered in the fresh-powder pack (set A), the variation of the weight gains in a batch of tubes was large and the tubes lost weight as the exchange proceeded. After vapour exchange the surface of the tubes became rough revealing the overgrown grains in the duplex microstructure. It was difficult to remove the salt from the tubes because the salt resided in the pores and microcracks. It was not possible to determine the % exchange by weight gain as previously observed by Breiter et al [57]. There was indication of chipping due to residual stress. Initially He gas-tight tubes became permeable due to pores and microcracks developed during the ion exchange. The XB2-SG tubes sintered in the used-powder pack (set B) were more reliable in K ion exchange than those sintered in the fresh-powder pack. No chipping was observed. After ion exchange, the surface was smooth and the salt was easy to remove. The % exchange is based on chemical analysis (7% Na_2O by weight corresponds to WG = 1.038). The

The difference between the fresh-powder and used-powder-packed tubes results from the difference in the microstructures. The former has a duplex structure with very overgrown grains (>100 μ). The fracture initiating flaws, as mentioned by Tan et al [61], are surface irregularities and large crystal grains which are abundant in duplex structures. From table II.2.1, the K ion exchange of Na β-alumina causes the *c* axis and *a* axis to increase by factors of 1.0088 and 1.0004, respectively. Thus if the *a* axis of a crystal is parallel to the *c* axis of another, a strain of 4.2×10^{-3} could be developed. Taking the grain boundary energy as 1 Jm^{-2} [61], Young's modulus as 210 *GPa* and the crystal dimension as 2*l*, the limiting condition is [124];

$$\varepsilon \equiv \sqrt{\frac{24\gamma_{gb}}{El}} \qquad \text{(IV.3.1)}$$

whence spontaneous cracking would occur with a grain size of ~12 μm. Thus, with duplex structures one can not ion exchange beta-aluminas satisfactorily.

α-alumina second phase particles in well-crystallized powder tubes also cause stresses during the ion exchange. Because of its small size (~10 μm), the effect of α-alumina particles is less serious than that of overgrown grains. However, the cracks observed in overtreated tubes would be related to the α-alumina particles.

IV.4) glass-sealing

For Na beta-alumina, the alumino-silicate glass (Corning 1720) was a good sealant for all three kinds of Na beta-aluminas. The sealing was strong and He gas-tight. However, the sealing of K beta-aluminas was not so satisfactory. Two kinds of cracking were observed. One

was due to the difference in the thermal expansion coefficients between α and β-aluminas and the other was failure between glass and α-alumina lid. The thermal expansion coefficients of Na and K β-aluminas were measured (fig. IV.4.1): 7.6×10^{-6} for Na and 8.5×10^{-6} (on cooling) and 8.9×10^{-6} $°C^{-1}$ (on heating) for K. In the K β-alumina, the expansion due to the stress relaxation was observed on heating at temperatures higher than 1000 °C. The thermal expansion coefficient of K β-alumina tube is 0.5×10^{-6} $°C^{-1}$ higher than that of α-alumina (7.9×10^{-6} $°C^{-1}$, < 540 °C), which will cause tension in the tube on cooling. On the other hand, Na β-alumina has a thermal expansion coefficient 0.3×10^{-6} $°C^{-1}$ less than α-alumina, resulting in compression in the tubes on cooling. Another factor is the mechanical degradation due to ion exchange. The second type of failure seemed related to bubble formation in the glass, along the edge between the tube and lid. In the K β-alumina seal, more bubbles were seen than for Na β-alumina. The residual salt in the tube after ion exchange may cause this problem. Prolonged washing of K β-alumina tubes enhanced the success rate.

The alumino-silicate glass is ion exchangeable and its thermal expansion coefficient is very sensitive to the amount of alkaline oxides [125]. Moreover, it is easy to be devitrified. Thus during the glass sealing, the time at high temperatures should be limited to suppress devitrification. However, a high rate of cooling may result in cracks due to thermal stress.

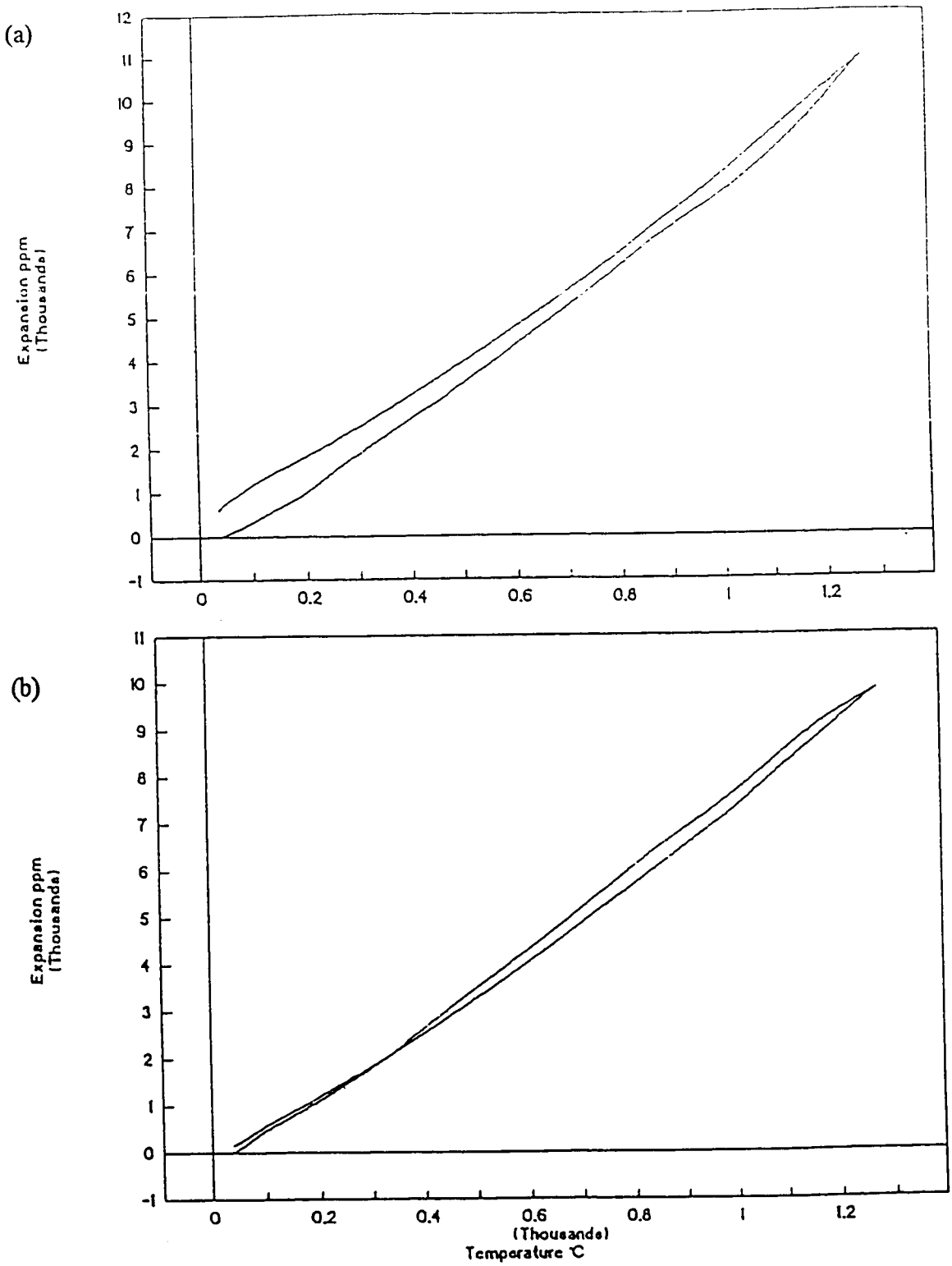

Figure IV.4.1. Thermal expansion of (a) K and (b) Na β-alumina.

IV.5) Na - C_{60}

IV.5.a) XRD

The X-ray diffraction pattern of pure C_{60} is shown in figure IV.5.1. The pattern is consistent with fcc as reported [94]. The X-ray scattering factor of the C_{60} molecule, S_G, is used as a first approximation with the assumption that the 60 C atoms are randomly distributed on a sphere of radius R [94].

$$\begin{aligned} S_G &= \sum_{j=1}^{60} f_C \exp(-i\mathbf{G}\cdot\mathbf{r}_j) \\ &= \frac{60 f_C}{4\pi}\int_0^{\pi} 2\pi R \sin\theta \exp(-iGR\cos\theta)d\theta \\ &= \frac{60 f_C \sin(GR)}{GR} \end{aligned} \qquad \text{(IV.5.1)}$$

where f_C is the atomic form factor of C and $\mathbf{G}$ is the reciprocal lattice vector. Since R = 3.52 Å and the lattice parameter a is 14.17 Å at room temperature, S_G is close to zero for $\mathbf{G} = (0, 0, 2n)$ where n is an integer.

$$\sin(G_{0,0,2n}R) = \sin\left(\frac{2\pi\cdot 2n}{14.17}3.52\right) = \sin(0.994\pi n)$$

Thus, peaks for (0, 0, $2n$) planes are rarely seen though they are allowed by the fcc selection rules (Table IV.5.1). C_{60} is so large a molecule, 10 Å in diameter, that S_G decreases rapidly as 2θ increases. Thus the intensities of the peaks in the high 2θ region (> 35 degrees) are too low to observe. Only 8 peaks are used to determine the lattice parameter.

In diffractometers the displacement of the specimen from the diffractometer axis is usually the largest single source of error which is given by

$$\frac{\Delta d}{d} = -\frac{D}{R}\frac{\cos^2\theta}{\sin\theta} \qquad \text{(IV.5.2)}$$

where D is the specimen displacement parallel to the reflection-plane normal and R is the diffractometer radius [126]. Since the lattice parameter a is proportional to d in cubic systems, the calculated parameters are extrapolated against $\frac{\cos^2\theta}{\sin\theta}$ (figure IV.5.2).

$$a = a_0 - a_0\frac{D}{R}\frac{\cos^2\theta}{\sin\theta} \qquad \text{(IV.5.3)}$$

By least-square approximation, a_0 is determined as 14.18 Å.

Table IV.5.1. The X-ray diffraction of pure C_{60}

	2θ (degree)	*h k l*	a_0 (Å)
1	10.837	1 1 1	14.129
2	17.719	2 2 0	14.146
3	20.795	3 1 1	14.155
4	21.737	2 2 2	14.152
5	27.438	3 3 1	14.158
6	28.110	4 2 0	14.185
7	30.900	4 2 2	14.165
8	32.839	3 3 3	14.160

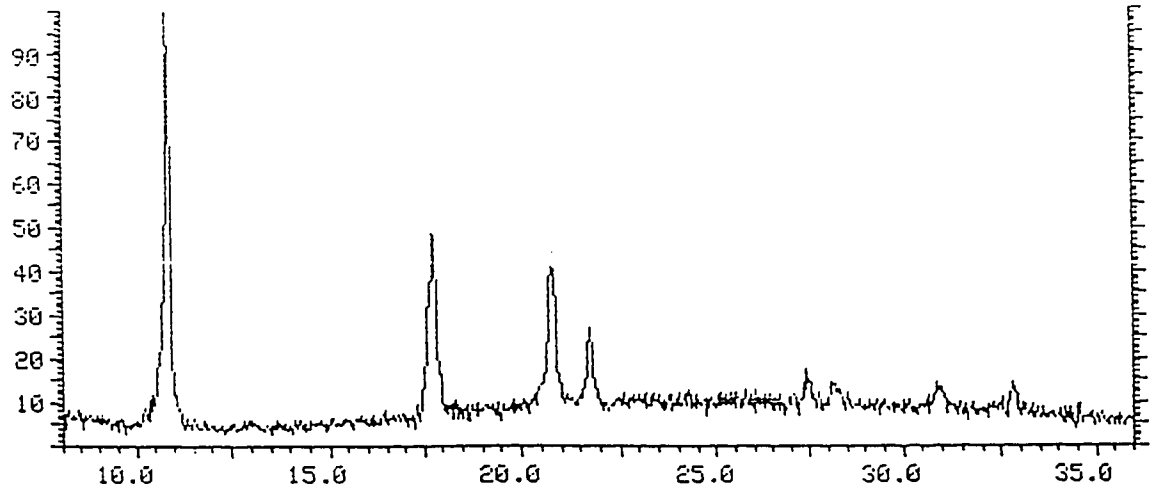

Figure IV.5.1. X-ray diffraction pattern of pure C_{60}.

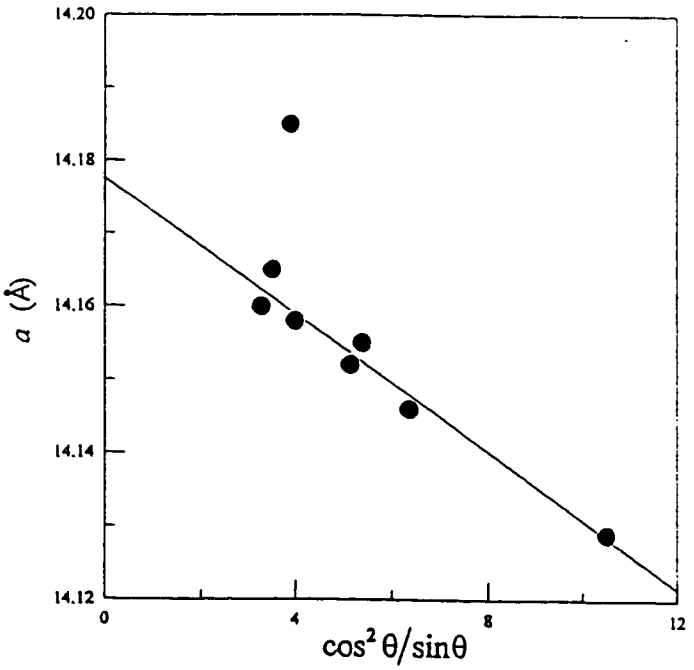

Figure IV.5.2. The accurate determination of the lattice parameter *a* of pure C_{60}. The error is assumed to be minimum at $\theta = 90$ degrees.

IV.5.b) EMF measurements

It will be instructive to derive the *EMF* in terms of the electrochemical potential. For the cell configuration

Ta | Na alloy | Na - β - Alumina | Na_xC_{60} | Ta

(L) (phase 1) (electrolyte) (phase 2) (R)

with the assumption that the transference number of Na in the solid electrolyte is unity, we need 6 equations to describe equilibrium; at the interfaces, from equation (II.4.4),

$$\tilde{\mu}_e\,(\mathrm{L}) = \tilde{\mu}_e\,(1) \qquad \text{(IV.5.4a)}$$

$$\tilde{\mu}_{Na^+}(1) = \tilde{\mu}_{Na^+}(\text{electrolyte}) = \tilde{\mu}_{Na^+}(2) \qquad \text{(IV.5.4b)}$$

$$\tilde{\mu}_e\,(2) = \tilde{\mu}_e\,(\mathrm{R}) \qquad \text{(IV.5.4c)}$$

in phases 1 and 2, from equation (II.4.5),

$$\mu_{Na}\,(1) = \tilde{\mu}_{Na^+}\,(1) + \tilde{\mu}_e\,(1) \qquad \text{(IV.5.5a)}$$

$$\mu_{Na}\,(2) = \tilde{\mu}_{Na^+}\,(2) + \tilde{\mu}_e\,(2) \qquad \text{(IV.5.5b)}$$

Thus

$$\mu_{Na}\,(2) - \mu_{Na}\,(1) = \tilde{\mu}_e\,(\mathrm{R}) - \tilde{\mu}_e\,(\mathrm{L}) \qquad \text{(IV.5.6)}$$

Since the chemical compositions of the right and left leads are the same, the chemical potentials of electrons in both Ta leads are equal. Thus,

$$\mu_{Na}\,(2) - \mu_{Na}\,(1) = -F\phi\,(\mathrm{R}) + F\phi\,(\mathrm{L}) = -F\Delta\phi \qquad \text{(IV.5.7)}$$

Equations (IV.5.4a to c) indicate that the electrolyte and the Ta leads are chemically inert to the electrode materials. Equations (IV.5.5a and b) imply that the phases 1 and 2 are chemically homogeneous.

The results of the *EMF* measurements are shown in figure IV.5.3. The electrochemical potential (equation IV.5.7) relates *EMF* to the chemical activity of sodium by the equation

$$EMF = \Delta\phi = -\frac{RT}{F}\ln a_{Na} \qquad \text{(IV.5.8)}$$

where R, T, F, and a_{Na} are respectively the gas constant, absolute temperature, Faraday constant, and chemical activity of sodium in the WE with respect to pure Na. For dilute solutions, *EMF* obeys the Nernst law

$$EMF = EMF^{\circ} - \frac{RT}{F}\ln X_{Na} \qquad \text{(IV.5.9)}$$

where the sodium atom fraction X_{Na} is calculated with respect to Na atoms and C_{60} molecules. (The C_{60} molecule is treated as an elementary unit in the solution since the covalent bonds between the sixty carbon atoms remain intact throughout the ionization process.) Figure IV.5.4 shows this relation at 599 K. The theoretical value of the slope (RT/F) is 51.6 mV, and based on this, the best fit of EMF° is 950 mV. The solubility of Na in C_{60} is less than 1 mole % (~ 0.7 %) at 599 K.

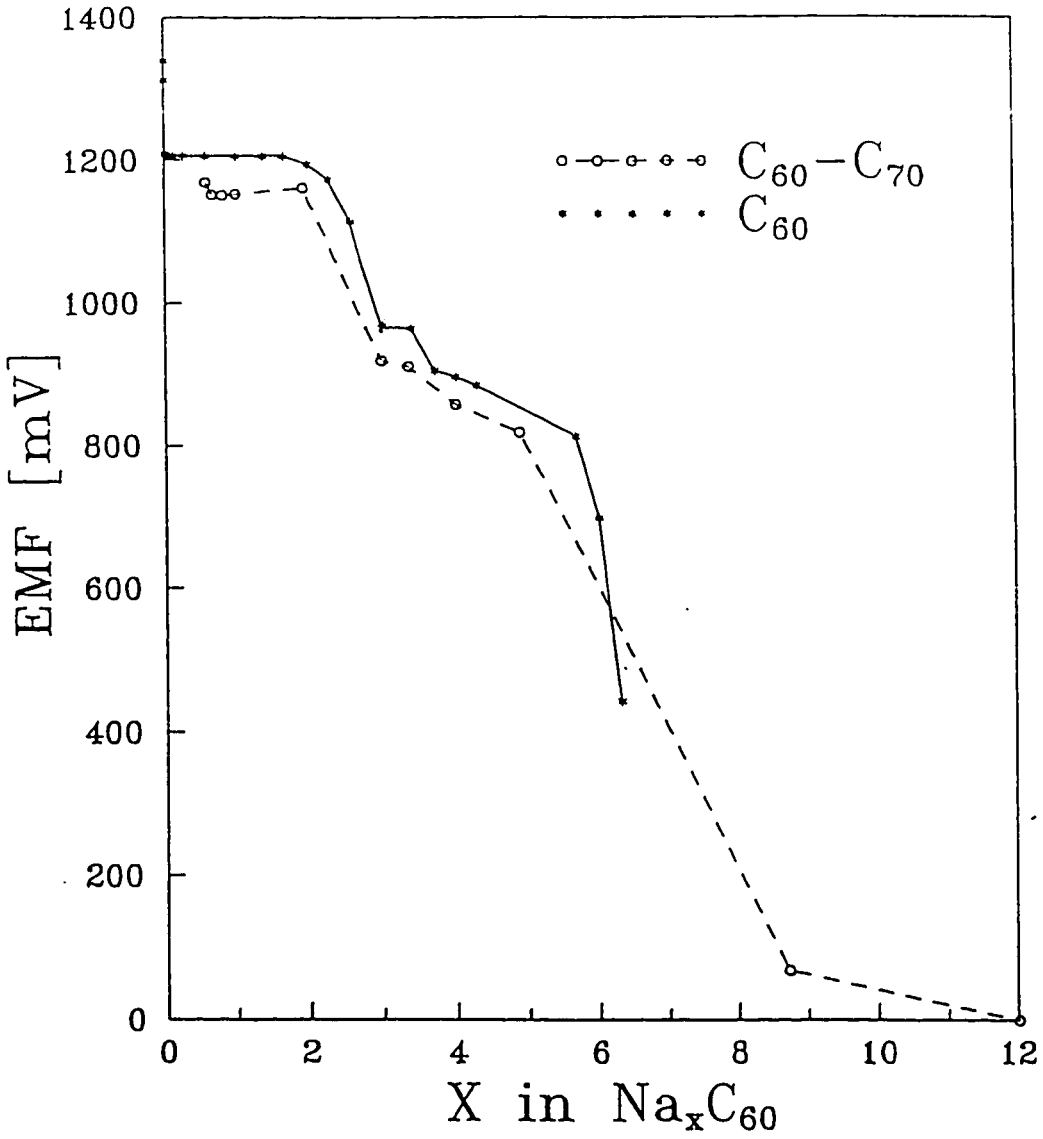

Figure IV.5.3. EMF versus x in Na_xC_{60} at 599 K.

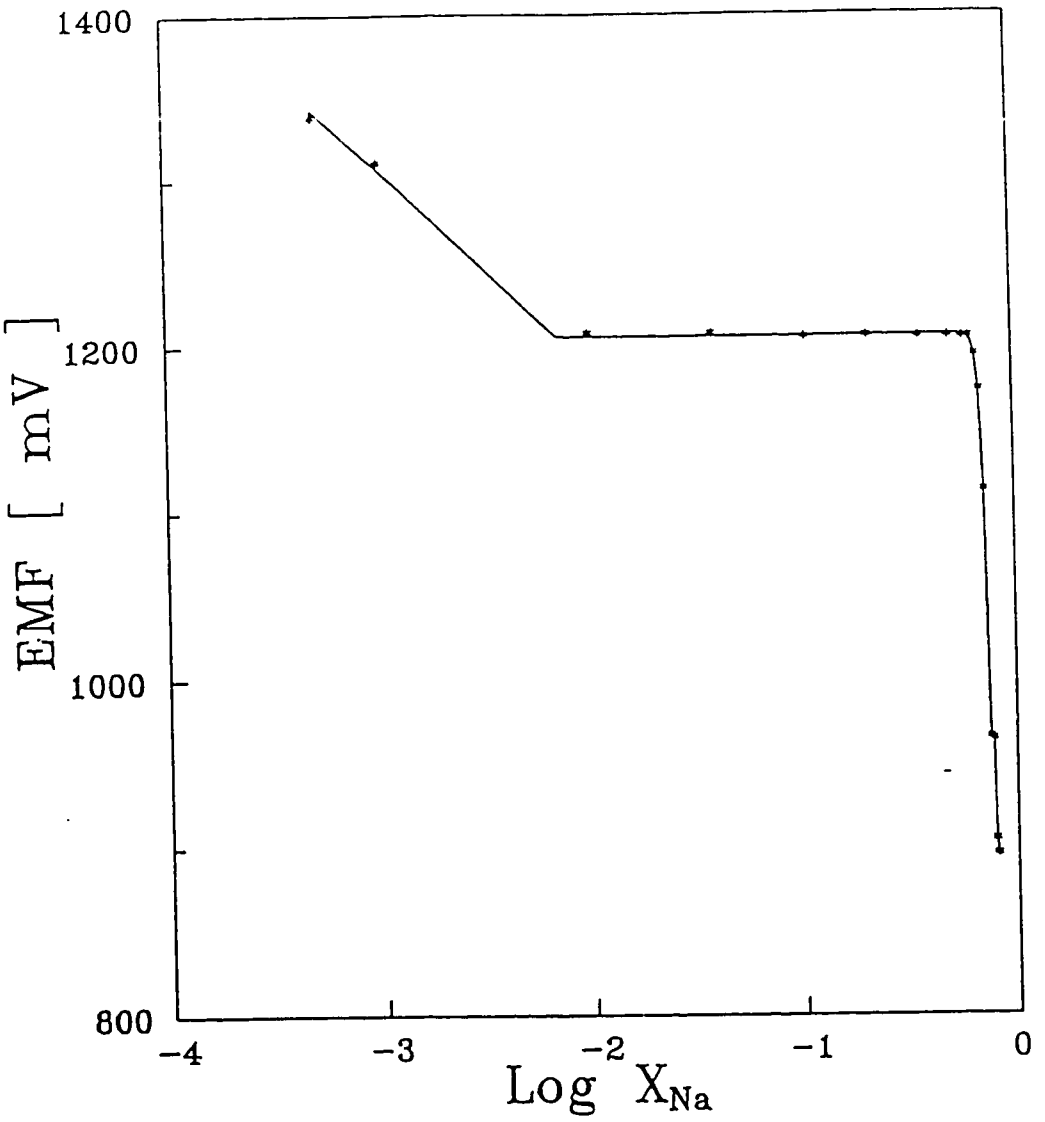

Figure IV.5.4. EMF in the dilute solution region. The theoretical Nernst slope is shown in the plot (see equation II.4.38).

In figure IV.5.3, the large plateau in EMF ($0 < x < 1.7$) represents a two phase region between fcc I and fcc II at 599 K. In the two-phase region the Na_xC_{60} in the WE is a mixture of $Na_{x1}C_{60}$ and $Na_{x2}C_{60}$ where $x1 \cong 0$ and $x2 \cong 1.7$. As the total amount of sodium increases the ratio of two phases changes. However, the chemical compositions of the two phases are fixed. Thus, the chemical activity of sodium is constant in this region, whereas, in a single-phase region (solid solution region), the chemical activity of sodium changes as a function of the composition. The region of gradual decrease in *EMF* ($1.7 < x < 3$) represents the domain of the fcc II phase. Another two phase region ($3 < x < 3.3$) exists between fcc II and the following phase. The phase relations at higher concentrations ($x > 3.3$) have not been determined. A sudden drop in *EMF* in the range of $3.3 < x < 3.7$ leaves the possibility that a line phase may exist at some stoichiometry between 3.3 and 3.7. The fcc III structure forms a large solution region beyond $x = 3.7$ (or 3.3). The existence of sodium atom clusters in the octahedral site suggests a range of compounds Na_xC_{60}, $3.7 < x < 11$. This is similar to Li_xC_{60} where a solution range $3 < x < 11$ has been observed [97]. However, it is possible that the fcc III phase has a miscibility gap: a lower x phase with four Na atoms per cluster and a higher x phase with nine Na atoms per cluster.

The phases in alkali-fullerides are listed in Table IV.5.2. The proposed phase equilibria in the Na_xC_{60} system are shown in figure IV.5.5. Since phases are not in complete agreement with the data from the literature, we have made arbitrary choices in

some cases. It appears that the size of the alkali ion and the related orientational ordering of the C_{60} molecule are major factors in determining the phase relations.

Table IV.5.2. The reported phases in alkali-fullerides

Composition	Structure	Temperature (K)	Remarks
C_{60} x = 0	*sc*	T < 260	orientationally ordered with two preferred orientations [71]
	fcc	260 < T < 400	anisotropic dynamic disorder [70]
	fcc	400 < T	isotropic dynamic disorder [20]
Li_xC_{60} x = 0.5, 2, 3 -11		T = 353	[97]
Na_xC_{60} x = 1, 2	*sc*	T < 325	the orientational order is the same as in pure C_{60} (sc) [94,95]
	fcc	325 < T < ?	[95]
2 < x < 3	*fcc*	? < T	merohedral disorder [127,128]
4 < x < 11	*fcc*	0 < T	ordered orientation, Na clusters [128,129]
M_xC_{60}* 0 < x < 1	*fcc*	T = 300	[82]
0 < x < 1			two-phase region [92]
x = 1	*fcc*	330 < T	disordered orientation, rock-salt structure [130]
	rhombo	T < 330	[130]
	ortho	T < 450	[93]
1.4 < x < 3	*fcc*	? < T < 433	unique to K [130]
x = 3	*fcc*	0 < T	except Cs, merohedral disorder [66,82,127]
x = 4	*bct*	0 < T	[82]
x = 6	*bcc*	0 < T	[82]

* M = K, Rb, Cs

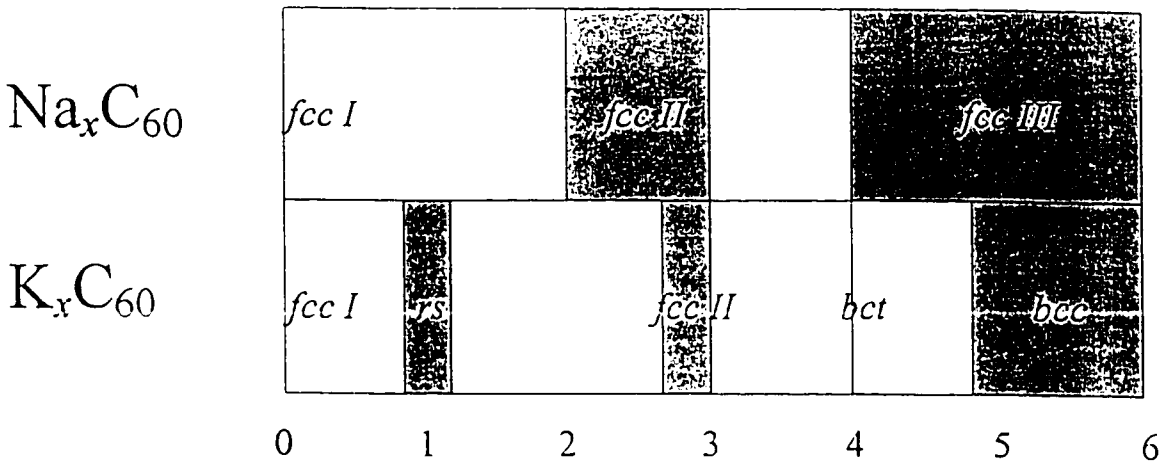

(a)

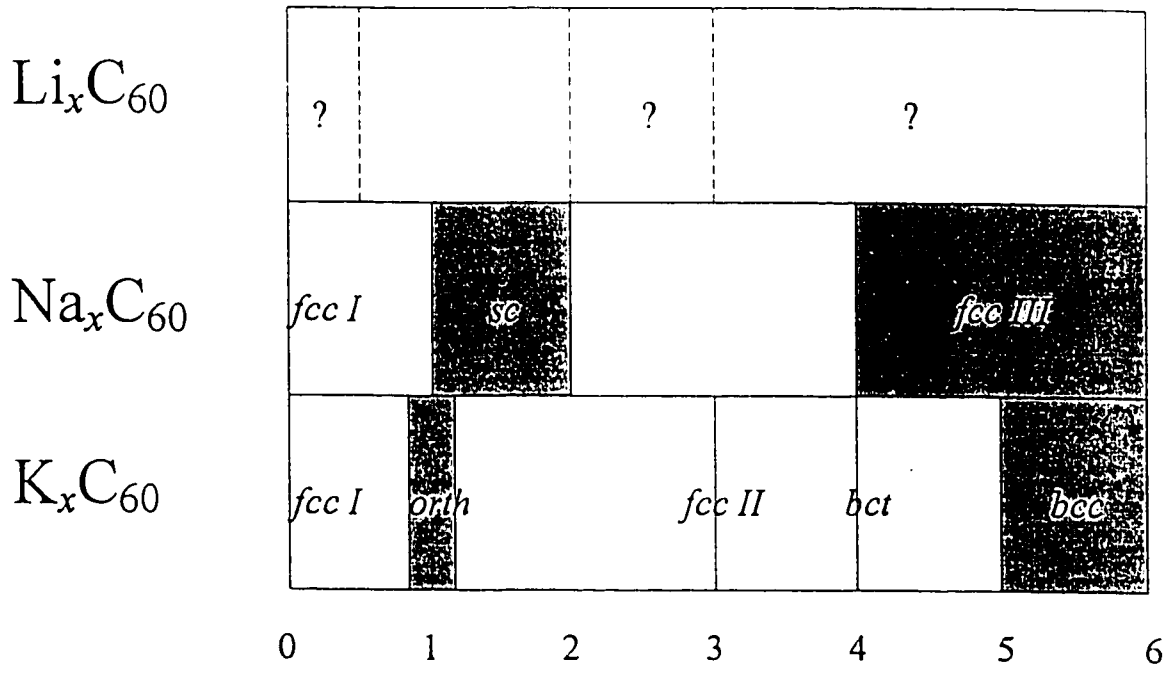

(b)

Figure IV.5.5 Proposed phases in M_xC_{60} at (a) high temperatures (T > 425 K) and (b) room temperature. *rs* and *ortho* represent rocksalt and orthorhombic, respectively.

From equation (IV.5.8), the activity of Na was calculated from the *EMF* data. The activity of C_{60} was derived by Gibbs-Duhem integration (equation II.4.54) using the α function (figure IV.5.6).

$$\alpha_i = \frac{\ln \gamma_i}{(1 - X_i)^2} \qquad \text{(IV.5.10a)}$$

$$\ln \gamma_2 = -\alpha_1 X_1 X_2 - \int_{X_2=1}^{X_2} \alpha_1 dX_2 \qquad \text{(IV.5.10b)}$$

The Gibbs energy of mixing (ΔG_m) was calculated from the measured activity of Na (equation IV.5.8) and the calculated activity of C_{60} (equation IV.5.10b) and is shown in figure IV.5.7. The Gibbs energy of mixing of $\frac{1}{4}Na_3C_{60}$ and $\frac{1}{7}Na_6C_{60}$ are evaluated as 85 and 81 kJ/mol, respectively.

$$\frac{x}{x+1}Na + \frac{1}{x+1}C_{60} = \frac{1}{x+1}Na_xC_{60} \qquad \Delta G_m^M \qquad \text{(IV.5.10c)}$$

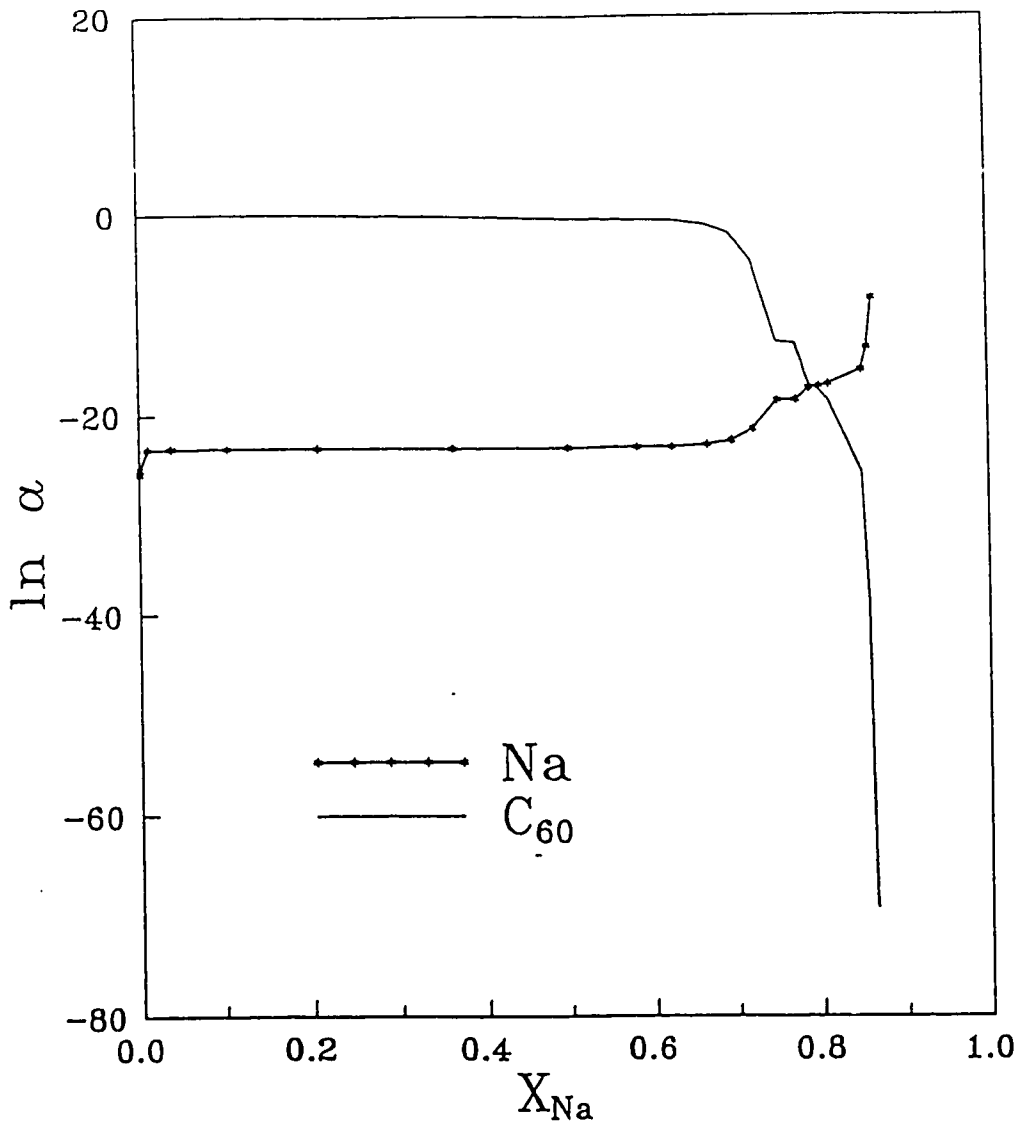

Figure IV.5.6. The activities of Na and C_{60}. The activities of Na were obtained from EMF measurements (equation IV.5.8) and the activities of C_{60} were calculated from Gibbs-Duhem relation (equation IV.5.10).

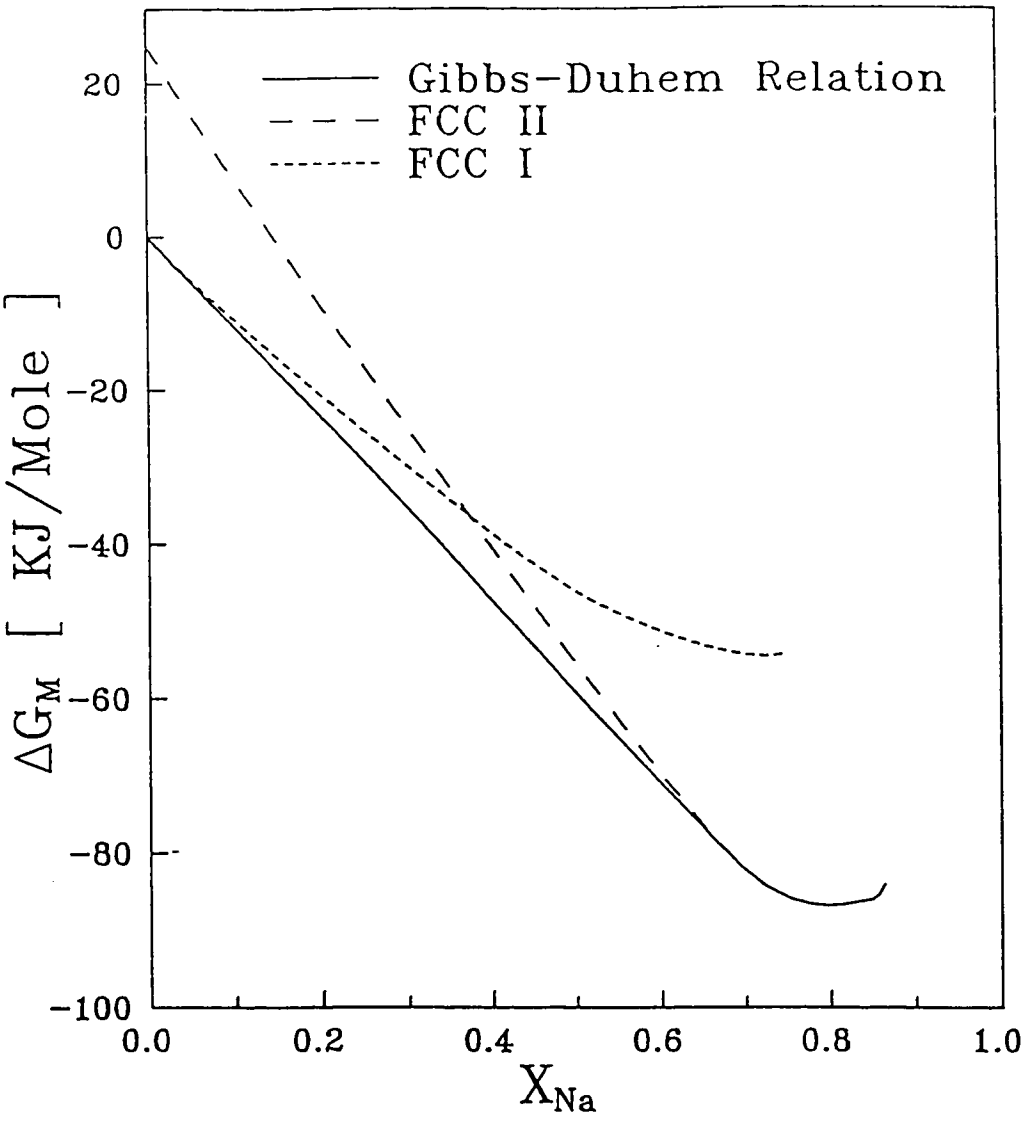

Figure IV.5.7. The formation energy of $\frac{1}{x+1}Na_xC_{60}$. The solid line is from the EMF measurements. The dashed line is for *fcc* II (equation IV.5.15) and the dotted line is for *fcc* I (equation IV.5.29).

IV.5.c) Ideal interstitial solution

The simplest model of the system may be the ideal interstitial solution [106, 112]. The assumptions are

1) the energies of the alkalis (A) and the bucky balls (B) are unaffected by their respective positions on the lattices.

2) the distribution of the A atoms are random.

3) every host site is filled with B; no vacancy.

Here, the complication is that the alkalis can be accommodated by both octahedral and tetrahedral interstitial sites.

If we consider the following reaction:

$$x\mathrm{Na} + \mathrm{C_{60}} = \mathrm{Na_x C_{60}}\ (fcc\ \mathrm{II}) \qquad \text{(IV.5.11)}$$

the Gibbs energy of each species can be written as

$$G_{\mathrm{A}} = -kT\ln\left(q_{\mathrm{A}}^{\bullet}\right)^{xN} + xNU_{\mathrm{A}} \qquad \text{(IV.5.12a)}$$

$$G_{\mathrm{B}} = -kT\ln\left(q_{\mathrm{B}}^{\bullet}\right)^{N} + NU_{\mathrm{B}} \qquad \text{(IV.5.12b)}$$

$$G_{\mathrm{A_xB}} = -kT\ln\left[\left(q_{\mathrm{A}}^{tet}\right)^{N_{\mathrm{A}}^{tet}}\left(q_{\mathrm{A}}^{oct}\right)^{N_{\mathrm{A}}^{oct}}\left(q_{\mathrm{B}}^{h}\right)^{N}\right] - kT\ln\Omega(x) + NU_{\mathrm{A_xB}} \qquad \text{(IV.5.12c)}$$

where q_j^i is the vibrational partition function of j in site i, N is the number of C_{60} and N_j^i is the number of j in site i. The relation between them is given as

$$N_{\mathrm{A}}^{tet} + N_{\mathrm{A}}^{oct} = xN \qquad \text{(IV.5.12d)}$$

From assumption 1 above, the energy of the mixture is given by

$$NU_{A,B} - xNU_A - NU_B = N_A^{tet} E_{tet} + N_A^{oct} E_{oct} \quad \text{(IV.5.13)}$$

From assumption 2 and the merohedral disorder of C_{60}, the degeneracy $\Omega(x)$ is

$$\Omega(x) = g \cdot 2^N \quad \text{(IV.5.14a)}$$

$$g = \frac{N_{tet}!}{N_A^{tet}!(N_{tet} - N_A^{tet})!} \frac{N_{oct}!}{N_A^{oct}!(N_{oct} - N_A^{oct})!} \quad \text{(IV.5.14b)}$$

where N_i is the total number of i sites. They are related by

$$N = N_{oct} = \frac{1}{2} N_{tet} \quad \text{(IV.5.14c)}$$

Thus, the Gibbs energy of mixing at constant temperature is given in the form of

$$\Delta G_m = AN_A^{tet} + BN_A^{oct} + CN - kT \ln g \quad \text{(IV.5.15a)}$$

where $A = -kT \ln\left(q_A^{tet} / q_A^{\bullet}\right) + E_{tet}$ (IV.5.15b)

$$B = -kT \ln\left(q_A^{oct} / q_A^{\bullet}\right) + E_{oct} \quad \text{(IV.5.15c)}$$

$$C = -kT \ln\left(q_B^{h} / q_B^{\bullet}\right) - kT \ln 2 \quad \text{(IV.5.15d)}$$

The condition for the equilibrium distribution of A in two distinct interstitials is

$$\left(\frac{\partial \Delta G_m}{\partial N_A^{tet}}\right)_{T,P,N,x} = 0 \quad \text{(IV.5.16a)}$$

or

$$A - B + kT \ln \frac{N_A^{tet}}{2N - N_A^{tet}} \Big/ \frac{N_A^{oct}}{N - N_A^{oct}} = 0 \quad \text{(IV.5.16b)}$$

We define M as

$$M = \exp(-\frac{A-B}{kT}) = \left(\frac{N_A^{tet}}{2N - N_A^{tet}} \Big/ \frac{N_A^{oct}}{N - N_A^{oct}} \right)_{equilibrium} \quad \text{(IV.5.17)}$$

The equilibrium distribution is given, if M = 1, as

$$\frac{N_A^{tet}}{N} = \frac{2}{3}x \quad \text{(IV.5.18a)}$$

and otherwise as

$$\frac{N_A^{tet}}{N} = \frac{M(x+2)+1-x-\sqrt{[M(x+2)+1-x]^2 - 8M(M-1)x}}{2(M-1)} \quad \text{(IV.5.18b)}$$

The chemical potential of A is defined as

$$\mu_A = \mathcal{N}\left[\frac{\partial \Delta G_m}{\partial (xN)}\right]_{P,T,N} \quad \text{(IV.5.19)}$$

where $\mathcal{N}$ is Avogadro's number. Using equation (IV.5.18), we have

$$\mu_A = \mathcal{N}\left[A + kT\ln\frac{N_A^{tet}}{2N - N_A^{tet}}\right] = \mathcal{N}\left[B + kT\ln\frac{N_A^{oct}}{N - N_A^{oct}}\right] \quad \text{(IV.5.20)}$$

Using equation (IV.5.8) and (IV.5.20), the *EMF* is related to the chemical potential by

$$-eEMF = A + kT\ln\frac{N_A^{tet}}{2N - N_A^{tet}} = B + kT\ln\frac{N_A^{oct}}{N - N_A^{oct}} \quad \text{(IV.5.21)}$$

where the number of A in tetrahedral sites is given by equation (IV.5.18).

We can determine the parameters A and B for which equation (IV.5.21) gives the best fit to the measured values. A plot of this relation, taking A and B as -1.34 and -1.14 eV, is shown in figure IV.5.8. Note that in Na_2C_{60}, about 90 % of tetrahedral sites are occupied; a higher occupancy of tetrahedral sites was experimentally observed at this composition [95, 128].

In order to complete equation (IV.5.15a), we need to determine the parameter C. The main difference between *fcc* I and *fcc* II may originate from the type of orientational disorder in molecules; though it may not be the case, it will show the importance of the orientational disorder. Assume that

$$-kT\ln\left(q_B^h/q_B^*\right) = -kT\ln\left(q_{lib}/q_{rot}\right) \qquad \text{(IV.5.22)}$$

where q_{lib} is due to the rotational libration of the molecule in Na_xC_{60} and q_{rot} is due to the free rotation of the molecule in pure C_{60} and the changes in the intramolecular and intermolecular vibrational frequencies are ignored. The rotational partition function [24] is given by

$$q_{rot} = \frac{\pi^{1/2}}{\sigma}\left(\frac{T}{\Theta_r}\right)^{3/2} \qquad \text{(IV.5.23a)}$$

$$\text{where } \Theta_r = \frac{h^2}{8\pi^2 Ik} \qquad \text{(IV.5.23b)}$$

The symmetry number σ is 60 and the moment of inertia I is 9.7×10^{-44} kg m^2. The vibrational partition function [24] is given as

$$q_{vib} = \prod_i \frac{\exp(-h\nu_i / 2kT)}{1 - \exp(-h\nu_i / kT)} \qquad \text{(IV.5.27)}$$

At 599 K, the parameter C in equation (IV.5.15d) is about 0.26 eV, where the librational frequency is estimated as that of K_3C_{60} (26 cm^{-1}) [131]. The resulting plot of equation (IV.5.15a) is shown in figure IV.5.7.

Consider the reaction:

$$x\text{Na} + C_{60} = \text{Na}_x\text{C}_{60}\,(fcc\ \text{I}) \qquad \text{(IV.5.28)}$$

Assuming that the number of C_{60} hindered in free rotation is proportional to the number of Na in interstitial sites, equation (IV.5.15a) is modified as

$$\Delta G_m = AN_A^{tet} + BN_A^{oct} + C(\alpha N_A^{tet} + \beta N_A^{oct}) - kT\ln g \qquad \text{(IV.5.29a)}$$

$$= A'N_A^{tet} + B'N_A^{oct} - kT\ln g \qquad \text{(IV.5.29b)}$$

Equation (IV.5.29b) is shown in figure IV.5.7 with A' = -0.65 and B′ = -0.95 eV, which are determined from figure IV.5.3.

The miscibility gap in A_xC_{60} where A is alkali can be partly explained by above model; it has only two or three parameters. The orientational disorder must play an important role in alkali fullerides as in the pure fullerite, which could be related to the size effects of alkalis.

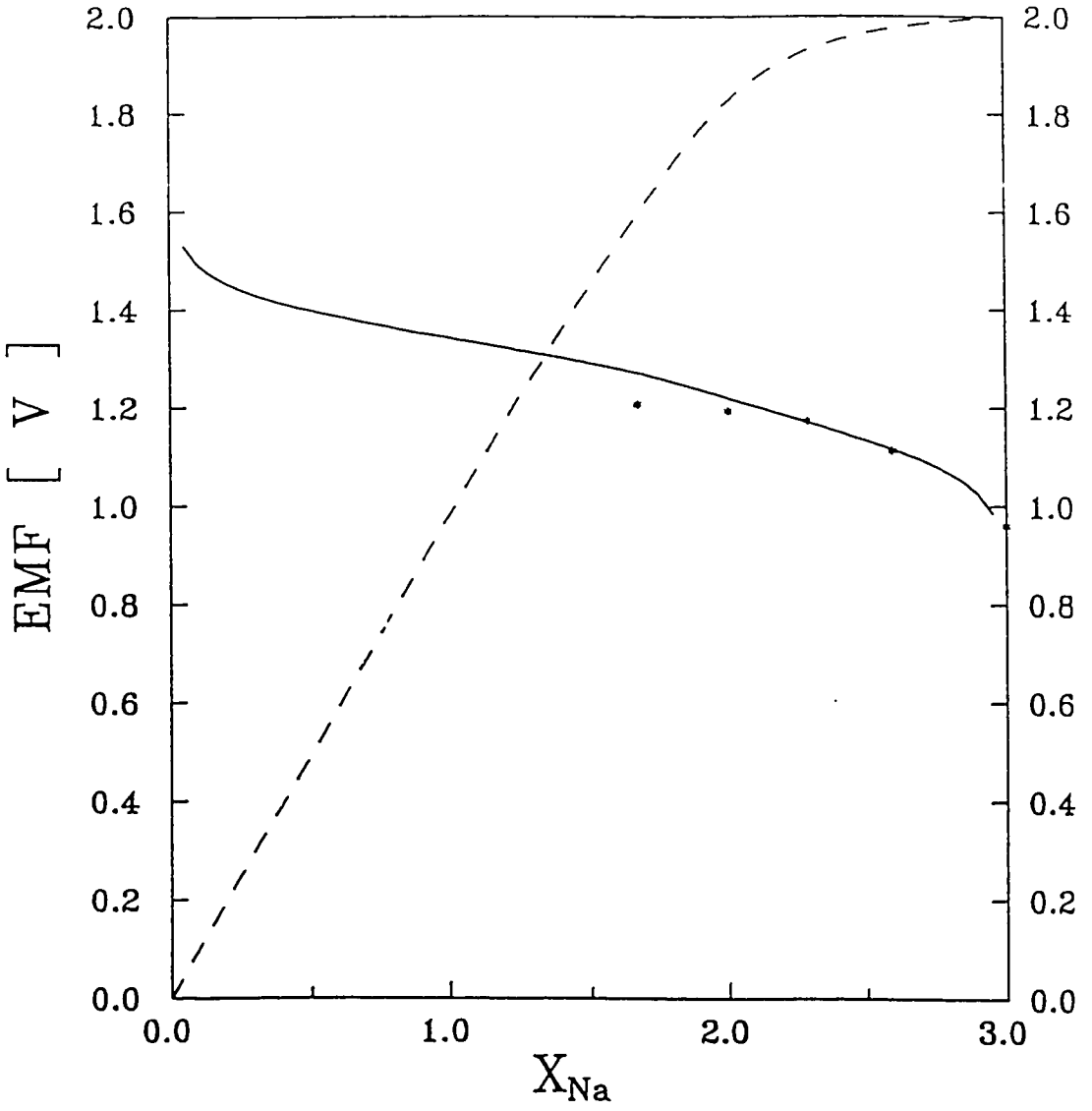

Figure IV.5.8. EMF (solid line) calculated from equation (II.5.21). The parameters were determined by the fitting to the data. The dashed line is the ratio of the number of Na ions in tetrahedral sites to the total number of C_{60} molecules, $\left(\frac{N_A^{tet}}{N}\right)$, calculated by equation (II.5.18).

IV.6) Models for C_{60}

IV.6.a) The symmetry of simple cubic C_{60}

The symmetry elements of $Pa\bar{3}$ [132], the low-temperature form of C_{60}, are given as

$$T_h^6 = Pa\bar{3} = T^4 + T^4 I$$

$$T^4 = \left\{ \begin{array}{l} E, C_3^{xyz}, C_3^{2xyz}, \left\{C_3^{x\bar{y}\bar{z}} \middle| \frac{a}{2} 0 \frac{a}{2}\right\}, \left\{C_3^{2x\bar{y}\bar{z}} \middle| 0 \frac{a}{2} \frac{a}{2}\right\}, \left\{C_3^{\bar{x}y\bar{z}} \middle| \frac{a}{2} \frac{a}{2} 0\right\}, \left\{C_3^{2\bar{x}y\bar{z}} \middle| \frac{a}{2} 0 \frac{a}{2}\right\}, \\ \left\{C_3^{\bar{x}\bar{y}z} \middle| 0 \frac{a}{2} \frac{a}{2}\right\}, \left\{C_3^{2\bar{x}\bar{y}z} \middle| \frac{a}{2} \frac{a}{2} 0\right\}, \left\{U^x \middle| \frac{a}{2} \frac{a}{2} 0\right\}, \left\{U^y \middle| 0 \frac{a}{2} \frac{a}{2}\right\}, \left\{U^z \middle| \frac{a}{2} 0 \frac{a}{2}\right\} \end{array} \right\} \quad \text{(IV.6.1)}$$

where the symmetry elements are represented in the Seitz notation (equation II.6.45) and C_3, C_3^2 and U denote 120, 240 and 180 degree rotation, respectively, about the axis which is given as the superscript following them. The orthogonal matrices for the proper rotations can be derived by the Eulerian angles (Appendix A) and are listed in Appendix B.

As mentioned in section II.3, *sc* C_{60} has a basis with 4 molecules, each of which is rotated about 4 different <1 1 1> directions through an equal angle γ which is not fixed by the symmetry of the crystal (see figure II.3.3). XRD showed that the rotation angle γ was about 22 degrees clock-wise (orientation α) from the standard orientation A and there were orientational defects at about 82 degrees clock-wise rotation (orientation β) from the standard orientation A [69] (see figure II.3.2). In cubic-close-packing, a C_{60} molecule has 12 nearest neighbors; 6 of them are on the plane normal to its rotation axis (plane A) and

rest of them are on planes (plane B and C) adjacent to plane A. Note that for orientation α and β, a molecule has 6 double bonds facing 6 nearest neighbor molecules on plane A and 6 pentagons (orientation α) or 6 hexagons (orientation β) facing 6 nearest neighbor molecules on plane B and C. Thus, there are four motifs for the two adjacent molecules;

(1) a pentagon of a molecule with 22 degrees rotation facing a double bond of the adjacent molecule with 22 degrees rotation (Pα-Dα),

(2) a pentagon of a molecule with 22 degrees rotation facing a double bond of the adjacent molecule with 82 degrees rotation (Pα-Dβ),

(3) a hexagon of a molecule with 82 degrees rotation facing a double bond of the adjacent molecule with 22 degrees rotation (Hβ-Dα),

(4) a hexagon of a molecule with 82 degrees rotation facing a double bond of the adjacent molecule with 82 degrees rotation (Hβ-Dβ).

When we take the [1 1 1] direction as the rotation axis for the molecule at the origin (0, 0, 0), then the positions and rotation axes of the remaining 3 molecules are determined by the symmetry of the crystal. For example, applying $\left\{U^{x}\middle|\frac{a}{2}\frac{a}{2}0\right\}$ to the molecule at the origin produces a molecule at (*a*/2, *a*/2, 0) with rotation axis $[1\,\bar{1}\,\bar{1}]$, which can be shown by the operations of

$$U^x\begin{bmatrix}1\\1\\1\end{bmatrix}=\begin{bmatrix}1&0&0\\0&-1&0\\0&0&-1\end{bmatrix}\begin{bmatrix}1\\1\\1\end{bmatrix}=\begin{bmatrix}1\\-1\\-1\end{bmatrix} \qquad \text{(IV.6.2)}$$

$$(0,0,0)+\left(\frac{a}{2},\frac{a}{2},0\right)=\left(\frac{a}{2},\frac{a}{2},0\right)$$

The positions and the rotation axes of 4 molecules are given in table IV.6.1.

Table IV.6.1. The positions and the rotation axes of 4 molecules in a basis.

κ	X(κ)	Rotation axis
1	(0, 0, 0)	[111]
2	(1/2, 1/2, 0)	$[1\bar{1}\bar{1}]$
3	(1/2, 0, 1/2)	$[\bar{1}\bar{1}1]$
4	(0, 1/2, 1/2)	$[\bar{1}1\bar{1}]$

IV.6.b) Models for the intermolecular interactions between C_{60} molecules

Several attempts to model the interactions between molecules by the Lennard-Jones potential and Coulombic interactions from local-charge distributions have been reported [133,134,135,136,137]. Because the Lennard-Jones interactions between C atoms can not explain the 22 degree configuration of *sc* fullerite, they introduced many types of interaction centers at the centers of the double and single bonds as well as the C atoms [133,136]. However, as the types of interaction centers increase, the number of parameters to be determined increases geometrically. For example, the number of

parameters for 1, 2 and 3 types of interaction centers is 2, 6 and 12, respectively. On the contrary, only 12 interaction centers of a type were used to simulate the symmetry of the icosahedron [134]. For Coulombic interactions, point charges were introduced at the C atoms, the centers of the bonds [135] and the hexagonal or pentagonal faces [137]. However, the assignment of positive charges at the centers of the bonds or faces is not physical. A simpler and more physical model has been developed in this section.

The philosophy to develop a model is to minimize the number of parameters so far as the model is physical and reflects the experimental results. In this section the following results of experiments for the low-temperature form of pure C_{60} were used as conditions to develop a model and determine the parameters:

1) According to the XRD data [69], the $Pa\bar{3}$ structure with rotation angle $\gamma = 22$ degrees is the ground state.

2) The molecule with orientation α is more stable than the molecule (orientational defect) with orientation β by about 12 meV/molecule, which is the formation energy of the defect ΔE_d ($\approx 6(E_4 - E_1)$, see equation IV.6.10).

3) The NMR data showed that the activation energy for the jump between two orientations (α and β) is about 250 *m*eV (E_a) [138].

Condition (2) is employed to predict the population of orientational defects in the temperature range of 90 to 260 K and condition (3) is chosen to explain the freezing of the reorientational motion below 90 K.

The potential energy between two molecules is the sum of the Lennard-Jones (LJ) potential and the Coulomb potential.

$$V(l\kappa;l'\kappa') = \sum_{i}\sum_{i'} 4\varepsilon_{ii'}\left[\left(\frac{\sigma_{ii'}}{|\mathbf{X}(l\kappa i)-\mathbf{X}(l'\kappa' i')|}\right)^{12} - \left(\frac{\sigma_{ii'}}{|\mathbf{X}(l\kappa i)-\mathbf{X}(l'\kappa' i')|}\right)^{6}\right] + \sum_{j}\sum_{j'}\frac{q_j q_{j'}}{|\mathbf{X}(l\kappa j)-\mathbf{X}(l'\kappa' j')|} \quad \text{(IV.6.3)}$$

where l, κ, i and j are the cell, the molecule, the LJ interaction center and the Coulomb interaction center, respectively. In this calculation 1.45 and 1.40 Å were taken as the lengths of the single and double bonds, respectively [66]. The positions of C atoms and other interaction centers of a molecule with the rotation angle γ from the standard orientation A were computed from the table II.3.1 using the Eulerian angles (equation A.A.2) and the symmetry of the crystal (equation IV.6.1). The results of two previous models [135,136] are shown in figure IV.6.1. Lu et al. [135] (figure IV.6.1.a and b) used C atoms as the LJ interaction centers and introduced effective charges, positive q and negative $-2q$ for single and double bonds, respectively. In figure IV.6.1a, the LJ potential favors $\gamma = 87$ degrees and the Coulomb potential makes $\gamma = 22$ degrees as the ground state phase. In figure IV.6.1b, the 22 degree phase has point defects ($\theta = 82$) which cause an energy increase of 200 meV per defect and the activation energy for the jump between two orientations is about 800 meV. Though $\Delta E_d = 200$ and $E_a = 800$ meV are much different from experimental results, this model is qualitatively correct. Lamoen et al. [136]

introduced as LJ interaction centers single bonds and double bonds as well as C atoms (figure IV.6.1c and d). This model is good not only qualitatively but also quantitatively; E_d = 10 meV and E_a = 150 meV. The only drawback of this model is the low activation energy E_a and the large number (12) of parameters that need to be fixed.

The model proposed here substitutes the LJ interaction centers at C atoms with the effective LJ interaction centers which are initially located at the C atoms and begin to move toward the center of the adjacent double bonds. When the shift x is zero, the γ = 87 degree phase is the most stable (figure IV.6.2a) and ΔE_d is negative (figure IV.6.2b). As the shift x increases, the 22 degree phase becomes more stable relative to 87 degree phase and the formation energy of the defect ΔE_d increases. At about x = 0.06 Å, the LJ potential which is close to that of Lamoen almost satisfies both conditions (1) and (2). However, E_a = 150 meV is too small compared to condition (3). Thus, the effective Coulomb interaction centers are introduced at C atoms and at the centers of single and double bonds. For charge neutrality, the negative charges imposed on the centers of single (q_S) and double (q_D) bonds were compensated by the positive charge (q_C) at C atoms.

$$q_C = -q_S - \frac{q_D}{2} \qquad \text{(IV.6.4)}$$

The behavior of the Coulomb potential is shown in figure IV.6.3a and b. When $0 < q_S < q_D$, the Coulomb potential increases E_a and ΔE_d simultaneously and it stabilizes another phase (γ = 90 degree) over the γ = 22 degree phase. Thus, when choosing parameters such

that E_a > 200 meV, conditions (1) and (2) can not be satisfied at the same time for 0 < q_S < q_D. Four sets of parameters are shown in table IV.6.2, which are chosen with some arbitrariness. σ is taken from graphite data. The behavior of the model is shown in figure IV.6.4. The contribution of Coulomb potential to the lattice energy is less than 2 %. However, it increases E_a by 30 to 110 meV (20 to 40 %). Set 1 satisfies the three conditions best (figure IV.6.4a and b). In set 2, the parameters are chosen intentionally to obtain not the 22 degree phase but the 68 degree phase as the ground state (figure IV.6.4c). However, at a certain temperature the presence of the defects (orientation β) with small formation energy ΔE_d (about 12 meV) in the 22 degree phase makes the 22 degree phase more stable than the 68 degree phase, owing to the configurational entropy; the 68 degree phase also has defects (orientation α) with formation energy ΔE_d larger than 100 meV (figure IV.6.5). It shows that the 22 degree phase is not necessarily the ground state. In set 3, q_S is chosen as zero, which seems more physical than q_S/q_D larger than unity. However, E_a at only 180 meV is too small compared to condition (3). Set 4 is determined to consider the bulk modulus and the lattice energy of pure C_{60} (see section IV.7) in addition to the above three conditions. The behavior of set 4 is the same as set 1 except that the bulk modulus (17.7 GPa) and the cohesive energy (1.86 eV) of set 4 are more acceptable [139,140,141,142] than those of set 1 (23.4 GPa and 2.4 eV). However, the activation energy E_a of set 4 is much smaller than condition (3).

Contrary to the belief that the most important factor which stabilizes the 22-degree phase is the Coulomb potential due to the local charge distribution and that the

stabilization comes from the tendency for electron-rich double bonds to face electron-poor pentagons [69,133,135,137], this model shows that the LJ potential plays the most important role in stabilizing the 22-degree phase, which agrees with Lamoen [136]. In set 1 and 2, the choice of q_S/q_D larger than unity seems unphysical. However, it was required to obtain an E_a larger than 200 meV. The result can be explained in two ways. One is that the large E_a may be due to other types of potential such as charge-transfer interactions. The other is that the true value of E_a may not be as high as 250 meV. Another NMR study [143] concluded that E_a = 180 ± 52 meV which is too low to cause the freezing of the reorientational motion below 90 K. The answer to this problem could be the set 2 type parameters, that is, transition to another structure which has high activation energy for the reorientational motion.

Table IV.6.2. Four sets of parameters which satisfy three conditions.

set	ε	σ	x	q_D	q_S/q_D	$6(E_1-E_4)$	$6\Delta E$	E_a	α	β
1	4.150	3.40	0.040	-0.380	1.565	-12.47	1.31	260	21.4	82.0
2	3.830	3.40	0.040	-0.578	1.300	-16.66	-2.90	250	21.3	81.6
3	4.150	3.40	0.057	-0.212	0	-11.89	2.89	180	21.3	82.0
4	3.192	3.40	0.040	-0.410	1.460	-12.25	-0.04	215	21.3	81.8

*energies in meV, length in Å, angles in degree and charges in elementary charge. For $6(E_1-E_4)$ and $6\Delta E$ see equation (IV.6.7). Lattice parameter a = 14.06 Å was used.

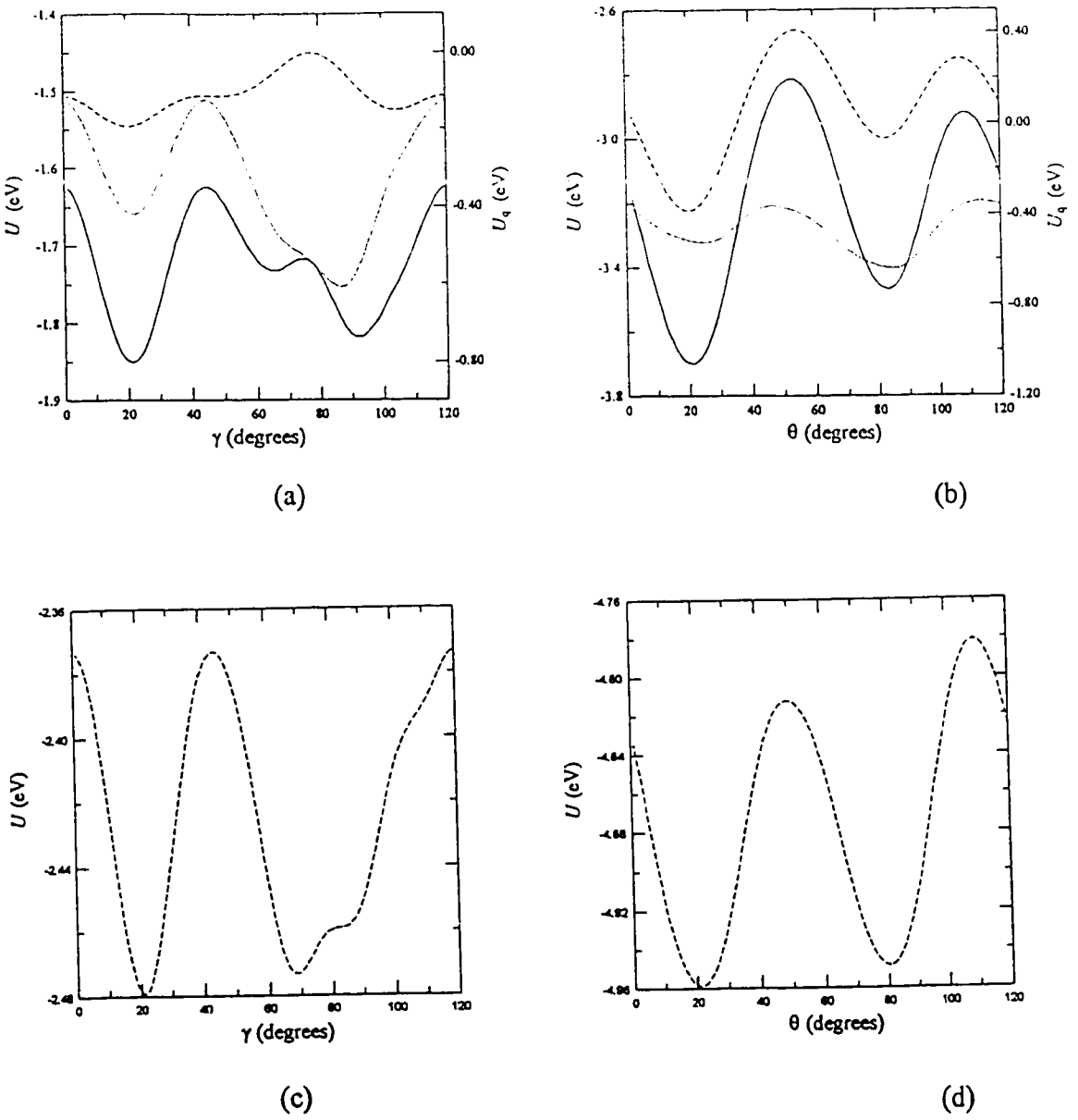

Figure IV.6.1 (a), (c) the cohesive energy U [eV/molecule] of *sc* C_{60} as a function of γ. (b), (d) the potential increase due to the rotation θ of a molecule whose 12 neighbors are fixed at orientation α (γ = 22 degrees). (a), (b) are from Lu's model [135] and (c), (d) are from Lamoen's model [136]. Dashed, dotted and solid lines are for Coulomb potential U_q, Lennard-Jones potential U_{LJ} and overall potential U, respectively.

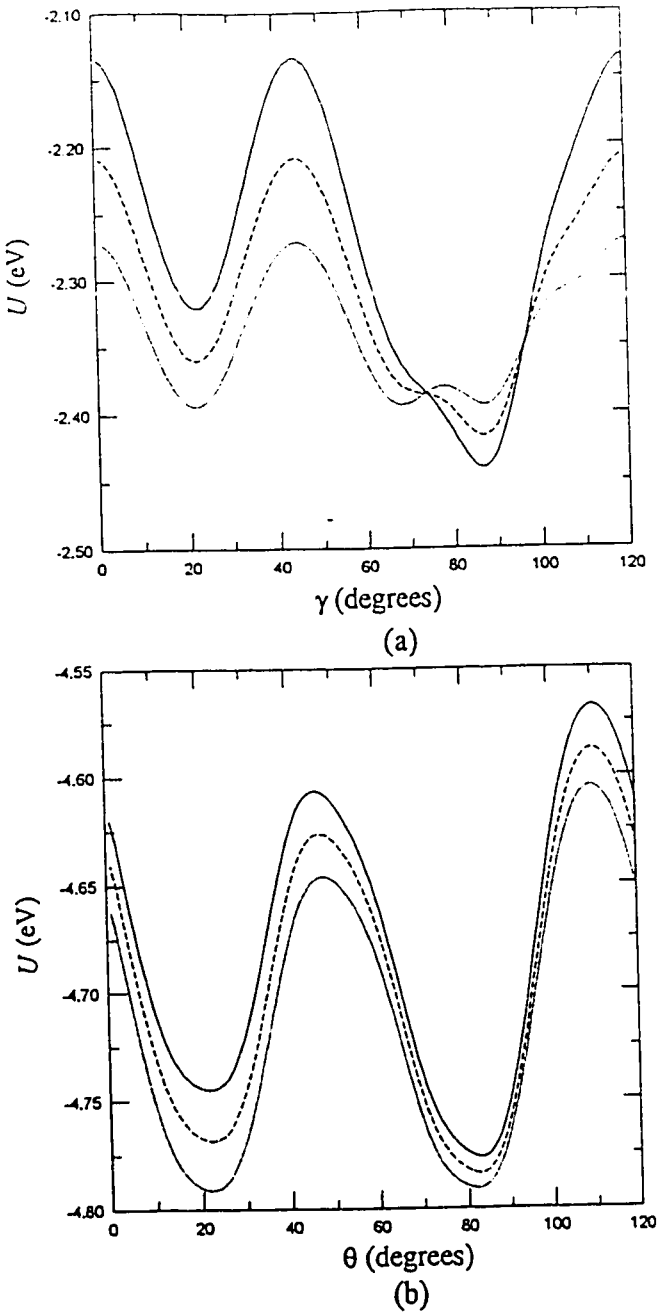

Figure IV.6.2 (a) The Lennard-Jones (LJ) potential U_{LJ} [eV/molecule] of *sc* C_{60} as a function of γ. The shift x of effective interaction centers towards the center of the double bonds is 0, 0.03 and 0.06 Å for solid, dashed and dotted lines, respectively. (b) the LJ potential increase due to the rotation θ of a molecule whose 12 neighbors are fixed at orientation α (γ = 22 degrees). The shift x is 0.04, 0.05 and 0.06 Å for solid, dashed and dotted lines, respectively.

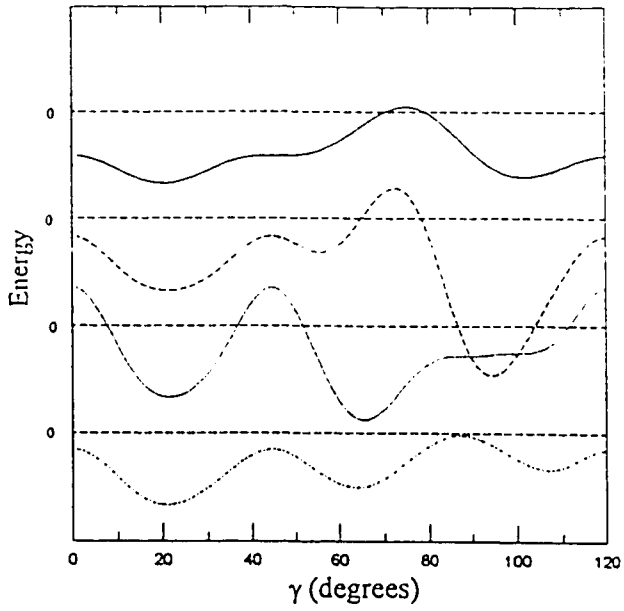

(a)

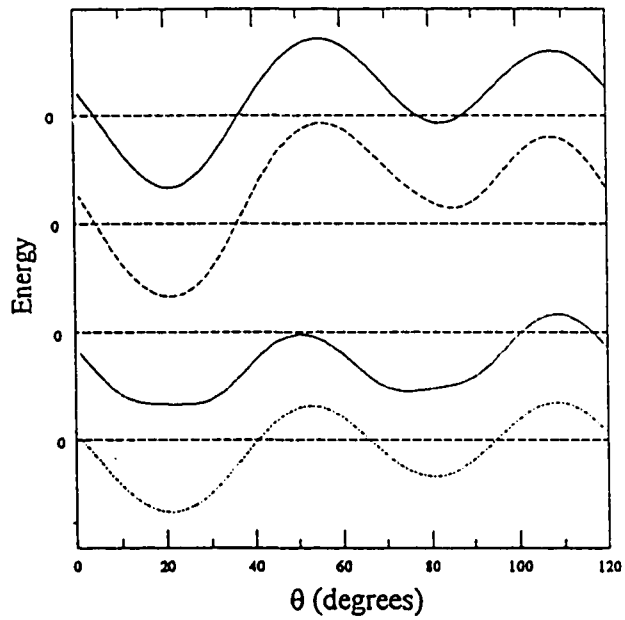

(b)

Figure IV.6.3 (a) The Coulomb potential U_q [eV/molecule] of *sc* C_{60} as a function of γ. (b) The Coulomb potential increase due to the rotation θ of a molecule whose 12 neighbors are fixed at orientation α (γ = 22 degrees). The ratio of q_S to q_D is 0, 0.5, 1.0 and 1.5 for solid, dashed, dotted and mixed lines, respectively.

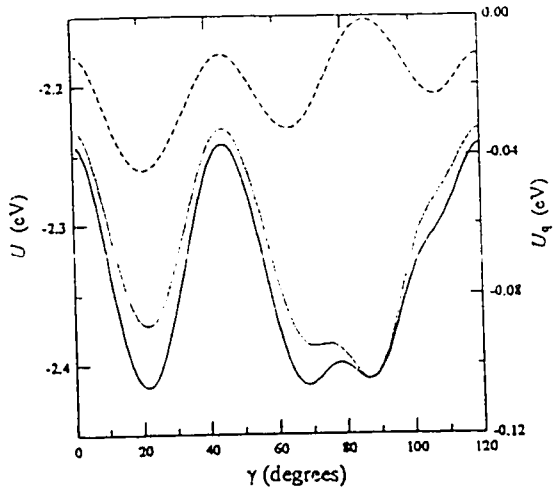
U (eV)
U_q (eV)
γ (degrees)

(a)

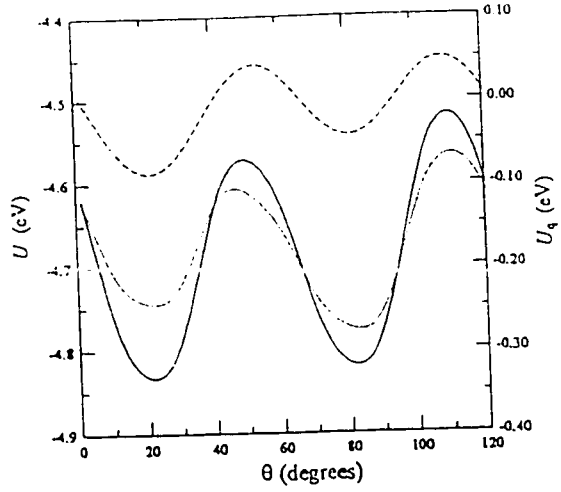
U (eV)
U_q (eV)
θ (degrees)

(b)

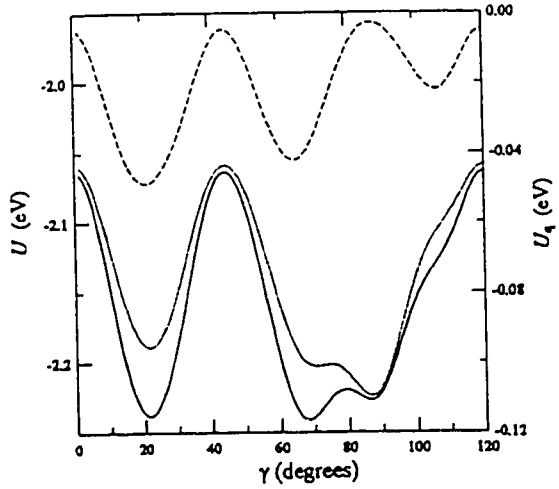
U (eV)
U_q (eV)
γ (degrees)

(c)

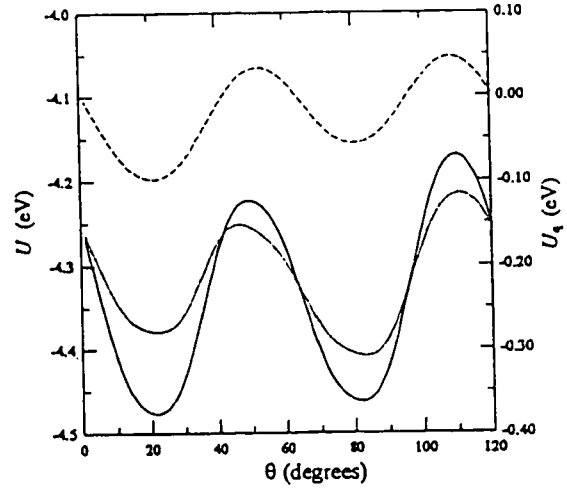
U (eV)
U_q (eV)
θ (degrees)

(d)

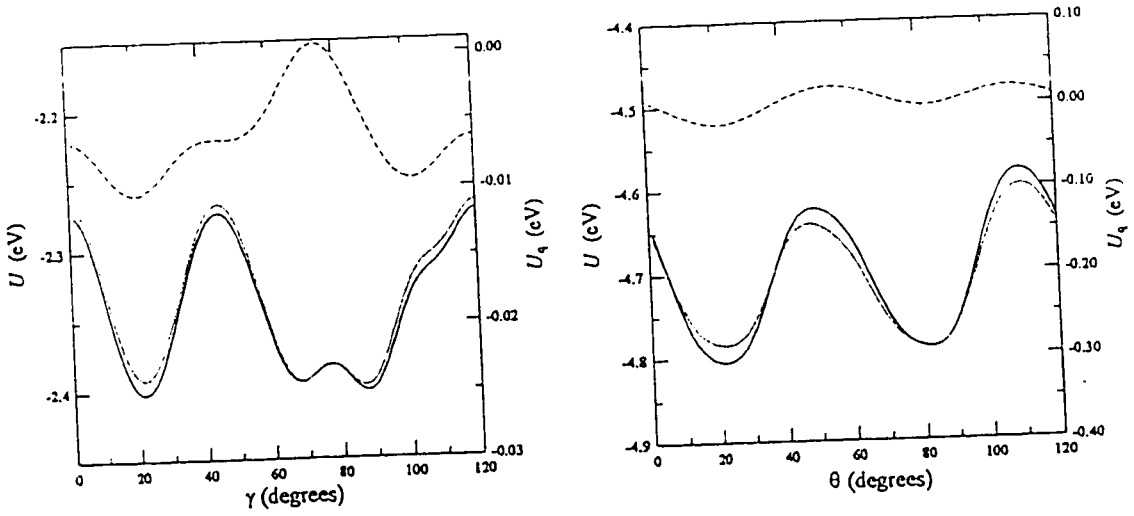

Figure IV.6.4 (a), (c), (e) the cohesive energy U [eV/molecule] of *sc* C_{60} as a function of γ. (b), (d), (f) the potential increase due to the rotation θ of a molecule whose 12 neighbors are fixed at orientation α (γ = 22 degrees). (a), (b) are from Set 1 parameters, (c), (d) are from Set 2, (e), (f) are from Set 3 parameters. Dashed, dotted and solid lines are for Coulomb potential U_q, Lennard-Jones potential U_{LJ} and overall potential U, respectively.

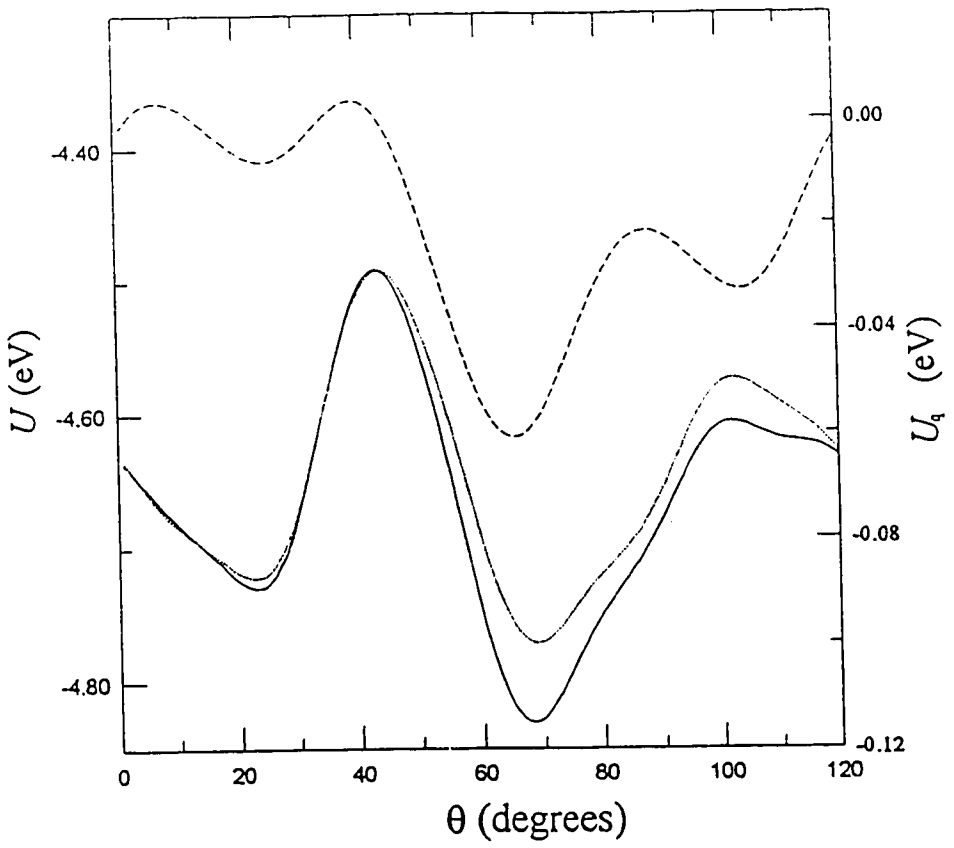

Figure IV.6.5. The potential increase due to the rotation θ of a molecule whose 12 neighbors are fixed at orientation γ = 68 degrees. Set 2 parameters were used for the calculation. Dashed, dotted and solid lines are for Coulomb potential U_q, Lennard-Jones potential U_{LJ} and overall potential U, respectively.

IV.6.c) Lattice statistics of C_{60}

Model 1. Regular solution model

In *sc* C_{60}, the molecules have one of two orientations; orientation α (γ = 22 degree) and β (γ = 82 degree). In this sense it is like ferromagnetism. However, the internal energy term is not so simple as in the Ising model because of the 4 motifs between 2 adjacent molecules, which are defined in section IV.6.a. Assume that there are no vacancies and that every molecule at orientation α or β is randomly distributed. Because of the overall charge neutrality and the high symmetry of the molecule, the Coulomb interaction due to the local charge distribution decays as R^{-13} at long distance [135]. Thus, it would be sufficient to consider only the nearest neighbor interactions since both the Van der Waals interaction and the Coulomb interaction are short-ranged. The number of bonds N_i between molecules with motif i (i = 1 to 4) is given as

$$N_1 = 6NX_\alpha^2 \qquad \text{(IV.6.5a)}$$

$$N_2 = N_3 = 6NX_\alpha X_\beta \qquad \text{(IV.6.5.b)}$$

$$N_4 = 6NX_\beta^2 \qquad \text{(IV.6.5.c)}$$

where N = total number of molecules and X_j = fraction of the molecules with orientation j (j = α or β). Thus, the energy of the lattice and the configurational degeneracy are given as

$$E = E_1N_1 + E_2N_2 + E_3N_3 + E_4N_4 \qquad \text{(IV.6.6a)}$$

$$= 6N\left\{X_\alpha E_1 + X_\beta E_4 + X_\alpha X_\beta\left[E_2 + E_3 - (E_1 + E_4)\right]\right\} \qquad \text{(IV.6.6b)}$$

$$\Omega = \frac{N!}{N_\alpha ! N_\beta !} \qquad \text{(IV.6.6c)}$$

where E_i = the energy per bond between two molecules with the motif i (which is computed from equation IV.6.3) and N_j = the number of molecules with orientation j. Thus, the free energy is written as

$$A = N\left\{6\left(X_\alpha E_1 + X_\beta E_4 + X_\alpha X_\beta \Delta E\right) + kT\left(X_\alpha \ln X_\alpha + X_\beta \ln X_\beta\right)\right\} \qquad \text{(IV.6.7a)}$$

where $\Delta E = E_2 + E_3 - (E_1 + E_4)$ (IV.6.7b)

The equilibrium condition is given as

$$\left(\frac{\partial A}{\partial X_\alpha}\right)_{T,V,N} = 0 \qquad \text{(IV.6.8a)}$$

or

$$6\left[(E_1 - E_4) + (X_\beta - X_\alpha)\Delta E\right] + kT \ln \frac{X_\alpha}{X_\beta} = 0 \qquad \text{(IV.6.8b)}$$

If we know the energy terms, we can compute A and X_α as a function of temperature (unfortunately the solution is not exact). Conversely, equation (IV.6.8) can be solved as a function of X_α.

$$T = -\frac{6\left[(E_1 - E_4) + (X_\beta - X_\alpha)\Delta E\right]}{k \ln\left(X_\alpha / X_\beta\right)} \qquad \text{(IV.6.9a)}$$

$$A = 6N\left\{X_\alpha E_1 + X_\beta E_4 + X_\alpha X_\beta \Delta E - \frac{\left[(E_1 - E_4) + (X_\beta - X_\alpha)\Delta E\right]}{\ln\left(X_\alpha / X_\beta\right)}\left(X_\alpha \ln X_\alpha + X_\beta \ln X_\beta\right)\right\} \qquad \text{(IV.6.9b)}$$

The entropy term is obtained by

$$TS = E - A \qquad \text{(IV.6.9c)}$$

The results of equation (IV.6.6.b) and (IV.6.9a to c) are shown in figures IV.6.7a to d, where E_i was computed from equation (IV.6.3) with the first set parameters in table IV.6.2.

Since the Lennard-Jones interactions are short-ranged, $E_1 \approx E_2$ and $E_3 \approx E_4$ could be a good approximation. In this case, ΔE in equation (IV.6.8b) can be ignored.

$$X_\beta \approx \left\{\exp\left[\frac{6(E_4 - E_1)}{kT}\right] + 1\right\}^{-1} \qquad \text{(IV.6.10)}$$

By fitting equation (IV.6.10) to the experimental data [69], $6(E_4 - E_1)$ is determined as about 12 meV, which is used to determine the parameters in the models for the intermolecular interactions between C_{60} molecules.

Model 2. Cluster variation method

The cluster variation method [107] was presented in the section on substitutional solid solutions (II.5.b). The cluster variation method has the advantage over the regular solution model in that it reflects the short-range order and provides better estimation of the entropy.

A cluster of 10 molecules has been used as a group (figure IV.6.6). A molecule has Z (= 12) nearest neighbors. There are v (= 24) bonds and p (= 10) sites in a group. For N molecules, there is N_g (= N/4) groups. Each site belongs to 5/2 (= pN_g/N) groups. Table IV.6.3 shows some of the parameters used in the computation where k refers to an energy level ε_k (k = 1 to 240) with multiple configurations, ω_k = the number of configurations of type k, $p_{\beta k}$ = the number of sites occupied by orientation β and N_i = the number of bonds with motif i in a group. The energy ε_k is given as

$$\varepsilon_k = E_1 N_1 + E_2 N_2 + E_3 N_3 + E_4 N_4 \qquad \text{(IV.6.11)}$$

where E_i was computed from equation (IV.6.3) with set 1 of parameters in table IV.6.2.

For substitutional solid solutions, the cluster variation method shows that at equilibrium, equations (II.5.96), (II.5.98), (II.5.101) and (II.5.102) hold.

$$X_i = \frac{1}{p}\sum_k p_{ik}\omega_k\psi_k \qquad \text{(II.5.96)}$$

$$H_1(V,\mu_i,\psi_k,N) = N_g\sum_k \varepsilon_k\omega_k\psi_k - N\sum_i^s \mu_i X_i \qquad \text{(II.5.98)}$$

$$\frac{\psi_k}{\psi_l} = \exp\left(\frac{\varepsilon_l-\varepsilon_k}{kT}\right)\prod_i^{s-1}\left[\left(\frac{X_i}{X_s}\right)^{1-\frac{2v}{Zp}}\exp\frac{2v(\mu_i-\mu_s)}{ZpkT}\right]^{p_{ik}-p_{il}} \qquad \text{(II.5.101)}$$

$$f(T,V,\mu_i)=\frac{F(T,V,\mu_i)}{N}=\frac{Z}{2\nu}\left\{kT\ln\psi_1+\varepsilon_1-\sum_i^s p_{i1}\left[\left(1-\frac{2\nu}{Zp}\right)kT\ln X_i+\frac{2\nu}{Zp}\mu_i\right]\right\} \tag{II.5.102}$$

where ψ_k = the probability that a group has a specific configuration of type k, μ_i = the chemical potential of species i and s = the number of species in the system.

For C_{60} the situation is a little bit different. That is, X_i is not fixed and $\mu_\alpha = \mu_\beta$ at equilibrium. Thus, by taking $\mu_\alpha = \mu_\beta = 0$,

$$\begin{aligned}A(T,V,N)&=F(T,V,\mu_i)\\&=\frac{ZN}{2\nu}\left\{kT\ln\psi_1+\varepsilon_1-p_{\alpha 1}\left(1-\frac{2\nu}{Zp}\right)kT\ln X_\alpha\right\}\end{aligned} \tag{IV.6.12}$$

We can compute X_α and ψ_k at given T, V and N by iteration, repeating the following 5 steps until X_α converges.

(1) $X_\alpha = X_\alpha$ and $X_\beta = 1 - X_\alpha$ (IV.6.13a)

(2) $$\psi_1=\left[1+\sum_k^{240}\omega_k\exp\left(-\frac{\varepsilon_k-\varepsilon_1}{kT}\right)\left(\frac{X_\beta}{X_\alpha}\right)^{\frac{3}{5}p_{\beta k}}\right]^{-1}$$ (IV.6.13b)

(3) $$\psi_k=\psi_1\exp\left(-\frac{\varepsilon_k-\varepsilon_1}{kT}\right)\left(\frac{X_\beta}{X_\alpha}\right)^{\frac{3}{5}p_{\beta k}}$$ (IV.6.13c)

(4) $$X_\beta=\frac{1}{p}\sum_k p_{\beta k}\omega_k\psi_k$$ (IV.6.13d)

(5) $X_\alpha = 1 - X_\beta$ (IV.6.13e)

With the results of iteration (figure IV.6.7a), we can compute the Helmholtz energy from equation (IV.6.12) (figure IV.6.7b). The internal energy (figure IV.6.7c) is given as

$$E(V, \psi_k, N) = N_g \sum_k \varepsilon_k \omega_k \psi_k \quad \text{(IV.6.14)}$$

The entropy term given by equation (IV.6.9c) is shown in figure (IV.6.7d).

Figures IV.6.7. a to d show that the results of regular solution and cluster variation method are similar to each other, especially in the high temperature region where random mixing is more likely. The difference in the energy terms between the two methods is very small because the defect formation energy is only about 10 meV. One may initially suspect the result that, at temperatures lower than 100 K, the entropy term ($-TS$) for the cluster variation method is lower than that for the regular solution (figure IV.6.7d) since the random mixing approximation used in the regular solution model will always have the lower entropy term ($-TS$) than any other method if the system is defined in terms of (T, V, X_i). However, for the C_{60} system, X_i is not fixed. Since the cluster variation method reflects the short-range order better than the regular solution model, in the cluster variation method the introduction of a given number of defects into the system gains less internal energy than in the regular solution model and the random mixing approximation outweighs the entropy term less as the solutions become dilute. Thus, in the temperature range between 25 and 75 K, the cluster variation method has more defects than the regular solution model (figure IV.6.7a) while the internal energy of the

cluster variation method is equal to or even lower than that of the regular solution model (figure IV.6.7.c).

Table IV.6.3. Parameters used in cluster variation method

k	ω_k	$p_{\beta k}$	N_1	N_2	N_3	N_4
1	1	0	24	0	0	0
2	1	1	21	0	3	0
3	3	1	18	4	2	0
4	3	1	21	2	1	0
5	3	1	18	2	4	0
6	3	2	16	3	4	1
7	3	2	18	2	4	0
8	3	2	15	2	7	0
9	3	2	13	7	3	1
10	3	2	18	4	2	0
11	3	2	13	3	7	1
12	3	2	16	5	2	1
13	6	2	15	6	3	0
14	6	2	13	5	5	1
15	3	2	12	6	6	0
16	3	2	16	3	4	1
17	6	2	15	4	5	0
18	3	3	12	5	4	3
19	3	3	14	4	4	2
20	6	3	13	5	5	1
21	6	3	11	4	7	2
22	3	3	10	5	8	1
23	3	3	15	4	5	0
24	3	3	13	3	7	1
25	6	3	12	4	8	0

*There are 240 k's. Only first 25 are given in the table.

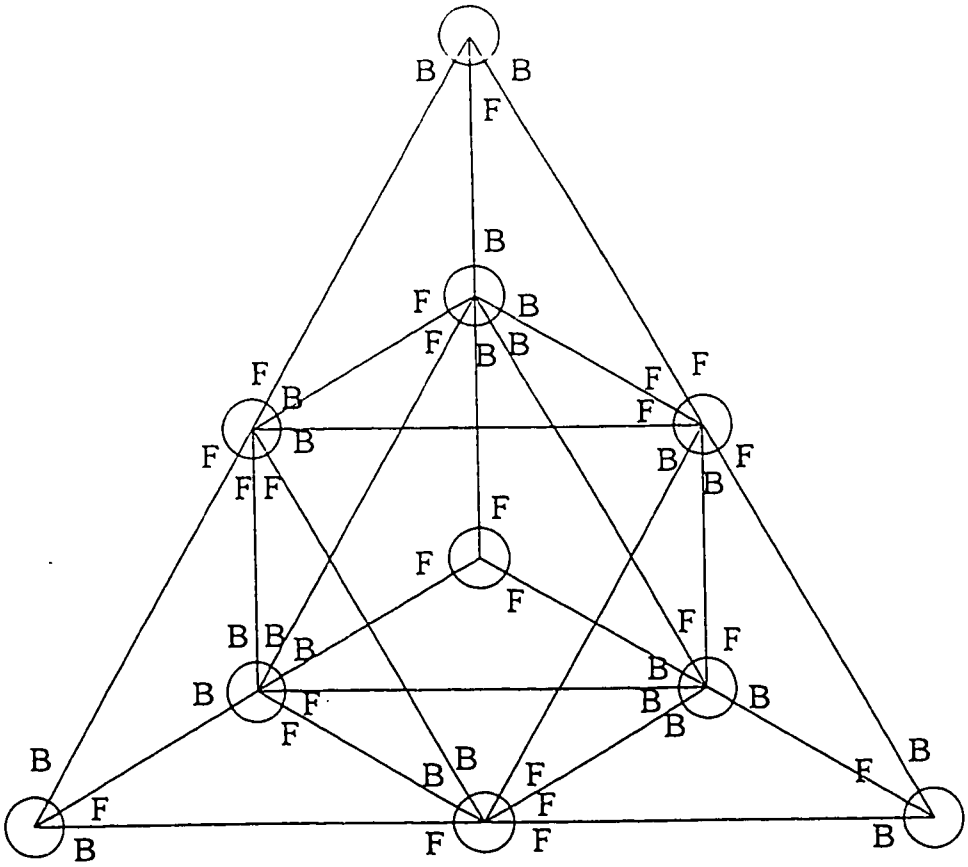

Figure IV.6.6. Cluster of 10 molecules in sc C_{60}. Line connects nearest neighbors. F and B represent face (hexagon or pentagon) and double bond, respectively. There are only 4 motifs for a pair of molecules (see the text).

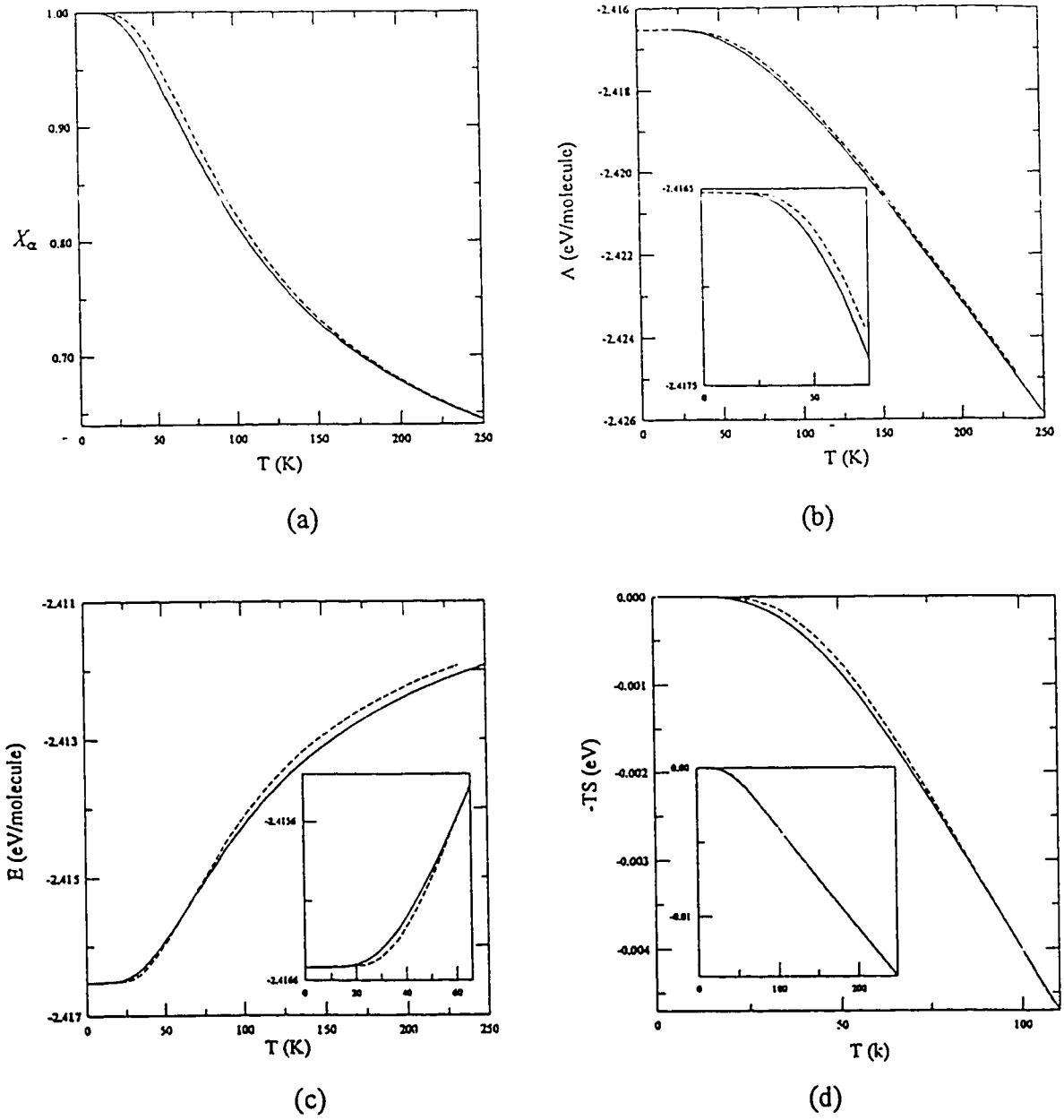

Figure IV.6.7. (a) The fraction of molecules at orientation α. (b) Helmholtz free energy of sc C_{60}. (c) The lattice energy. (d) The entropy term (-TS). Solid and dashed lines are for cluster variation and regular solution models, respectively.

IV.6.d) Orientational order-disorder transformation in C_{60}

It is assumed that in the high temperature form of C_{60} the interaction centers in a molecule are randomly distributed on a sphere of radius R (= 3.5485 Å) [22] and that the molecules are rotating freely. Thus the potential energy between two molecules at the distance r (figure IV.6.8) is given as

$$V_{fcc}(r) = \int_0^{\pi} \frac{60}{4\pi R^2} \int_0^{\pi} \frac{60}{4\pi R^2} v(s_2) 2\pi R \sin\theta_2 R d\theta_2 \, 2\pi R \sin\theta_1 R d\theta_1$$

$$= 60^2 \frac{\varepsilon}{rR^2} \left\{ \frac{\sigma^{12}}{90} \left[\frac{1}{(r+2R)^9} - \frac{2}{r^9} + \frac{1}{(r+2R)^9} \right] - \frac{\sigma^6}{12} \left[\frac{1}{(r+2R)^3} - \frac{2}{r^3} + \frac{1}{(r+2R)^3} \right] \right\} \qquad \text{(IV.6.15)}$$

where $v(s_2) = 4\varepsilon \left[\left(\frac{\sigma}{s_2} \right)^{12} - \left(\frac{\sigma}{s_2} \right)^{6} \right]$

$$s_2 = \sqrt{s_1^2 + R^2 - 2 s_1 R \cos\theta_2}$$

$$s_1 = \sqrt{r^2 + R^2 - 2 r R \cos\theta_1}$$

Using equation (IV.5.23) and (IV.5.27), the free energies of the high temperature (*fcc*) and low temperature (*sc*) forms are compared with each other in figure IV.6.9.

$$G_{fcc} = V_{fcc} - kT \ln \left[\frac{\sqrt{\pi}}{60} \left(\frac{8\pi^2 IkT}{h^2} \right)^{\frac{3}{2}} \right] \qquad \text{(IV.6.16)}$$

$$G_{sc} = V_{sc} + \frac{1}{4}\sum_{i}^{12}\left\{\frac{\hbar\omega_i}{2} + kT\ln\left[1 - \exp\left(-\frac{\hbar\omega_i}{kT}\right)\right]\right\} + kT\left[X_\alpha \ln X_\alpha + X_\beta \ln X_\beta\right]$$

(IV.6.17)

where V_{fcc} and V_{sc} are the cohesive energies computed from equations (IV.6.15) and (IV.6.3) with the parameters from set 4 in table IV.6.2. The ω_i's are the libron frequencies computed by a pseudo harmonic approximation (see section IV.7, Lattice dynamics of C_{60}). The difference in the translational vibrations between two phases is ignored. In the computation, X_α = 0.63 was used and the lattice parameters of *fcc* and *sc* phases were fixed to 14.16 and 14.10 Å, respectively. In this model the transition temperature is about 245 K which is close to the experimental results of 249 K [67,68] or 260 K [69].

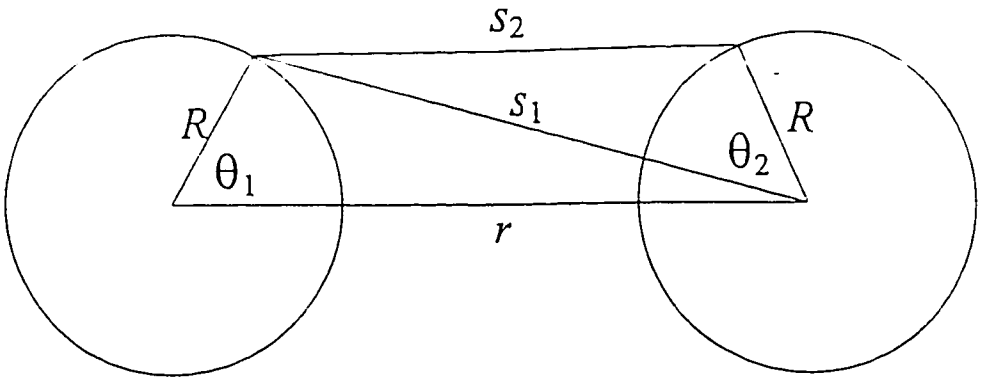

Figure IV.6.8. Fused interaction centers. See equation (IV.6.15).

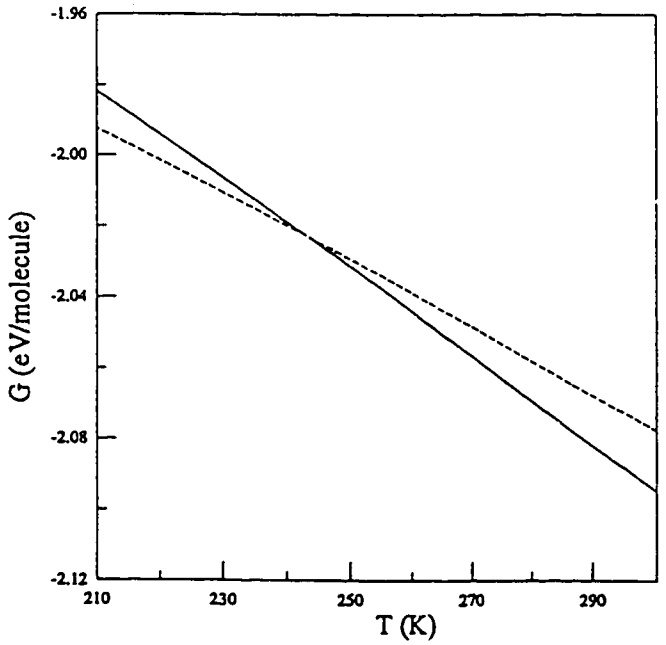

Figure IV.6.9. The free energy curves for *sc* (dashed line) and *fcc* (solid line) C_{60}, computed by equations (IV.6.16) and (IV.6.17).

IV.7) Lattice dynamics of C_{60}

IV.7.a) sc C_{60}

The dispersion curves of external modes of *sc* C_{60} were computed by the pseudo-harmonic approximation. All the molecules were assumed to be at the 22 degree orientation. The intermolecular interaction model with parameters of set 4 (table IV.6.2) was used and only the nearest neighbor interactions were considered. The dynamic matrix was computed by a Fortran program and the eigenvalues were obtained by Matlab.

Since the molecule is spherical top ($I_x = I_y = I_z = I$), the frame of reference is fixed to the lattice vectors and the mass-weighed or inertia-weighed displacements [26] are used instead of linear and angular displacements in equation (II.6.1 and 2).

$$t_\alpha^t(l\kappa) = \sqrt{m}u_\alpha^t(l\kappa) \qquad \text{(IV.7.1a)}$$

$$t_\alpha^r(l\kappa) = \sqrt{I}u_\alpha^r(l\kappa) \qquad \text{(IV.7.1b)}$$

where subscript α represents coordinates ($\alpha = x, y, z$) and superscript t and r denote linear and angular displacements, m is the mass of the molecule, l and κ (κ = 1 to 4) represent lth cell and κth molecule, respectively. Thus, equation (II.6.16) is rewritten as

$$\left|\mathbf{B}(\mathbf{q}) - \omega^2(\mathbf{q})\mathbf{I}\right| = 0 \qquad \text{(IV.7.2)}$$

where the element of 24×24 matrix $\mathbf{B}(\mathbf{q})$ is given as

$$B_{\alpha\beta}^{ii'}(\mathbf{q}, \kappa\kappa') = \sum_{l'} \phi_{\alpha\beta}^{ii'}(0\kappa; l\kappa') \exp[i\mathbf{q}\cdot\mathbf{X}(l')] \quad (i = r \text{ or } t \text{ and } \alpha,\beta = x, y \text{ or } z) \text{ (II.6.15)}$$

Since the mass-weighed or inertia-weighed displacements are chosen, the coupling coefficients (equation II.6.7) are modified as

$$\phi_{\alpha\beta}^{ii'}(l\kappa;l'\kappa') = \frac{\partial^2\Phi}{\partial t_\alpha^i \partial t_\beta^{i'}} \qquad \text{(IV.7.3)}$$

Thus, the coupling coefficients given in terms of the Born-von Karman constants by equations (II.6.31a to d) are also rewritten as

$$\phi_{\alpha\beta}^{\pi}(0\kappa;l'\kappa') = m\sum_{kk'}\phi_{\alpha\beta}(0\kappa k;l'\kappa'k') \qquad \text{(IV.7.4a)}$$

$$\phi_{\alpha\beta}^{\pi\sigma}(0\kappa;l'\kappa') = \sqrt{mI}\sum_{kk'}\sum_{\gamma\delta}\phi_{\alpha\gamma}(0\kappa k;l'\kappa'k')\varepsilon_{\gamma\beta\delta}X_\delta(k') \qquad \text{(IV.7.4b)}$$

$$\phi_{\alpha\beta}^{\sigma\pi}(0\kappa;l'\kappa') = \sqrt{mI}\sum_{kk'}\sum_{\mu\nu}\phi_{\mu\beta}(0\kappa k;l'\kappa'k')\varepsilon_{\mu\alpha\nu}X_\nu(k) \qquad \text{(IV.7.4c)}$$

$$\phi_{\alpha\beta}^{\sigma\sigma}(0\kappa;l'\kappa') = I\sum_{kk'}\sum_{\mu\nu}\sum_{\gamma\delta}\phi_{\mu\gamma}(0\kappa k;l'\kappa'k')\varepsilon_{\mu\alpha\nu}\varepsilon_{\gamma\beta\delta}X_\nu(k)X_\delta(k') \qquad \text{(IV.7.4d)}$$

where $\phi_{\alpha\beta}(0\kappa k;l'\kappa'k') = \dfrac{\partial^2\Phi}{\partial u_\alpha(0\kappa k)\partial u_\beta(l'\kappa'k')}$ (II.6.28)

$\varepsilon_{\alpha\beta\gamma}$ = 0 if any two of (α, β, γ) are equal

= 1 if (α, β, γ) corresponds to a cyclic order of (x,y,z)

= -1 if (α, β, γ) corresponds to a noncyclic order of (x,y,z)

k = Lennard-Jones and local charge interaction centers.

In pair-wise interactions the potential energy Φ is written as

$$\Phi = \frac{1}{2}\sum_{hh'}\sum_{\mu\mu'}\sum_{ss'}V\left(r\left(h\mu s;h'\mu's'\right)\right) \qquad \text{(IV.7.5)}$$

where h, μ and s represent the hth cell, μth molecule and sth interaction center, respectively and

$$r(h\mu s; h'\mu' s') = \left|\mathbf{X}(h\mu s) - \mathbf{X}(h'\mu' s')\right| \qquad \text{(IV.7.6)}$$

The potential between two interaction centers are given as

$$V\left(r(h\mu s; h'\mu' s')\right) = 4\varepsilon\left[\left(\frac{\sigma}{r(h\mu s; h'\mu' s')}\right)^{12} - \left(\frac{\sigma}{r(h\mu s; h'\mu' s')}\right)^{6}\right] \qquad \text{(LJ interaction)}$$

$$= \frac{q_s q_{s'}}{r(h\mu s; h'\mu' s')} \qquad \text{(Coulomb interaction)}$$

$$= 0 \qquad (h\mu = h'\mu') \qquad \text{(IV.7.7)}$$

The first derivative of the potential Φ with respect to the displacement is given as

$$\frac{\partial \Phi}{\partial u_\alpha(l\kappa k)} = \sum_{h\mu s} \frac{\partial V\left(r(l\kappa k; h\mu s)\right)}{\partial u_\alpha(l\kappa k)} \qquad \text{(IV.7.8)}$$

Thus the Born-von Karman constant is written as

(1) for $l\kappa k = l'\kappa' k'$

$$\frac{\partial^2 \Phi}{\partial u_\alpha(l\kappa k)\partial u_\beta(l\kappa k)} = \sum_{h\mu s} \frac{\partial^2 V\left(r(l\kappa k; h\mu s)\right)}{\partial u_\alpha(l\kappa k)\partial u_\beta(l\kappa k)} \qquad \text{(IV.7.9a)}$$

(2) for $l\kappa = l'\kappa'$ and $k \neq k'$

$$\frac{\partial^2 \Phi}{\partial u_\alpha(l\kappa k)\partial u_\beta(l\kappa k')} = 0 \qquad \text{(IV.7.9b)}$$

(3) for $l\kappa \neq l'\kappa'$

$$\frac{\partial^2 \Phi}{\partial u_\alpha(l\kappa k)\partial u_\beta(l'\kappa' k')} = \frac{\partial^2 V\left(r(l\kappa k; l'\kappa' k')\right)}{\partial u_\alpha(l\kappa k)\partial u_\beta(l'\kappa' k')} \qquad \text{(IV.7.9c)}$$

The second derivative of pair-wise interaction $V(r)$ with respect to displacements is given as

$$\frac{\partial^2 V\left(r\left(l\kappa k;h\mu s\right)\right)}{\partial^2 u_\alpha(l\kappa k)}=\left(\frac{\partial^2 V}{\partial r^2}\right)\left[\frac{X_\alpha(l\kappa k)-X_\alpha(h\mu s)}{r}\right]^2+\frac{\partial V}{\partial r}\left\{\frac{r^2-\left[X_\alpha(l\kappa k)-X_\alpha(h\mu s)\right]^2}{r^3}\right\} \tag{IV.7.10a}$$

$$\frac{\partial^2 V\left(r\left(l\kappa k;h\mu s\right)\right)}{\partial u_\alpha(l\kappa k)\partial u_\beta(l\kappa k)}=\left(\frac{\partial^2 V}{\partial r^2}\right)\frac{\left[X_\alpha(l\kappa k)-X_\alpha(h\mu s)\right]\left[X_\beta(l\kappa k)-X_\beta(h\mu s)\right]}{r^2}-\frac{\partial V}{\partial r}\frac{\left[X_\alpha(l\kappa k)-X_\alpha(h\mu s)\right]\left[X_\beta(l\kappa k)-X_\beta(h\mu s)\right]}{r^3} \tag{IV.7.10b}$$

$$\frac{\partial^2 V\left(r\left(l\kappa k;h\mu s\right)\right)}{\partial u_\alpha(l\kappa k)\partial u_\alpha(h\mu s)}=-\left(\frac{\partial^2 V}{\partial r^2}\right)\left[\frac{X_\alpha(l\kappa k)-X_\alpha(h\mu s)}{r}\right]^2-\frac{\partial V}{\partial r}\left\{\frac{r^2-\left[X_\alpha(l\kappa k)-X_\alpha(h\mu s)\right]^2}{r^3}\right\} \tag{IV.7.10c}$$

$$\frac{\partial^2 V\left(r\left(l\kappa k;h\mu s\right)\right)}{\partial u_\alpha(l\kappa k)\partial u_\beta(h\mu s)}=-\left(\frac{\partial^2 V}{\partial r^2}\right)\frac{\left[X_\alpha(l\kappa k)-X_\alpha(h\mu s)\right]\left[X_\beta(l\kappa k)-X_\beta(h\mu s)\right]}{r^2}+\frac{\partial V}{\partial r}\frac{\left[X_\alpha(l\kappa k)-X_\alpha(h\mu s)\right]\left[X_\beta(l\kappa k)-X_\beta(h\mu s)\right]}{r^3} \tag{IV.7.10d}$$

The resulting **B(q)** has the following scheme.

$$\mathbf{B}(\mathbf{q})=\begin{bmatrix}\mathbf{B}(\mathbf{q}|11) & \mathbf{B}(\mathbf{q}|12) & \mathbf{B}(\mathbf{q}|13) & \mathbf{B}(\mathbf{q}|14)\\ \mathbf{B}(\mathbf{q}|21) & \mathbf{B}(\mathbf{q}|22) & \mathbf{B}(\mathbf{q}|23) & \mathbf{B}(\mathbf{q}|24)\\ \mathbf{B}(\mathbf{q}|31) & \mathbf{B}(\mathbf{q}|32) & \mathbf{B}(\mathbf{q}|33) & \mathbf{B}(\mathbf{q}|34)\\ \mathbf{B}(\mathbf{q}|41) & \mathbf{B}(\mathbf{q}|42) & \mathbf{B}(\mathbf{q}|43) & \mathbf{B}(\mathbf{q}|44)\end{bmatrix} \tag{IV.7.11a}$$

$$\mathbf{B}(\mathbf{q}|\kappa\kappa') = \begin{bmatrix} B^{tt}_{xx}(q|\kappa\kappa') & B^{tt}_{xy}(q|\kappa\kappa') & B^{tt}_{xz}(q|\kappa\kappa') & \vdots & B^{tr}_{xx}(q|\kappa\kappa') & B^{tr}_{xy}(q|\kappa\kappa') & B^{tr}_{xz}(q|\kappa\kappa') \\ B^{tt}_{yx}(q|\kappa\kappa') & B^{tt}_{yy}(q|\kappa\kappa') & B^{tt}_{yz}(q|\kappa\kappa') & \vdots & B^{tr}_{yx}(q|\kappa\kappa') & B^{tr}_{yy}(q|\kappa\kappa') & B^{tr}_{yz}(q|\kappa\kappa') \\ B^{tt}_{zx}(q|\kappa\kappa') & B^{tt}_{zy}(q|\kappa\kappa') & B^{tt}_{zz}(q|\kappa\kappa') & \vdots & B^{tr}_{zx}(q|\kappa\kappa') & B^{tr}_{zy}(q|\kappa\kappa') & B^{tr}_{zz}(q|\kappa\kappa') \\ \cdots & \cdots & \cdots & & \cdots & \cdots & \cdots \\ B^{rt}_{xx}(q|\kappa\kappa') & B^{rt}_{xy}(q|\kappa\kappa') & B^{rt}_{xz}(q|\kappa\kappa') & \vdots & B^{rr}_{xx}(q|\kappa\kappa') & B^{rr}_{xy}(q|\kappa\kappa') & B^{rr}_{xz}(q|\kappa\kappa') \\ B^{rt}_{yx}(q|\kappa\kappa') & B^{rt}_{yy}(q|\kappa\kappa') & B^{rt}_{yz}(q|\kappa\kappa') & \vdots & B^{rr}_{yx}(q|\kappa\kappa') & B^{rr}_{yy}(q|\kappa\kappa') & B^{rr}_{yz}(q|\kappa\kappa') \\ B^{rt}_{zx}(q|\kappa\kappa') & B^{rt}_{zy}(q|\kappa\kappa') & B^{rt}_{zz}(q|\kappa\kappa') & \vdots & B^{rr}_{zx}(q|\kappa\kappa') & B^{rr}_{zy}(q|\kappa\kappa') & B^{rr}_{zz}(q|\kappa\kappa') \end{bmatrix} \quad \text{(IV.7.11b)}$$

where the element of the dynamic matrix is given by equation (II.6.15).

The mass- or inertia-weighed displacement vector is given as

$$\mathbf{t}(\mathbf{q}) = \begin{bmatrix} \mathbf{t}(\kappa = 1|\mathbf{q}) \\ \mathbf{t}(\kappa = 2|\mathbf{q}) \\ \mathbf{t}(\kappa = 3|\mathbf{q}) \\ \mathbf{t}(\kappa = 4|\mathbf{q}) \end{bmatrix} \quad \text{(IV.7.12a)}$$

$$\mathbf{t}(\kappa = \mu|\mathbf{q}) = \begin{bmatrix} t^t_x(\kappa = \mu|\mathbf{q}) \\ t^t_y(\kappa = \mu|\mathbf{q}) \\ t^t_z(\kappa = \mu|\mathbf{q}) \\ t^r_x(\kappa = \mu|\mathbf{q}) \\ t^r_y(\kappa = \mu|\mathbf{q}) \\ t^r_z(\kappa = \mu|\mathbf{q}) \end{bmatrix} \quad \text{(IV.7.12b)}$$

where the element is given by equation (IV.7.1).

The dynamic matrix is block-diagonalized by the symmetry-adapted vectors (equation II.6.59).

$$\mathbf{B}_\mathbf{D}(\mathbf{q}) = \xi^+(\mathbf{q})\mathbf{B}(\mathbf{q})\xi(\mathbf{q}) \quad \text{(II.6.61a)}$$

where subscript **D** represents a block-diagonal matrix and the symmetry-adapted vectors are obtained from section group theory of C_{60} (IV.8). The use of $\mathbf{B_D(q)}$ makes not only

the computation of eigenvalues easier but also the classification (labeling) of eigenvalues possible. The results of equation (IV.7.2) in which $\mathbf{B_D(q)}$ is replaced for $\mathbf{B(q)}$ are shown in figure IV.7.1 and table IV.7.1. In figure IV.7.1 two features should be noted. One is that two modes of the same symmetry cannot have dispersion curves that cross (anti-crossing). The other is that some wave vectors normal to the plane of the surface of the Brillouin zone have non-zero gradient of dispersion curves at the zone boundary. It is typical for non-symmorphic crystals that the frequencies of pairs of branches for some zone boundary wave vectors become degenerate, with the gradient of the upper branch equal to the negative of the gradient of the lower branch [115]. Experimental evidence of 3 phonon modes at 39, 40 and 54 cm^{-1} and 4 libron modes at 15, 19, 22 and 32 cm^{-1} was observed by an inelastic neutron scattering study [144] at 200 K. When we consider that the lattice parameter is about 14.08 Å at 200 K [69], the model seems to predict the phonon modes quite accurately. The large difference between the computed and reported libron frequencies may be due to the fact that the potential well is flattened from the parabolic form and that the vibrational amplitude is too large to apply the harmonic approximation (see section IV.7.c).

Table IV.7.1. External vibrational frequencies [cm^{-1}] of sc C_{60} at Γ ($\mathbf{q} = 0$).

a [Å]	14.05	14.06	14.07	14.08	14.09	14.10	200 K
A_u	42.07	41.35	40.63	39.93	39.23	38.55	39
E_u	44.18	43.42	42.67	41.93	41.21	40.49	
T_{u1}	0	0	0	0	0	0	0
T_{u2}	43.39	42.64	41.90	41.18	40.46	39.75	40
T_{u3}	59.86	58.78	57.72	56.67	55.63	54.61	54
A_g	17.94	17.50	17.06	16.63	16.21	15.78	19
E_g	19.42	18.97	18.52	18.08	17.65	17.21	
T_{g1}	14.26	13.89	13.51	13.14	12.77	12.39	16
T_{g2}	19.21	18.78	18.36	17.94	17.52	17.11	22
T_{g3}	26.17	25.68	25.19	24.71	24.24	23.77	32

* The first 5 rows with subscript **u** are phonons and the next 5 with **g** are librons. The degeneracies of A, E and T are 1, 2 and 3, respectively and **a** is the lattice parameter. The frequencies in the last column observed at 200 K [144] are arranged to compare with those computed and not necessarily belong to the labels in the first column.

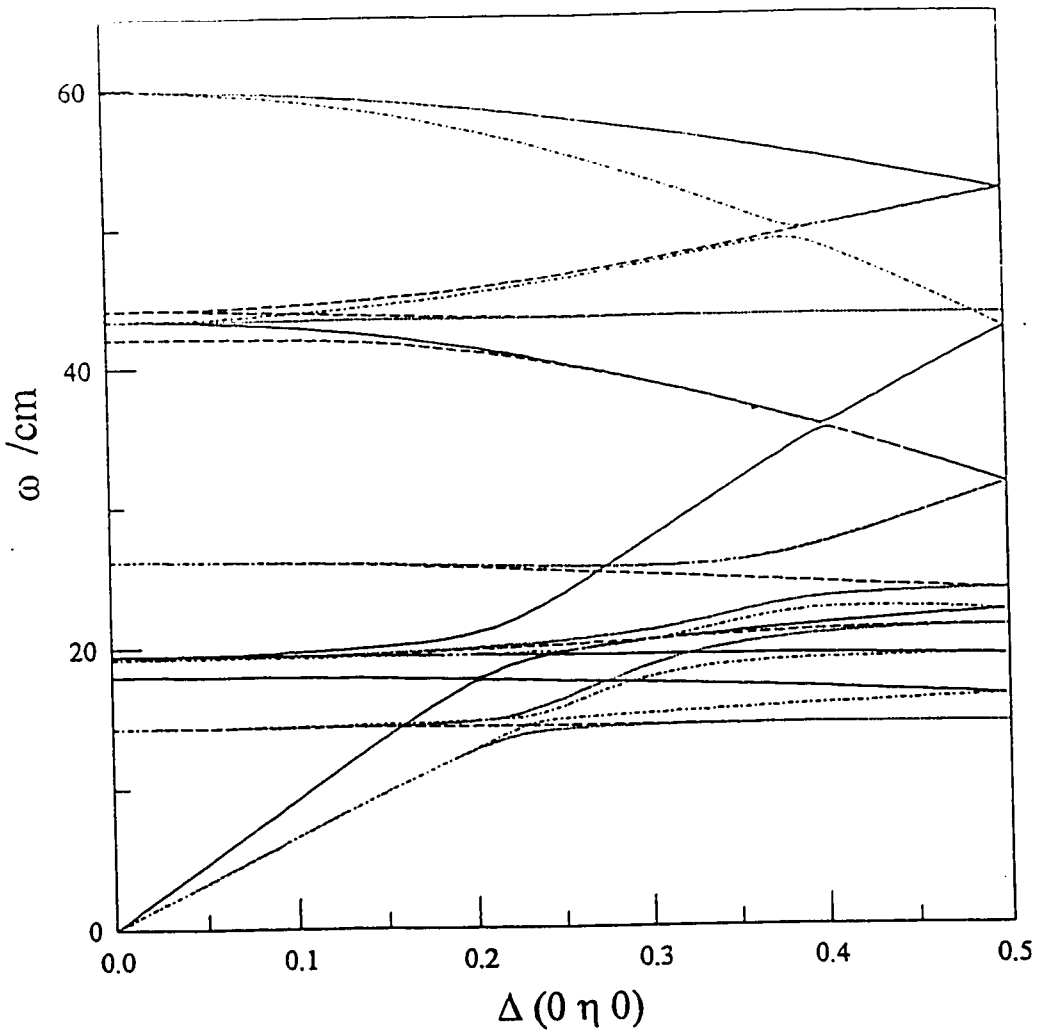

Figure IV.7.1. (a) Dispersion curves for sc C_{60}. $\mathbf{q} = \frac{2\pi}{a}(0 \quad \eta \quad 0)$. Solid, dashed, dotted and mixed lines are for A_1, A_2, B_1 and B_2, respectively.

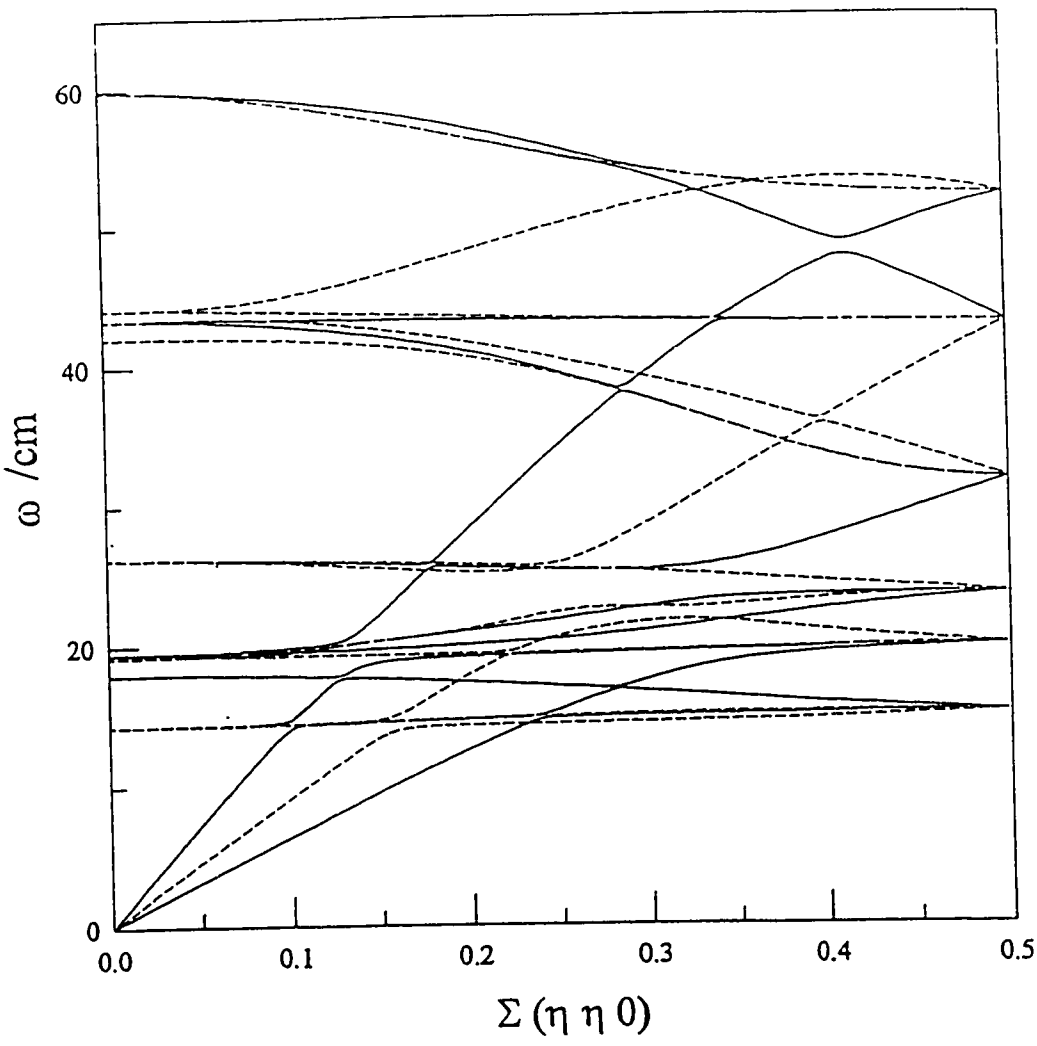

Figure IV.7.1. (b) Dispersion curves for sc C_{60}. $\mathbf{q} = \frac{2\pi}{a}(\eta \quad \eta \quad 0)$. Solid and dashed lines are for A′ and A″, respectively.

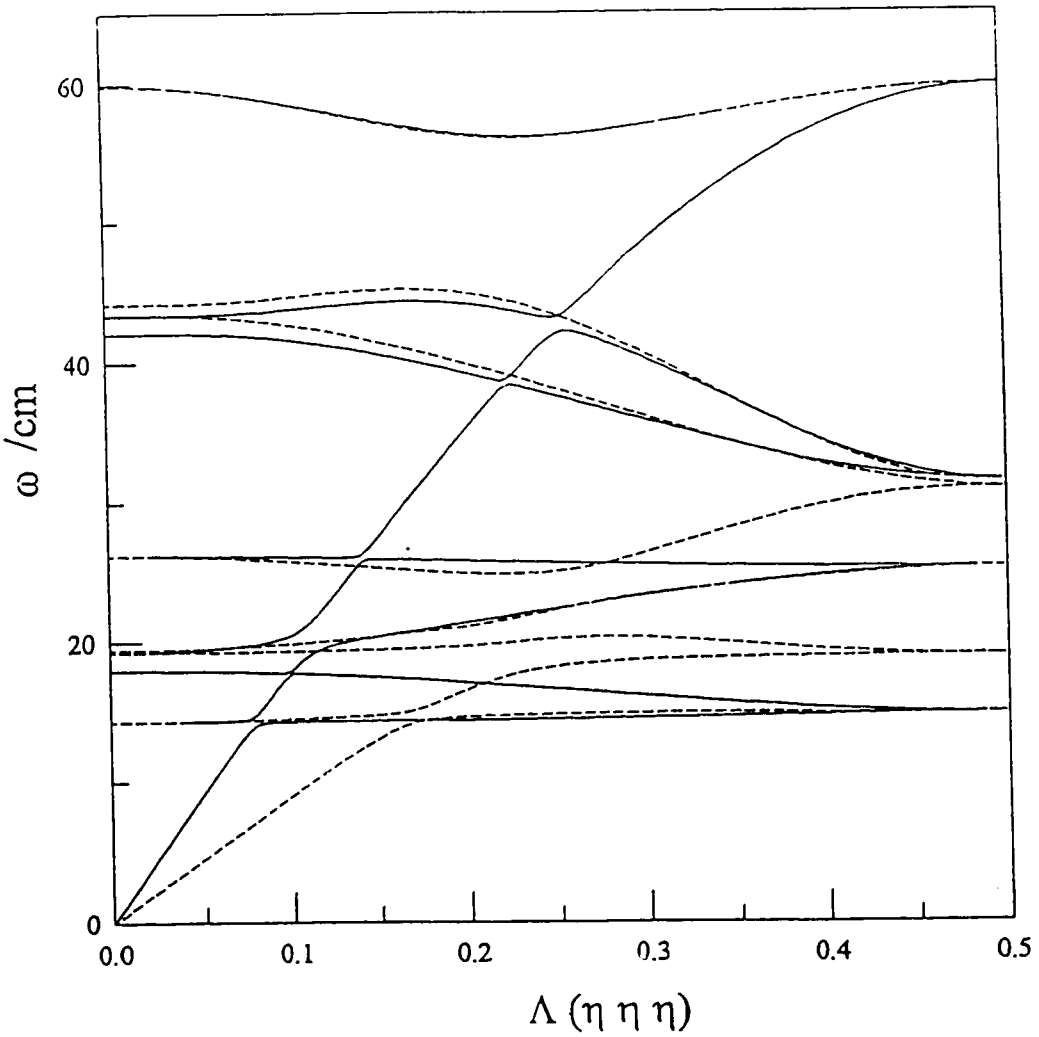

Figure IV.7.1. (c) Dispersion curves for sc C_{60}. $\mathbf{q} = \frac{2\pi}{a}(\eta \quad \eta \quad \eta)$. Solid and dashed lines are for A and E, respectively.

IV.7.b) M_3C_{60}

The external vibrational frequencies of M_3C_{60} (M = K, Rb) at Γ (**q** = (0 0 0)) were computed. The potential energy is assumed to be the sum of the LJ potential for C-C interactions and the Coulomb potential (CL) for M^{+1}-M^{+1}, C_{60}^{-3}- C_{60}^{-3} and M^{+1}-C_{60}^{-3} and the Born-Mayer-type repulsion (BM) for M^{+1}-M^{+1}, M^{+1}-$C_{60}^{-3/60}$. Thus, the Born-von Karman constants in equation (IV.7.4) are given as

$$\phi_{\alpha\beta}^{ii'} = \phi_{\alpha\beta}^{ii'}(\mathrm{LJ}) + \phi_{\alpha\beta}^{ii'}(\mathrm{CL}) + \phi_{\alpha\beta}^{ii'}(\mathrm{BM}) \qquad \text{(IV.7.13)}$$

(1) $\phi_{\alpha\beta}^{ii'}(\mathrm{LJ})$

This has been computed by the same model used for *sc* C_{60} (equation IV.7.5 and IV.7.7). The effects of net charge ($-\frac{3}{60}e$) to this type of interaction were ignored.

(2) $\phi_{\alpha\beta}^{ii'}(\mathrm{CL})$

Since the Coulomb interaction is long-range, it is not appropriate to approximate the potential by the sum of the nearest and second-nearest interactions. Ewald and Kellerman's formalism is employed as in equations (II.6.34) and (II.6.35).

(3) $\phi_{\alpha\beta}^{ii'}(\mathrm{BM})$

The Born-Mayer type repulsion [145] is given as

$$V_{rep}(r) = \lambda \exp\left(-\frac{r}{\rho}\right) \qquad \text{(IV.7.14)}$$

For ionic solids ρ is about 0.345 Å and λ has a form of

$$\lambda_{ij} = b\left(1 + \frac{Z_i}{n_i} + \frac{Z_j}{n_j}\right)\exp\left(\frac{r_i + r_j}{\rho}\right) \qquad \text{(IV.7.15)}$$

where Z_i is the valence and n_i is the number of the valence electrons and r_i is the radius of ion i. The parameters used for this calculation are given as

$\rho_{K\text{-}K}$ = 151 MJ/mol $\quad\quad$ $\lambda_{K\text{-}K}$ = 0.337 Å [146]

$\rho_{Rb\text{-}Rb}$ = 331.4 MJ/mol $\quad\quad$ $\lambda_{Rb\text{-}Rb}$ = 0.335 Å

$\rho_{K\text{-}C}$ = 293 MJ/mol $\quad\quad$ $\lambda_{K\text{-}C}$ = 0.27 Å [146]

$\rho_{Rb\text{-}C}$ = 426 MJ/mol $\quad\quad$ $\lambda_{Rb\text{-}C}$ = 0.27 Å

The parameters for M-C (M = K, Rb) were obtained by fitting the computed bulk modulus to the reported values [66].

The calculated frequencies are given in table IV.7.2. There are three K and one C_{60} in a unit cell. Each K contributes to the external modes three degrees of freedom and each C_{60} six degrees of freedom. Thus, there are 15 ($= 3 \times 3 + 6 \times 1$) vibrational modes.

Table IV.7.2. The frequencies computed at Γ

	K_3C_{60}	Rb_3C_{60}
Phonons	0	0
	26.3	31.7
	68.3	86.1
	77.5	90.6
Librons	26.1	34.1

*All of them have a degeneracy of three. The lattice parameters of 14.17 and 14.30 Å were used for K and Rb fullerides, respectively.

IV.7.c) Quantum mechanical consideration of angular vibration of *sc* C_{60}

The angular vibration of a molecule at the origin about the [1 1 1] axis (figure II.3.3) has been studied in sc C_{60}. The 12 nearest molecules are assumed to be fixed at orientation α (γ = 22 degrees). Only nearest neighbor interactions are considered.

The Schrödinger equation is given as

$$-\frac{\hbar^2}{2I}\psi'' + V(\theta)\psi = \varepsilon\psi \qquad \text{(IV.7.16)}$$

where I is the moment of inertia of the molecule. Using equation (IV.6.3), the potential energy of the molecule at the origin is computed as a function of rotation θ with the set A parameters in table IV.6.2 (figure IV.6.4.b). The computed potential energy is approximated by a Fourier series of

$$V(\theta) = \sum_G U_G e^{iG\theta} \qquad \text{(IV.7.17)}$$

where $G = 3m$ (m = integer) since the periodicity of the potential is $\frac{2\pi}{3}$. The coefficients U_G ($-12 < m < 12$) are determined by least-squares fitting.

Harmonic approximation

The potential energy in equation IV.7.17 is rewritten as

$$V(\theta) = V(\theta_\bullet) + V'(\theta_\bullet)\Delta\theta + \frac{1}{2}V''(\theta_\bullet)\Delta\theta^2 \qquad \text{(IV.7.18)}$$

where $\theta_\bullet$ is 22 degrees, the second term on the right side is zero and in the third term $V''(\theta) = \sum_G -G^2 U_G e^{iG\theta}$. The solution of equation (IV.7.16) is

$$\varepsilon_n = \hbar\omega\left(n+\tfrac{1}{2}\right) \qquad \text{(IV.7.19)}$$

$$\omega = \sqrt{\frac{V''(\theta_o)}{I}} \qquad \text{(IV.7.20)}$$

Thus, the vibrational frequency is 12.2 cm^{-1}.

Central equation

The wavefunction may be expressed as a Fourier series summed over all values of the wavevector permitted by the boundary conditions [147].

$$\psi = \sum_k C_k e^{ik\theta} \qquad \text{(IV.7.21)}$$

Using the boundary condition of $\psi(\theta) = \psi(\theta + 2\pi)$, we obtain k = an integer. Thus, substituting equations (IV.7.17) and (IV.7.21) into equation (IV.7.16) results in

$$\left(\frac{\hbar^2 n^2}{2I} - \varepsilon\right) C_n + \sum_m U_{3m} C_{n-3m} = 0 \qquad (-12 < m < 12 \text{ and } n = \text{any integer}) \qquad \text{(IV.7.22)}$$

which is called the central equation. Equation (IV.7.22) forms an infinite matrix, a portion of which is given as

$$\begin{matrix}
\cdots & 0 & 0 & U_{-36} & U_{-33} & \cdots & U_{-3} & \frac{\hbar^2(n-3)^2}{2I}-\varepsilon & U_3 & \cdots & U_{33} & U_{36} & 0 & 0 & 0 & 0 & \cdots \\
\cdots & 0 & 0 & 0 & U_{-36} & U_{-33} & \cdots & U_{-3} & \frac{\hbar^2 n^2}{2I}-\varepsilon & U_3 & \cdots & U_{33} & U_{36} & 0 & 0 & 0 & \cdots \\
\cdots & 0 & 0 & 0 & 0 & U_{-36} & U_{-33} & \cdots & U_{-3} & \frac{\hbar^2(n+3)^2}{2I}-\varepsilon & U_3 & \cdots & U_{33} & U_{36} & 0 & 0 & \cdots
\end{matrix}$$

It is sufficient to set equal to zero the determinant of a portion of the matrix (400×400). We obtain 400 eigenvalues ε and 400 corresponding eigenvectors $\{C_i\}$ from equation (IV.7.22). The first ten energy levels and their probability densities for k (= n) = 0 are

shown in figure IV.7.2. The energy difference between successive levels is about 2.7 meV which corresponds to a vibrational frequency of 21.7 cm^{-1} since $\frac{1}{\lambda} = \frac{\Delta\varepsilon}{hc}$ (c = the velocity of light).

The vibrational frequency computed by the central equation is 1.8 times that computed by the harmonic approximation, which suggests that the harmonic approximation is not sufficiently rigorous for angular vibrations. The failure of the harmonic approximation is due to the fact that the potential well around $\theta = 22$ degrees is flattened from the parabolic form and that the amplitude of the vibration is somewhat large (about 7 degrees for the 9th level, see figure IV.7.2).

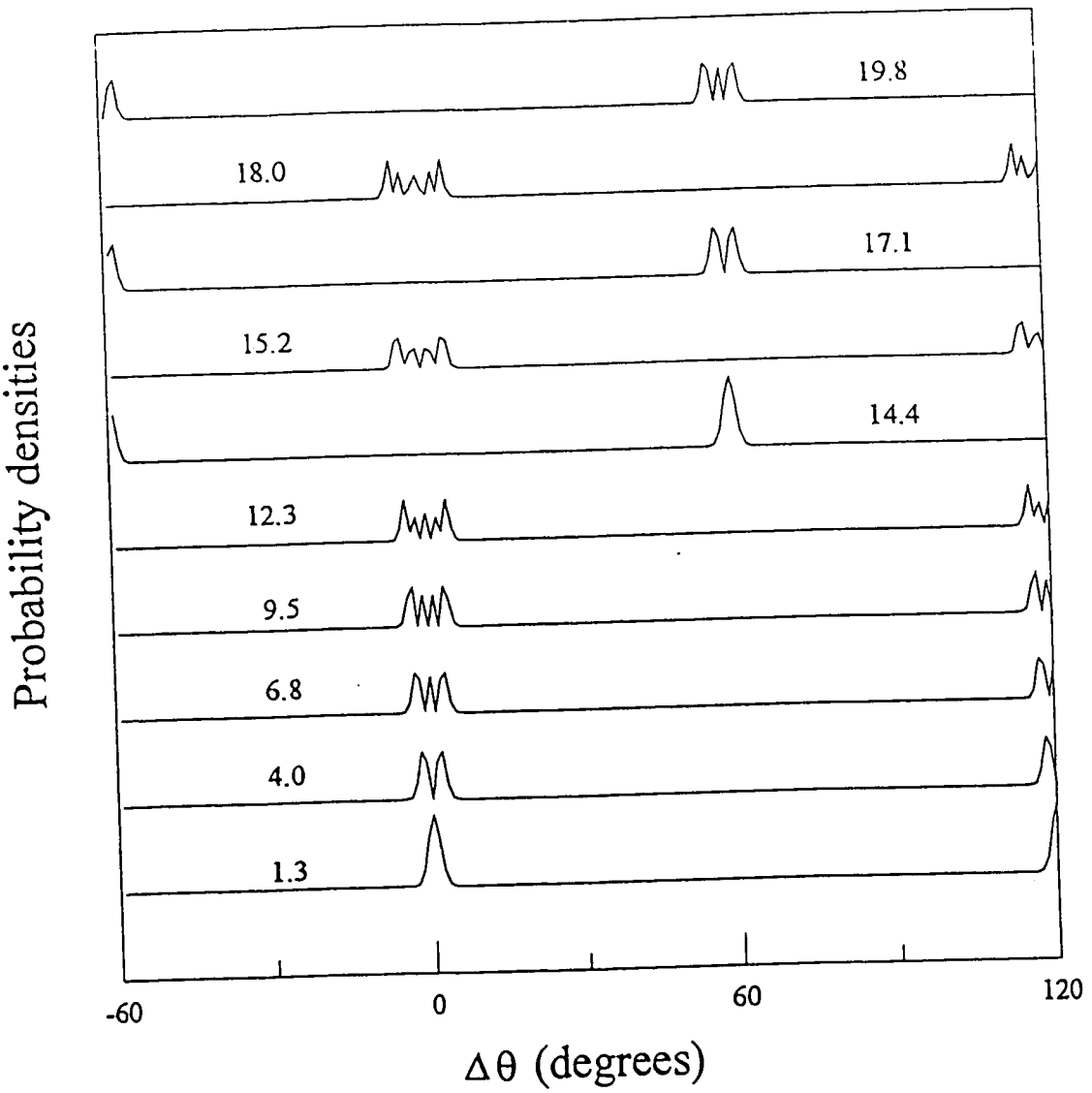

Figure IV.7.2. The probability densities of the first 10 energy levels for angular vibrations about [1 1 1] axis. The energy of each level is in meV from the ground state.

IV.8) Group theory of C_{60}

Group theory was applied to the eigenvalue problem (equation IV.7.2). The symmetry-adapted vectors for Γ, Δ, Λ and Σ were obtained and the external vibrational modes of *sc* C_{60} were labeled. The dispersion curves, given in figure IV.7.1, were used for thermodynamic calculations in section IV.9.

The procedure to obtain the symmetry-adapted vectors which will block-diagonalize the dynamic matrix (equation II.6.61a) is

(1) to determine $G_0(\mathbf{q})$, the point group of the wave vector **q** by the equation

$$\mathbf{Rq} = \mathbf{q} + \mathbf{G}, \tag{II.6.48}$$

(2) to construct a unitary matrix **T(q;R)** associated with each element **R** of the point group $G_0(\mathbf{q})$ (equation II.6.51)

$$\mathbf{T}(\mathbf{q};\mathbf{R}) = \exp\left[i\mathbf{q}\cdot(\mathbf{V}(R) + \mathbf{X}(m)\right]\Gamma(\mathbf{q};R_m) \tag{II.6.51a}$$

where $T_{\alpha\beta}(\kappa\kappa'|\mathbf{q};\mathbf{R}) = R_{\alpha\beta}\delta(\kappa, F_0(\kappa';R))\exp\left[i\mathbf{q}\cdot(\mathbf{X}(\kappa) - \mathbf{RX}(\kappa')\right]$, (II.6.51b)

(3) to obtain c_s by equation (II.6.55)

$$c_s = \frac{1}{h}\sum_{\mathbf{R}\in G_0(\mathbf{q})}\chi(\mathbf{q};\mathbf{R})\chi^{(s)}(\mathbf{q};\mathbf{R})^*, \tag{II.6.55}$$

(4) to project out symmetry-adapted vectors using the projection operators (equation II.6.57 and 58)

$$P^{(s)}_{\lambda\lambda}(\mathbf{q}) = \frac{f_s}{h}\sum_{\mathbf{R}\in G_0(\mathbf{q})}\tau^{(s)}_{\lambda\lambda}(\mathbf{q};\mathbf{R})^*\mathbf{T}(\mathbf{q};\mathbf{R}) \tag{II.6.57}$$

$$P_{\mu\lambda}^{(s)}(\mathbf{q}) = \frac{f_s}{h} \sum_{\mathbf{R} \in G_0(\mathbf{q})} \tau_{\mu\lambda}^{(s)}(\mathbf{q};\mathbf{R})^* \mathbf{T}(\mathbf{q};\mathbf{R}) \qquad (\mu = 1 \text{ to } f_s,\ \mu \neq \lambda), \qquad \text{(II.6.58)}$$

(5) and finally, to block-diagonalize the dynamic matrix (equation II.6.61a).

$$\mathbf{B}_D(\mathbf{q}) = \xi^+(\mathbf{q})\mathbf{B}(\mathbf{q})\xi(\mathbf{q}) \qquad \text{(II.6.61a)}$$

The dispersion curves are shown in figure IV.7.1.

The symmetry elements of $Pa\bar{3}$ [132], the low-temperature form of C_{60}, are given by equation (IV.6.1). If we take as the invariant subgroup $\mathscr{S}$ the set of the infinite number of translational elements, then for nonsymmorphic crystal $Pa\bar{3}$, the factor group is isomorphic with the point group T_h (see equation II.6.54). The character table of T_h is given in table IV.8.1.

Table IV.8.1. The character table for T_h [117].

	E	C_3	C_3^2	C_2	I	IC_3	IC_3^2	IC_2
A_g	1	1	1	1	1	1	1	1
E_g	1	ϕ	ϕ^2	1	1	ϕ	ϕ^2	1
	1	ϕ^2	ϕ	1	1	ϕ^2	ϕ	1
T_g	3	0	0	-1	3	0	0	-1
A_u	1	1	1	1	-1	-1	-1	-1
E_u	1	ϕ	ϕ^2	1	-1	$-\phi$	$-\phi^2$	-1
	1	ϕ^2	ϕ	1	-1	$-\phi^2$	$-\phi$	-1
T_u	3	0	0	-1	-3	0	0	1

$\phi = \exp(2\pi i/3)$

IV.3.a) $\Gamma\left[\mathbf{q}=\frac{2\pi}{a}(0\quad 0\quad 0)\right]$

Since **q** = **0**, every rotational part **R** of space group $Pa\bar{3}$ satisfies the equation (II.6.48). Thus, the point group of the wave vector **q** = **0** is T_h and the character table is given in table IV.8.1. The unitary matrices $T(\mathbf{0};R)$ are given in Appendix C.

Using equation (II.6.55), we have

$$c_{Ag}=1 \qquad c_{Eg}=1 \qquad c_{Tg}=3$$

$$c_{Au}=1 \qquad c_{Eu}=1 \qquad c_{Tu}=3 \qquad \text{(IV.8.1)}$$

Thus

$$\Gamma = A_g + E_g + 3T_g + A_u + E_u + 3T_u \qquad \text{(IV.8.2)}$$

Among them one of the T_u corresponds to the acoustic modes. The other two T_u are IR active and all of A_g, E_g and T_g modes are Raman active [148].

Using equations (II.6.57 and 58), the projection operator $P^{(s)}$ is constructed and applying this operator on 24 orthogonal vectors, c_s times f_s independent vectors are projected out. The 12 symmetric modes with respect to I have the following symmetry-adapted vectors.

$$\left\langle A_g\right| = \frac{1}{\sqrt{12}}\langle \quad 0 \quad 1\ 1\ 1 \quad 0 \quad \bar{1}\ \bar{1}\ 1 \quad 0 \quad \bar{1}\ 1\ \bar{1} \quad 0 \quad 1\ \bar{1}\ \bar{1}\right|$$

$$\left\langle E_g^{\,1}\right| = \frac{1}{\sqrt{12}}\langle \quad 0 \quad 1\ \varepsilon\ \varepsilon^* \quad 0 \quad \bar{1}\ \bar{\varepsilon}\ \varepsilon^* \quad 0 \quad \bar{1}\ \varepsilon\ \bar{\varepsilon}^* \quad 0 \quad 1\ \bar{\varepsilon}\ \bar{\varepsilon}^*\right|$$

$$\left\langle E_g^{\,2}\right| = \frac{1}{\sqrt{12}}\langle \quad 0 \quad 1\ \varepsilon^*\ \varepsilon \quad 0 \quad \bar{1}\ \bar{\varepsilon}^*\ \varepsilon \quad 0 \quad \bar{1}\ \varepsilon^*\ \bar{\varepsilon} \quad 0 \quad 1\ \bar{\varepsilon}^*\ \bar{\varepsilon}\right|$$

$$\left\langle T_g^{\,1}\right|_1 = \frac{1}{\sqrt{4}}\langle \quad 0 \quad 1\ 0\ 0 \quad 0 \quad \bar{1}\ 0\ 0 \quad 0 \quad \bar{1}\ 0\ 0 \quad 0 \quad 1\ 0\ 0\right|$$

$$\langle T_g^{\,2}|_1 = \frac{1}{\sqrt{4}}\langle \; \mathbf{0} \quad 0\ 1\ 0 \quad \mathbf{0} \quad 0\ 1\ 0 \quad \mathbf{0} \quad 0\ \bar{1}\ 0 \quad \mathbf{0} \quad 0\ \bar{1}\ 0|$$

$$\langle T_g^{\,3}|_1 = \frac{1}{\sqrt{4}}\langle \; \mathbf{0} \quad 0\ 0\ 1 \quad \mathbf{0} \quad 0\ 0\ 1 \quad \mathbf{0} \quad 0\ 0\ 1 \quad \mathbf{0} \quad 0\ 0\ 1|$$

$$\langle T_g^{\,1}|_2 = \frac{1}{\sqrt{4}}\langle \; \mathbf{0} \quad 0\ 1\ 0 \quad \mathbf{0} \quad 0\ \bar{1}\ 0 \quad \mathbf{0} \quad 0\ 1\ 0 \quad \mathbf{0} \quad 0\ \bar{1}\ 0|$$

$$\langle T_g^{\,2}|_2 = \frac{1}{\sqrt{4}}\langle \; \mathbf{0} \quad 0\ 0\ 1 \quad \mathbf{0} \quad 0\ 0\ \bar{1} \quad \mathbf{0} \quad 0\ 0\ \bar{1} \quad \mathbf{0} \quad 0\ 0\ 1|$$

$$\langle T_g^{\,3}|_2 = \frac{1}{\sqrt{4}}\langle \; \mathbf{0} \quad 1\ 0\ 0 \quad \mathbf{0} \quad 1\ 0\ 0 \quad \mathbf{0} \quad 1\ 0\ 0 \quad \mathbf{0} \quad 1\ 0\ 0|$$

$$\langle T_g^{\,1}|_3 = \frac{1}{\sqrt{4}}\langle \; \mathbf{0} \quad 0\ 0\ 1 \quad \mathbf{0} \quad 0\ 0\ 1 \quad \mathbf{0} \quad 0\ 0\ \bar{1} \quad \mathbf{0} \quad 0\ 0\ \bar{1}|$$

$$\langle T_g^{\,2}|_3 = \frac{1}{\sqrt{4}}\langle \; \mathbf{0} \quad 1\ 0\ 0 \quad \mathbf{0} \quad \bar{1}\ 0\ 0 \quad \mathbf{0} \quad 1\ 0\ 0 \quad \mathbf{0} \quad \bar{1}\ 0\ 0|$$

$$\langle T_g^{\,3}|_3 = \frac{1}{\sqrt{4}}\langle \; \mathbf{0} \quad 0\ 1\ 0 \quad \mathbf{0} \quad 0\ 1\ 0 \quad \mathbf{0} \quad 0\ 1\ 0 \quad \mathbf{0} \quad 0\ 1\ 0|$$

(IV.8.3)

where **0** = (0 0 0) and the coordinates of the symmetry-adapted vectors are

$$\langle u^t(\kappa=1) \quad u^r(\kappa=1) \quad u^t(\kappa=2) \quad u^r(\kappa=2) \quad u^t(\kappa=3) \quad u^r(\kappa=3) \quad u^t(\kappa=4) \quad u^r(\kappa=4)|$$

(IV.8.4)

The 12 antisymmetric modes with respect to I have symmetry-adapted vectors which are the same as those for symmetric modes except that the vectors for linear displacements and angular displacements are switched. For example,

$$\langle A_u| = \frac{1}{\sqrt{12}}\langle 1 \ 1 \ 1 \quad \mathbf{0} \quad \bar{1} \ \bar{1} \ 1 \quad \mathbf{0} \quad \bar{1} \ 1 \ \bar{1} \quad \mathbf{0} \quad 1 \ \bar{1} \ \bar{1} \quad \mathbf{0} \ |$$

(IV.8.5)

Thus we obtain the matrix ξ of symmetry-adapted vectors in equation (II.6.58) given as

$$\xi = [\langle A_g|;\langle E_g^{\,1}|;\langle E_g^{\,2}|;\langle T_g^{\,1}|_1;\langle T_g^{\,2}|_1;\langle T_g^{\,3}|_1;\langle T_g^{\,1}|_2;\langle T_g^{\,2}|_2;\langle T_g^{\,3}|_2;\langle T_g^{\,1}|_3;\langle T_g^{\,2}|_3;\langle T_g^{\,3}|_3;$$
$$\langle A_u|;\langle E_u^{\,1}|;\langle E_u^{\,2}|;\langle T_u^{\,1}|_1;\langle T_u^{\,2}|_1;\langle T_u^{\,3}|_1;\langle T_u^{\,1}|_2;\langle T_u^{\,2}|_2;\langle T_u^{\,3}|_2;\langle T_u^{\,1}|_3;\langle T_u^{\,2}|_3;\langle T_u^{\,3}|_3;]^t$$

(IV.8.6)

where semicolon and superscript t represent the end of rows and the transpose of the matrix, respectively.

Finally, we can block-diagonalize **B(q)** by equation (II.6.61a)

$$\mathbf{B_D(q)} = \xi^{+}(\mathbf{q})\mathbf{B(q)}\xi(\mathbf{q}) \qquad \text{(II.6.61a)}$$

The block-diagonalized form is

$$\mathbf{B_D} = \begin{bmatrix} \mathbf{A_g} & & & & & & & & & & & \\ & \mathbf{E_g^{\,1}} & & & & & & & & & & \\ & & \mathbf{E_g^{\,2}} & & & & & & & & & \\ & & & \mathbf{T_{g1}} & & & & & & & & \\ & & & & \mathbf{T_{g2}} & & & & & & & \\ & & & & & \mathbf{T_{g3}} & & & & & & \\ & & & & & & \mathbf{A_u} & & & & & \\ & & & & & & & \mathbf{E_u^{\,1}} & & & & \\ & & & & & & & & \mathbf{E_u^{\,2}} & & & \\ & & & & & & & & & \mathbf{T_{u1}} & & \\ & & & & & & & & & & \mathbf{T_{u2}} & \\ & & & & & & & & & & & \mathbf{T_{u3}} \end{bmatrix}$$

(IV.8.7)

where **A**'s and **E**'s are one by one matrices and **T**'s are three by three matrices and off-diagonal elements are zero.

IV.8.b) $\Delta\left[\mathbf{q}=\frac{2\pi}{a}(0 \quad \eta \quad 0)\right]$

From equation (II.6.48) the point group of the wave vector **q** is determined as $C_{2v}(y)$. The character table is given in table IV.8.2. The exponent term in equation (II.6.51b) is given in table IV.8.3. The method to obtain unitary matrices is the same as for **q** = **0** except it is necessary to multiply by the factors in table IV.8.3.

$c_{A1} = c_{A2} = c_{B1} = c_{B2} = 6$ (IV.8.8)

$$\langle A_1| = \frac{1}{2}\begin{vmatrix} 1 & \bar{\mu} & 1 & \bar{\mu} \\ 1 & \mu & 1 & \mu \\ 1 & \mu & \bar{1} & \bar{\mu} \\ 1 & \mu & \bar{1} & \bar{\mu} \\ 1 & \bar{\mu} & \bar{1} & \mu \\ 1 & \bar{\mu} & 1 & \bar{\mu} \end{vmatrix}$$

$$\langle A_2| = \frac{1}{2}\begin{vmatrix} 1 & \mu & \bar{1} & \bar{\mu} \\ 1 & \bar{\mu} & \bar{1} & \mu \\ 1 & \bar{\mu} & 1 & \bar{\mu} \\ 1 & \bar{\mu} & 1 & \bar{\mu} \\ 1 & \mu & 1 & \mu \\ 1 & \mu & \bar{1} & \bar{\mu} \end{vmatrix}$$

$$\langle B_1| = \frac{1}{2}\begin{vmatrix} 1 & \bar{\mu} & \bar{1} & \mu \\ 1 & \mu & \bar{1} & \bar{\mu} \\ 1 & \mu & 1 & \mu \\ 1 & \mu & 1 & \mu \\ 1 & \bar{\mu} & 1 & \bar{\mu} \\ 1 & \bar{\mu} & \bar{1} & \mu \end{vmatrix}$$

$$\langle B_2| = \frac{1}{2}\begin{vmatrix} 1 & & & \mu & & & 1 & & & \mu & \\ & 1 & & & \bar{\mu} & & & 1 & & & \bar{\mu} \\ & & 1 & & & \bar{\mu} & & & \bar{1} & & & \mu \\ & & & 1 & & & \bar{\mu} & & & \bar{1} & & & \mu \\ & & & & 1 & & & \mu & & & \bar{1} & & & \bar{\mu} \\ & & & & & 1 & & & \mu & & & 1 & & & \mu \end{vmatrix}$$

(IV.8.9)

where only non-zero elements are shown.

$$\xi = \begin{bmatrix} \langle A_1| \\ \langle A_2| \\ \langle B_1| \\ \langle B_2| \end{bmatrix}^t \qquad \text{(IV.8.10)}$$

$$\mathbf{B_D} = \begin{bmatrix} \mathbf{A_1} & & & \\ & \mathbf{A_2} & & \\ & & \mathbf{B_1} & \\ & & & \mathbf{B_2} \end{bmatrix} \qquad \text{(IV.8.11)}$$

where $\mathbf{A_i}$ and $\mathbf{B_i}$ are 6 by 6 matrices.

Table IV.8.2. The character table of $C_{2v}(y)$ [117].

	E	C_{2y}	$\sigma_z (= IC_{2z})$	$\sigma_x (= IC_{2x})$
A_1	1	1	1	1
A_2	1	1	-1	-1
B_1	1	-1	-1	1
B_2	1	-1	1	-1

Table IV.8.3. The exponent term in equation (II.6.51b).

	$\kappa' = 1$	2	3	4
$\kappa = 1$	1	μ^*	1	μ^*
2	μ	1	μ	1
3	1	μ^*	1	μ^*
4	μ	1	μ	1

*$\mu = \exp(i\pi\eta)$

IV.8.c) $\Sigma\left[\mathbf{q} = \frac{2\pi}{a}(\eta \quad \eta \quad 0)\right]$

The point group of the wave vector **q** is $c_s(z)$. The character table is given in table IV.8.4. The exponent term in equation (II.6.51b) is given in table IV.8.5.

$c_{A'} = c_{A''} = 12$ (IV.8.12)

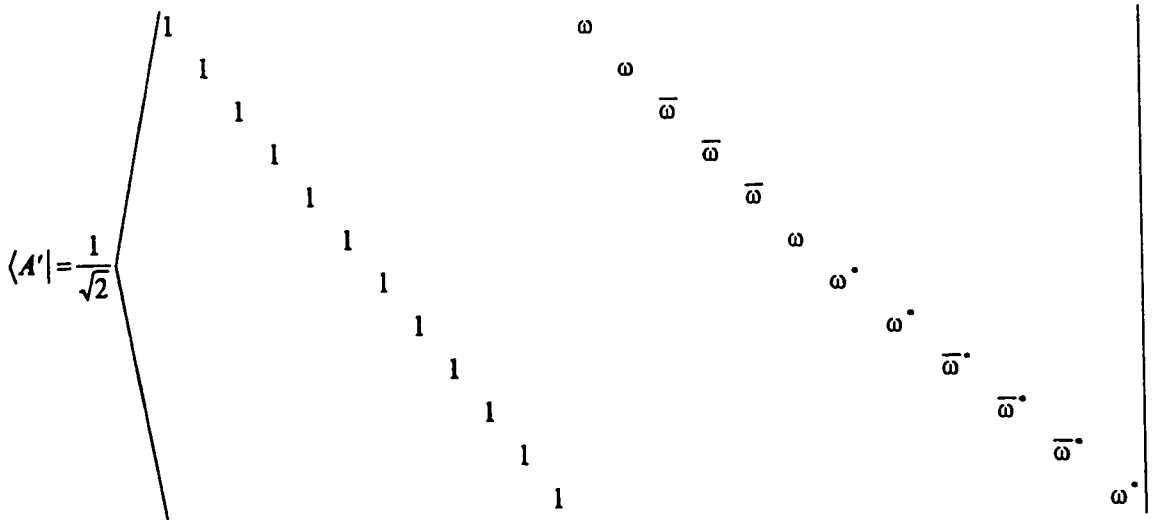

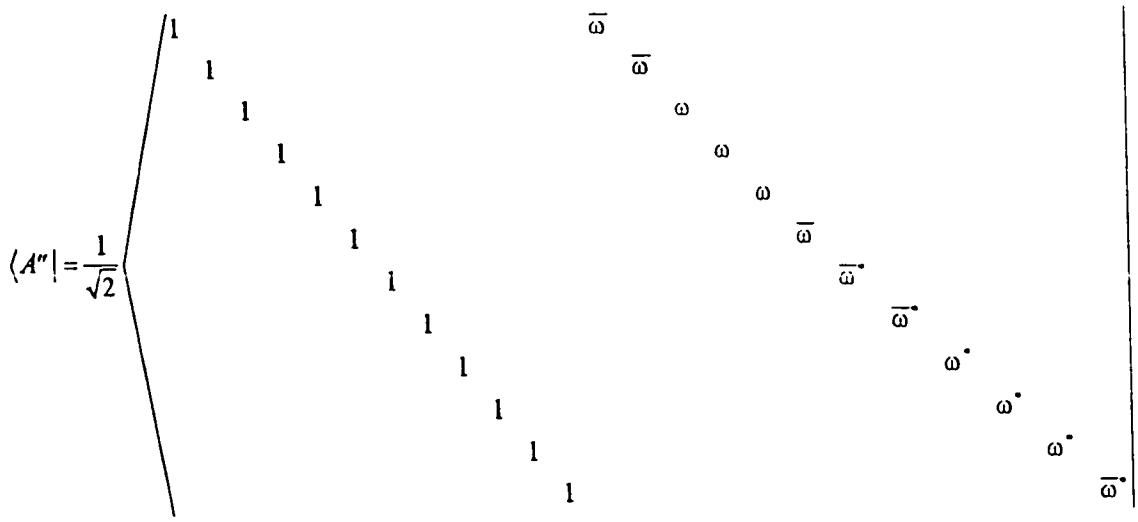

$$\langle A''| = \frac{1}{\sqrt{2}}$$

(IV.8.13)

where only non-zero elements are shown.

$$\xi = \begin{bmatrix} \langle A'| \\ \langle A''| \end{bmatrix}^t \tag{IV.8.14}$$

$$\mathbf{B_D} = \begin{bmatrix} \mathbf{A'} & \\ & \mathbf{A''} \end{bmatrix} \tag{IV.8.15}$$

where $\mathbf{A_i}$ is 12 by 12 matrix.

Table IV.8.4. The character table of $c_s(z)$ [117].

	E	$\sigma_z\ (= IC_{2z})$
A′	1	1
A″	1	-1

Table IV.8.5. The exponent term.

	$\kappa' = 1$	2	3	4
$\kappa = 1$	1	ν^*	ω^*	ω^*
2	ν	1	ω	ω
3	ω	ω^*	1	1
4	ω	ω^*	1	1

*$\nu = \exp(i2\pi\eta)$ and $\omega = \exp(i\pi\eta)$

IV.8.d) $\Lambda\left[\mathbf{q} = \frac{2\pi}{a}(\eta \quad \eta \quad \eta)\right]$

The point group of the wave vector **q** is c_3. The character table is given in table IV.8.6. The exponent term in equation (II.6.51b) is given in table IV.8.7.

$c_A = c_E = 8$ (V.8.16)

$\langle A| = \frac{1}{\sqrt{3}}$

1	1	1						
			1	1	1			
						1		
							1	
								1
								1
							1	
						1		
					1			

$\langle E^1| = \frac{1}{\sqrt{3}}$

1	ϕ	ϕ^*						
			1	ϕ	ϕ^*			
						1		
							ϕ^*	
								ϕ
							ϕ^*	
						ϕ		
					1			
				ϕ^*				
			1					
					ϕ^*			
						ϕ		
				1				
					ϕ^*			
							ϕ	
			1					
					ϕ^*			
								ϕ
				1				
					ϕ^*			
						ϕ		
			1					

$\langle E^2 |$ is the same as $\langle E^1 |$ except that ϕ and ϕ^* are switched. (IV.8.17)

where only non-zero elements are shown.

$$\xi = \begin{bmatrix} \langle A| \\ \langle E^1| \\ \langle E^2| \end{bmatrix}^t \tag{IV.8.18}$$

$$\mathbf{B_D} = \begin{bmatrix} \mathbf{A} & & \\ & \mathbf{E^1} & \\ & & \mathbf{E^2} \end{bmatrix} \tag{IV.8.19}$$

where submatrices are 8 by 8.

Table IV.8.6. The character table of $c_s(z)$ [117].

	E	C_3^{xyz}	C_3^{2xyz}
A	1	1	1
E	1	ϕ	ϕ^2
	1	ϕ^2	ϕ

*$\phi = \exp(2\pi i/3)$

Table IV.8.7. The exponent term.

	$\kappa' = 1$	2	3	4
$\kappa = 1$	1	ν^*	ν^*	ν^*
2	ν	1	1	1
3	ν	1	1	1
4	ν	1	1	1

*$\nu = \exp(i2\pi\eta)$

IV.9) Thermodynamics of C_{60}

The static (section IV.6) and dynamic (section IV.7) parts of free energy are combined to compute the thermodynamic properties of C_{60} such as the lattice parameter, the bulk modulus, the thermal expansion coefficient and heat capacity which are easy to measure. Only the intermolecular parts of the thermodynamic properties were computed. The main object of this section is to evaluate the model by comparing it with the experiments and to see how those properties are interrelated with one another. Or we may evaluate experiments by comparing them with the results of others.

IV.9.a) the equation of state for C_{60}

From equations (IV.6.7a) and (II.5.39) the free energy of *sc* C_{60} is written as

$$A = N\left\{6\left(X_\alpha E_1 + X_\beta E_4 + X_\alpha X_\beta \Delta E\right) + kT\left(X_\alpha \ln X_\alpha + X_\beta \ln X_\beta\right)\right\} + kT\sum_i\left\{\frac{\hbar\omega_i}{2kT} + \ln\left[1-\exp\left(-\frac{\hbar\omega_i}{kT}\right)\right]\right\} \qquad \text{(IV.9.1)}$$

where $\Delta E = E_2 + E_3 - (E_1 + E_4)$ (IV.6.7b)

Since in the acoustic modes the frequencies seem to be proportional to the wave vector and in the optical modes the frequencies seem to be less dependent of the wave vector (see figure IV.7.1a to c), the dynamic part of the free energy is approximated by the Debye model for acoustic modes and the Einstein model for the optical modes. Thus, from equations (IV.6.6), (II.5.46) and (II.5.47), the intermolecular part of the free energy is

$$A(T,V,N,X_\alpha) = NE(V,N,X_\alpha) + NkT\left(X_\alpha \ln X_\alpha + X_\beta \ln X_\beta\right) + \frac{N}{4}kT\sum_{j=1}^{21}\left\{\frac{\hbar\omega_j}{2kT} + \ln\left[1-\exp\left(-\frac{\hbar\omega_j}{kT}\right)\right]\right\} + \frac{N}{4}kT\left\{\frac{9}{8}\frac{\Theta}{T} + 3\ln\left[1-\exp\left(-\frac{\Theta}{T}\right)\right] - D\left(\frac{\Theta}{T}\right)\right\}$$

(IV.9.2)

where $E(V, N, X_\alpha) = 6\left(X_\alpha E_1 + X_\beta E_4 + X_\alpha X_\beta \Delta E\right)$ (IV.9.3)

and the Debye function $D(x)$ is numerically approximated in Appendix D.

With the assumption that the frequencies are independent of X_α, the relation between T and X_α is given in equation (IV.6.9a).

$$T = -\frac{6\left[(E_1 - E_4) + (X_\beta - X_\alpha)\Delta E\right]}{k \ln\left(X_\alpha / X_\beta\right)} \tag{IV.6.9a}$$

At the equilibrium state of (T, V, N, X_α) the state equation is given as

$$-P = \left(\frac{\partial A}{\partial V}\right)_{T,N} = N\left[\frac{\partial E(V,N,X_\alpha)}{\partial V}\right]_{T,N,X_\alpha} + \frac{N}{4} kT \sum_{j=1}^{21} \hbar\omega_j \left\{\frac{1}{2} + \frac{1}{\exp\left(\frac{\hbar\omega_j}{kT}\right) - 1}\right\}\left(-\frac{\gamma_j}{V}\right)$$
$$+ \frac{N}{4} k\Theta\left\{\frac{9}{8} + 3\frac{T}{\Theta} D\left(\frac{\Theta}{T}\right)\right\}\left(-\frac{\gamma_D}{V}\right) \tag{IV.9.4}$$

where Grüneisen constants are defined as

$$\gamma_i = -\frac{\partial \ln \omega_i(V)}{\partial \ln V} \tag{IV.9.5}$$

and assumed to be independent of V.

The equilibrium state at P = 0 atm was computed from equation (IV.6.9a) and (IV.9.4). The Debye velocity v and Debye characteristic temperature Θ were determined as 2.55×10^3 m/sec and 54.14 K from the dispersion curves in figure IV.7.1a to c. For optical modes the frequencies at 14.05 Å in table IV.7.1 were used. Pohl et al. reported that the

Einstein model with the characteristic temperature Θ_E = 35 K was much better agreement with the specific heat and thermal conductivity measurements than the Debye model and that from the low temperature specific heat they determined the Debye velocity and Debye temperature as 2.39×10^3 m/sec and 80 K [156]. David et al. found that a Debye-only model gave a significantly poorer fit to the lattice parameter data than an Einstein-only model and that a single Debye + single Einstein model gave an improved fit (the derived Debye and Einstein temperatures were 52 K and 93 K) [157]. The Grüneisen constants were assumed to be independent of both the volume of the crystal and the type of frequency. The procedure for the computation was

(1) to obtain the energy terms $E_i(V)$ and their first and second derivatives with respect to the volume at a fixed lattice parameter a (that is, fixed state of (V, N)) from equations (IV.6.3) and (IV.6.6) with parameters of set 4 in table IV.6.3.

(2) to compute T at a given (V, N, X_α) from equation (IV.6.9a)

(3) to compute P at a given (T, V, N, X_s) from equation (IV.9.4)

(4) to compare P calculated in (3) with zero and repeat (2) to (4) with varying X_α until $P = 0$

(5) to go back to (1) for a different lattice parameter a.

By the least-squares method the Grüneisen constant was determined as 8.73 from table IV.7.1. However, to fit the results to the reported values of the lattice parameters [69], thermal expansion coefficient [66] and bulk modulus [140,141,149], the Grüneisen constant is determined to be 7.5 as an optimum value. The resulting equilibrium state of (T, V, N, X_α, P = 0) is given in figure (IV.9.1a and b).

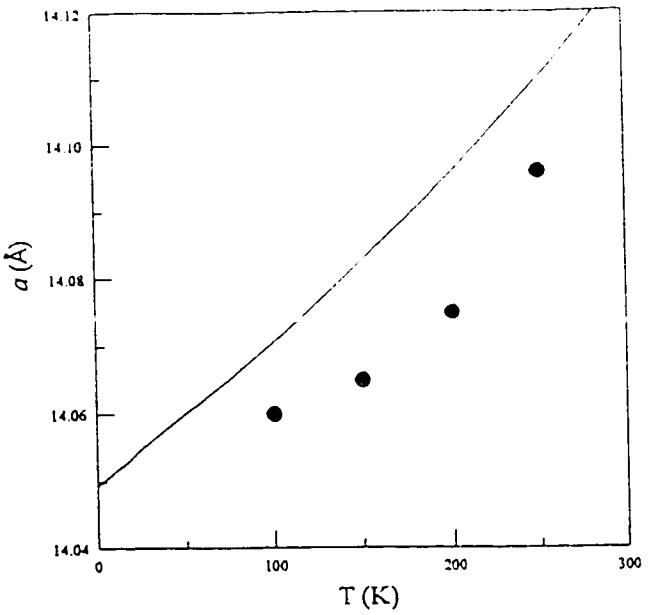

(a)

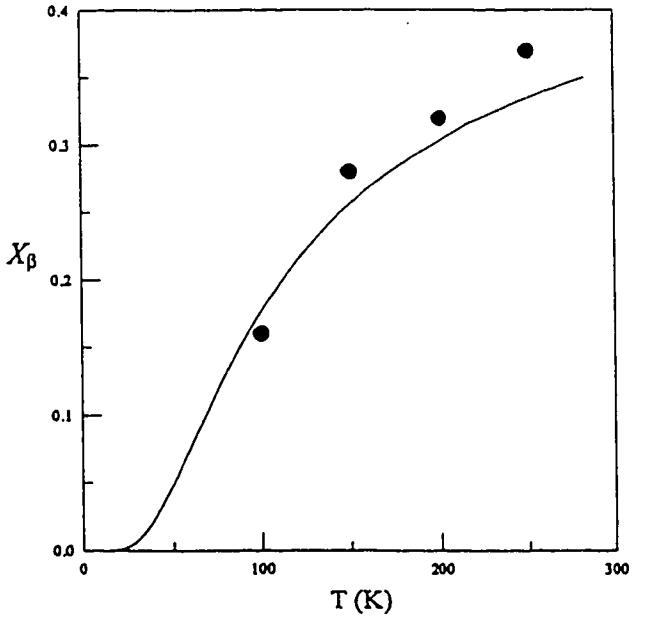

(b)

Figure IV.9.1 (a) Lattice parameters computed at P = 0. (b) The computed fraction of molecules at orientation β. Solid circles are from David et al. [69].

IV.9.b) the bulk modulus and the thermal expansion coefficient of C_{60}

From equation (II.5.7) and (IV.9.2) the bulk modulus B_T (= $1/\beta_T$) is written as

$$\begin{aligned} B_T &= V\left(\frac{\partial^2 A}{\partial V^2}\right)_{T,N} \\ &= VN\left[\frac{\partial^2 E(V,N,X_\alpha)}{\partial V^2}\right]_{T,N,X_\alpha} \\ &+ \frac{N}{4}\sum_{j=1}^{21}\frac{1}{V^2}\left\{\hbar\omega_j\left[\frac{1}{2}+\frac{1}{\exp\left(\frac{\hbar\omega_j}{kT}\right)-1}\right]\gamma_j(\gamma_j+1) - kT\left(\frac{\hbar\omega_j}{kT}\right)^2\frac{\exp\left(\frac{\hbar\omega_j}{kT}\right)}{\left[\exp\left(\frac{\hbar\omega_j}{kT}\right)-1\right]^2}\gamma_j\right\} \\ &+ \frac{N}{4}\frac{3}{V^2}\left[\frac{3}{8}k\Theta\gamma_D(\gamma_D+1) + kTD\left(\frac{\Theta}{T}\right)\gamma_D^2 + k\Theta D'\left(\frac{\Theta}{T}\right)\gamma_D^2\right] \end{aligned} \qquad \text{(IV.9.6a)}$$

where

$$\begin{aligned} \left[\frac{\partial^2 E(V,N,X_\alpha)}{\partial V^2}\right]_{T,N,X_\alpha} &= \left[\frac{\partial^2 E_1}{\partial a^2}X_\alpha + \frac{\partial^2 E_4}{\partial a^2}X_\beta + \frac{\partial^2 \Delta E}{\partial a^2}X_\alpha X_\beta\right]\left(\frac{\partial a}{\partial V}\right)^2 \\ &+ \left[\frac{\partial E_1}{\partial a} - \frac{\partial E_4}{\partial a} + \frac{\partial \Delta E}{\partial a}(1-2X_\alpha)\right]\left(\frac{\partial X_\alpha}{\partial V}\right)_{T,N}\left(\frac{\partial a}{\partial V}\right) \\ &+ \left[\frac{\partial E_1}{\partial a}X_\alpha + \frac{\partial E_4}{\partial a}X_\beta + \frac{\partial \Delta E}{\partial a}X_\alpha X_\beta\right]\left(\frac{\partial^2 a}{\partial V^2}\right) \end{aligned} \qquad \text{(IV.9.6b)}$$

$$\left(\frac{\partial X_\alpha}{\partial V}\right)_{T,N} = \frac{\left[\frac{\partial E_1}{\partial a} - \frac{\partial E_4}{\partial a} + \frac{\partial \Delta E}{\partial a}(1-2X_\alpha)\right]\left(\frac{\partial a}{\partial V}\right)}{2\Delta E - kT\left(\frac{1}{X_\alpha}+\frac{1}{X_\beta}\right)} \qquad \text{(IV.9.6c)}$$

From equation (IV.9.6a) the bulk moldlus B_T was computed at a given (T, V, N, X_α, $P = 0$) which is determined by equations (IV.6.9a) and (IV.9.4). The results plotted in figure IV.9.2 show that the vibrational part of the bulk modulus is very small (about 2 % at 200 K) and increases with temperature. The reported values of the bulk modulus are widely scattered [140,141,149]. There are large differences between the model and the experiments which may be due to the rigid molecule assumption or the assumption that the Grüneisen constant is independent of volume and X_α.

From equation (II.5.6) the thermal expansion coefficient is written as

$$\alpha_l = \frac{1}{3}\beta_T\left(\frac{\partial S}{\partial V}\right)_T \tag{IV.9.7a}$$

From equation (IV.9.2) the derivative of entropy with respect to volume is given as

$$\left(\frac{\partial S_{conf}}{\partial V}\right)_T = -Nk\ln\left(\frac{X_\alpha}{X_\beta}\right)\left(\frac{\partial X_\alpha}{\partial V}\right)_{T,N} \tag{IV.9.7b}$$

$$\left(\frac{\partial S_{vib}}{\partial V}\right)_T = \frac{N}{4}\sum_{j=1}^{21}\frac{1}{V}k\left(\frac{\hbar\omega_j}{kT}\right)^2\frac{\exp\left(\frac{\hbar\omega_j}{kT}\right)}{\left[\exp\left(\frac{\hbar\omega_j}{kT}\right)-1\right]^2}\gamma + \frac{3N}{4}\frac{1}{V}k\left[D\left(\frac{\Theta}{T}\right)-\frac{\Theta}{T}D'\left(\frac{\Theta}{T}\right)\right]\gamma_D \tag{IV.9.7c}$$

where $\left(\frac{\partial X_\alpha}{\partial V}\right)_{T,N}$ is given in equation (IV.9.6c). The results at given (T, V, N, X_α, $P = 0$) is shown in figure IV.9.3. The anomalous behavior in the temperature range between 20 and 80

K is due to the rapid increase in the population of molecules with β orientation (X_β) (see figure IV.9.1b).

IV.9.c) the heat capacity of C_{60}

From equation (II.5.4) and (IV.9.2) the heat capacity at constant volume is given as

$$C_V = N\left[E_1 - E_4 + \Delta E(1-2X_\alpha)\right]\left(\frac{\partial X_\alpha}{\partial T}\right)_{V,N} + \frac{N}{4}\sum_{j=1}^{21} k\left(\frac{\hbar\omega_j}{kT}\right)^2 \frac{\exp\left(\frac{\hbar\omega_j}{kT}\right)}{\left[\exp\left(\frac{\hbar\omega_j}{kT}\right)-1\right]^2} + \frac{3N}{4}k\left[D\left(\frac{\Theta}{T}\right) - \frac{\Theta}{T}D'\left(\frac{\Theta}{T}\right)\right] \quad \text{(IV.9.8a)}$$

$$\text{where } \left(\frac{\partial X_\alpha}{\partial T}\right)_{V,N} = \frac{k\ln\left(X_\alpha/X_\beta\right)}{2\Delta E - kT\left(\frac{1}{X_\alpha}+\frac{1}{X_\beta}\right)} \quad \text{(IV.9.8b)}$$

Note that the intramolecular part of the heat capacity is omitted in the above equations.

Using equation (II.9.5) the heat capacity at constant pressure (P = 0) is computed (figure IV.9.5).

$$C_P = C_V + \frac{TV\alpha_V^2}{\beta_T} \quad \text{(II.5.9)}$$

The contribution of the lattice energy part to C_V is the most interesting feature in *sc* C_{60}, which is due to the increase in the population of molecules with β orientation (X_β), significant in the low temperature range (20 to 100 K) in figure IV.9.4a. Since the optical modes outnumber the acoustic modes, C_V decreases as $\exp\left(-\frac{\hbar\omega}{kT}\right)$.

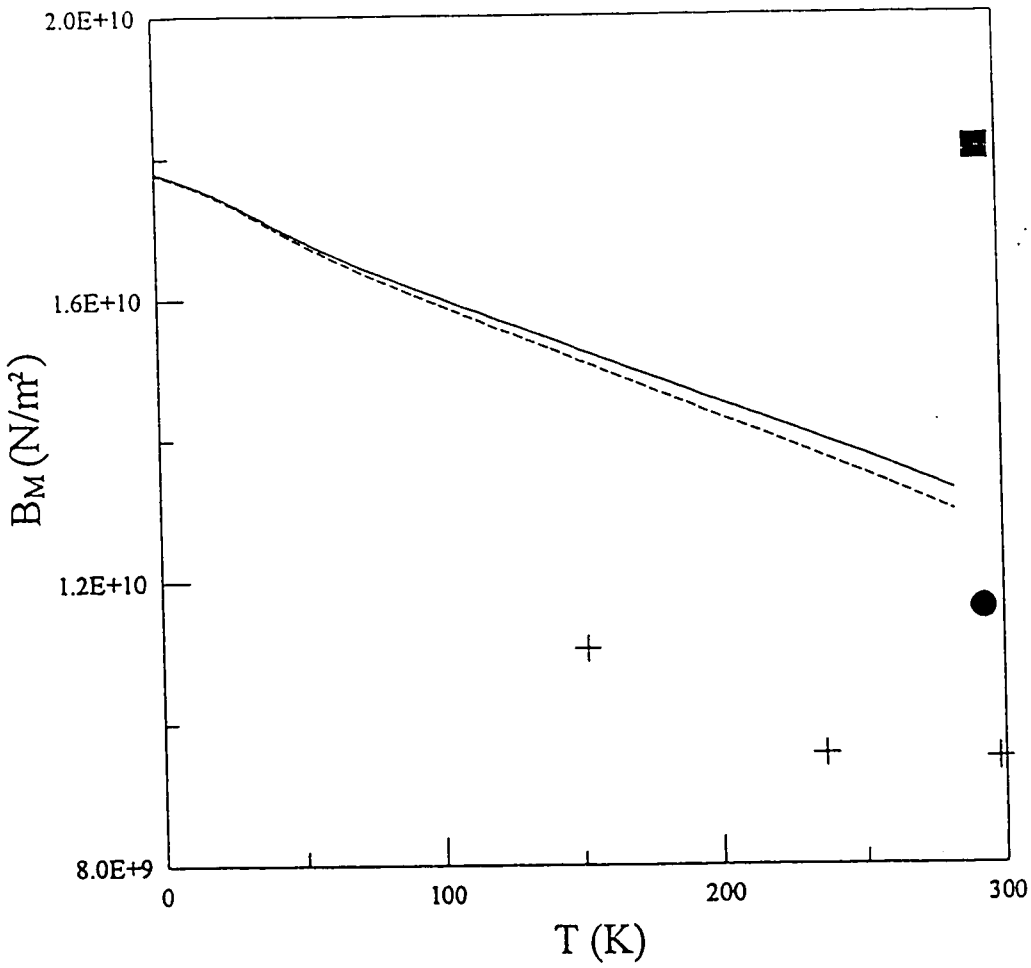

Figure IV.9.2. Computed bulk modulus of sc C_{60}. Dashed line is for $V\left(\frac{\partial^2 E}{\partial V^2}\right)_T$. Circle, square and cross are from reference [140], [141] and [149], respectively.

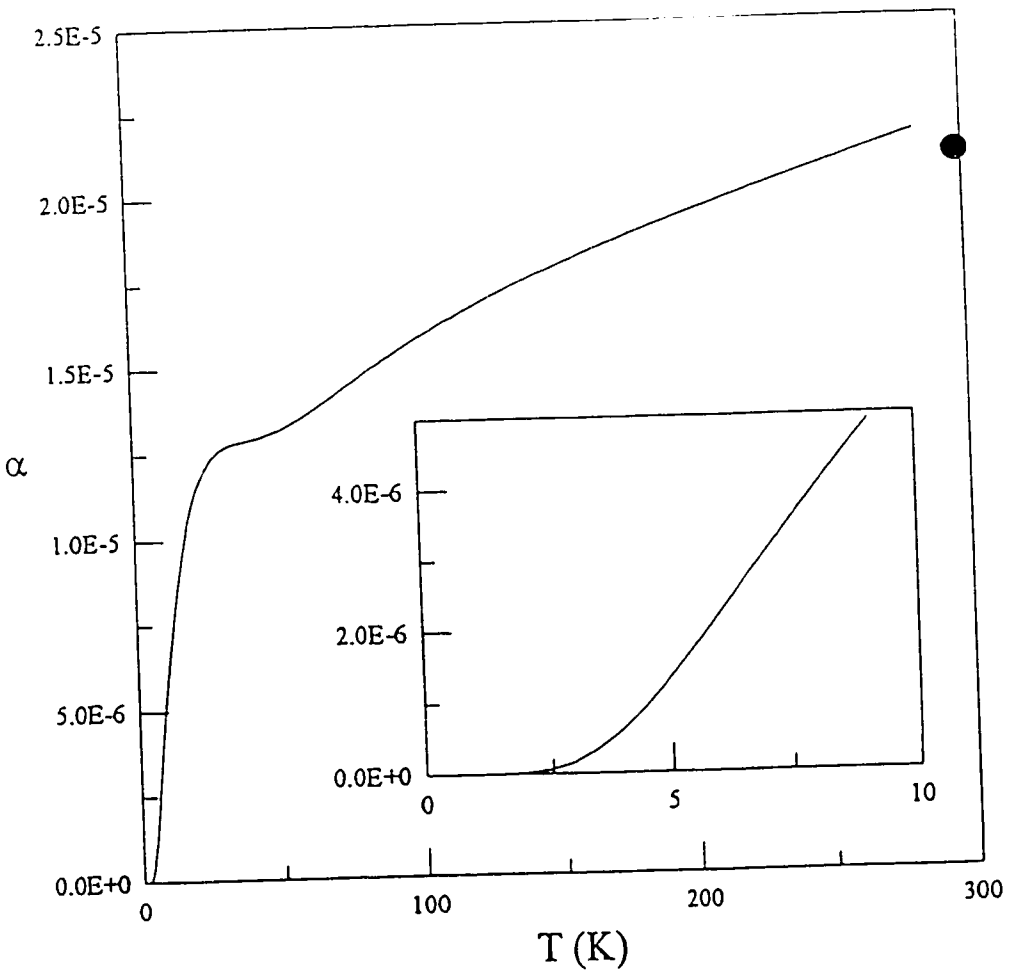

Figure IV.9.3. Computed linear thermal expansion coefficient. Circle is from reference [66]. The inset is for low temperatures.

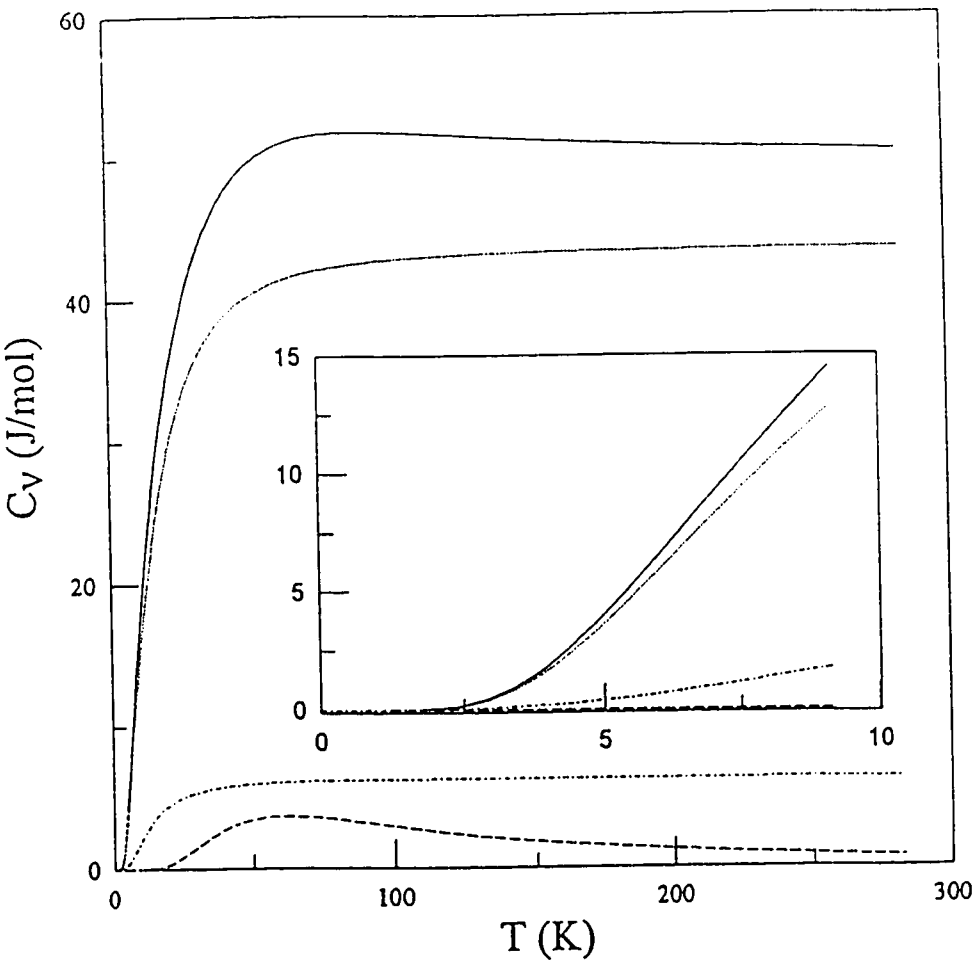

Figure IV.9.4. Computed constant volume heat capacity. Inset is for constant volume heat capacity at low temperatures. Dashed, dotted and mixed lines are for heat capacity due to the lattice energy, intermolecular optical modes, acoustic modes. Solid line is the sum of three.

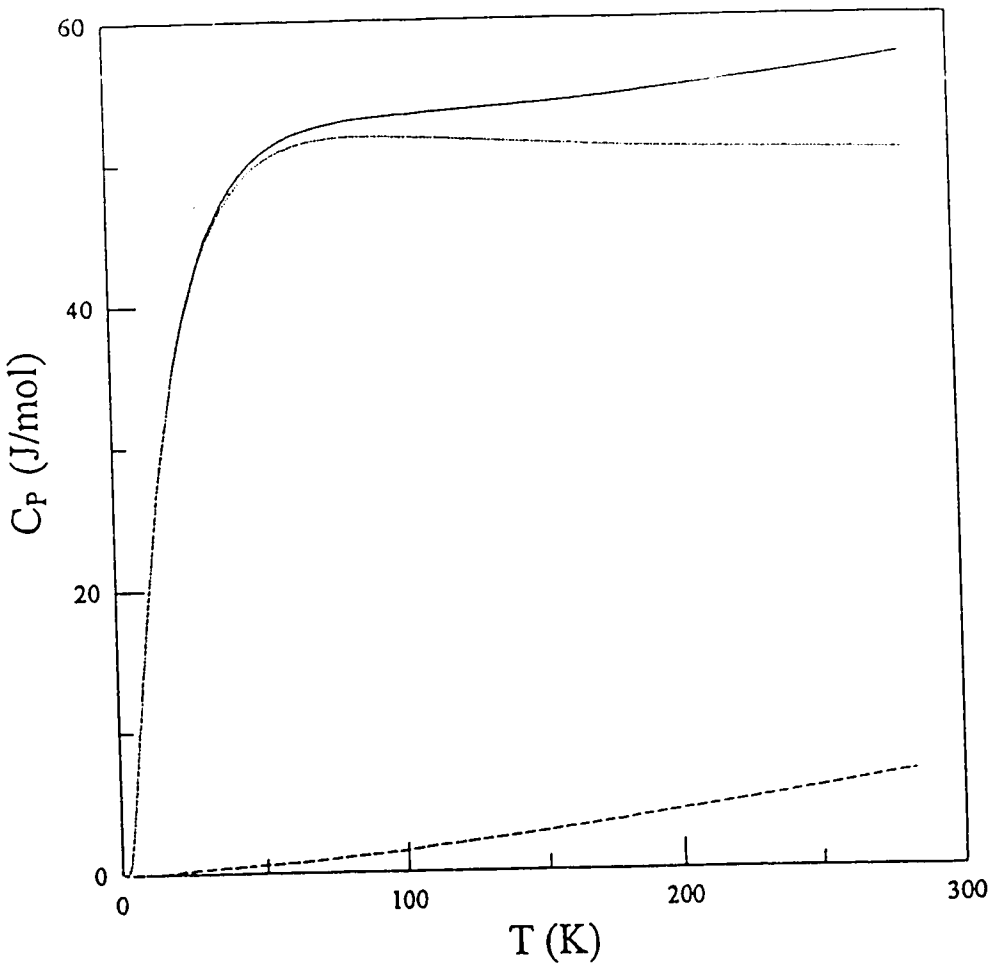

Figure IV.9.5. Computed constant pressure heat capacity ($P = 0$). Dotted line is for constant volume heat capacity. Dashed line is for the contribution of the anharmonicity of the vibrations to the heat capacity.

IV.10) K - C_{60}

Ion-exchanged and direct-synthesized K β-alumina tubes were used for EMF measurements. The green density of tubes synthesized from bohemite as the source of alumina was low due to the low stability of the slip. Ion-exchanged tubes were more likely to crack after sealing. The direct-synthesized tubes with α-alumina as the starting material showed better mechanical strength.

Cell measurements were made between a reference electrode (Pb : Bi : K = 3.3 : 41.6 : 55.1 by weight) calibrated against pure K and the working electrode containing C_{60} intercalated with K. EMF versus x at 572 K is shown in figure IV.10.1. Four plateaux are seen at 1720 ($0 < x < 1$), 1563 ($1 < x < 3$), 1354 ($3 < x < 4$) and 1271 mV ($4 < x$). Figure IV.10.2 displays the EMF in the dilute solution region. The Nernst slope (dashed line) is shown for comparison. The phases K_xC_{60} are listed in table IV.5.1. The formation energy of K_xC_{60} has been computed, assuming stoichiometric compounds (table IV.10.1). The reaction is given as

$$\frac{x}{x+1}K + \frac{1}{x+1}C_{60} = \frac{1}{x+1}K_xC_{60} \qquad \Delta G_f \qquad \text{(IV.10.1)}$$

Table IV.10.1. The formation energy of K_xC_{60} at 572 K

x	ΔG_f (KJ)
1	83
3	117
4	120
6	121

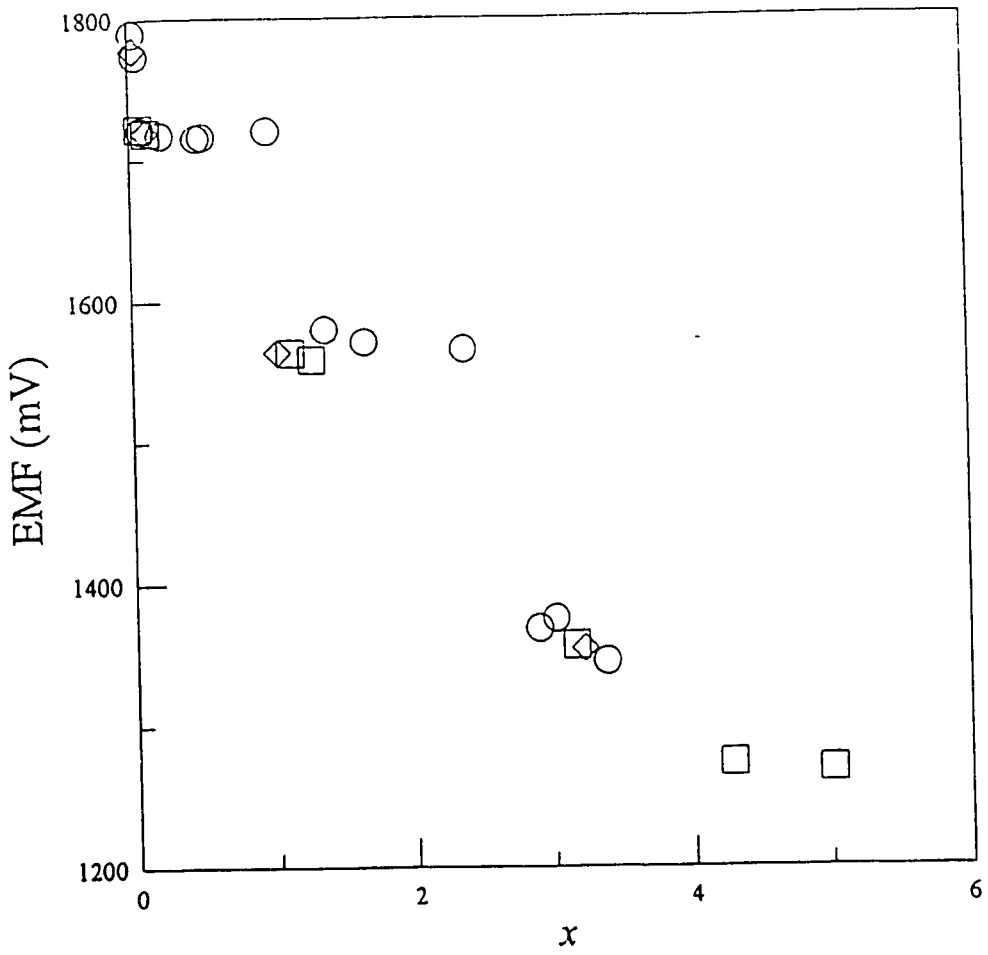

Figure IV.10.1. EMF of K_xC_{60} at 572 K.

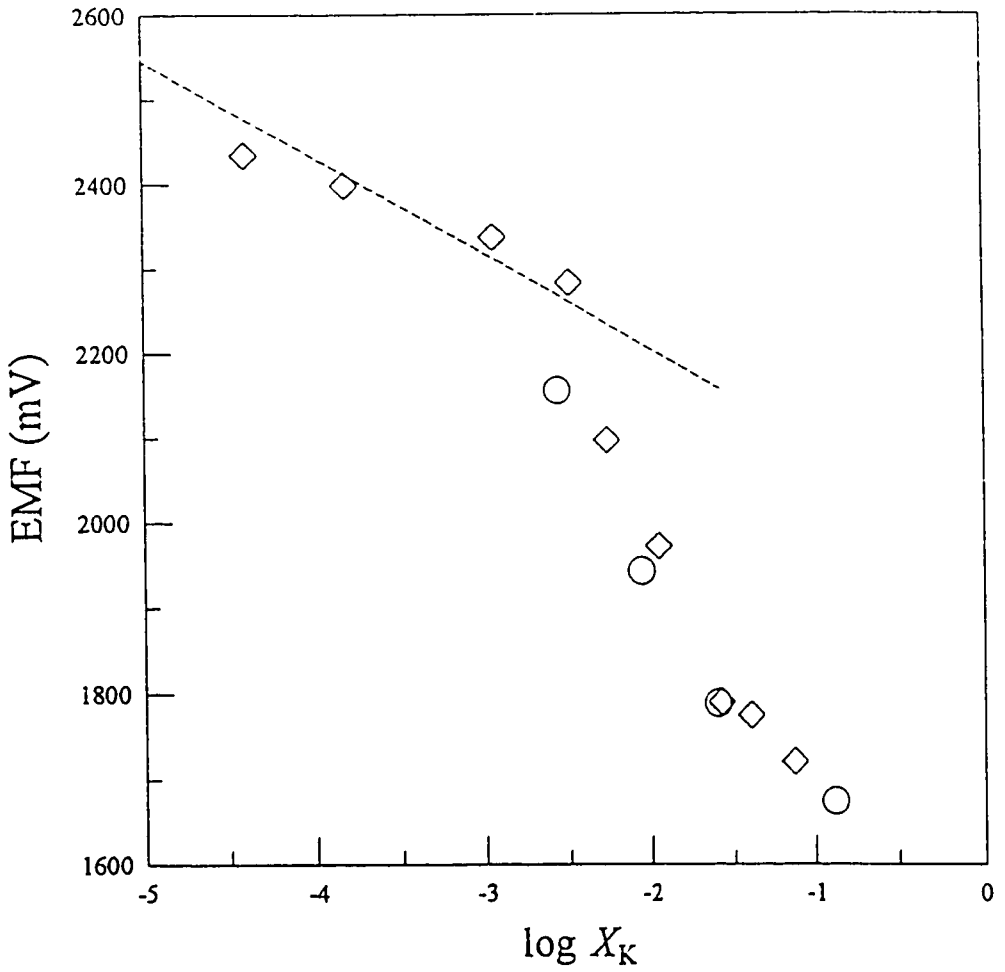

Figure IV.10.2. EMF of K_xC_{60} for dilute solution region. Dashed line is the guide for the theoretical Nernst slope.

IV.11) Sr - Al

Sr is an important addition to aluminum cast alloys containing Si because it modifies the acicular structure of the Al-Si eutectic. Sr beta-alumina is an obvious candidate material for an electrochemical sensor to monitor the concentration of Sr in Al in the range 0.001 to 0.1 % by weight. Ion-exchanged or direct synthesized Sr β - or β" - alumina tubes with good thermal shock resistance were developed and tested by Kirchnerova and Pelton [150]. Three reference electrodes (Al - Sr, $SrO6Fe_2O_3$/ Fe_2O_3/air and $SrCl_2$ - AgCl / Ag) were tested in molten Al baths. However, the EMF results were found to be scattered over a 100 mV range about expected values. Interfacial effects were suspected to be responsible either due to poor wetting of the ceramic by liquid Al or due to interfacial reaction resulting in a non-conducting phase. The objective of this work was to test the different probe assemblies in a high-purity Ar atmosphere in order to eliminate the cause of the problem and obtain good EMF results.

IV.11.a) EMF measurements

Three experiments were run, each with an independent working electrode, but with the same reference electrode and counter electrode. In each case, titration resistance at 720 °C was high (approximately 10^3 Ω), somewhat lower for β"-alumina, and equilibration was slow. In fact, we never established a stable reading until after a month of equilibration.

The first working electrode, Cell I was made from Sr β -alumina and was titrated from pure Al to Al-0.5 ppm Sr. No Nernst slope was observed in this cell. The semi-stable

EMF reading was in the range of 485 mV. As the Sr content was increased up to 26 ppm, the EMF increased and after a week, reached a value near 660 mV. EMF in this cell was hundreds mV lower than expected values.

Cell II was made from Sr β″-alumina. The EMF at Al-1 ppm Sr was in the vicinity of 1010 mV, close to the expected value, but continuously drifting downward.

Al-1 wt % $SrBr_2$ was used for Cell III in order to eliminate the possible interfacial problems, such as wetting of ceramic by molten Al. The EMF of Cell III was between those of Cell I and II and tended to decrease with time. Eventually, after a month, all three cells drifted to a common voltage near 390 mV.

IV.11.b) compatibility of Sr β-alumina with pure Al

EMF values were inconsistent from cell to cell and drifted with time. No Nernst slope was observed. The proposed cause of the problem is due not to the interface but due to thermodynamics. One of the requirements for good solid electrolytes is the compatibility with electrode materials. The compatibility of Sr beta-alumina with Al and Sr can be calculated. Thermodynamic data used in these calculations are given below.

$$2Al + \tfrac{3}{2}O_2 = Al_2O_3 \qquad \Delta G_1 = -1676000 + 320T \quad [151] \quad \text{(IV.11.1)}$$

$$Na_2O + xAl_2O_3 = Na_2O \cdot xAl_2O_3 \qquad \Delta G_2 = -314000 + 68.92T \quad [152] \quad \text{(IV.11.2)}$$

$$2Na_{(l)} + \tfrac{1}{2}O = Na_2O \qquad \Delta G_3 = -420015 + 146.022T \quad [152] \quad \text{(IV.11.3)}$$

$$Sr_{(l)} + 4Al_{(l)} = Al_4Sr \qquad \Delta G_4 = -225000 + 107.5T \quad [153] \quad \text{(IV.11.4)}$$

$$Sr_{(l)} + 2Al_{(l)} = Al_2Sr \qquad \Delta G_5 = -166500 + 86.7T \quad [153] \quad \text{(IV.11.5)}$$

$$Sr + \tfrac{1}{2}O_2 = SrO \qquad \Delta G_6 = -618300 + 100T \qquad [154] \quad (IV.11.6)$$

Though the formation energy of Sr β-alumina is not reported, it can be estimated by the comparison with Na β-alumina. The reported values of the formation energy of Na β-alumina are very consistent [152,155]. The formation of each compound is given by the following reactions:

$$2Na + \tfrac{1}{2}O_2 + xAl_2O_3 = Na_2O \cdot xAl_2O_3 \qquad \Delta G_7 = \Delta G_2 + \Delta G_3 \qquad (IV.11.7)$$

$$Sr + \tfrac{1}{2}O_2 + yAl_2O_3 = SrO \cdot yAl_2O_3 \qquad \Delta G_8 \qquad (IV.11.8)$$

Consider the Born-Haber cycle of reactions (IV.11.7) and (IV.11.8) and assume that x = y.

$$2Na_{(l)} = 2Na_{(g)} = 2Na^+ + 2e^- \qquad (IV.11.9)$$

$$Sr_{(s)} = Sr_{(g)} = Sr^{2+} + 2e^- \qquad (IV.11.10)$$

$$\tfrac{1}{2}O_2 + xAl_2O_3 + 2e^- = (xAl_2O_3 + 2O)^{2-} \qquad (IV.11.11)$$

$$2Na^+ + (xAl_2O_3 + 2O)^{2-} = Na_2O \cdot xAl_2O_3 \qquad (IV.11.12)$$

$$Sr^{2+} + (xAl_2O_3 + 2O)^{2-} = SrO \cdot xAl_2O_3 \qquad (IV.11.13)$$

Here we consider the change in enthalpy only. Reactions (IV.11.9) and (IV.11.10) are the sum of the cohesive energy and ionization energy. Thus the difference of (IV.11.10) and (IV.11.9) is 5.9 eV [= 1.72 + 16.72 - 2(1.113 + 5.14)] [147]. Reaction (IV.11.11) is common for both materials. In reactions (IV.11.12) and (IV.11.13) the sum of attractive Coulomb interactions between Sr ions and spinel blocks may be close to that for Na ions and spinel blocks since the Sr ion has twice the charge of the Na ion and the concentration

of Na ions is twice that of Sr ions. However the sums of repulsive Coulomb interactions between conducting cations for Sr and Na β-aluminas are quite different from each other. When we consider that the average distance between Sr ions on the same conduction plane is $\sqrt{2}$ times that between Na ions, the repulsion between Sr ions is stronger than that between Na ions. Thus Na β-alumina appears to be more stable than Sr β-alumina, $\Delta G_7 < \Delta G_8$.

The compatibility of Na β-alumina with Al can be determined by the following reaction.

$$Na_2O \cdot xAl_2O_3 + \tfrac{2}{3}Al = 2Na + (x + \tfrac{1}{3})Al_2O_3 \qquad \Delta G_9 \qquad \text{(IV.11.14)}$$

$$\Delta G_9 = (x + \tfrac{1}{3})\Delta G_1 - (\Delta G_7 + x\Delta G_1) = \tfrac{1}{3}\Delta G_1 - \Delta G_7 = 70 \text{ kJ at } 700\,^\circ\text{C} \qquad \text{(IV.11.15)}$$

Thus, Na β-alumina is compatible with Al (figure IV.11.1).

For Sr β-alumina,

$$SrO \cdot yAl_2O_3 + \tfrac{14}{3}Al = Al_4Sr + (y + \tfrac{1}{3})Al_2O_3 \qquad \Delta G_{10} \qquad \text{(IV.11.16)}$$

$$\Delta G_{10} = \tfrac{1}{3}\Delta G_1 - \Delta G_8 + \Delta G_4 \qquad \text{(IV.11.17)}$$

Since $\Delta G_7 < \Delta G_8$ and the last term in (IV.11.17) is -120 kJ at 700 °C, Sr β-alumina may decompose in the presence of Al. This can be seen from the proposed ternary phase diagram (figure IV.11.2) which shows that no tie line exists between Al and Sr β-alumina phase.

$SrO - Al_2O_3$ system has several intermediate compounds. Let's assume that the formation of these compounds are suppressed with the exception of SrO.

$$SrO \cdot yAl_2O_3 + 4ySr = yAl_2Sr + (3y+1)SrO \qquad \Delta G_{11} \qquad \text{(IV.11.18)}$$

$$\Delta G_{11} = (3y+1)\Delta G_6 + y\Delta G_5 - y\Delta G_1 - \Delta G_8 = -3035\ [kJ] - \Delta G_8 < 0 \text{ at } 700\ ^\circ C \qquad \text{(IV.11.19)}$$

where $y = 9$ is used in (IV.11.19). Thus Sr β-alumina is not compatible with Sr.

The EMFs of the ternary system at 700 °C are indicated on figure IV.11.2. In calculating these EMFs, the compounds are treated as point phases. For example, in Sr β-alumina - α-alumina - Al_4Sr system, the chemical potential and EMF of each component can be calculated as

$$\begin{bmatrix} \mu_{Sr} \\ \mu_{Al} \\ \mu_O \end{bmatrix} = \begin{bmatrix} 0 & 1 & 0 \\ 0 & 2/5 & 3/5 \\ 1/5 & 4/5 & 0 \end{bmatrix}^{-1} \begin{bmatrix} 0 \\ -273 \\ -24.1 \end{bmatrix} \quad [kJ] \qquad \text{(IV.11.20)}$$

$$EMF = -\frac{\mu_{Sr}}{2F} \qquad \text{(IV.11.21)}$$

Although the system is not thermodynamically stable, we should also consider whether the reaction may be kinetically inhibited. If the kinetics is slow enough, a stable EMF could be obtained on the measuring time scale. The direct-synthesized Sr β-alumina may have an appreciable fraction of α-alumina. In this case, the energy barrier for the reaction (IV.11.16) can be easily overcome at 700 °C. The initial low EMF in working Cell I may result from the Sr β-alumina - α-alumina - Al system. The initial high EMF in ion-exchanged Sr β-alumina may be due to the absence of α-alumina. The heat treatment

for the glass-sealing may introduce more α-alumina. Slow degradation in the reference electrode can also be explained by the energy barrier for the formation of the oxides.

IV.11.c) Conclusion

Sr β-alumina is not thermodynamically stable with respect to both Al and Sr. If the operating temperature of the electrochemical cells is so high that the system can overcome the energy barrier for the decomposition of Sr β-alumina, the Sr β-alumina may not be an adequate probe for Al and Sr electrodes. (And this appears to be the case.) One possible solution is to reduce the measuring temperature as low as possible. Alternatively, a sample of Al-Sr alloy could be mixed with a predetermined amount of metal such as Sn or Pb to reduce the chemical potential of Al. Development of new solid electrolytes or introduction of separator could be yet another solution.

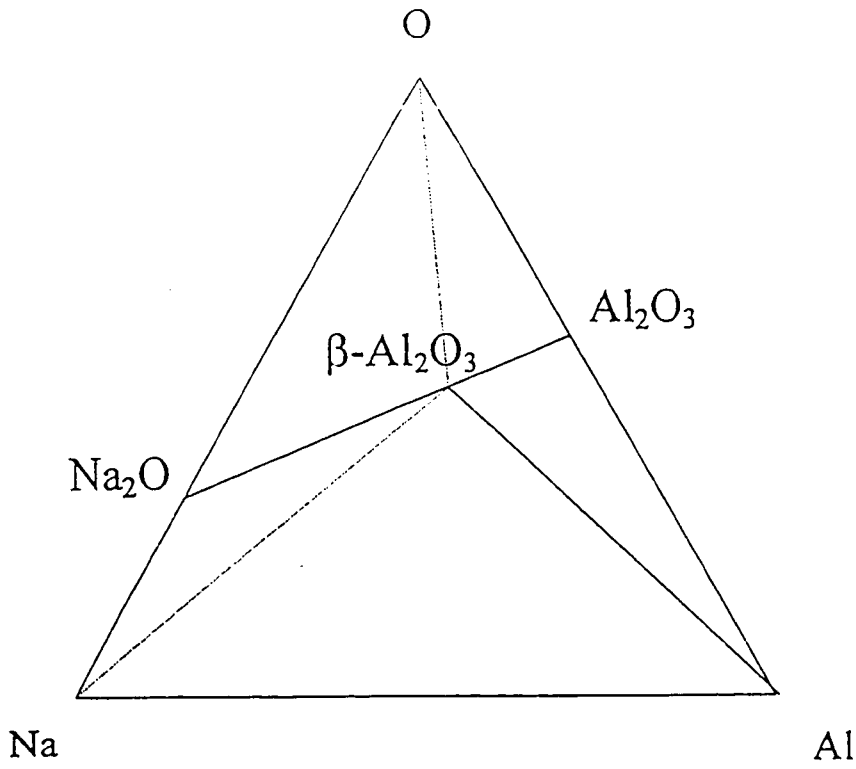

Figure IV.11.1. Schematic diagram of Na-Al-O. We assumed that the formation of oxides that do not appear in the diagram was prohibited.

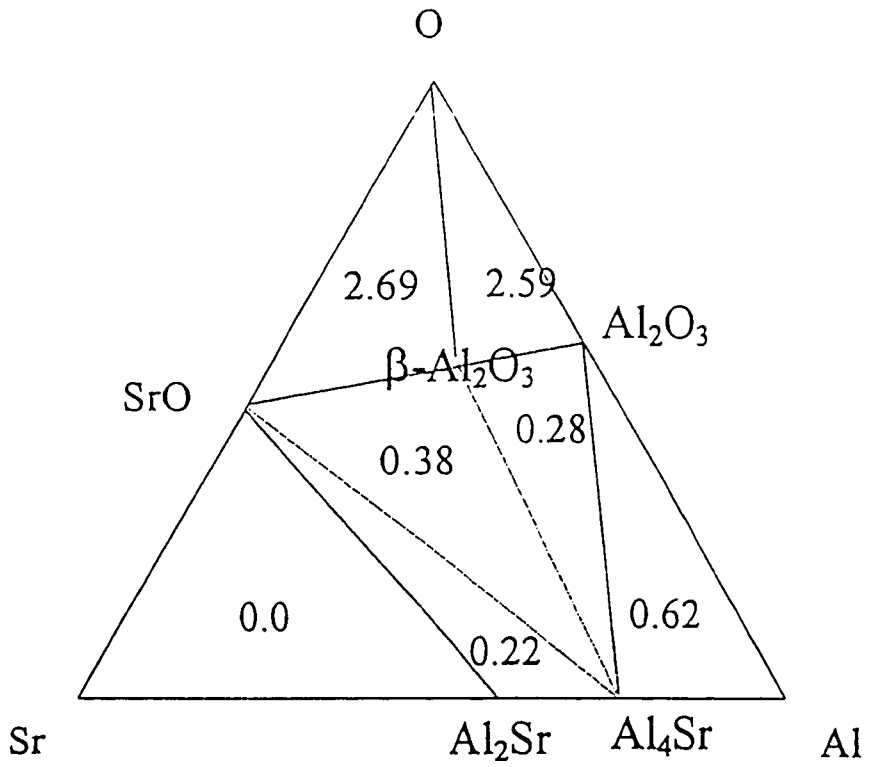

Figure IV.11.2. EMF of pseudo ternary systems in Sr-Al-O where the formation energy of Na β-alumina is used for Sr β-alumina.

V. Conclusions

Conclusions are as follows.

1) Dense green beta-alumina tubes were successfully formed by slip-casting, using ethanol as a liquid vehicle. The most important factor in this process is to control the amount of the moisture in the slip. Batchwise drying over molecular sieves is effective to obtain extremely dry ethanol. The stability of the slips decreased in the order of well-crystallized, XB2-SG and Ceramatec powder.

2) Dense (>98 %) beta-alumina tubes were obtained by sintering. Green tubes were packed with coarse beta-alumina powder in an α-alumina crucible covered with an α-alumina lid. The critical factor is the sodium oxide vapour pressure. The compositions of not only tubes but also packing powder should be controlled carefully to attain fine microstructures.

3) K beta-alumina tubes were prepared by ion-exchanging Na beta-alumina tubes. Ion-exchange in a vapor phase (KCl) and subsequent liquid phase (KNO_3) is effective. To avoid mechanical degradation, the size of grains should be small (< 10 μm).

4) Na and K beta-alumina tubes were successfully sealed to α-alumina lids with aluminosilicate glass. The sealing was strong and impermeable to He (< 10^{-8} cm^3/s).

5) EMF measurements of Na_xC_{60} system at 599 K showed solution regions of $1.7 < x < 3$ and $3.3 < x < 12$. (A sudden drop in EMF in the range of $3.3 < x < 3.7$ leaves the

possibility that a line phase may exit in this range). No compounds were found in the composition range of $0 < x < 1.7$. From EMF measurements, the Gibbs energies of mixing of $\frac{1}{4}Na_3C_{60}$ and $\frac{1}{7}Na_6C_{60}$ are determined as 85 and 81 kJ/mol, respectively.

6) Na_xC_{60} was modeled by an ideal interstitial solution. By fitting the parameters in the model to experimental data, the model showed that tetrahedral sites are favored by Na (90 % occupancy of tetrahedral sites at Na_2C_{60}, figure IV.5.8).

7) From EMF measurements of the K_xC_{60} system at 572 K, the Gibbs energies of mixing of $\frac{1}{x+1}K_xC_{60}$ are determined as 83, 117, 120 and 121 kJ/mol for x = 1, 3, 4 and 6, respectively.

8) A model for the intermolecular interactions between C_{60} molecules is proposed. As the effective Lennard-Jones interaction centers move from C atoms to the centers of adjacent double bonds, the 22 degree phase in the $Pa\bar{3}$ structure of pure C_{60} becomes stabilized relative to the 87 degree phase (figure IV.6.2). By assigning charges to C atoms and the centers of bonds, we can increase the activation energy for the jump between 22 and 82 degree orientations (figure IV.6.3).

9) The $Pa\bar{3}$ structure of *sc* C_{60} is modeled by both regular solution and cluster variation methods. In this model, four motifs between two adjacent molecules are considered. Using the model for the intermolecular interactions between C_{60} molecules, thermodynamic properties of *sc* C_{60} were computed (figure IV.6.7). The difference between regular

solution and cluster variation methods results from the short-range order reflected by cluster variation method.

10) For the $Pa\bar{3}$ structure of *sc* C_{60}, the 22 degree phase is not necessarily the ground state. The presence of 82 degree oriented molecules with a small formation energy (~12 meV/molecule) makes the 22 degree phase more stable at some temperature, owing to the configurational entropy.

11) External vibrational frequencies of *sc* C_{60} were computed by the harmonic approximation (table IV.7.1 and figure IV.7.1), using the model for the intermolecular interactions between C_{60} molecules. The computed frequencies of phonons are quite consistent with experimental results. However, the difference between calculated and experimental results for librons suggests that harmonic approximation is not adequate for librons.

12) Using group theory, the external vibrational modes of *sc* C_{60} at Γ, Σ, Δ and Λ are labeled and the corresponding symmetry adapted vectors are obtained.

13) Using the results of (8) to (11), thermodynamic properties of *sc* C_{60} were computed (figure IV.9.1 to IV.9.5). The dispersion curves were approximated by the Debye model for acoustic modes and by the Einstein model for optical modes. The Debye characteristic temperature and optimum Grüneisen constant are determined as 54.14 K and 7.5, respectively.

14) The large difference between the computed and reported bulk moduli may be due to the failure of the rigid molecule model (figure IV.9.2).

15) The contribution of the formation of an 82 degree orientation among molecules to the constant volume heat capacity is significant in the temperature range of 20 to 100 K (figure IV.9.4).

16) The failure to obtain reproducibility in EMF measurements of Sr - Al alloys using Sr beta-alumina as a solid electrolyte seems to be related to the thermodynamic stability of Sr beta-alumina. Thermodynamic considerations suggest that Sr beta-alumina is not compatible with pure Al or Sr (figure IV.11.2).

Appendices

Appendix A. Eulerian angles

Assume that an object is at the origin of a Cartesian coordinate system (x, y, z). As the object rotates through angle γ clock-wise about an axis z', the coordinate (p, q, r) on the object will move to the new coordinate (p', q', r'). Here, the new coordinate will be derived as a function of the rotation angle γ and the direction (θ, ϕ) of the rotation axis z' using Eulerian angles (see figure A.A.1).

The rotation of a coordinate system through an angle θ counter-clock-wise about the x, y or z axis is given by three matrices.

$$R_z(\theta)=\begin{bmatrix} \cos\theta & \sin\theta & 0 \\ -\sin\theta & \cos\theta & 0 \\ 0 & 0 & 1 \end{bmatrix} \quad R_y(\theta)=\begin{bmatrix} \cos\theta & 0 & -\sin\theta \\ 0 & 1 & 0 \\ \sin\theta & 0 & \cos\theta \end{bmatrix} \quad R_x(\theta)=\begin{bmatrix} 1 & 0 & 0 \\ 0 & \cos\theta & \sin\theta \\ 0 & -\sin\theta & \cos\theta \end{bmatrix} \tag{A.A.1}$$

The rotation of the object at the origin through an angle θ counter-clock-wise about x, y or z axis corresponds to the above matrices with negative θ instead of θ .

When the axis of the rotation z' is given by (θ, ϕ), the first step is to align the new coordinate system (x', y', z') in such a way that the z' axis and the axis of the rotation coincide; thus, rotate the coordinate system by $R_z(\theta)$ and then by $R_y(\phi)$. The second step is to rotate the object through γ clock-wise about the z' axis: $R_z(\gamma)$. The final step is to rotate

the coordinate system (x', y', z') back to the original system (x, y, z): $R_y(-\phi)$ and then $R_z(-\theta)$. Thus the whole procedure is given as

$$\mathbf{R}(\gamma;\theta,\phi) = T^{-1}(\theta,\phi)R_z(\gamma)T(\theta,\phi) \qquad \text{(A.A.2a)}$$

$$T(\theta,\phi) = R_y(\phi)R_z(\theta) \qquad \text{(A.A.2b)}$$

$$\begin{bmatrix} p' \\ q' \\ r' \end{bmatrix} = \mathbf{R}(\gamma;\theta,\phi)\begin{bmatrix} p \\ q \\ r \end{bmatrix} \qquad \text{(A.A.2c)}$$

where $\mathbf{R}(\gamma; \theta, \phi)$ and $T(\theta, \phi)$ denote the rotation through angle γ clock-wise about axis (θ, ϕ) and the transformation of the coordinate system from (x, y, z) to (x', y', z'), respectively.

If the rotation axis z' is given as [u v w], then instead of using (θ,ϕ) we can substitute $\cos\phi = \frac{w}{r}$, $\sin\phi = \sqrt{1-\cos^2\phi}$, $\cos\theta = \frac{u}{r\sin\phi}$ and $\sin\theta = \frac{v}{r\sin\phi}$ into equation (A.A.2).

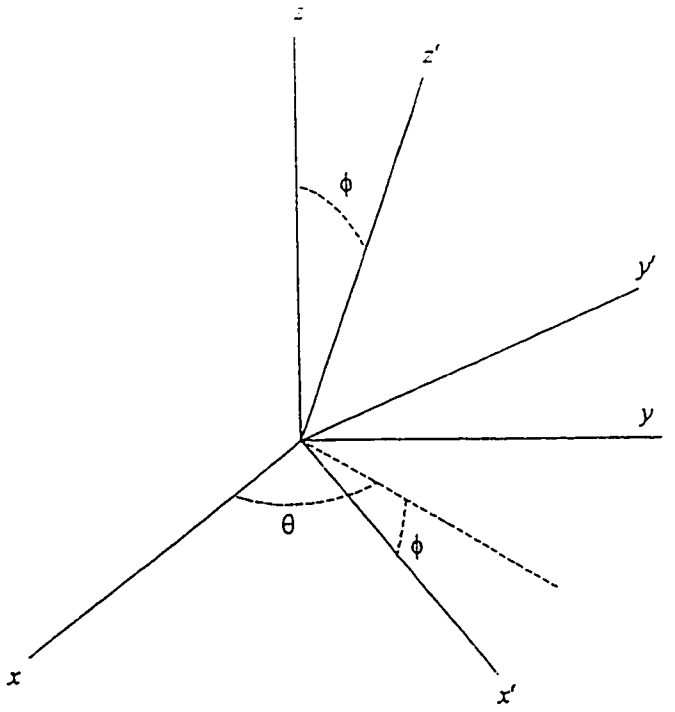

Figure A.A.1. Transformation of coordinates form (x, y, z) to (x', y', z').

Appendix B. Orthogonal matrices for proper rotations

$$R_1 = R(E) = \begin{pmatrix} 1 & 0 & 0 \\ 0 & 1 & 0 \\ 0 & 0 & 1 \end{pmatrix}$$

$$R_2 = R(C_3^{xyz}) = \begin{pmatrix} 0 & 0 & 1 \\ 1 & 0 & 0 \\ 0 & 1 & 0 \end{pmatrix} \qquad R_3 = R(C_3^{2xyz}) = \begin{pmatrix} 0 & 1 & 0 \\ 0 & 0 & 1 \\ 1 & 0 & 0 \end{pmatrix}$$

$$R_4 = R(C_3^{x\bar{y}\bar{z}}) = \begin{pmatrix} 0 & 0 & -1 \\ -1 & 0 & 0 \\ 0 & 1 & 0 \end{pmatrix} \qquad R_5 = R(C_3^{2x\bar{y}\bar{z}}) = \begin{pmatrix} 0 & -1 & 0 \\ 0 & 0 & 1 \\ -1 & 0 & 0 \end{pmatrix}$$

$$R_6 = R(C_3^{\bar{x}\bar{y}z}) = \begin{pmatrix} 0 & 0 & 1 \\ -1 & 0 & 0 \\ 0 & -1 & 0 \end{pmatrix} \qquad R_7 = R(C_3^{2\bar{x}\bar{y}z}) = \begin{pmatrix} 0 & -1 & 0 \\ 0 & 0 & -1 \\ 1 & 0 & 0 \end{pmatrix}$$

$$R_8 = R(C_3^{\bar{x}yz}) = \begin{pmatrix} 0 & 0 & -1 \\ 1 & 0 & 0 \\ 0 & -1 & 0 \end{pmatrix} \qquad R_9 = R(C_3^{2\bar{x}yz}) = \begin{pmatrix} 0 & 1 & 0 \\ 0 & 0 & -1 \\ -1 & 0 & 0 \end{pmatrix}$$

$$R_{10} = R(U^x) = \begin{pmatrix} 1 & 0 & 0 \\ 0 & -1 & 0 \\ 0 & 0 & -1 \end{pmatrix} \qquad R_{11} = R(U^y) = \begin{pmatrix} -1 & 0 & 0 \\ 0 & 1 & 0 \\ 0 & 0 & -1 \end{pmatrix}$$

$$R_{12} = R(U^z) = \begin{pmatrix} -1 & 0 & 0 \\ 0 & -1 & 0 \\ 0 & 0 & 1 \end{pmatrix} \qquad R_{13} = R(I) = \begin{pmatrix} -1 & 0 & 0 \\ 0 & -1 & 0 \\ 0 & 0 & -1 \end{pmatrix}$$

Appendix C. Construction of the unitary multiplier representation at the symmetry point Γ for *sc* C_{60}.

Since **q** = 0, the multiplier (equation II.6.53a) is zero and the exponent term in equation (II.6.51b) is zero. The symmetry elements of the space group $Pa\bar{3}$ and the character table of the factor group T_h are given in section IV.8 (equation IV.6.1 and table IV.8.1). The orthogonal matrices for proper rotations are given in Appendix B.

Set matrix κ which represents the positions of 4 molecules in a cell.

$$\kappa = \begin{bmatrix} 0 & \frac{1}{2} & \frac{1}{2} & 0 \\ 0 & \frac{1}{2} & 0 & \frac{1}{2} \\ 0 & 0 & \frac{1}{2} & \frac{1}{2} \end{bmatrix} = \begin{bmatrix} 1 & 2 & 3 & 4 \end{bmatrix}$$

where each column represents the κth position in a cell (see table IV.6.1).

The unitary matrix for the element R will be in the form of

$$T(\mathbf{0};R) = \kappa' \otimes \begin{bmatrix} R & \mathbf{0} \\ \mathbf{0} & \pm R \end{bmatrix}$$

where κ' represents 4×4 matrix of $\delta(\kappa, F_0(\kappa';R))$ in equation (II.6.51b) and R and $\pm R$ in the second matrix represent the orthogonal matrices for linear and angular coordinates, respectively. The sign is positive for proper rotation and negative for improper rotation (see equation II.6.1 and 2).

a) $\mathbf{V}(R) = (0 \quad 0 \quad 0)$

1) E

$$T(\mathbf{0};E) = \begin{bmatrix} 1 & 0 & 0 & 0 \\ 0 & 1 & 0 & 0 \\ 0 & 0 & 1 & 0 \\ 0 & 0 & 0 & 1 \end{bmatrix} \otimes \begin{bmatrix} R(E) & \mathbf{0} \\ \mathbf{0} & R(E) \end{bmatrix} = \begin{bmatrix} \mathbf{E} & \mathbf{0} & \mathbf{0} & \mathbf{0} \\ \mathbf{0} & \mathbf{E} & \mathbf{0} & \mathbf{0} \\ \mathbf{0} & \mathbf{0} & \mathbf{E} & \mathbf{0} \\ \mathbf{0} & \mathbf{0} & \mathbf{0} & \mathbf{E} \end{bmatrix}$$

where the last matrix shows the definition of the operation $\otimes$ and 6×6 matrix **E** is given as

$$\mathbf{E} = \begin{bmatrix} R(E) & \mathbf{0} \\ \mathbf{0} & R(E) \end{bmatrix}$$

2) C_3^{xyz}

$$R(C_3^{xyz}) \cdot \boldsymbol{\kappa} = \begin{bmatrix} 0 & 0 & \frac{1}{2} & \frac{1}{2} \\ 0 & \frac{1}{2} & \frac{1}{2} & 0 \\ 0 & \frac{1}{2} & 0 & \frac{1}{2} \end{bmatrix}$$

Thus $\boldsymbol{\kappa}' = [1\ 4\ 2\ 3]$

where each number κ represents the column vector for κth position.

$$\boldsymbol{\kappa}' = \begin{bmatrix} 1 & 0 & 0 & 0 \\ 0 & 0 & 1 & 0 \\ 0 & 0 & 0 & 1 \\ 0 & 1 & 0 & 0 \end{bmatrix}$$

$$T(\mathbf{0};C_3^{xyz}) = \begin{bmatrix} 1 & 0 & 0 & 0 \\ 0 & 0 & 1 & 0 \\ 0 & 0 & 0 & 1 \\ 0 & 1 & 0 & 0 \end{bmatrix} \otimes \begin{bmatrix} R(C_3^{xyz}) & \mathbf{0} \\ \mathbf{0} & R(C_3^{xyz}) \end{bmatrix}$$

3) C_3^{2xyz}

$$T(\mathbf{0};C_3^{2xyz})=\begin{bmatrix}1&0&0&0\\0&0&0&1\\0&1&0&0\\0&0&1&0\end{bmatrix}\otimes\begin{bmatrix}R(C_3^{2xyz})&\mathbf{0}\\\mathbf{0}&R(C_3^{2xyz})\end{bmatrix}$$

4) $I = IE$

$$T(\mathbf{0};I)=\begin{bmatrix}1&0&0&0\\0&1&0&0\\0&0&1&0\\0&0&0&1\end{bmatrix}\otimes\begin{bmatrix}R(IE)&\mathbf{0}\\\mathbf{0}&-R(IE)\end{bmatrix}=\begin{bmatrix}1&0&0&0\\0&1&0&0\\0&0&1&0\\0&0&0&1\end{bmatrix}\otimes\begin{bmatrix}-R(E)&\mathbf{0}\\\mathbf{0}&R(E)\end{bmatrix}$$

5) IC_3^{xyz}

$$T(\mathbf{0};IC_3^{xyz})=\begin{bmatrix}1&0&0&0\\0&0&1&0\\0&0&0&1\\0&1&0&0\end{bmatrix}\otimes\begin{bmatrix}-R(C_3^{xyz})&\mathbf{0}\\\mathbf{0}&R(C_3^{xyz})\end{bmatrix}$$

6) IC_3^{2xyz}

$$T(\mathbf{0};IC_3^{2xyz})=\begin{bmatrix}1&0&0&0\\0&0&0&1\\0&1&0&0\\0&0&1&0\end{bmatrix}\otimes\begin{bmatrix}-R(C_3^{2xyz})&\mathbf{0}\\\mathbf{0}&R(C_3^{2xyz})\end{bmatrix}$$

b) $\mathbf{V}(R)=\begin{pmatrix}\frac{1}{2}&\frac{1}{2}&0\end{pmatrix}$

$$\begin{bmatrix}\frac{1}{2}&\frac{1}{2}&\frac{1}{2}&\frac{1}{2}\\\frac{1}{2}&\frac{1}{2}&\frac{1}{2}&\frac{1}{2}\\0&0&0&0\end{bmatrix}+\begin{bmatrix}0&\frac{1}{2}&\frac{1}{2}&0\\0&\frac{1}{2}&0&\frac{1}{2}\\0&0&\frac{1}{2}&\frac{1}{2}\end{bmatrix}=\begin{bmatrix}\mathbf{2}&\mathbf{1}&\mathbf{4}&\mathbf{3}\end{bmatrix}$$

$$\text{set } \kappa'' = \begin{bmatrix} 0 & 1 & 0 & 0 \\ 1 & 0 & 0 & 0 \\ 0 & 0 & 0 & 1 \\ 0 & 0 & 1 & 0 \end{bmatrix}$$

7) $\left\{C_2^x \middle| \frac{1}{2} \quad \frac{1}{2} \quad 0\right\}$

$$\kappa' = C_2^x \cdot \begin{bmatrix} 1 & 0 & 0 & 0 \\ 0 & 1 & 0 & 0 \\ 0 & 0 & 1 & 0 \\ 0 & 0 & 0 & 1 \end{bmatrix} = \begin{bmatrix} 1 & 0 & 0 & 0 \\ 0 & 1 & 0 & 0 \\ 0 & 0 & 1 & 0 \\ 0 & 0 & 0 & 1 \end{bmatrix}$$

$$T(\mathbf{0}; C_2^x) = \kappa'' \cdot \kappa' \otimes \begin{bmatrix} R(C_2^x) & \mathbf{0} \\ \mathbf{0} & R(C_2^x) \end{bmatrix} = \begin{bmatrix} 0 & 1 & 0 & 0 \\ 1 & 0 & 0 & 0 \\ 0 & 0 & 0 & 1 \\ 0 & 0 & 1 & 0 \end{bmatrix} \otimes \begin{bmatrix} R(C_2^x) & \mathbf{0} \\ \mathbf{0} & R(C_2^x) \end{bmatrix}$$

8) $\left\{C_3^{\bar{x}y\bar{z}} \middle| \frac{1}{2} \quad \frac{1}{2} \quad 0\right\}$

$$\kappa' = R(C_3^{\bar{x}y\bar{z}}) \cdot \kappa = [1\ 4\ 2\ 3]$$

$$\kappa' = \begin{bmatrix} 1 & 0 & 0 & 0 \\ 0 & 0 & 1 & 0 \\ 0 & 0 & 0 & 1 \\ 0 & 1 & 0 & 0 \end{bmatrix}$$

$$T(\mathbf{0}; C_3^{\bar{x}y\bar{z}}) = \kappa'' \cdot \kappa' \otimes \begin{bmatrix} R(C_3^{\bar{x}y\bar{z}}) & \mathbf{0} \\ \mathbf{0} & R(C_3^{\bar{x}y\bar{z}}) \end{bmatrix} = \begin{bmatrix} 0 & 0 & 1 & 0 \\ 1 & 0 & 0 & 0 \\ 0 & 1 & 0 & 0 \\ 0 & 0 & 0 & 1 \end{bmatrix} \otimes \begin{bmatrix} R(C_3^{\bar{x}y\bar{z}}) & \mathbf{0} \\ \mathbf{0} & R(C_3^{\bar{x}y\bar{z}}) \end{bmatrix}$$

9) $\left\{C_3^{2\bar{x}y\bar{z}} \middle| \frac{1}{2} \quad \frac{1}{2} \quad 0\right\}$

$$T(\mathbf{0};C_3^{2\bar{x}\bar{y}z})=\begin{bmatrix}0&0&0&1\\1&0&0&0\\0&0&1&0\\0&1&0&0\end{bmatrix}\otimes\begin{bmatrix}R(C_3^{2\bar{x}\bar{y}z})&\mathbf{0}\\\mathbf{0}&R(C_3^{2\bar{x}\bar{y}z})\end{bmatrix}$$

10,11,12) $\left\{IC_2^x\middle|\frac{1}{2}\quad\frac{1}{2}\quad 0\right\}\left\{IC_3^{\bar{x}\bar{y}\bar{z}}\middle|\frac{1}{2}\quad\frac{1}{2}\quad 0\right\}\left\{IC_3^{2\bar{x}\bar{y}z}\middle|\frac{1}{2}\quad\frac{1}{2}\quad 0\right\}$

$$T(\mathbf{0};IR)=\boldsymbol{\kappa}'\cdot\boldsymbol{\kappa}''\otimes\begin{bmatrix}-R(R)&\mathbf{0}\\\mathbf{0}&R(R)\end{bmatrix}$$

c) $\mathbf{V}(R)=\left(\frac{1}{2}\quad 0\quad\frac{1}{2}\right)$

$$\begin{bmatrix}\frac{1}{2}&\frac{1}{2}&\frac{1}{2}&\frac{1}{2}\\0&0&0&0\\\frac{1}{2}&\frac{1}{2}&\frac{1}{2}&\frac{1}{2}\end{bmatrix}+\begin{bmatrix}0&\frac{1}{2}&\frac{1}{2}&0\\0&\frac{1}{2}&0&\frac{1}{2}\\0&0&\frac{1}{2}&\frac{1}{2}\end{bmatrix}=\begin{bmatrix}\mathbf{3}&\mathbf{4}&\mathbf{1}&\mathbf{2}\end{bmatrix}$$

$$\text{set }\boldsymbol{\kappa}''=\begin{bmatrix}0&0&1&0\\0&0&0&1\\1&0&0&0\\0&1&0&0\end{bmatrix}$$

13) $\left\{C_2^z\middle|\frac{1}{2}\quad 0\quad\frac{1}{2}\right\}$

$$T(\mathbf{0};C_2^z)=\begin{bmatrix}0&0&1&0\\0&0&0&1\\1&0&0&0\\0&1&0&0\end{bmatrix}\otimes\begin{bmatrix}R(C_2^z)&\mathbf{0}\\\mathbf{0}&R(C_2^z)\end{bmatrix}$$

14) $\left\{C_3^{x\bar{y}\bar{z}}\middle|\frac{1}{2}\quad 0\quad\frac{1}{2}\right\}$

$$T(\mathbf{0};C_3^{xy\bar{z}})=\begin{bmatrix}0&0&0&1\\0&1&0&0\\1&0&0&0\\0&0&1&0\end{bmatrix}\otimes\begin{bmatrix}R(C_3^{xy\bar{z}})&\mathbf{0}\\\mathbf{0}&R(C_3^{xy\bar{z}})\end{bmatrix}$$

15) $\left\{C_3^{2\bar{x}y\bar{z}}\middle|\frac{1}{2}\quad 0\quad\frac{1}{2}\right\}$

$$T(\mathbf{0};C_3^{2\bar{x}y\bar{z}})=\begin{bmatrix}0&1&0&0\\0&0&1&0\\1&0&0&0\\0&0&0&1\end{bmatrix}\otimes\begin{bmatrix}R(C_3^{2\bar{x}y\bar{z}})&\mathbf{0}\\\mathbf{0}&R(C_3^{2\bar{x}y\bar{z}})\end{bmatrix}$$

16,17,18) $\left\{IC_2^{z}\middle|\frac{1}{2}\quad 0\quad\frac{1}{2}\right\}\left\{IC_3^{xy\bar{z}}\middle|\frac{1}{2}\quad 0\quad\frac{1}{2}\right\}\left\{IC_3^{2\bar{x}y\bar{z}}\middle|\frac{1}{2}\quad 0\quad\frac{1}{2}\right\}$

$$T(\mathbf{0};IR)=\boldsymbol{\kappa}'\cdot\boldsymbol{\kappa}''\otimes\begin{bmatrix}-R(R)&\mathbf{0}\\\mathbf{0}&R(R)\end{bmatrix}$$

d) $\mathbf{V}(R)=\left(0\quad\frac{1}{2}\quad\frac{1}{2}\right)$

$$\begin{bmatrix}0&0&0&0\\\frac{1}{2}&\frac{1}{2}&\frac{1}{2}&\frac{1}{2}\\\frac{1}{2}&\frac{1}{2}&\frac{1}{2}&\frac{1}{2}\end{bmatrix}+\begin{bmatrix}0&\frac{1}{2}&\frac{1}{2}&0\\0&\frac{1}{2}&0&\frac{1}{2}\\0&0&\frac{1}{2}&\frac{1}{2}\end{bmatrix}=\begin{bmatrix}\mathbf{4}&\mathbf{3}&\mathbf{2}&\mathbf{1}\end{bmatrix}$$

$$\text{set }\boldsymbol{\kappa}''=\begin{bmatrix}0&0&0&1\\0&0&1&0\\0&1&0&0\\1&0&0&0\end{bmatrix}$$

19) $\left\{C_2^{y}\middle|0\quad\frac{1}{2}\quad\frac{1}{2}\right\}$

$$T(\mathbf{0};C_2^y)=\begin{bmatrix}0&0&0&1\\0&0&1&0\\0&1&0&0\\1&0&0&0\end{bmatrix}\otimes\begin{bmatrix}R(C_2^y)&\mathbf{0}\\\mathbf{0}&R(C_2^y)\end{bmatrix}$$

20) $\left\{C_3^{\bar{x}\bar{y}z}\middle|0\quad\frac{1}{2}\quad\frac{1}{2}\right\}$

$$T(\mathbf{0};C_3^{\bar{x}\bar{y}z})=\begin{bmatrix}0&1&0&0\\0&0&0&1\\0&0&1&0\\1&0&0&0\end{bmatrix}\otimes\begin{bmatrix}R(C_3^{\bar{x}\bar{y}z})&\mathbf{0}\\\mathbf{0}&R(C_3^{\bar{x}\bar{y}z})\end{bmatrix}$$

21) $\left\{C_3^{2x\bar{y}\bar{z}}\middle|0\quad\frac{1}{2}\quad\frac{1}{2}\right\}$

$$T(\mathbf{0};C_3^{2x\bar{y}\bar{z}})=\begin{bmatrix}0&0&1&0\\0&1&0&0\\0&0&0&1\\1&0&0&0\end{bmatrix}\otimes\begin{bmatrix}R(C_3^{2x\bar{y}\bar{z}})&\mathbf{0}\\\mathbf{0}&R(C_3^{2x\bar{y}\bar{z}})\end{bmatrix}$$

22,23,24) $\left\{IC_2^y\middle|0\quad\frac{1}{2}\quad\frac{1}{2}\right\}\left\{IC_3^{\bar{x}\bar{y}z}\middle|0\quad\frac{1}{2}\quad\frac{1}{2}\right\}\left\{IC_3^{2x\bar{y}\bar{z}}\middle|0\quad\frac{1}{2}\quad\frac{1}{2}\right\}$

$$T(\mathbf{0};IR)=\boldsymbol{\kappa}'\cdot\boldsymbol{\kappa}''\otimes\begin{bmatrix}-R(R)&\mathbf{0}\\\mathbf{0}&R(R)\end{bmatrix}$$

Appendix D. The numerical method for calculation of the Debye function

The Debye function is defined as

$$D(x)=\frac{3}{x^3}\int_0^x f(z)dz \qquad \text{(A.D.1)}$$

where $f(z)=\frac{z^3}{e^z-1}$ (A.D.2)

(1) for large x

$$\text{Since } f(z)=z^3\left(e^{-z}+e^{-2z}+e^{-3z}+\cdots\right)=\sum_{n=1}^{m_1} z^3 e^{-nz} \qquad \text{(A.D.3)}$$

thus by partial integration we have

$$D(x)=3\sum_{n=1}^{m_1}\frac{6}{n^4}x^{-3}-e^{-nx}\left(\frac{1}{n}+\frac{3}{n^2}x^{-1}+\frac{6}{n^3}x^{-2}+\frac{6}{n^4}x^{-3}\right) \qquad \text{(A.D.4)}$$

With $m_1 = 16$, the error is less than 10^{-8} in the range of x > 1. However, as x goes to zero, we need more terms.

(2) for small x

$f(z)$ has been approximated by the polynomial series.

$$f(z)=z^2+az^3+bz^4+\cdots=\sum_{n=1}^{m_2} a_n z^{n+1} \qquad \text{(A.D.5)}$$

Then

$$D(x)=\sum_{n=1}^{m_2}\frac{3a_n}{n+2}x^{n-1} \qquad \text{(A.D.6)}$$

For $m_2 = 6$ the coefficients a_n have been determined by the least-square method in the range of $0 \le x \le 1.2$ (table A.D.1). In that range the error is less than 10^{-8}.

The derivative of Debye function is given as

$$D'(x) = -\frac{3}{x}D(x) + \frac{3}{e^x - 1} \qquad \text{(A.D.7)}$$

The $f(z)$ is shown in figure A.D.1 where the solid line ($0< x <1.16$) is for equation (A.D.5) and the dashed line ($1.16 < x$) is for equation (A.D.3). In figure A.D.2 the solid line is for Debye function $D(x)$ given by equation (A.D.6) for $0 < x < 1.16$ and equation (A.D.4) for $1.16 < x$. The dashed line is for its derivative given by equation (A.D.7).

Table A.D.1. The coefficients in equation (A.D.6)

n	a_n
1	1.0000000
2	-0.4999934
3	0.0832852
4	0.0001339
5	-0.0015694
6	0.0001204

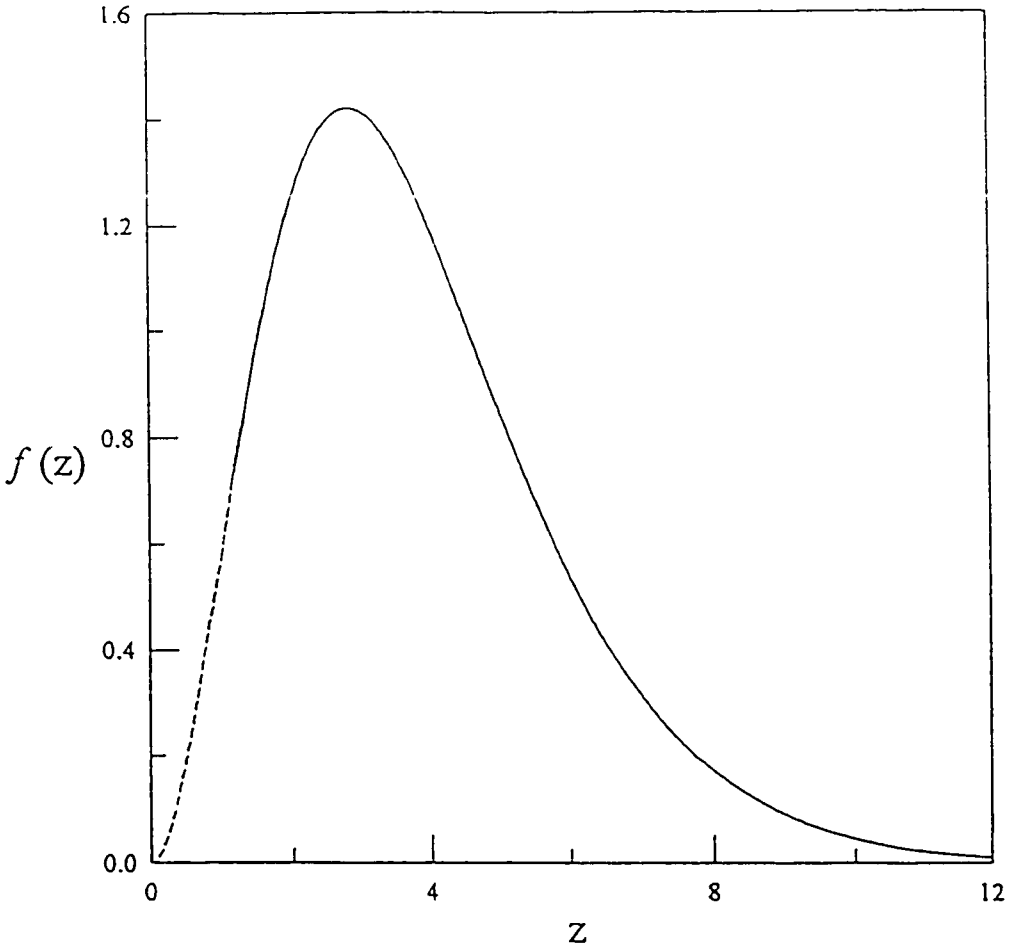

Figure A.D.1. $f(z)=\frac{z^3}{e^z-1}$ approximated by equation (A.D.3) for 1.16 < x and by equation (A.D.5) for 0< x < 1.16.

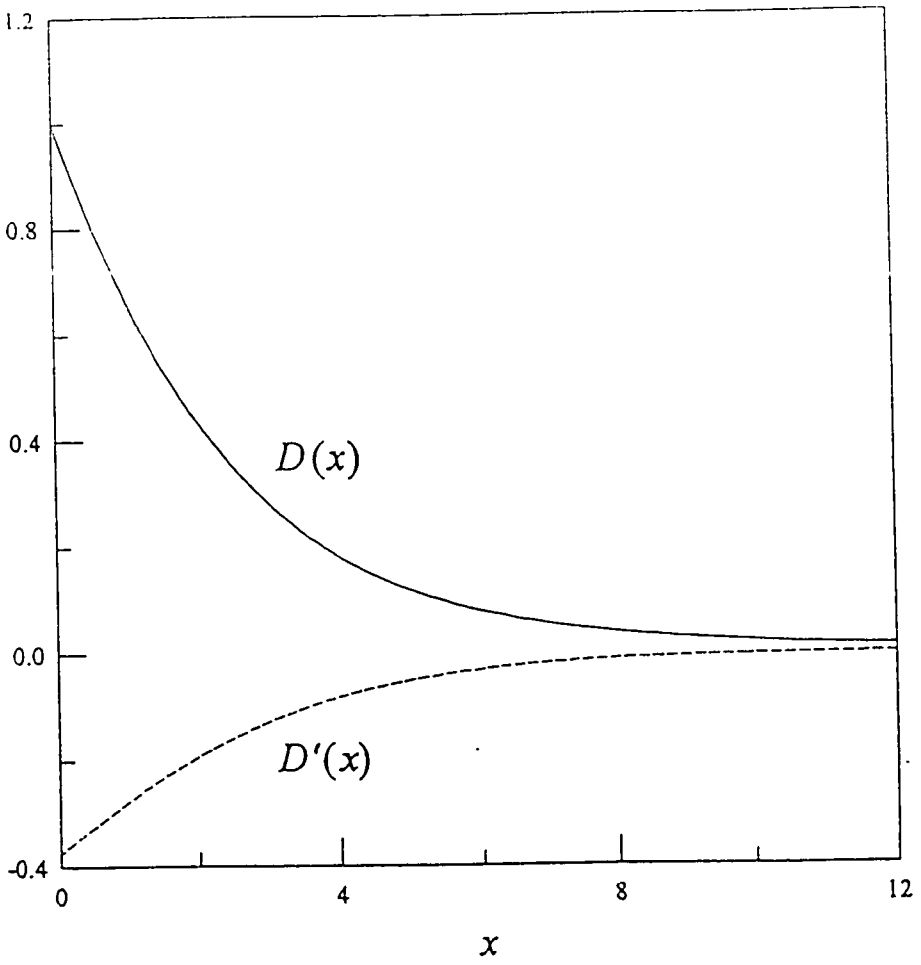

Figure A.D.2. Debye function approximated by equation (A.D.4) for $1.16 < x$ and by equation (A.D.6) for $0 < x < 1.16$.

References

[1] R.A. Huggins, High Conductivity Solid Ionic Conductors: Recent Trends and Applications, ed. by T. Takahashi, World Science, NJ, (1988) 664.

[2] J. Maier, Science and Technology of Fast Ion Conductors, ed. by H.L. Tuller and M. balkanski, NATO ASI Series B: Physics V. 199, Plenum Press, NY, (1989) 299.

[3] H.L. Tuller, Science and Technology of Fast Ion Conductors, ed. by H.L. Tuller and M. balkanski, NATO ASI Series B: Physics V. 199, Plenum Press, NY, (1989) 303.

[4] M. Bettman and C.R. Peters, J. Phys. Chem., 73 (1969) 1774.

[5] G.C. Farrington and J.L. Briant, Mat. Res. Bull., 13 (1978) 763.

[6] Y.F. Yu Yao and J.T. Kummer, J. Inorg. Nucl. Chem., 29 (1967) 2453.

[7] G.C. Farrington and B. Dunn, Solid State Ionics, 7 (1982) 267.

[8] R.F. Curl and R.E. Smalley, Scientific American, October (1991) 54.

[9] D.E. Koshland, Jr., Science, 254 (1991)1705.

[10] H.W. Kroto, A.W. Allaf and S.P. Balm, Chem. Rev., 91 (1991) 1213.

[11] L.F. Lindoy, Nature, 357 (1992) 443.

[12] A.F. Herard, M.J. Roseeinsky, R.C. Haddon, D.W. Murphy, S.H. Glarum, T.T.M. Palstra, A.P. Ramirez and A.R. Kortan, Nature, 350 (1991) 600.

[13] M.J. Rosseinsky, A.P. Ramirez, S.H. Glarum, D.W. Murphy, R.C. Haddon, A.F. Hebard, T.T.M. Palstra, A.R. Kortan, S.M. Zahrurak and A.V. Makhija, Physical Review, 66 (1991) 2830.

[14] K. Tanigaki, I. hirosawa, T.W. Ebbesen, J. Mizuki, Y. Shimakawa, Y. Kubo, J.S. Tsai and S. Kuroshima, Nature, 356 (1992) 419.

[15] M.J. Roseinsky, D.W. Murphy, R.M. Fleming, R.Tycko, A.P. Ramirez, T. Siegrist, G. Dabbagh and S.E. Barrett, Nature, 356 (1992) 416.

[16] P.W.Stephens, L. Mihaly, P.L. Lee, R.L. Whetten, S.M. Huang, R. Kaner, F. Deiderich and K. Holczer, Nature, 351 (1991) 632.

[17] R.M. Fleming, A.P. Ramirez, M.J. Rosseinsky, D.W. Murphy, R.C. Haddon, S.M. Zahurak and A.V. Makhija., Nature, 352 (1991) 787.

[18] A.R. Kortan, N. Kopylov, S. Glarum, E.M. Gyorgy, A.P. Ramirez, R.M. Fleming, F.A. Thiel and R.C. Haddon, Nature, 355 (1992) 529.

[19] J.T. Mckinnon, J. Phys. Chem., 95 (1991) 8941.

[20] Y. Hamanaka, S. Nakashima, M. Hangyo, H. Shinohara and Y. Saito, Phys. Rev. B, 48 (1993) 8510.

[21]. W.I.F. David, R.M. Ibberson, J.C. Mattewman, K. Prassides, T.J.S. Dennis, J.P. Hare, H.W. Kroto, R. Taylor and D.R.M. Walton, Nature, 353 (1991) 147.

[22] M.S. Dresselhaus, G. Dresselhaus and P.C. Eklund, Science of fullerenes and carbon nanotubes, Academic Press, NY, (1995).

[23] J.D. Wright, Molecular crystals, Cambridge University Press, (1987).

[24] D.A. McQuarrie, Statistical Thermodynamics, Harper & Row, NY, (1973).

[25] K. Huang, Statistical mechanics 2nd ed., John Wiley & Sons, NY, (1987).

[26] A.I. Kitaigorodsky, Molecular crystals and molecules, Academic Press, NY 1973.

[27] G. Venkataraman and V.C. Sahni, Review of modern physics, 42 (1970) 409.

[28] A.A. Maradudin and S.H. Vosko, Review of modern physics, 40 (1968) 1.

[29] S. Chandra, Superionic Solid: Principles and Applications, North-Holland, Asterdam, (1981) 17 - 128.

[30] J.S. Kasper, Solid Electrolytes: General Principles, Characterization, Materials, Applications, ed. by P. Hagenmuller and W.V. Gool, Academic Press, NY, (1978) 217.

[31] G.C. Farrington and J.L. Briant, Science, 204 (1979) 1371.

[32] W.D. Kingery, Introduction to Ceramics 2nd. ed., John Wiley & Sons, NY, (976).

[33] R.A. Huggins, Solid Electrolytes: General Principles, Characterization, Materials, Applications, ed. by P. Hagenmuller and W.V. Gool, Academic Press, NY, (1978) 27.

[34] H.L. Tuller, Science and Technology of Fast Ion Conductors, ed. by H.L. Tuller and M. balkanski, NATO ASI Series B: Physics V. 199, Plenum Press, NY, (1989) 51.

[35] M. Armand and M. Gauthier, High Conductivity Solid Ionic Conductors: Recent Trends and Applications, ed. by T. Takahashi, World Science, NJ, (1988) 114.

[36] J.B. Wagner, Jr., High Conductivity Solid Ionic Conductors: Recent Trends and Applications, ed. by T. Takahashi, World Science, NJ, (1988) 146.

[37] J. Maier, Science and Technology of Fast Ion Conductors, ed. by H.L. Tuller and M. balkanski, NATO ASI Series B: Physics V. 199, Plenum Press, NY, (1989) 89.

[38] F.W. Poulsen, High Conductivity Solid Ionic Conductors: Recent Trends and Applications, ed. by T. Takahashi, World Science, NJ, (1988) 166.

[39] I. Riess, Science and Technology of Fast Ion Conductors, ed. by H.L. Tuller and M. balkanski, NATO ASI Series B: Physics V. 199, Plenum Press, NY, (1989) 23.

[40] B.C.H. Steele, High Conductivity Solid Ionic Conductors: Recent Trends and Applications, ed. by T. Takahashi, World Science, NJ, (1988) 402.

[41] J.T.S. Irvine and A.R. West, High Conductivity Solid Ionic Conductors: Recent Trends and Applications, ed. by T. Takahashi, World Science, NJ, (988) 201.

[42] A.K. Viswanath and S. Radhakrishina, High Conductivity Solid Ionic Conductors: Recent Trends and Applications, ed. by T. Takahashi, World Science, NJ, (1988) 280.

[43] B. Dunn and Farrington, Solid State Ionics, 18/19 (1985) 31.

[44] P.T. Moseley, in Sodium Sulfur Battery (eds. Sudworth J L and Tilley A R) Chapman and Hall, (1985) 19.

[45] R. Stevens and J.G.P. Binner, J.Mater. Sci., 19 (1984) 695.

[46] J.M. Newsam, Solid State Ionics, 6 (1982) 129.

[47] J. Fally, C. Lasne, Y. Lazennec, Y.L. Cars and P. Margotin, J. Electrochem. Soc., 120 (1973) 1296.

[48] J.H. Duncan, R.S. Gordon, R.W. Powers and R.J. Bones, in Sodium Sulfur Battery (eds. Sudworth J L and Tilley A R) Chapman and Hall, (1985) 79.

[49] A.V. Virkar, US Patent 4 113 928, (1978).

[50] R.W. Powers, Am. Ceram. Soc. Bull., 65 (1986) 1270.

[51] R.W. Powers, Am. Ceram. Soc. Bull., 65 (1986) 1277.

[52] G.D. Parfitt, in Dispersion of Powders in liquid 2nd ed. (ed. Parfitt G D) Wiley-Interscience, NY, (1973) 1.

[53] B.J. McEntire, G.R. Miller and R.S. Gordon, Ceram. Bull., 63 (1984) 792.

[54] J.H. Duncan and W.G. Bugden, Proc. Bt. Ceram. Soc., no. 31, (1981) 221.

[55] G.E. Youngblood, A.V. Virkar, W.R. Cannon and R.S. Gordon, Am. Ceram. Soc. Bull., 56 (1977) 206.

[56] A.D. Jatkar, I.B. Cutler and R.S. Gordon, in Ceramic Microstructures (eds. Fulrath R M and Pask J A) Westview Press, Boulder, Colorado, (1976) 414.

[57] M.W. Breiter, M. Maly-Schreiber, G. Allitsch and P. Linhardt, Solid State Ionics, 28-30 (1988) 369.

[58] A. Tan and P.S. Nicholson, Solid State Ionics, 26 (1988) 217.

[59] M. Masri and A. Petric, Mat. Res. Bull., 36 (1991) 917.

[60] G.W. Schäfer and W. Weppner, Key Eng. Mater., 59-60 (1991) 145.

[61] S.R. Tan, G.J. May, J.R. McLaren, G. Tappin and R.W. Davidge, Trans. J. Br. Ceram. Soc., 79 (1980) 120.

[62] H.W. Kroto, S.C. O'Brien, R.F. Curl and R.E. Smalley, Nature, 318 (1985) 162.

[63] M.D. Newton and R.E. Stanton, J. Am. Chem. Soc., 108 (1986) 2469.

[64] W. Krätschmer, L.D. Lamb, K. Fostiropoulos and D.R. Huffman, Nature, 347 (1990) 354.

[65] M.A. Wilson, L.S.K. Pang and A.M. Vassallo, Nature, 355 (1992) 117.

[66] O. Zhou and D.E. Cox, J. Phy. Chem. solids, 53 (1992) 1373.

[67] J.S. Tse, D.D. Klug, D.A. Wilkinson and Y.P. Handa, Chem. Phys. Letters, 183 (1991) 387.

[68] P.A. Heiney, J.E. Fischer, A.R. McGhie, W.J. Romanow, A.M. Denenstein, J.P. McCauley Jr., A.B. Smith III and D.E. Cox, Phys. Review Letters, 66 (1991) 2911.

[69] W.I.F. David, R.M. Ibberson, T.J.S. Dennis, J.P. Hare and K. Prassidies, Europhys. Lett., 18 (1992) 219.

[70] P.C. Chow, X. Jiang, G. Reiter, P. Wochner, S.C. Moss, J.D. Axe, J.C. Hanson, R.K. McMullan, R.L. Meng and C.W. Chu, Phys. Rev. letters, 16 (1992) 2943.

[71] P.A. Heiney, J. Phys. Chem. Solids, 53 (1992) 1333.

[72] T. Atake, T. Tanaka, H. Hawaji, K. Kikuchi, K. Saito, S. Suzuki, I. Ikemoto and Y. Achiba, Physica C, 427 (1991) 185.

[73] W.V. Steele, R.D. Chirico, N.K. Smith, W.E. Billups, P.R. Elmore and A.E. Wheeler, J. Phys. Chem., 96 (1992) 4731.

[74] V. Piacente, G. Gigli, P. Scardala, A. Giustini and D. Ferro, J. Phys. Chem., 99 (1995) 14052.

[75] P.C. Eklund, P. Zhou, K.A. Wang, G. Dresselhaus and M.S. Dresselhaus, J. Phys. Chem. Solids, 53 (1992) 1391.

[76] D.S. Bethune, G. Mijer, W.C. Tang, H.J. Rosen, W.G. Golden, H. Seki, C.A. Brown and M.S. de Vries, Chem. Phys. Lett., 179 (1991) 181.

[77] C.I. Frum, R. Engleman Jr., H.G. Hedderich, P.F. Bernath, L.D. Lamb and D.R. Huffman, Chem. Phys. Lett., 176 (1991) 504.

[78] J.R.D. Copley, D.A. Neumann, R.L. Cappelletti and W.A. Kamitakahara, J. Phys. Chem. Solids, 53 (1992) 1353.

[79] D.E. Weeks and W.G. Harter, J. Chem. Phys., 90 (1989) 4744.

[80] F. Negri, G. Orlandi and F. Zerbetto, J. Am. Chem. Soc., 113 (1991) 6037.

[81] O. Zhou, J.E. Fischer, N. Coustel, S. Kycia, Q. Zhu, A.R. McGhie, W.J. Romanow, J.P. McCauley Jr., A.B. Smith III and D.E. Cox, Nature, 351 (1991) 462.

[82] Q. Zhu, O. Zhou, N. Coustel, G.B.M. Vaughan, J.P. McCauley Jr., W.J. Romanow, J.E. Fischer, A.B. Smith III, Science, 254 (1991) 545.

[83] R.C. Haddon, A.F. Hebard, M.J. Rosseinsky, D.W. Murphy, S.J. Duclos, K.B. Lyons, B. Miller, J.M. Rosamilia, R.M. Fleming, A.R. Kortan, S.H. Glarum, A.V.

Makhija, A.J. Muller, R.H. Eick, S.M. Zahurak, R. Tycko, G. Dabbagh and F.A. Thiel, Nature, 350 (1991) 320.

[84] W.E. Pickett, Nature, 351 (1991) 602.

[85] P.J. Benning, J.L. Martins, J.H. Weaver, L.P.F. Chibante and R.E. Smalley, Science, 252 (1991) 1417.

[86] P.W. Stephens, Nature, 356 (1992) 383.

[87] S.P. Kelty, C.C. Chen and C.M. Lieber, Nature, 352 (1991) 223.

[88] J.E. Schriber, D.L. Overmeyer, H.H. Wang, J.M. Williams, K.D. Carlson, A.M. Kini, U. Welp and W.K. Kwok, Physica C, 178 (1991) 137.

[89] G. Spam, J.D. Thomson, S.M. Huang, R.B. Kaner, F. Diederich, R.L. Whetten, G. Grüner and K. Holczer, Science, 252 (1991) 1829.

[90] T.W. Ebbesen, J.S. Tsai, K. Tanigaki, J. Tabuchi, Y. Shimakawa, Y. Kubo, I. Hirosawa and J. Mizuki, nature, 355 (1992) 620.

[91] R.M. Fleming, M.J. Rosseinsky, A.P. Ramirez, D.W. Murphy, J.C. Tully, R.C. Haddon, T. Siegrist, R. Tycko, S.H. Glarum, P. Marsh, G. Dabbagh, S.M. Zahurak, A.V. Makhija and C. Hampton, Nature, 352 (1991) 701.

[92] D.M. Poirier, D.W. Owens and J.H. Weaver, Phys. Rev. B, 51 (1995) 1830.

[93] P.W. Stephens, G. Bortel, G. Faigel, M. Tegze, A. Janossy, S. Pekker, G. Oszylanyl and L. Forro, Nature, 370 (1994) 636.

[94] J.E. Fischer and P.A. Heiney, J. Phys. Chem. Solids, 54 (1993) 1725.

[95] T. Yildirim, J.E. Fischer, A.B. Harris, P.W. Stephens, D. Lin, L. Brars, R.M. Strongin, A.B. Smith III, Phys. Rev. Lett., 71 (1993) 1383.

[96] J.E. Fischer, Materials Science and Engineering, B19 (1993) 90.

[97] Y. Chabre, D. Djurado, M. Armand, W.R. Romanow, N. Coustel, J.P. McCauley Jr., J.E. Fischer and A.B. Smith III, J. Am. Chem. Soc., 114 (1992) 764.

[98] S. Trasatti, in Comprehensive treatise of electrochemistry V. 5, ed. by J. O'M Bockris, Plenum Press, NY, (1980) 45.

[99] J. O'M Bockris and S.U.M. Kahn, Surface electrochemistry a molecular level approach, Plenum Press, NY, (1993).

[100] W. Weppner, Solid state electrochemistry, ed.by Peter G. Bruce, Cambridge, University Press, (1995) 199.

[101] T. Kudo and K. Fueki, Solid state ionics, Kodansha, Tokyo, (1990).

[102] H. Rickert, Electrochemistry of solids an introduction, Springer-Verlag, NY, (1982).

[103] K.S. Forland, T. Forland and S.K. Ratkje, Irreversible thermodynamics theory and application, John Willey & Sons, NY, (1988).

[104] W. Weppner, Science and Technology of Fast Ion Conductors, ed. by H.L. Tuller and M. Balkanski, NATO ASI Series B: Physics V. 199, Plenum Press, NY, (1989) 197.

[105] J. Schoonman and P.H. Bottelberghs, Solid Electrolytes: General Principles, Characterization, Materials, Applications, ed. by P. Hagenmuller and W.V. Gool, Academic Press, NY, (1978) 335.

[106] C.H.P. Lupis, Chemical Thermodynamics of Materials, North-Holland, NY, (1983).

[107] G.M. Bell and D.A. Lavis, Statistical mechanics of lattice models, Ellis Horwood ltd., Chichester, England, (1989).

[108] N.W. Ashcroft and N.D. Mermin, Solid state physics, Saunders College Publishing, NY, (1976).

[109] W.R. McKinnon, in Solid state electrochemistry ed. by P.G. Bruce, University Press, Cambridge, (1995) 163.

[110] N.A. Gokcen, Statistical thermodynamics of alloys, Plenum Press, NY, (1986).

[111] R.A. Swalin, Thermodynamics of solids 2nd ed., John Wiley & Sons, NY, (1972) 117.

[112] W.A. Oates, J. of Materials Science, 16 (1981) 3235.

[113] G. Venkataraman, Dynamics of perfect crystals, MIT Press, (1975).

[114] H. Goldstein, Classical mechanics 2nd ed., Addison-Wesley, Massachusetts, (1981).

[115] M. T. Dove, Introduction to lattice dynamics, Cambridge University Press, (1993).

[116] J.S. Blakemore, Solid state physics 2nd ed.,Cambridge University Press (1985).

[117] J. F. Cornwell, Group theory in physics, Academy Press, (1984).

[118] G. Burns, Introduction to group theory with applications, Academic press, NY, (1977)

[119] M. Rivier and A.D. Pelton, Ceram. Bull., 57 (1978) 183.

[120] S.G. Whiteway, M. Coll-Palagos and C.R. Masson, Ceram. Bull., 40 (1961) 432.

[121] D.R. Burfield and R.H. Smithers, J. Org. Chem., 48 (1983) 2420.

[122] M. Casey, J. Leonard, B. Lygo and G. Proter, Advanced Practical Organic Chemistry, Blackie, Glasgow and London, (1990) 28.

[123] J.T. Kummer, Prog. in Solid State Chem., 7 (1972) 114.

[124] R.W. Davidge, Mechanical Behaviour of Ceramics, Cambridge University Press, Oxford, (1979) 84.

[125] W.H. Dumbaugh and P.S. Danielson, in Commercial Glasses, Advances in Ceramics V18 (ed. Boyd D C), (1986) 115.

[126] B.D. Cullity, Elements of X-ray diffraction 2nd ed., Addison-Wesley, Massachusetts, (1978)

[127] D.W. Murphy, M.J. Rosseinsky, R.M. Fleming, R. Tycko, A.P. Ramirez, R.C. Haddon, T. Siegrist, G. Dabbagh, J.C. Tully and R.E. Walstedt, J. Phys. Chem. Solids, 53 (1992) 1321.

[128] M.J. Rosseinsky, D.W. Murphy, R.M. Fleming, R. Tycko, A.P. Ramirez, T. Siegrist, G. Dabbagh and S.E. Barrett, Nature, 356 (1992) 416.

[129] T. Yildirim, O. Zhou, J.E. Fischer, N. Bykovetz, R.A. Strongin, M.A. Cichy, A.B. Smith III, C.L. Lin and R. Jelinek, Nature, 360 (1992) 568.

[130] Q. Zhu, O. Zhou, J.E. Fischer, A.R. McGhie, W.J. Romanow, R.M. Strongin, M.A. Cichy and A.B. Smith III, Phys. Rev. B, 47 (1993) 13948.

[131] V.R. Belosludov and V.P. Shpakov, Mod. Phys. Lett. B, 6 (1992) 1209.

[132] J. Zak, The irreducible representations of space groups, W.A. Benjamin Inc., NY, (1969).

[133] M. Sprik, A. Cheng and M.L. Klein, J. Phys. Chem, 96 (1992) 2029.

[134] Z. Gamba, J. chem. phys., 97 (1992) 553.

[135] J.P. Lu, X.P. Li and R.M. Martin, Phys. Rev. Letters, 68 (1992) 1551.

[136] D.Lamoen and K.H. Michel, Z. Phys. B, 91 (1993) 323.

[137] T. Yildrim, A.B. Harris and S.C. Erwin, Phys. Rev. B, 48 (1993) 1888.

[138] R. Tycko, G. Dabbagh, R.M. Fleming, R.C. Haddon, A.V. Makhija and S.M. Zahurak, Phys. Review Letters, 67 (1991) 1886.

[139] C. Pan, M.P. Sampson, Y. Chai, R.H. Hauge and J.L. Margrave, J. Phys. Chem., 95 (1991) 2945.

[140] A. Lundin, B. Sundqvist, P. Skoglund, Å Fransson and S. Patterson, Solid state communications, 84 (1992) 879.

[141] S.J. Duclos, K. Brister, R.C. Haddon, A.R. Kotran and F.A. Thiel, Nature, 351 (1991) 380.

[142] J.E. Fischer, P.A. Heiney, A.R. McGhie, W.J. Romanow, A.M. Denenstein, J.P. McCauley Jr. and A.B. Smith III, Science 252 (1991) 1288.

[143] R.D. Johnson, C.S. Yannoni, H.C. Dorn, J.R. Salem and D.S. Bethune, Science, 255 (1992) 1235.

[144] L. Pintschovius, S.L. Chaplot, R. Heid, M. Haluska and H. Kuzmany, in Electronic properties of fullerenes, series in Solid state sciences V.117 ed.by H. Kuzmany, Springer 162.

[145] F. Seitz, Modern theory of solids, McGraw Hill, (1940).

[146] M. Ferrario, I.R. McDonald and M.L. Klein, J. Chem. Phys., 84 (1986) 3975.

[147] C. Kittel, Introduction to solid state physics 6th ed., John Wiley & sons, Inc., (1986).

[148] T. Yildrim and A.B. Harris, Physcal Review B, 46 (1992) 7878.

[149] A. Lundin and B. Sundqvist, Physical review B, 53 (1996) 8329.

[150] J. Kirchnerova and A.D. Pelton, Solid State Ionics, 93 (1996) 159.

J. Kirchnerova and A.D. Pelton, Solid State Ionics, 93 (1996) 165.

[151] D.R. Gaskell, Introduction to metallurgical thermodynamics 2nd ed., Mcgraw-Hill, (1981).

[152] F.A. Elrefaie and W.W. Smeltzer, J. Electrochem. Soc., 128 (1981) 1443.

[153] Srikanth and K.T. Jacob, Zeitschrift fur Metallkude, 82 (1991) 675.

[154] Data taken from FACT (Facility for the Analysis of Chemical Thermodynamics), a program developed by Center for Research in Computational Thermochemistry, Ecole Polytechnique, Montreal, Quebec and Chemical and Materials Engineering, Royal Military College, Kingston, Ontario.

[155] A. Petric, Pro. High Temperature Materials Chemistry IX, State College, PA, (1997).

[156] J.R. Olson, K.A. Topp and R.O. Pohl, Science, 259 (1993) 1145.

[157] W.I.F. David, R.M. Ibberson and T. Matsuo, Proc. Roy. Soc. Lond. A, 442 (1993) 129.